PERFORMANCE OF INELASTIC STRUCTURES ON MITIGATED AND UNMITIGATED LIQUEFIABLE SOILS: EVALUATION OF NUMERICAL SIMULATIONS WITH CENTRIFUGE TESTS

by

Jenny Ramirez

B.Sc., Escuela Superior Politécnica del Litoral, Ecuador, 2006

M.Sc., Universidad Nacional Autónoma de México, México, 2011

A thesis submitted to the

Faculty of the Graduate School of the

University of Colorado in partial fulfillment

of the requirements for the degree of

Doctor of Philosophy

Department of Civil, Environmental and Architectural Engineering

2019

This thesis entitled:

Performance of Inelastic Structures on Mitigated and Unmitigated Liquefiable Soils: Evaluation of Numerical Simulations with Centrifuge Tests

written by Jenny Ramirez

has been approved for the Department of Civil, Environmental and Architectural Engineering

_____

Prof. Shideh Dashti

_____

Prof. Abbie Liel

_____

Prof. Pedro Arduino

_____

Prof. Richard Regueiro

_____

Prof. Guido Camata

Date _____

The final copy of this thesis has been examined by the signatories, and we find that both the content and the form meet acceptable presentation standards of scholarly work in the above mentioned discipline

Jenny Ramirez (Ph.D. Civil Engineering)

Performance of Inelastic Structures on Mitigated and Unmitigated Liquefiable Soils: Evaluation of Numerical Simulations with Centrifuge Results

Thesis directed by Professors Shideh Dashti and Abbie Liel

Abstract

A series of dynamic centrifuge experiments involving soil-foundation-mitigation-structure (SFMS) interaction on liquefiable soils are used to evaluate the ability of state-of-the-art numerical modeling in reliably predicting system performance (*e.g.*, in terms of foundation settlement, rotation, roof accelerations, and column strains). This research comprises of two major components: (1) calibration and validation of two soil constitutive models with a series of fully drained and undrained, monotonic and cyclic, triaxial tests as well as a free-field centrifuge test on a layered, liquefiable soil deposit (without a building or a mitigation technique); and (2) numerical simulation of centrifuge tests that include multi-degree-of-freedom, shallow-founded, inelastic structures on mitigated and unmitigated liquefiable soil profiles, investigating the strengths and shortcomings of the available continuum numerical tools in capturing the key engineering demand parameters of interest.

Solid-fluid, fully-coupled, nonlinear, effective stress, 3D, finite element analyses are performed in parallel OpenSEES finite element platform with two different soil constitutive models. Overall, the numerical predictions agreed well with the experimental measurements in terms of acceleration, pore pressure, and settlement under structure in the presence of a relatively thin liquefiable layer or a mitigation strategy (when the extent of soil softening and volumetric strains due to sedimentation was reduced). However, these numerical simulations (and a continuum framework in general) could not capture volumetric strains due to sedimentation. This

shortcoming became critical in thicker, unmitigated liquefiable layers and in the far-field, leading to a notable underestimation of total settlements. The cumulative foundation rotation or tilt was also generally underestimated numerically, regardless of the constitutive model. Improvements are needed to better capture numerically the accumulation of localized shear and volumetric strains below the foundation's edges. The dynamic response of the soil-foundation-structure system and the required analysis time were highly sensitive to the choice of small-strain soil damping, soil constitutive model, and element type. They were also sensitive to the characteristics of the soil-foundation interface, but to a lesser extent. The results presented in this dissertation aim to guide future numerical modelers in simulating the seismic response of highly nonlinear SFMS systems and in better understanding the modeling sensitivities and uncertainties.

DEDICATION

To my dear parents

ACKNOWLEDGEMENTS

Unlike the shallow founded structures evaluated numerically in this study, the foundation of this dissertation lies on the deep gratitude for all of those who lit my path during this journey. It is a titanic task to count all the individuals who were a flame of encouragement, motivation, cooperation, and support during my doctoral studies. Therefore, my heartfelt apologies in case I involuntary forget to name you.

Lighting the path of others requires dedication. Prof. Shideh Dashti is a devoted advisor who tirelessly illuminated my road. She offered me numerous opportunities to mold me academically, professionally, and personally. I sincerely thank her for believing in me since day one (or even before). I was very fortunate to interact with her as her teaching assistant, her research assistant, and her student in the classrooms and in the field. I will never be able to thank her enough for all the meticulous feedback that I got from her. She inspired me to pursue no less than excellence, which will influence to the future roads I walk. I am thankful for all the time that she generously granted me to discuss my research progress. This is surely a gift that I cannot repay. Because I was instilled with her bright intellectual rigor, I hope that one day I can be a spark to others as well.

Since the beginning of my journey, I have been fortunate to be co-advised by a structural faculty, Prof. Abbie Liel. She has been an incandescent permanent light in this journey. Her excellent questions and advice were a necessary component for my academic and professional formation. Her enthusiasm for research and teaching taught me valuable lessons for my future endeavors. I cannot thank her enough for all the positive energy and abundant help that she gave me during my research.

As part of my comprehensive and defense committee, I must also thank to Prof. Richard Regueiro. I greatly appreciate his feedback during the preparation of this document as well as for all the lessons during class.

Despite the lucent lines (with clear goals) that my advisors traced for me every week, I must acknowledge that I did not walk alone in the route. Juan Olarte and Balaji Paramasivam were the greatest coworkers that I could ever asked for. They were responsible for all the centrifuge experiments employed in this research. From “Dear Eng. Juan” to “John”, Juan was a great support and, undoubtedly, a resplendent light in my journey. I cannot imagine walking this path without his company. I must thank him for always assuring my well-being along this path.

An extraordinary source of enlightenment takes credits with Prof. Pedro Arduino and Prof. Mahdi Taiebat. Working together for a journal publication gave me abundant feedback that turned into substantial contributions for my dissertation. I thank them for all the time they invested in me. Moreover, this recognition would be incomplete without acknowledging their former students who tirelessly worked with me: Long Chen, Alborz Ghofrani, and Andres Barrero. The synergy of all team working together made Chapter 3 of this dissertation possible.

As I was walking down this path, I gratefully met Prof. Guido Camata. I have him to thank for all the invaluable feedback that he provided me. With his structural expertise and his practical approach, our conversations had a high impact during the preparation of Chapter 4 of this dissertation. Among all his great ideas, there was one particularly important one he told me: “Jenny: email Massimo and tell him that you are ready to create a model in STKO”. Since then, Massimo Petracca became a bright torch in my route. Our several meetings were incredibly helpful and cannot thank him enough for all the time that he generously dedicated to me. I will always be in debt to him.

Reflecting upon present (and also past) lights of my life, I am particularly grateful for all the support to Dr. Xavier Vera. Since the day I met him (almost 15 years ago), he has never ceased to believe in me. He has not only been my professor, advisor, and boss, but more importantly, he has been my lifelong mentor and friend. I will forever thank him for introducing me to Prof. Dashti. He was convinced that I would be a good fit to her group, and his premonitions were extraordinarily true.

While walking this path, there were special individual candles that filled my life with light and joy. Friends who firmly stood by me regardless the circumstances. First of all, thanks to Johanna Coronel for helping me at the beginning of this path in those NYC times. Her generosity allowed me to encounter endless opportunities later on, and I will be thankful to her for life. Once I got to CU Boulder, Juan Pablo Gevaudan lighted up one of the first matches among all my friends at graduate school. I will always thank him for holding that flame with perseverance and enlightening fruitful paths of opportunities for me. It is incredibly hard to imagine my route at CU without his support and trust. Great thanks also go to Adriana Souto for coming to Boulder and bringing humor and adventures to my journey. Immense thanks to Sara Welsh-Huggins for being my English mentor during my first year at CU and my friend. I also want to thank her for sharing important family moments with me. Many thanks to Xavi Espinet for the bright light he gave me along this journey during our insightful conversations. Thanks to Brittany Carl for all the laughers and for thinking that I am "Ecuadoriable". I cannot forget to say thanks to "Los Patricios", my dear Nadia Yoza and Jefferson Yarce. Their unconditional support radiated above any standards. Thanks to Jorge Luis Barrera for his support and time along the way. Thanks to Sara Al-Haddad for trusting in me. I may say thanks to Marti Garriga for being such a great partner for team projects and "W2-tax parties". I also thank Raniero Beber for patiently interacting with me while discussing

our numerical challenges. Immense gratitude also goes to Yu-wei Hwang. It was a tremendous pleasure to work with him during my last semester at CU. His questions and help were incredibly valuable during the preparation of Chapter 4. I would like to thanks to other (current and past) friends from the CIEST: Peter Kirkwood, Brad Wham, Hiral Ghandi, and Lauren Strand. Many thanks also to my structural engineering friends: Rob Chase, Jakub Valigura, Travis Marcilla, Zachary Bullock, Dustin Cook, Polly Murray. They patiently enlightened me when I discussed my structural questions with them.

Walking along the route, nothing was more rewarding than mentoring students. They made me grow along this way and strengthen my dormant skills. Thanks to Lianne Brito, Merarys Caquias, Joshua McDuffin, and all those incredible students that I interacted with during the SMART program and PCDP at CU. I would like to thank them for teaching me infinite lessons and for all the times they asked for my feedback. It is important to mention that those experiences couldn't have been possible without the support of faculty and staff: Barbara Kraus, Kristen Lopez, Amahl Turczyn, Tammy Maldonado, and Kristin Swihart.

When the path seemed dark and tough at times, there were places I felt energized. This was nearby Lindsey Bugbee and Hernan Villanueva (and now little Remy), who have always opened the doors of their welcoming house and warm hearts to me. Sincere thanks for receiving me always with a big smile. Likewise, another warm and bright place that I found was close to Paola Almeida and her husband (Pete). Their trustworthy friendship shines at the necessary hearty touch. I am very grateful for their assistance and advices.

At times, people promised me that more light was coming. As every promised light the sparks that the Tiznado-Lozano brought to my life were warm and pleasant. After some semesters of their promised arrival, they finally came. I immeasurably thank Juan Carlos for his advices,

ideas, patience, friendship, and kind words in the most important moments. His light came to my path in the perfect stage of this route. His support was priceless and will be always treasured. In parallel, Titi generously conveyed her thoughts with festivity as well as maturity, giving me the trust that I needed in a friend during crucial decisions. Her friendship was (and will always be) treasured. Thanks also to Rafi for all those invaluable hugs that always made come back home with gratification. Meeting them taught me that, yes, light will come at the correct juncture.

As most of the paths in life, this route had valleys and mountains, and from time to time I needed more and more illumination. June and Bill Krantz were an incomparable source of light along this path. I must thank June for all her charisma and hospitality. I would also like to offer my special thanks to Bill for all those incredible chats and coffee/tea times on Sunday, which rekindled the sense of perseverance for every week. His transparent advice and passion for life were fundamental for my growth as student, engineer, and better human being.

I will warmly keep in my heart the special support and care that Caro Herrera has given me over the last ten years. I must thank her for rising our friendship to the highest levels. I truly appreciate that she has been in my side since I met her, as family members do.

Every time I needed it, a beam of light came from my little sister, Jessie Ramirez. I would like to express my great appreciation for her support and for always believing in me. I thank her for talking to me with her heart, looking always after my personal and spiritual growth. She is the clement soul that have not found anywhere else.

And at every moment of this path, and my life, I have always been fortunate to have in my hands two bright treasures: Yeny Calderon and Raul Ramirez, my exceptional parents. It is unmeasurable the gratitude I have for them; I definitely owe them all what I am today. I want to thank them for letting me dream big and supporting me at every step. My mom perfectly balances love and

rightness, encouraging me to give the best of myself in any situation. Without her moral lessons, I could not have even crawled half of my life. My dad takes the credits for my patience in life and passion for engineering. I will always admire him for the positive way he sees life and his curiosity for engineering. His attitude instilled me the right courage for my educational, professional, and personal activities. Thanks to God for accommodating all these lights in this path, where he walked with me.

****

This research is based upon work supported in part by the National Science Foundation (NSF) under Grant No. 1362696. Any opinions, findings, and conclusions or recommendations expressed in this thesis are those of the author and do not necessarily reflect the views of the NSF. This thesis was partially supported by the College of Engineering and Applied Science through the Dean's Graduate Assistantship for 2014-2015 academic year. In addition, this thesis was also founded by the Department of Civil, Environmental and Architectural Engineering at the University of Colorado Boulder through a Doctoral Assistantship for Dissertation Completion fir the Fall 2018.

****

This work utilized the Summit supercomputer, which is supported by the National Science Foundation (awards ACI-1532235 and ACI-1532236), the University of Colorado Boulder, and Colorado State University. The Summit supercomputer is a joint effort of the University of Colorado Boulder and Colorado State University.

CONTENTS

LIST OF TABLES

LIST OF FIGURES

CHAPTER 1

1 INTRODUCTION

1.1 Research Motivation

Soil liquefaction has caused excessive settlement and rotation of structures during previous earthquakes. Over the years, various mitigation techniques have evolved to address this hazard. Examples include ground densification, reinforcement with in-ground structural walls, and prefabricated vertical drains (PVDs), among others. Even though some of these mitigation methods have proved to effective in reducing the potential for liquefaction triggering and the resulting permanent deformations, previous case histories and physical model studies have shown that these improvements are not necessarily sufficient (down to acceptable levels). Further, seismic demand on the superstructure can increase on mitigated ground, adversely impacting the overall performance of soil-foundation-structure (SFS) systems if not considered in design. Currently, the influence of mitigation strategies on the seismic performance of the SFS system (in terms of acceleration demand, settlement, and tilt potential, as well as damage to the superstructure) is not well-understood under different conditions. This lack of understanding and the unavailability of well-calibrated and validated numerical tools limits our ability to reliably mitigate the liquefaction hazard in a performance-based framework.

In this dissertation, centrifuge experimental results are used to evaluate the limitations and capabilities of state-of-the-art, 3D, nonlinear, fully-coupled, effective stress numerical simulations

of the soil-(mitigation)-foundation-structure (SMFS) system on layered, liquefiable soil profiles. This understanding is essential, before these numerical tools can be used in design or in parametric studies, toward future performance-based mitigation procedures.

1.2 Research Objectives and Methodology

This research is part of a larger, integrated experimental and numerical study in geotechnical and structural engineering to evaluate the performance of multi-degree-of-freedom (MDOF), inelastic, shallow-founded structures on liquefiable soils, both with and without mitigation. This dissertation mainly focuses on the numerical modeling of the seismic response of two different MDOF structures on two layered liquefiable soil deposits, without mitigation and with ground densification and prefabricated vertical drains.

In the first phase of this study, a large number of static and cyclic, drained and undrained triaxial tests and a free-field centrifuge experiment (with a layered, liquefiable soil profile) were used to calibrate two, state-of-the-art, nonlinear soil constitutive models (The Pressure Dependent Multi-Yield plasticity surface PDMY02 and Simple Anisotropic sand SANISAND) implemented in the OpenSEES[1] finite-element platform. After an extensive calibration process of model parameters (Class C and Class C1 calibration), the two aforementioned constitutive models were shown to mostly capture soil's response at an element level, while also predicting the response in a boundary-value problem (free-field site response) in terms of accelerations and excess pore pressures, but not volumetric strains and settlements. This exercise pointed to the importance of capturing the time history of stress-strain and rate of excess pore pressure generation in soil under the strain range of interest at an element level as well as access to a more realistic boundary value problem with simultaneous generation, dissipation, and redistribution of pore pressures, in order

[1] OpenSEES is an Open Source Earthquake Engineering Simulator for developing application to simulate the performance of structural and geotechnical systems subjected to earthquakes

to better capture seismic site response. In no case did capturing number of cycles to liquefaction at an element level assist in better predicting the key demand parameters. Both models implemented in a continuum framework largely under-estimated settlements in the free-field, which are governed by volumetric strains due to sedimentation and partial drainage. After calibrating soil parameters at an element level or free-field, the nonlinear properties of structural models in OpenSEES were calibrated separately using monotonic and cyclic beam-column component tests on structural fuses as well as hammer impact tests under fixed-base conditions.

In the second phase of this investigation, 3D nonlinear, solid-fluid, fully-coupled, effective stress, dynamic finite-element (FE) analyses of seven additional centrifuge tests were performed in OpenSEES to simulate the seismic response of potentially inelastic, MDOF structures founded on mitigated and unmitigated, layered liquefiable soils. Soil parameters from Class C1 calibration (from the first stage of this research) were used for all the simulations that followed. Two potentially-inelastic, 3-story and 9-story, steel moment-resisting framed structures were considered on a 1m-thick mat and a 3m-high basement, respectively. Two layered, liquefiable soil profiles were considered, with variations in the thickness of loose Ottawa sand layer (*i.e.*, 4m and 6m). Two commonly used mitigation techniques were considered: 1) ground densification, and 2) enhanced drainage with prefabricated vertical drains (PVDs). The main goal was to evaluate the influence of selected mitigation mechanisms on the seismic performance and damage potential of the soil-foundation-structure (SFS) system, while varying the properties of the soil profile, structure, and foundation. Numerical results were compared with centrifuge experimental recordings (Olarte et al. 2017, 2018a, 2018b and Paramasivam et al. 2018a) to assess the limitations and capabilities of two state-of-the-art soil constitutive models, element types, and the

FE method in capturing key experimental observations and the sensitivity of the predictions to various modeling assumptions.

1.3 Organization of this Dissertation

This dissertation is organized into four chapters:

Chapter 1 describes the motivation of this research, the objectives, methodology, and organization of this dissertation.

Chapter 2 presents a literature review on observations from previous liquefaction case histories, physical, and numerical models.

Chapter 3 presents a manuscript published in the ASCE's *Journal of Geotechnical and Geoenvironmental Engineerin*g. The paper presents the calibration of two state-of-the-art soil constitutive models (multi-yield and bounding surface) and their limitations and capabilities in predicting seismic site response in a layered, liquefiable deposit based on a free-field centrifuge test. First, calibration was performed using element test results followed by a blind prediction of seismic site response in centrifuge. This comparison helped identify a number of important shortcomings, leading to a second calibration phase. The centrifuge experiment with no structure (free-field test) was particularly valuable in calibrating the soil parameters, as the tests involved a more realistic boundary value problem with simultaneous generation and dissipation of pore pressures.

Chapter 4 presents a manuscript that will be submitted to the ASCE's *Journal of Geotechnical and Geoenvironmental Engineerin*g. This paper focuses on the numerical simulation of the soil-foundation-mitigation-structure systems as modeled in seven centrifuge tests. These experiments were conducted by other graduate students using the 5.5 m-radius centrifuge facility at the University of Colorado Boulder. Two different types of structures, two different liquefaction

mitigation techniques, and two different soil profiles were investigated. Numerical predictions were compared with experimental data in terms of acceleration, pore pressure, settlement and tilt of foundation, bending strains of structural fuses, and roof accelerations. The capabilities and limitations of the advanced soil constitutive models are discussed, as well as some key considerations for modeling the SFMS systems.

Chapter 5 summarizes the conclusions of this research and provides recommendations for future research investigating the consequences and mitigation of the liquefaction hazard facing structures.

Appendices A, B, and C show the data and results concerned with the calibration of soil parameters shown in Chapter 3. Appendix D indicates the computational time and memory of the simulations presented in Chapter 4, and Appendix E shows the detailed comparison of all numerical and centrifuge experimental results involving the SFMS system.

CHAPTER 2

2 LITERATURE REVIEW

Many liquefaction mitigation techniques have evolved over the past years driven by recent earthquakes and damage to infrastructure due to soil liquefaction (*e.g.*, during the M_w=7.5 1964 Niigata earthquake in Japan; the M_w=7.7 1990 Luzon earthquake in Philippines; the M_w=7.5 1999 Kocaeli earthquake in Turkey; the M_w=6.3 to 7.1 2010-2011 sequence of earthquakes in Christchurch-New Zealand; among others). These techniques, which include ground densification, soil reinforcement, grouting and mixing techniques, and prefabricated vertical drains (PVDs), have the intent of reducing settlement, tilt, and damage on shallow-founded structures. Yet, the effectiveness and reliability of these techniques and the impact on the seismic performance of soil-foundation-structure (SFS) systems remain unclear. In particular, it is not clear what is the impact of different mitigation techniques on site response (*e.g.*, accelerations, excess pore pressures, and deformations) and the demand transferred to the foundation and superstructure (*e.g.*, floor/roof accelerations and story displacements), taking into account kinematic and inertial interaction in the SFS system. A better understanding of these responses and interactions is required, before one can realize the benefits of performance-based earthquake engineering in addressing and mitigating liquefaction and its consequences. Numerical modeling can provide insights into these mechanisms of behavior. But one first needs to understand the reliability of the existing numerical tools, before used in design.

2.1 Observations from Prior Case histories

Soil liquefaction has severely damaged the built environment in previous earthquakes. Excessive settlement, tilt, and lateral displacement on shallow-founded structures have been reported that exceeded those in the free-field (away from buildings) during previous strong earthquakes (*e.g.*, 1964 Niigata, Japan; 1989 Loma Prieta, United States; 1995 Kobe, Japan; 1999 Kocaeli, Turkey; 2010 Port-au-Prince, Haiti; 2011 Christchurch, New Zealand; 2016 Muisne, Ecuador; 2018 Palu, Indonesia). Despite previous observations, the current state of practice for evaluating liquefaction triggering and its consequences continues to rely heavily on empirical or semi-empirical procedures that assume free-field conditions (*e.g.*, Ishihara 1985; Cooke and Mitchell 1999; Youd et al. 2001; Seed et al. 2003; Idriss and Boulanger 2008). These procedures either completely ignore the presence of the structure or bring it in simplistically as an added pressure alone. Although such procedures have been repeatedly shown to be inadequate through prior case history and physical model studies, they continue to be used for assessing the effectiveness of mitigation strategies (like ground densification).

A few documented case histories have provided evidence that liquefaction countermeasures can reduce the negative effects of liquefaction on structures, but these measures have not always performed satisfactorily. For instance, after the 1964 Niigata, Japan earthquake (M_w=7.6), a four-story building on compacted ground experienced an unacceptable settlement and tilt (about 50 cm and 1 degree) due to soil liquefaction (Watanabe 1966). On the other hand, case histories from the 1989 Loma Prieta earthquake (M_w=6.9) showed that buildings on compacted soils mostly suffered minimal or no damage (Mitchell and Wentz 1991, and EERI 1989). However, an earthquake with a similar magnitude (the 1995 Kobe earthquake) revealed that buildings on soils treated (mitigated) with sand drains did not performed well in all cases (BTL Committee

1998; Fudo 1995, Hamada et al. 1995; Nakakita and Watanabe 1981; Shibata et al. 1996; Yasuda et al. 1996). The range of deformation in these cases and the reasons of failure are not known. More recently, during the 2011 Christchurch earthquake, liquefaction continued to cause settlement and tilt to unmitigated low- and mid-rise structures (Cubrinovski and McCahon 2012) and mitigated structures using stone columns (Wotherspoon et al. 2014). Hence, the effectiveness and reliability of liquefaction mitigation needs to be evaluated more rigorously, before the profession can employ performance-based methodologies in their design. In the absence sufficiently well documented case histories of buildings on mitigated liquefiable soils with instrumentation, physical and numerical modeling can provide valuable insight.

2.2 Prior Physical Model Studies

Over the past few years, physical modeling has been used to create new "case histories" under more controlled and simplistic conditions. With adequate instrumentation, these studies have enabled a better understanding of the timing and location of liquefaction triggering, soil-foundation-structure interaction (SFSI) effects on softened soils, various mechanisms of deformation active below structures, and effects of mitigation strategies on SFSI. Such experiments have also provided a better understanding of the potential tradeoffs associated with liquefaction mitigation which, on the one hand reduces a building's net settlement and possibly tilt, but on the other hand, amplifies the seismic demand transferred to the superstructure, potentially increasing shaking-induced damage. Physical modeling can also provide the data required to calibrate and validate advanced numerical tools, before they are used in practice.

Several researchers have performed shaking table tests in 1g or under increased gravity (in the geotechnical centrifuge) to evaluate the seismic performance of buildings on unmitigated liquefiable soil deposits (*e.g.*, Yoshimi and Tokimatsu 1977; Liu and Dobry 1997; Hausler 2002;

Adalier et al. 1998; Dashti at al. 2010a, b; Mitrani and Madabhushi 2013; Jones 2013; Chandra and Gueguen 2017). In most cases, the structure was represented by a simplistic surface-loaded rigid footing or linear-elastic, single-degree-of-freedom (SDOF) models. Fewer experimental studies have examined the response of model structures on mitigated soils (*e.g.*, Liu and Dobry 1997; Hausler 2002; Takemura et al. 2009; Kuriki et al. 2012; and Rasouli et al. 2015). These experimental studies generally showed that ground densification, soil reinforcement, and vertical drains can reduce settlement of shallow-founded structures. However, the structures were often represented as rigid blocks, which limited their ability to properly represent inertial interaction and ratcheting or their ability to evaluate deformations and damage in the superstructure.

More recently, as part of this integrated numerical-experimental study, Olarte et al. (2017, 2018a, b) and Paramasivam et al. (2018a, 2018b) investigated the performance of more realistic, multi-degree-of-freedom (MDOF), inelastic structures with different properties on both unmitigated and mitigated, liquefiable soil profiles in the centrifuge. In their experiments, they varied the properties of the structure (*e.g.*, inertial mass, height, force-deformation behavior, embedment depth), soil profile (thickness of the looser deposit, and variations in permeability), mitigation strategy (densification, reinforcement, and drainage), and base ground motion. Olarte et al. (2018) showed that the accelerations and forces in the superstructure can be amplified by increasing stiffness of the underlying soil. Likewise, Paramasivam et al. (2018a) concluded that adding PVDs can reduce the duration of large excess pore pressures and foundation's permanent settlement. However, PVDs can amplify the seismic demand transferred to the superstructure, which can amplify the flexural drifts and P-Δ effects about the foundation, which would in turn amplify tilt. The experiments by Olarte et al. (2017; 2018a, 2018b) and Paramasivam et al. (2018a) indicated the importance of evaluate the nonlinearity of structures in mitigated soils. The also

provided valuable insight into seismic interactions among soil, foundation, structure, and the mitigation strategy as well as a comprehensive dataset for the calibration and validation of numerical models.

2.3 Prior Numerical Studies

Followed by rapid advances in computational tools, fully-coupled, nonlinear, effective-stress, dynamic numerical modeling is a potent tool to simulate the seismic response of the soil-foundation-structure system in liquefiable ground. However, considerable attention is needed in the selection of the constitutive models and their calibration, in order to capture soil nonlinearity, softening due to the buildup of excess pore pressures, dilation at large shear strains, volumetric strains that result from shearing as well as dissipation and redistribution of pore water, and kinematic and inertial interactions resulting from SFSI.

Over the years, extensive research has been devoted to developing mathematical models to capture the stress-strain behavior of cohesionless soils under different loading paths. Based on traditional laboratory element tests, several researchers initially proposed elasto-plastic stress-strain theories with various degrees of complexity (*e.g.*, Duncan and Chang 1970; Lade 1977; Valanis 1982; Lade 1988), but these models (based on isotropic plastic hardening rules) could only capture the static response of sand. Subsequently, more complex material models have been developed that can simulate the cyclic behavior of frictional materials (*e.g.*, Prevost 1978; Dafalias and Hermann 1980; Mroz et al. 1981; Ghaboussi and Momen 1982; Prevost 1985; Elgamal et al. 1998; Kramer and Arduino 1999; Yang et al. 2003 Dafalias and Manzari 2004; Boulanger and Ziotopoulou 2015). Some of these model parameters can be directly derived from element tests, but others require a comprehensive calibration to obtain an overall fit to an experimental data. After an extensive calibration process, Ramirez et al. (2018) lately showed that PDMY02 and

SANISAND predict relatively well the accelerations and excess pore pressures in a layered liquefiable soil profile in the far-field (without a structure). However, models still have limitation in capturing volumetric strains due to sedimentation. It is not clear how these strengths and shortcomings affect the predicted performance of the structure and its underlying soil.

Some of the aforementioned constitutive models have been implemented in the finite-element or finite-difference platforms. A few examples include: the UBCSAND model developed by Puebla et al. (1997) and Park and Byrne (2004); the pressure-dependent-multiyield surface PDMY02 model developed by Elgamal et al. (2002) and Yang et al. (2008); the bounding surface Simple ANIsotropic SANISAND model and its variations originally developed by Dafalias and Manzari (2004); the UBC3D-PLM implemented by Tsegaye (2010); NTUA-SAND developed by Andrianopoulos et al. (2010a, 2010b); and PM4SAND developed by Boulanger and Ziotopoulou (2015).

The predictive capabilities of these recent models have often been evaluated individually either based on element-level tests or centrifuge results, typically with a single uniform sand layer with different geometries and configurations (*e.g.*, Manzari and Arulanandan and Scott 1993; Parra 1996; Elgamal et al. 2002; Manzari and Dafalias 2004; Andrianopoulos 2006; Taiebat et al. 2007; Yang et al 2008; Tasiopoulou et al. 2015a; Ghofrani and Arduino 2016; Ziotopoulou 2016; and Ekstrom and Ziotopoulou 2017). Popescu and Prevost (1993) and Popescu and Prevost (1995), among other researchers, calibrated their constitutive model parameters using both element and centrifuge test results as part of the VELACS project (Arulanandan and Scott 1993, 1994). Likewise, the Liquefaction Experiments and Analysis Project (LEAP) (Kutter et al. 2015) has recently enabled researchers to evaluate the response of uniform, sloped liquefiable deposits via a centrifuge experiment repeated at multiple facilities followed by blind predictions by numerical

modelers. However, the seismic response of more complex and realistically layered soil profiles was not investigated in LEAP, nor was the presence of a structure or mitigation.

A number of prior researchers have studied the dynamic interactions between a softened ground and structure using advanced soil models, but typically with simple representations of the superstructure. For instance, Adrianopoulos et al. (2006) used a rigid foundation on a layered soil deposit, including a liquefiable layer represented by a bounding surface soil model (Papadimitriou et al. 2001; Papadimitriou and Bouckovalas 2002). Popescu et al. (2006) carried out a plain-strain analysis of structures (modeled as a rigid foundation in 2D) on liquefiable soils represented with a multi-yield constitutive model.

Other researchers (*e.g.*, Lopez-Caballero and Farahmand-Razavi 2008; Dashti and Bray 2013; Karimi and Dashti 2016b; Luque and Bray 2017) numerically represented the structures as linear-elastic, single degree-of-freedom (SDOF) or multi-degree-of-freedom (MDOF) systems on 2D and 3D nonlinear soil domains (*e.g.*, UBCSAND, PDMY02). The studies generally found that it was critical to properly model's the building's inertial response to evaluate its critical influence on soil deformations. Karimi and Dashti (2016a,2016b) also showed the importance of modeling the system in 3D, as opposed to 2D (that is only appropriate for structures long in one direction), to capture the 3D nature of shear deformations and flow patterns below 3D foundations. These latter studies were a notable improvement to prior models with rigid foundations, and their use of linear-elastic SDOF structural models was deemed appropriate on unmitigated soil deposits, because the superstructure typically behaves elastically, and damage is due to foundation tilt and settlement. However, when mitigation techniques are employed, nonlinearity and damage in the superstructure may play an important role in the performance of the overall soil-foundation-structure (SFS) system, which could not be studied in prior models. Simultaneous modeling of soil

and structure's nonlinear response and interactions, however, requires careful calibration, validation, and knowledge of the underlying sensitivities, limitations, and capabilities, prior to use in practice or a parametric study.

In this dissertation, we present the capabilities and limitations of two state-of-the-art soil constitutive models in capturing the response of structures founded on mitigated and unmitigated layered liquefiable soils observed experimentally. The centrifuge experiments investigated the influence of mitigation on the response of potentially inelastic, MDOF structural models on shallow foundations (Olarte et al. 2017,2018a; Paramasivam et al. 2018a) and layered, liquefiable soil profiles. Two different mitigation techniques were employed: ground densification (DS) and enhanced drainage with prefabricated vertical drains (PVDs or DR). Subsequently, three-dimensional (3D), nonlinear, solid-fluid, fully-coupled, effective stress, dynamic finite-element (FE) analyses of the centrifuge tests were performed in the OpenSEES platform (Mazzoni et al. 2006) using two state-of-the-art soil constitutive models. The soil models were first calibrated based on a large number of static and cyclic, drained and undrained triaxial tests and a free-field centrifuge test (Chapter 3 of this dissertation). The structural models and fuses were calibrated based on beam-column component tests and hammer impact tests (Olarte et al. 2017; 2018a). In this dissertation, these calibrated component models are combined to represent the dynamic response of the SFS system with and without mitigation. After an overview of the centrifuge experiments and the required considerations in their numerical simulations, we discuss results focusing on the limitations and capabilities of 3D, fully-coupled, nonlinear numerical modeling in capturing the key experimental observations related to the performance of structures on unmitigated and mitigated liquefiable soils. The results presented aim to guide future numerical modelers in simulating the response of SFS systems and understanding the underlying modeling

limitations and uncertainties, before developing future performance-based mitigation design procedures.

CHAPTER 3

3 SITE RESPONSE IN A LAYERED LIQUEFIABLE DEPOSIT: EVALUATION OF DIFFERENT NUMERICAL TOOLS AND METHODOLOGIES WITH CENTRIFUGE EXPERIMENTAL RESULTS

This chapter presents a paper submitted to and published by the ASCE's Journal of Geotechnical and Geoenvironmental Engineering. This paper was co-authored by other graduate students and faculty members (list of authors noted below) and is based on the following reference:

Ramirez, J., A. R. Barrero, L. Chen, S. Dashti, A. Ghofrani, M. Taiebat, P. Arduino. (2018). "Site Response in a layered liquefiable deposit: evaluation of different numerical tools and methodologies with centrifuge experimental results". *Journal of Geotechnical and Geoenvironmental Engineering*, 144 (10). DOI: 10.1061/(ASCE)GT.1943-5606.0001947.

3.1 Introduction

Soil liquefaction continues to cause significant damage to the built environment during earthquakes. Over the past few decades, great progress has been made in understanding and predicting liquefaction triggering and its effects via case history observations, laboratory tests, and advanced numerical modeling. However, simultaneous numerical prediction of accelerations, generation and redistribution of excess pore pressures, and the resulting deformations remains challenging even under relatively simplistic level ground free-field conditions (*i.e.*, in absence of

soil-structure interaction or lateral spread), uniform properties within each soil layer, and 1D horizontal shaking. Further, most efforts in the past have focused on the calibration and validation of one constitutive model and numerical platform with a given set of laboratory tests. The influence of numerical framework, constitutive model (as two independent variables or ingredients to numerical modeling) has not been evaluated adequately in a consistent manner.

A relatively reliable numerical prediction of liquefaction triggering and consequences usually requires performing fully-coupled, nonlinear, elasto-plastic, site response analyses. This is to capture soil behavior under large shear strains (*e.g.*, tendency for volume change or excess pore pressure generation followed by dilation) and the redistribution and dissipation of excess pore pressures. A number of nonlinear, elasto-plastic soil constitutive models have been developed in the past 30 years to simulate the seismic response of saturated sand under dynamic loading (*e.g.*, Prevost 1985; Finn et al. 1986; Byrne 1991; Beaty and Byrne 1998; Elgamal et al. 1998; Kramer and Arduino 1999; Yang et al. 2003; Dafalias and Manzari 2004; Boulanger and Ziotopoulou 2015). These models require a number of parameters to characterize the response of granular soils undergoing elastic or elasto-plastic deformations as well as common features in soils susceptible to liquefaction (*e.g.*, accumulation of volumetric strains under cyclic shear, dilation at large shear strains, excess pore pressure generation, dependency of dilatancy on fabric history, etc.).

The predictive capabilities of these models in a given numerical platform have often been evaluated individually either based on element-level tests or centrifuge results typically with a single uniform sand layer with different geometries and configurations. Examples include centrifuge experiments conducted as a part of VELACS (Arulanandan and Scott 1993, 1994), LEAP (Kutter et al. 2015) or those by other researchers. For example, Manzari and Arulanandan (1993), Parra (1996), Elgamal et al. (2002), Taiebat et al. (2007), Tasiopoulou et al. (2015a),

Ghofrani and Arduino (2016), Ziotopoulou (2016), and Ekstrom and Ziotopoulou (2017) separately evaluated their soil constitutive models and numerical approaches in simulating site response in a uniform layer of saturated sand (at times sloped or layered and often saturated with water instead of viscous fluid) as modeled and measured in centrifuge. A systematic comparison of the capabilities and limitations of different numerical platforms and soil constitutive models used by different operators in capturing distinct features of site performance (*i.e.*, in terms of accelerations, excess pore pressures, and settlements) under similar conditions would be beneficial in advancing our knowledge not only on the accuracy of the numerical models but also in terms of insights that can be gained from the numerical models and platforms (*i.e.*, in terms of stress-strain histories).

A similar approach is under way by researchers following the LEAP centrifuge experiments evaluating the response of uniform and sloped liquefiable deposits (Kutter et al. 2015). This systematic comparison of different models with the same set of laboratory data for calibration and validation, and for a more realistic yet simple level, layered soil profile saturated with viscous fluid, which properly satisfies the dynamic and diffusion scaling laws in centrifuge, can provide valuable insights to guide future research developments as well as practice.

In this work, nonlinear, soil-fluid, fully-coupled, effective stress, dynamic analyses were performed by three teams using the finite element platform Open Source Earhtquake Engineering Simulator (OpenSEES, version 2.4.4) in three dimensions (3D) (Mazzoni et al. 2006) and the finite difference platform Fast Lagrangian Analysis of Continua (FLAC, version 7) in two dimensions (2D) (Itasca 2012). Team 1 (from University of Colorado Boulder) used the Pressure-Dependent-Multi-Yield version 02 (PDMY02) soil model developed and implemented in OpenSEES by Elgamal et al. (2002) and Yang et al. (2008), with brickUP elements. Team 2 (from University of

Washington) used the bounding surface constitutive model SANISAND developed by Dafalias and Manzari (2004) and implemented in OpenSEES (with the model tag of ManzariDafalias) by Ghofrani et al. (2016) with SSPbrickUP (Stabilized single point brickUP) elements implemented by McGann et al. (2015). Team 3 (from University of British Columbia) also used SANISAND, with an additional overshooting correction made by Dafalias and Taiebat (2016), and implemented in FLAC in 2D by Barrero (2019). They used quadrilateral elements with coupled solid-pore fluid interaction.

Although common in research, the widespread use of these two constitutive models in geotechnical engineering practice is currently limited because of the need for a rigorous calibration process of a relatively large number of parameters. A series of monotonic and cyclic triaxial tests (fully undrained and drained) followed by one centrifuge experiment modeling the seismic response of a layered soil profile under 1D horizontal earthquake loading were performed at the University of Colorado Boulder. The numerical models' calibration process was performed in two phases by each team. The first phase, referred to as "Calibration C", only focused on capturing the soil behavior at an element level based on results of fully drained and undrained triaxial tests, with no access to centrifuge experimental results. Different teams used different calibration philosophies during in this phase. Subsequently, using Calibration C model parameters, all teams performed Class C (*i.e.*, as defined by Lambe 1973) predictions of site performance in a larger boundary value problem modeled in the centrifuge. Certain shortcomings in capturing soil response in the centrifuge became evident, after which different teams performed a second phase of model calibration referred to as "Calibration C1". This was subsequently followed by Class C1 predictions (*i.e.*, Lambe 1973) of the centrifuge results, which are detailed in this chapter.

In summary, this chapter quantifies and compares the accuracy of two numerical platforms and two constitutive models in simultaneously capturing the seismic response of a layered soil deposit in terms of settlements, accelerations, and excess pore pressures among three teams and between their Class C and Class C1 simulations. Further, calibration challenges are discussed and recommendations provided on calibration methodologies and priorities appropriate for each soil constitutive model and numerical platform to better capture site performance. The authors acknowledge that centrifuge modeling has its limitations, uncertainties, and simplifications that don't necessarily reflect the complexities of the field. However, it presents a more realistic boundary value problem with simultaneous generation and redistribution of excess pore pressures and deformations during earthquake shaking when compared to small element tests that are either fully drained or undrained. These aspects of centrifuge experimental results are shown to be valuable in evaluating the capabilities and limitations of the different numerical models and also in guiding their calibration.

3.2 Physical Modeling

3.2.1 Triaxial tests

A series of drained and undrained, monotonic and cyclic triaxial compression tests were conducted on Ottawa sand F65 at the University of Colorado Boulder. The purpose of these tests was to provide data to calibrate the two soil constitutive models at an element level before analyzing the response of the larger, layered soil system. Ottawa sand F65 (D_{50}=0.15 mm, Cu≈1.45, e_{min}≈0.53, e_{max}≈0.82) is a uniform silica sand classified as SP (Unified Soil Classification System). The purpose of these tests was to provide data for calibrating the two soil constitutive models at an element level before analyzing the response of the larger layered soil system. Similar to stress-controlled tests, strain-controlled element tests can provide important information on a

soil's stress-strain response and rate and magnitude of excess pores pressure during cyclic loading. Grain-size distribution and maximum and minimum void ratios were first determined following ASTM D422 (ASTM 2007), ASTM D4254 (ASTM 2000), and ASTM D4253 (ASTM 2006). Then, triaxial tests were performed using an automatic triaxial apparatus in accordance with well-established techniques developed for clean sand [Head 1998; ASTM D4767 (ASTM 2011b), ASTM D7181 (ASTM 2011a), and ASTM D5311/D5311M (ASTM 2013)]. All soil specimens were prepared by air pluviation at three relative densities ($D_r \approx 40$, 60, and 90%) to adequately represent the fabric of soil used subsequently in the centrifuge.

Samples were prepared in a mold 70 mm in diameter and 140 mm in height. Dimensions of the sample inside a 0.3 mm latex membrane were registered before every tests as well as the dry unit weight. Carbon dioxide was applied to the sample for approximately 10 min at a low pressure of 3.5 kPa under a cell pressure of 20 kPa. De-aired water was then flushed into the sample from the bottom drain lines. For all samples tested, the average B-values (Skempton 1954) of the specimens after back pressure saturation was higher than 0.96.

For the nine drained monotonic triaxial compression tests, all specimens ($D_r \approx 40$, 60 and 90%) were isotropically consolidated to three levels of effective stress (*i.e.*, 100, 200, and 300 kPa). For the nine undrained monotonic triaxial compression tests with the same set of relative densities, the isotropic effective consolidation stress was 50, 100, and 200 kPa. All the monotonic tests were performed under a strain controlled axial compression rate of 0.35 mm/min. For the undrained cyclic triaxial tests, the specimens were all consolidated isotropically under an effective confining pressure of 100 kPa. Strain-controlled, sinusoidal, cyclic axial loading was subsequently applied to the sample (frequency = 1 Hz, and axial strain amplitudes ranging from 0.042% to

0.44%). A summary of the most important soil properties is presented in Table 3.1, and a detailed description of triaxial tests is included in Appendix A.

Table 3.1Summary of soil sample properties used in the triaxial tests

	Aprox. relative density, D_r (%)		
	40	60	90
Void ratio, *e*	0.69 - 0.70	0.64 - 0.65	0.55 - 0.56
Hydraulic conductivity, *k* (m/s)	1.41e-4	1.36e-4	1.19e-4
Peak friction angle, ϕ_p (°)*	32.0 - 32.5	34.8 - 36.5	41.5 - 42.1
Phase transformation angle, ϕ_{PT} (°)**	25.1 - 31.2	24.5 - 30.0	22.2 - 28.5

Obtained from *Monotonic drained triaxial test;
**Monotonic undrained triaxial test

3.2.2 Centrifuge experiment

A series of ten centrifuge experiments were conducted at the University of Colorado Boulder 5.5m-radius centrifuge facility (Ko 1988) to evaluate seismic site response and soil-structure interaction on layered liquefiable soil deposits (*e.g.*, Kirkwood and Dashti 2018; Olarte et al. 2017). This chapter only focuses on the centrifuge experiment that approximately modeled free-field conditions (with no structure) to validate the predictive capabilities of numerical models in capturing seismic site performance without the complexities of soil-structure interaction (SSI).

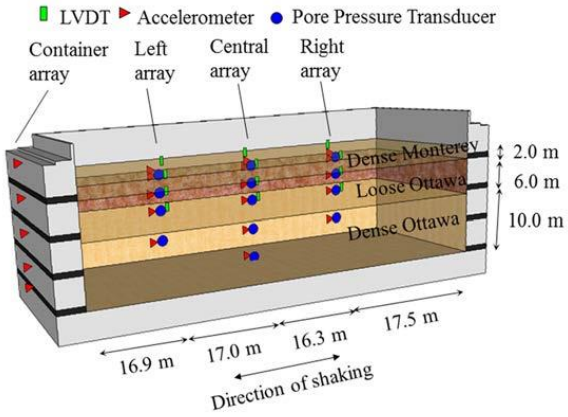

Figure 3.1 Schematic of centrifuge experiment simulating free-field soil conditions (dimensions are presented in prototype scale at 70g of centrifugal acceleration).

Table 3.2 Initial soil conditions in the centrifuge experiment

Thickness / D_r / Layer	e	γ_{sat} (kN/m^3)	k (m/s)
2m / 90% / Monterey Sand 0/30	0.57	19.81	5.30e-04
6m / 40% / Ottawa Sand F65	0.70	19.05	1.41e-04
10m / 90% / Ottawa Sand F65	0.56	19.89	1.19e-04

The total thickness of the soil specimen, H, was 18 m in prototype scale. As shown in Figure 3.1, the lower deposit was prepared by dry pluviating a dense layer of Ottawa sand with a thickness of 10 m and an initial D_r of approximately 90%. The same Ottawa sand with a $D_r \approx 40\%$ was subsequently dry pluviated as the liquefiable layer with a thickness of 6 m. Finally, 2 m of Monterey 0/30 sand (D_{50} = 0.40 mm, Cu = 1.3, e_{min} = 0.54, e_{max} = 0.84) (Dashti 2010a) was dry pluviated at $D_r \approx 90\%$. The initial soil properties of each layer are summarized in Table 3.2. An automated pluviation system (Olarte et al. 2017; Kirkwood and Dashti 2018) was employed to improve the uniformity of soil properties across the container. The pluviation technique used in preparing the centrifuge model mimicked the technique used in preparing the triaxial specimens (prior section) to keep the fabric consistent and reduce the number of variables. The soil deposit was prepared inside a flexible-shear-beam (FSB) container constructed of aluminum and rubber, to reduce boundary effects (Olarte et al. 2017).

The test was instrumented with accelerometers, pore pressure transducers, and vertical linear variable displacement transducers (LVDTs) at three different arrays distant from the container boundaries to the extent possible (Figure 3.1). Accelerations, pore water pressures, and vertical displacements were measured at the boundaries between layers and also at their mid-depth. A solution of methylcellulose in water (Stewart et al. 1998) with a viscosity 70 times that of water was used to saturate the soil specimen under vacuum with an automated saturation technique (Olarte et al. 2017). The model was then spun to a nominal centrifugal acceleration of 70*g*

estimated at the center of the loose Ottawa sand layer. The subsequent numerical analyses were conducted in prototype scale units, and all the units presented in this dissertation are in prototype scale unless indicated otherwise.

One-dimensional (1D) horizontal earthquake motions were applied to the base of the container in flight. This work focuses on the first motion (referred to as Kobe-L) that corresponded to a scaled version of the north-south, fault normal, horizontal component of the 1995 Kobe, Japan earthquake recorded at the Takatori station (Kobe-Japan). The peak ground acceleration (PGA), Arias Intensity (I_a), significant duration ($D_{5\text{-}95}$), and mean period (T_m) of this motion as measured at the base of the container in centrifuge are reported in Figure 3.2.

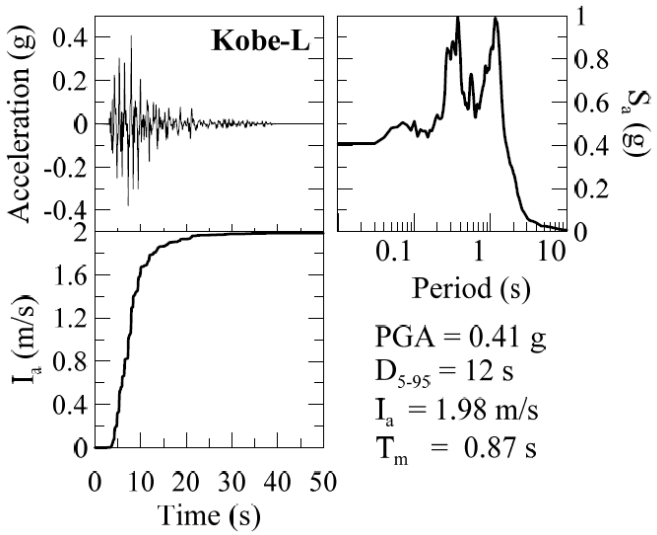

Figure 3.2 The acceleration and Arias Intensity (I_a) time histories and response spectrum (5%-damped) of the Kobe-L earthquake motion recorded at the base of the container in the centrifuge and used as input to the single soil column numerical analyses.

3.3 Numerical Modeling

3.3.1 Choice of numerical platforms and elements

Two numerical platforms were chosen for this study: OpenSEES (Mazzoni et al. 2006) and FLAC. These tools were chosen based on their demosntrated capabilities to capture the response on soil systems subject to earthquake events and their availability of advanced constitutive models

capable of reproducing cyclic mobility and liquefaction. OpenSEES is an object-oriented, open-source, finite element (FE) computational platform. It allows users to create both serial and parallel finite element computer applications for simulating the response of structural and geotechnical systems subject to earthquakes and other hazards. OpenSEES uses explicit and implicit time integration techniques to march in time and several nonlinear algorithms to solve the equilibrium equations. Teams 1 and 2, respectively, used the PDMY02 and SANISAND models implemented in OpenSEES. FLAC is a finite difference (FD) computational platform for fast Lagrangian analysis of continua. It uses an explicit time-integration scheme, coupled solid-pore fluid interaction, large strain formulation, and is well suited for solving dynamic problems for stable or unstable systems. Since FLAC does not need to form a global stiffness matrix, memory requirements are always at a minimum, a small amount of computational effort is needed per time step, and large displacements and strains are accommodated without additional computational efforts. These benefits, however, come at the cost of a small time step requirement to keep the speed of the calculation front greater than the maximum speed of travelling waves. Team 3 used SANISAND implemented in FLAC.

Based on well-established, coupled formulations of poromechanics originated by Biot (1941), and later extended to finite elements by Zienkiewicz and Shiomi (1984) and presented by Yang and Elgamal (2000) for application in OpenSEES and by Detournay and Cheng (1993) in FLAC, both programs include functionality to represent the response of saturated soils, undrained behavior, and dissipation during consolidation. In a fully-coupled analysis, the constitutive model interacts with the element and responds to the undrained or partially drained conditions as well as the dissipation demand. The pore pressure is a quantity carried by element nodes (FE) or zone grid points (FD) similar to displacements, velocities, and accelerations, while stresses and strains are

carried and adjusted by the constitutive model at the Gauss points (FE) or subzones (FD) within the element.

Team 1 employed 3D, 8-node, hexahedral solid-fluid, fully-coupled, brickUP elements in OpenSEES, during all phases of simulation in this study. The OpenSEES manual (Mazzoni et al. 2006) recommends either using eight-node brickUP or 20-8 brickUP elements to simulate undrained or partially drained soil response in 3D with PDMY02. Team 1 used lower-order elements for computational efficiency. All nodes had four degrees of freedom (DOFs), three for displacement in different orthogonal directions and one for fluid pressure. Team 2 modeled the soil response with 3D eight-node hexahedral solid–fluid fully-coupled SSPbrickUP elements in OpenSEES (McGann et al. 2015). Both SSPbrickUP and brickUP use the standard trilinear interpolation functions for displacement and pressure fields. However, the volumetric integrals are performed using a single integration (Gauss) point on SSPbrickUP, which is more computationally efficient while preserving similar accuracy compared with the eight integration points in brickUP. Team 3, on the other hand, used axisymmetric quadrilateral zones in FLAC with an axisymmetric configuration for the calibration at an element level and with a plane-strain configuration for modeling the centrifuge test, with coupled solid–pore fluid interaction where needed. A water bulk modulus of 2.0×10^6 kPa and density of 1000 kg/m^3 were assigned to the fluid in all simulations.

3.3.2 Choice of soil constitutive models

Two advanced constitutive models were chosen in this study to represent the nonlinear cyclic response of granular materials. The Pressure Dependent Multi-yield surface (PDMY02) and SANISAND models were chosen due to their capabilities and availability in current numerical platforms, as detailed subsequently.

3.3.2.1 Pressure dependent multi-yield surface PDMY02 constitutive model

Parra (1996) and Yang and Elgamal (2000) developed the framework for the nonlinear, pressure-dependent, multi-yield-surface-plasticity based soil constitutive model PDMY02 (Elgamal et al. 2002 and Yang et al. 2008), which was implemented in the finite element platform OpenSEES. PDMY02 uses kinematic hardening and includes functionality to capture cyclic response of pressure dependent materials. This elastoplastic constitutive model is based on multiple yield criteria defined by a number of open conical-shaped yield surfaces with a common apex at the origin of the principal stress space and with different sizes that form the hardening zone. The multi-yield approach allows the user to introduce G/G_{max} curves to specify evolution of the plastic moduli, which is advantageous during calibration.

The model follows a non-associative flow rule to simulate volumetric dilation and contraction under shear. However, due to the use of open-ended yield surfaces, no volumetric plasticity is captured under constant stress ratios. Due to this limitation, the model cannot accurately simulate a 1D consolidation path and as a result underestimates post-liquefaction volumetric strains (Yang and Elgamal 2000). The model also has difficulty capturing the full amplitude of dilation after liquefaction initiation. Further, similar to many other models, such as modified Konder-Zelasko (MKZ) model (Matasovic and Vucetic 1993), University of British Columbia sand model (UBCSAND) (Beaty and Byrne 1998), and extended MKZ (Hashash and Park 2001), PDMY02 overstimates soil damping at large strains. Partly because this model does not depend on a soil's critical state, its calibration needs to be specifically performed for the relative density and confining pressure of interest. However, not depending on critical-state soil properties facilitates its calibration in practice because laboratory tests that reach a soil's critical state are rare.

The model requires calibration of 13 parameters and optional specification of G/G_{max} curves. For the elastic range of material behavior, the model is mainly defined by the reference low-strain shear modulus, G_{ref}, and the reference bulk modulus, B_{ref} or poisson ratio, ν. The nonlinear stress-strain backbone curve in this model is represented by piecewise linear segments with a certain number of yield surfaces or user-defined pairs of normalized secant shear modulus versus shear strain points. The peak friction angle, ϕ_p, defines the outermost yield surface, while the phase transformation angle, ϕ_{PT}, establishes the boundary where the soil transitions from contractive to dilative behavior. The evolution of excess pore pressures over time and coupling between shear and volumetric strains is defined by a number of contraction (c1, c2, and c3) and dilation (d1, d2, and d3) parameters that need to be determined during calibration for each soil relative density and reference pressure (*e.g.*, Karimi and Dashti 2016a, b).

3.3.2.2 SANISAND constitutive model

SANISAND is the name for a class of Simple ANIsotropic SAND constitutive models extended from the original two-surface plasticity model developed by Manzari and Dafalias (1997). The modeling approach is based on bounding surface plasticity and critical state soil mechanics concepts, allowing for a unified description at any pressure and density. The SANISAND class includes various extensions developed by Dafalias and Manzari (2004), Dafalias et al. (2004), Taiebat and Dafalias (2008), where the name SANISAND was first adopted, Li and Dafalias (2012), and Dafalias and Taiebat (2016). The work by Manzari and Dafalias (1997) represents the core of the constitutive model and the above-referenced subsequent studies present additional constitutive ingredients. To involve fewer model parameters and for simplicity, the version of SANISAND with fabric change effects (Dafalias and Manzari 2004) has been considered as the soil constitutive model for this study by Teams 2 (with the model tag of

ManzariDafalias) and Team 3 (with the model tag of SANISAND in FLAC). The base model for Teams 2 and 3 is essntially the same, and that is why they are addressed with the same name.

SANISAND uses hypo-elasticity with a pressure and density dependent shear modulus, using parameters G_0 and ν. This model uses a functional relation to represent the evolution of plastic modulus that is continuous and related to its bounding condition, but does not allow the user to define G/Gmax curves. The parameter m controls the size of the yield surface cone, chosen with a small value so that plastic strain is developed almost immediately after the application of shearing. The critical state surface is defined by *M* and *c* in the $q-p'$ space, and by λ_c, e_0, and ξ in the $p'-e$ space. The plastic modulus, governing the hardening behavior of the model in the deviatoric space, is defined by h_0, c_h, n^b. The volumetric hardening rule follows Rowe's dilatancy theory by coupling the volumetric to deviatoric plastic strains through parameters A_o and n^d. Parameters $z_{\max}$ and c_z define the evolution of the fabric dilatancy tensor, which in turn control the dilation-contraction behavior of the material in the cyclic loading regime. The known overshooting response upon small unloading-loading scenarios in the bounding surface models was controlled by Team 3 using the overshooting correction via parameters $\bar{e}^p_{eq}$ and *n*.

3.4 First Calibration Phase

The calibration of different constitutive model parameters was performed in two phases. During the first phase (Calibration C), all teams had access to the same triaxial test data (Appendix A) and no access to centrifuge recordings. The calibration priorities and objectives during this phase were not the same among different teams, as detailed below.

3.4.1 PDMY02 parameter calibration

The PDMY02 model parameters were first calibrated prioritizing the number of cycles to liquefaction (defined as the condition for which r_u=0.99) at different levels of cyclic shear strain, while simultaneously capturing the time histories of stress, strain, and excess pore pressure in triaxial tests to the extent possible. Capturing the number of cycles to liquefaction by Team 1 was intended to mimic the strategy adopted often in practice. The PDMY02 model parameters needed to be calibrated for different soil relative densities and also ideally for different confining pressures. In this context, Team 1 chose to calibrate one set of unified parameters for each soil relative density. It was also important to follow the recommendations and trends for various parameters (*e.g.*, contraction and dilation parameters) suggested in the OpenSEES Manual (Mazzoni et al. 2006) for PDMY02, and maintain a logical trend among all parameters for different soil relative densities. A single element was used during calibration. This methodology has been verified in the past using an independent implicit mixed-control constitutive driver (Alawaji et al. 1992 and Ghofrani and Arduino 2016).

A key challenge in the calibration of PDMY02 parameters was to reproduce, with a single set of parameters, the number of cycles to liquefaction at different cyclic shear strains in dense Ottawa Sand. For instance, one set of parameters could be obtained to provide satisfactory results at small shear strains, but not larger strains. Further, prioritizing the number of cycles to liquefaction at times comprimised the rate of excess pore pressure buildup.

The PDMY02 model parameters obtained from Calibration C are presented in Table 3.3 for the relative densities applicable to the centrifuge model. The low-strain, maximum shear modulus value of Ottawa Sand, $G_{ref} = G_{\max, s'_m = 1atm}$, was estimated based on empirical relationships proposed by Hardin (1965); Drnevich and Richart (1970); Hardin and Drenevich (1972); Seed and Idriss

(1970); and Bardet et al. (1993); and Menq (2003) at σ'_m = 1atm. A poisson ratio, ν , of 0.33 was selected to compute the reference bulk modulus, $B_{ref} = 2/3G_{ref}(1+\nu)/(1-2\nu)$.

Yield surfaces were manually incorporated as discrete pairs of secant shear modulus ratio (G/G_{max}) and shear strain during calibration, shown for different relative densities in Figure 3.3 (Darendeli 2001). These surfaces define the nonlinear shear stress-strain backbone curve with a piecewise-linear approximation that can be represented by a hyperbolic curve (*i.e.*, used when automatic surfaces are used). As suggested by Hashash et al. (2015), the implemented shear modulus reduction curves were adjusted to an appropriate friction angle obtained from the triaxial tests (Table 3.1). The implementation of manual yield surfaces was observed to improve the calibration results, particularly in small to moderate range of strains. The material damping provided by the constitutive model was not modified because the user does not have direct control over this aspect of the constitutive model modulus reduction and damping ratio curves produced by the calibrated model are shown in Figure 3.3 and are notably greater than that recommended empirically. The computed material damping becomes constant or reduced after 1% shear strain, because of the nature of the backbone curves. The phase transformation angle was chosen based on laboratory test results. Calibration of contraction and dilation parameters was performed through an iterative process for each relative density with considerations and priorities and priorities as mentioned previously.

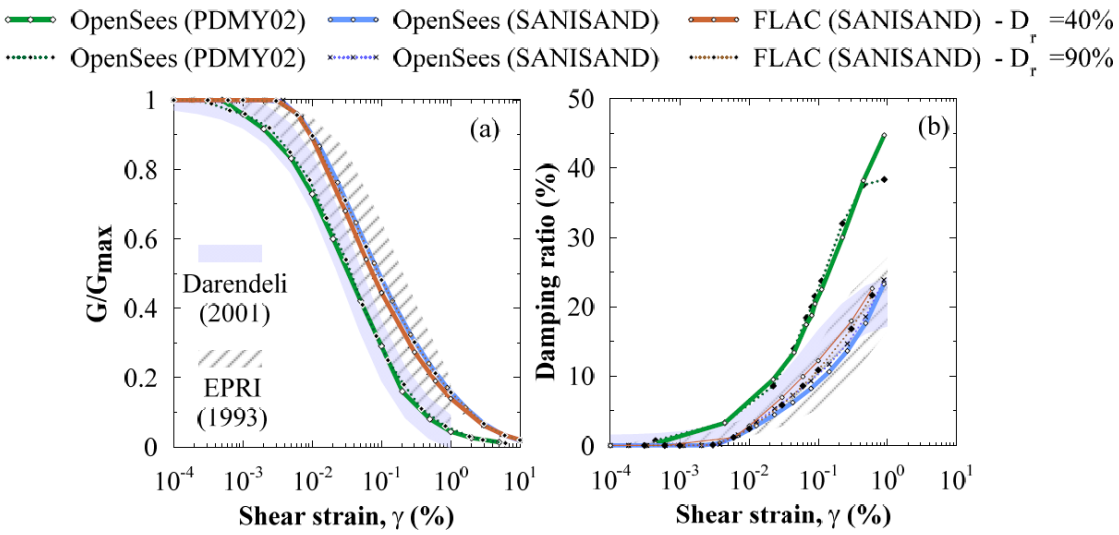

Figure 3.3 Comparison of model properties in Calibration C: (a) shear modulus reduction curves (strength corrected) imposed on the PDMY02 and obtained from the default SANISAND constitutive models; (b) damping ratio curves obtained from the models.

Table 3.3 Summary of model parameters for the PDMY02 constitutive model in OpenSEES

Description	Calibration C & C1	Calibration C		Calibration C1	
	Monterey sand	Ottawa sand		Ottawa sand	
Relative density, D_r (%)	85	40	90	40	90
Ref. effective confining pressure, p'_r (kPa)	101	101	101	101	101
Pressure dependence coeff., d	0.5	0.5	0.5	0.5	0.5
Octahedral reference low-strain shear modulus, G_{ref} (MPa)	133.3	108	156	108	130
Triaxial peak friction angle, ϕ'_p (°)	42.0	31.2	43.9	32.0	40.8
Phase transformation angle, ϕ_{PT} (°)	32.0	27.5	22.0	27.5	28.0
Control shear-induced volumetric change, contraction tendency and overburden effect, c1, c2 and c3	0.014	0.051	0.002	0.070	0.045
	2.0	4.0	1.5	4.0	1.5
	0.15	0.95	0.80	0.95	0.50
Reflect dilatation tendency, stress history and overburden stress, d1, d2 and d3	0.36	0.03	0.05	0.01	0.03
	3.0	3.0	3.0	3.0	3.0
	0.005	0.00	0.00	0.00	0.00
Number of yield surfaces	20▫	15▪	19▪	99▪	44▪

▫Automatic yield surfaces;▪user defined yield surfaces

The PDMY02 parameters for Monterey sand were the same as those described in Karimi and Dashti (2016b), which were in turn calibrated to capture the number of cycles to liquefaction observed in available cyclic simple shear tests (Kammerer et al. 2004). Detailed calibration of this soil is not presented in this dissertation due to the layer's small thickness and relatively minor influence on this site response compared to the Ottawa sand layers. The model parameters for Monterey sand are summarized in Table 3.3.

3.4.2 SANISAND parameter calibration

The SANISAND model parameters were consistently calibrated by Teams 2 and 3 at this stage, to capture to the extent possible the stress-strain response and generation of excess pore pressures seen in the triaxial tests, both drained and undrained monotonic and undrained cyclic (Appendix A). Both teams have verified the response of a single element using their stand-alone mixed-control constitutive drivers based on Alawaji et al. (1992) and Bardet and Choucair (1991). The calibrated SANISAND model parameters are presented in Table 3.4. The elastic parameters G_0 and ν were obtained from those used by Dafalias and Manzari (2004) for Toyoura sand. The critical state stress ratio (M) was calculated directly from the estimated critical state friction angle. The ratio of M in triaxial extension and compression (c) was roughly estimated using the extension part of cyclic tests. The critical state line in the $p' - e$ space (Figure 3.4) was defined Li and Wang (1998) by λ_c, e_0, and ξ . These parameters were calibrated using the results from monotonic triaxial tests. The A_0 and n^d parameters were calibrated to roughly capture volumetric strains in drained tests and excess pore pressure buildup in undrained tests. The bounding surface parameter (n^b) and the dilatancy surface parameter (n^d) were calibrated using the procedure described by Taiebat et al. (2010). Fabric parameters z_{max} and c_z were calibrated using an

optimization technique to capture the rate of pore water pressure generation during cyclic undrained tests. The overshooting correction parameters, $\bar{e}_{eq}^{p}$ and n, were adopted from Dafalias and Taiebat (2016).

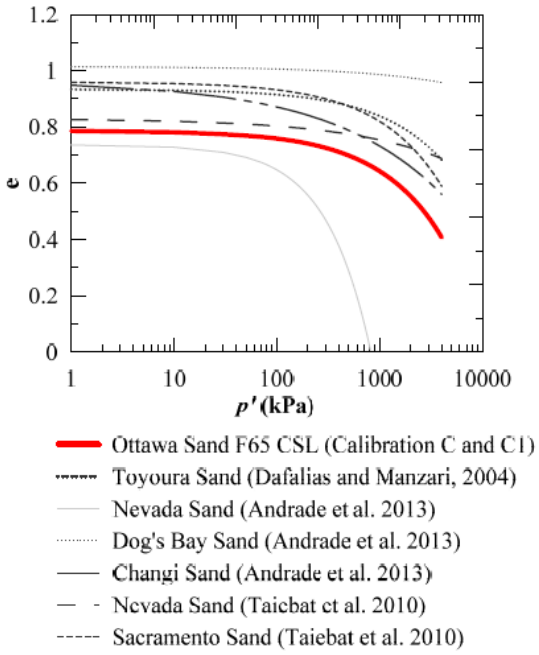

Figure 3.4 The critical state line used for Ottawa Sand (F65) compared to other types of sand from the literature.

The modulus reduction and damping curves predicted by the SANISAND model in OpenSEES and FLAC under drained cyclic loading after Calbiration C are shown in Figure 3.3. Comparisons of SANISAND curves to those from PDMY02 show notably greater shear stiffness and lower damping over a range of strains, which may lead to greater shear stresses and accelerations when simulating site response. The SANISAND model parameters were also calibrated for Monterey sand to capture the stress-strain response as observed in cyclic simple shear tests (Kammerer et al. 2004). The model parameters for Monterey sand are also summarized in Table 3.4.

Table 3.4 Summary of model parameters for the SANISAND constitutive model in OpenSEES

Description	Calibration C & C1	Calibration C	Calibration C1	
	Monterey sand	**Ottawa sand OpenSEES & FLAC**	**Ottawa sand OpenSEES**	**Ottawa sand FLAC**
Elasticity				
Elastic material constant, G_0	130	125	100	125
Poisson's ratio, ν	0.05	0.05	0.05	0.05
Critical state stress				
Critical state stress ratio M	1.27	1.26	1.26	1.26
Ratio of critical state stress ratio in extension and compression, c	0.712	0.735	0.73	0.735
State line constant, λ_c	0.02	0.0287	0.0287	0.0287
Void ratio at p=0, e_0	0.858	0.78	0.78	0.78
State line constant, ξ	0.69	0.70	0.70	0.70
Yield surface constant, m	0.02	0.02	0.02	0.02
Plastic modulus				
h_0	8.50	5.0	5.0	5.0
c_h	0.968	0.968	0.968	0.968
n^b	1.05	2.30	0.64	0.60
Dilatancy				
A_0	0.60	0.626	0.45	0.50
n^d	2.50	2.50	0.50	0.50
Fabric-dilatancy tensor parameters				
z_{max}	4.00	11.00	11.0	11.0
c_z	50.0	500	500	500
Overshooting correction *				
$\bar{e}^p_{ep}$ (%)	0.01	0.01		0.01
n	1	1		1

*Only applies to FLAC

3.4.3 Element level numerical and experimental comparison (Calibration C)

A comparison of the experimentally measured and numerically computed monotonic drained triaxial tests is shown in Figure 3.5 for loose Ottawa sand. Results for dense sand are included in Appendix B. The plots indicate the initial stiffness and peak deviatoric strength was captured well by all models for loose conditions and the range of confining pressures evaluated. The user-defined shear modulus reduction curve was a salient feature of the PDMY02 model to

improve its predictions in terms of shear stiffness in small to moderate ranges of strain, compared to the default (automatic) curve generation in the constitutive model. The decrease in deviatoric stresses following the peak (*i.e.*, softening) in dense specimens was better predicted by Teams 2 and 3 using SANISAND. The predicted residual deviatoric stresses and volumetric strains from SANISAND were also in better agreement with the experimental data compared to PDMY02. This was expected due to the critical state nature of the SANISAND bounding surface formulation.

Predicting the stress-strain behavior was particularly difficult with PDMY02 in dense sand, when the priority in calibration was capturing the number of cycles to liquefaction (corresponding to large strains) for all stress levels. Further, under drained loading the PDMY02 model caps the shear stress beyond its maximum value, after which the elastoplastic shear modulus (H) associated with the last yield surface is assumed to be zero. Hence, it is not possible to predict post peak softening, which is important for dense states in sand. Differences between the PDMY02 predictions and the experimental results were accentuated at higher confining pressures in denser soils.

Results for all monotonic undrained tests (both loose and dense conditions) are included in Appendix B. In general, predicting the stress-strain response of soil was more difficult under undrained loading, particularly for denser samples. All teams were able to predict the deviatoric stress at an axial strain of about 0.1%, but after this point, the differences in predictions became more prominent.

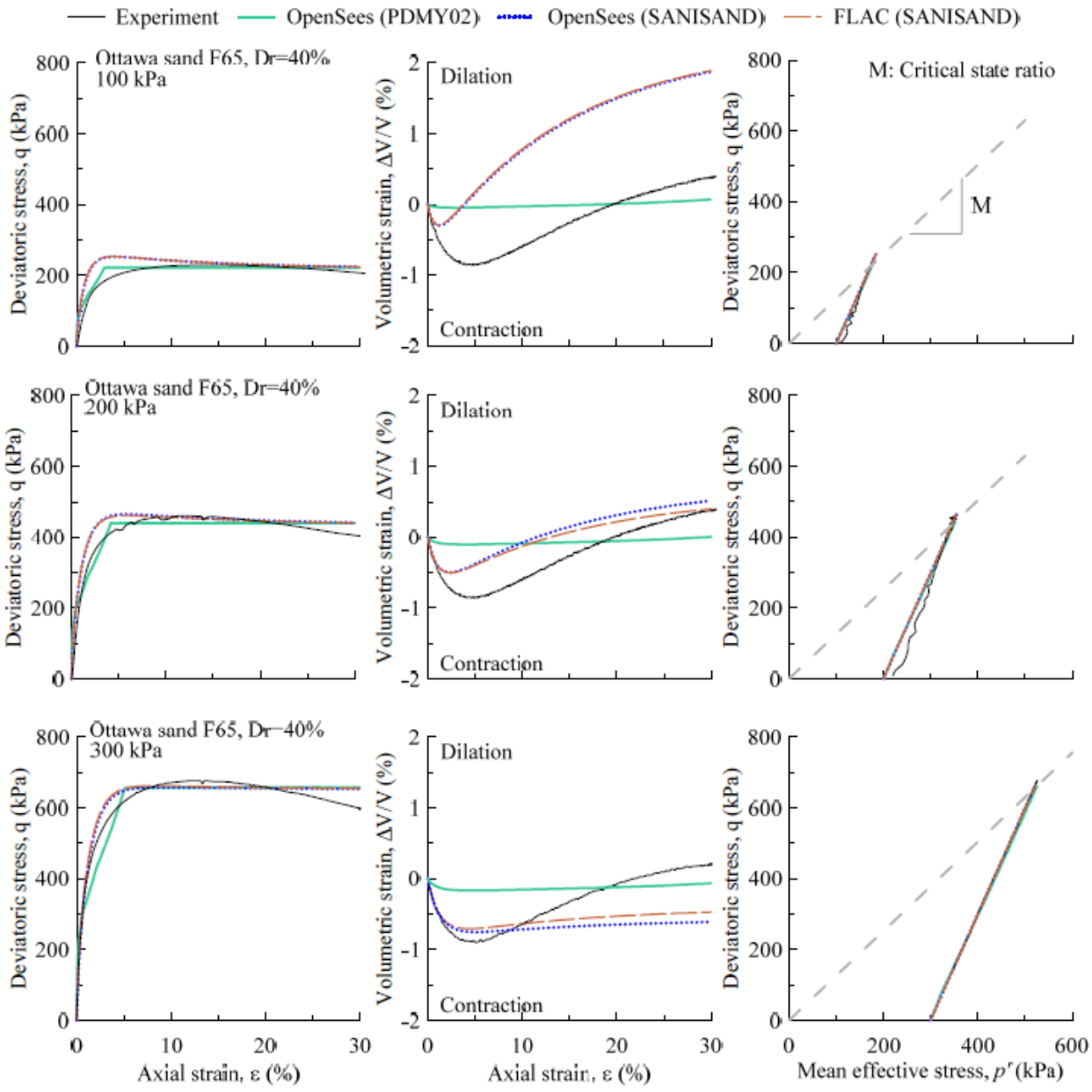

Figure 3.5 Comparison between experimental monotonic drained triaxial tests and numerical (Calibration C) simulations for Ottawa sand F65 (D_r = 40%).

At lower confining stresses (*i.e.*, 50 kPa, near the average p' experienced in the centrifuge model), PDMY02 captured the variation of deviatoric stress and generation of excess pore pressures fairly well. The calibration of the PDMY02 model required selection of a phase transformation angle (obtained from lab test results, shown in Table 3.1), as well as contraction and dilation parameters, which improved the predictions at lower confining pressures in looser

soils. Due to the applicability of lower confining pressures to the centrifuge conditions, Team 1 prioritized the response at 50 kPa. As a result, the model overpredicted soil's contractive tendencies at greater confining pressures. The SANISAND model employed by Teams 2 and 3 largely overpredicted soil's dilative tendencies (both in drained and undrained tests) at lower confining pressures, but their predictions improved at higher confining pressures. All models predicted excessive dilation (or negative excess pore pressures under undrained loading) in denser sand with almost no contraction as illustrated in the $q - p'$ diagrams.

The experimental and numerical results of two representative cyclic undrained triaxial tests are shown in Figure 3.6 and Figure 3.7 for loose and dense conditions. The remaining results are included in Appendix B. The comparisons indicate reasonable match in terms of cyclic stress-strain and rate of excess pore pressure generation among all models for loose soils. The quality of the comparisons degraded for denser soils, particularly with the PDMY02 model. Because Team 1 prioritized capturing the number of cycles to liquefaction (r_u = 0.99) during the first phase of calibration, excessive dilation was necessary when calibrating the response of denser soils (Figure 3.8). This led to poor predictions of the rate of excess pore pressure generation over time in denser soils. In contrast, the SANISAND model used by Teams 2 and 3 generally captured better the stress-strain and excess pore pressure response as observed during cyclic undrained triaxial tests. Despite the differences in the numerical platform and element type, the two teams using SANISAND had consistent results at an element level under monotonic and cyclic loading.

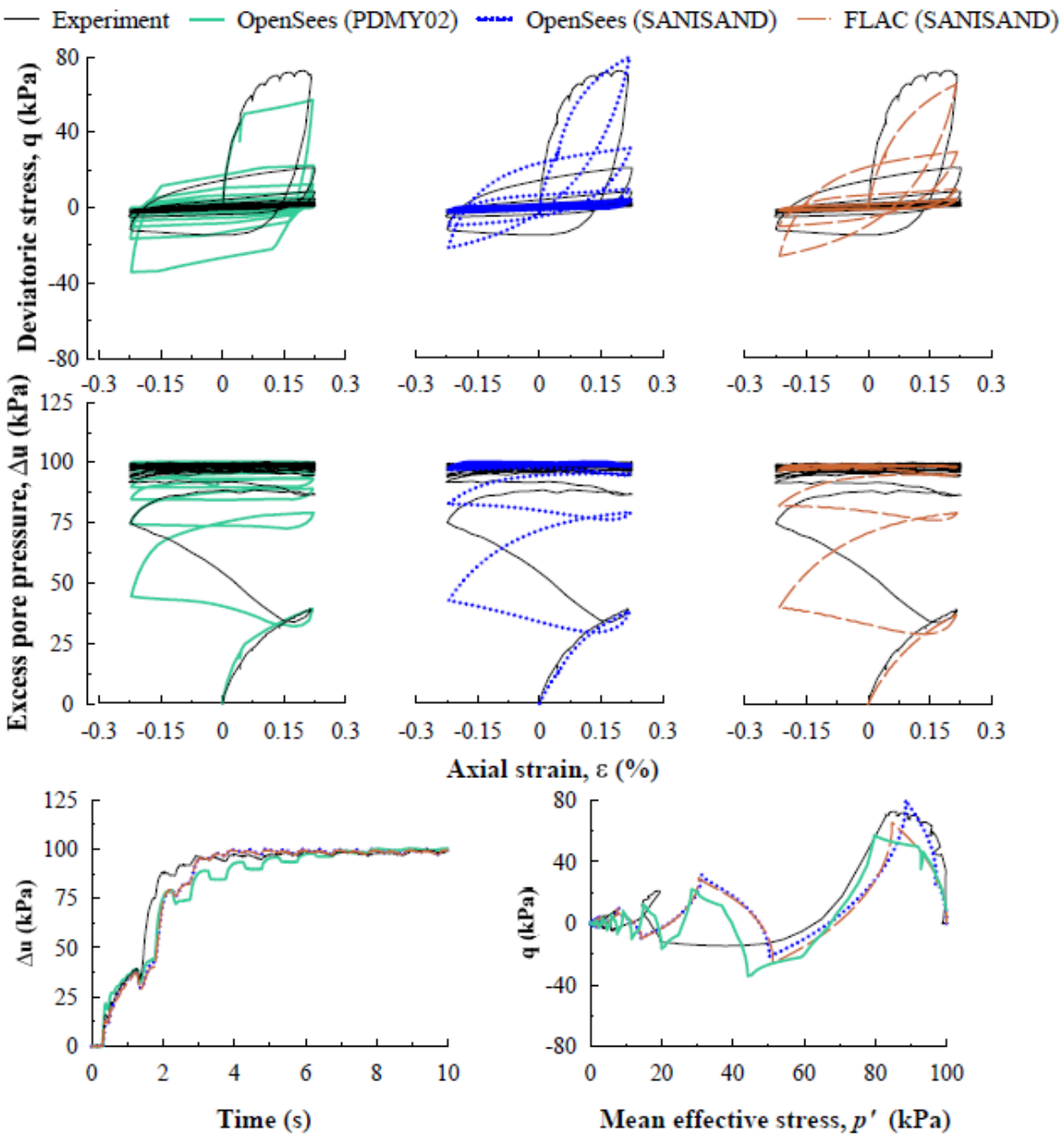

Figure 3.6 Comparison between experimental and numerical simulations (Calibration C) for Ottawa sand F65 with D_r = 40% and a cyclic shear strain amplitude of 0.33% (or axial strain amplitude of 0.22%).

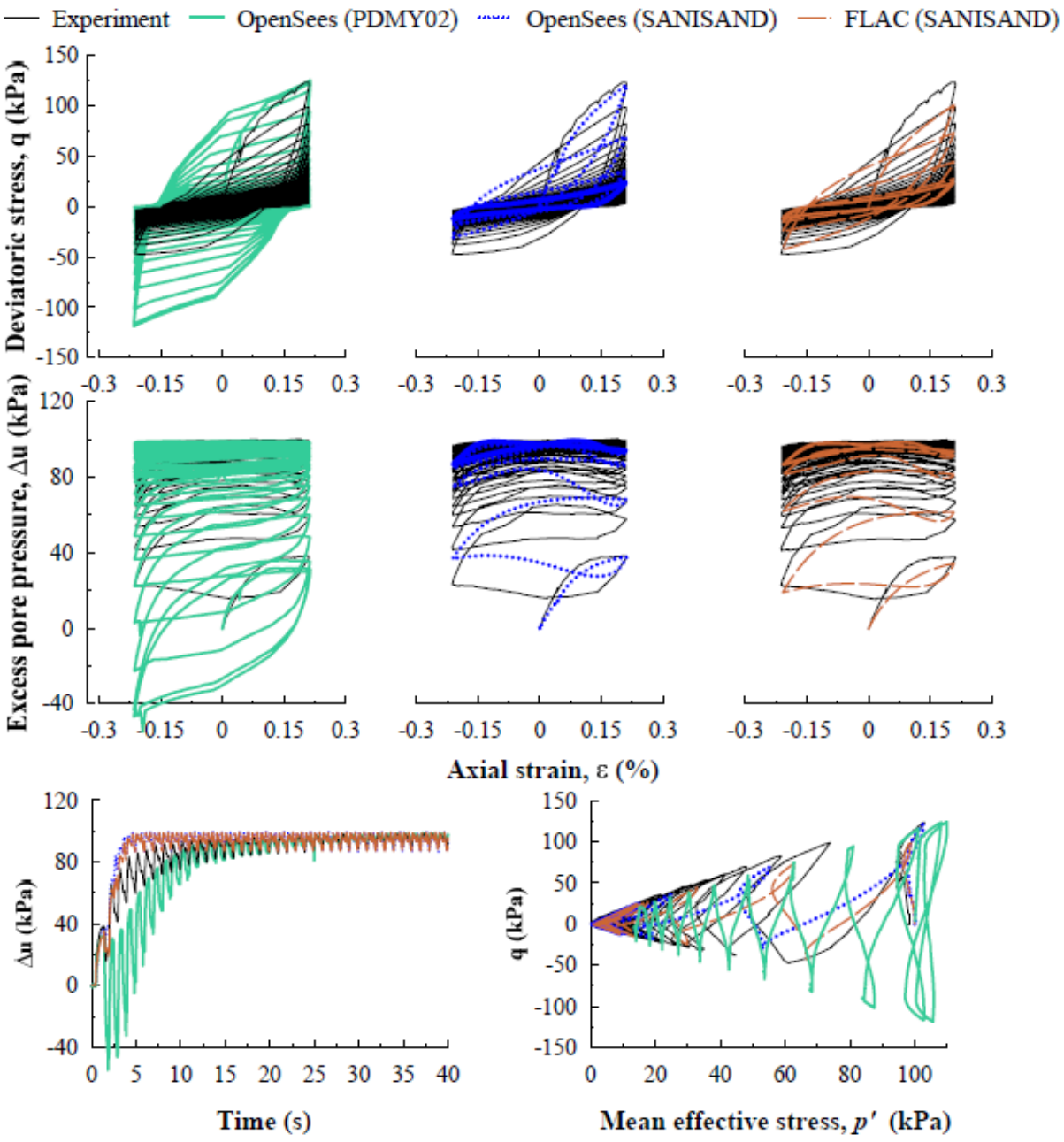

Figure 3.7 Comparison between experimental and numerical simulations (Calibration C) for Ottawa sand F65 with D_r = 90% and a cyclic shear strain amplitude of 0.315% (or axial strain amplitude of 0.21%).

Figure 3.8 compares the cyclic strain versus number of cycles to liquefaction as predicted by each constitutive model and observed experimentally from cyclic, strain-controlled, undrained triaxial tests. As shown in this figure, since Team 1 prioritized this response, the PDMY02

predictions compared well with experimental results for all relative densities. Yet, the other two teams did not prioritize nor capture the number of cycles to liquefaction for any of the relative densities, particularly for denser soils.

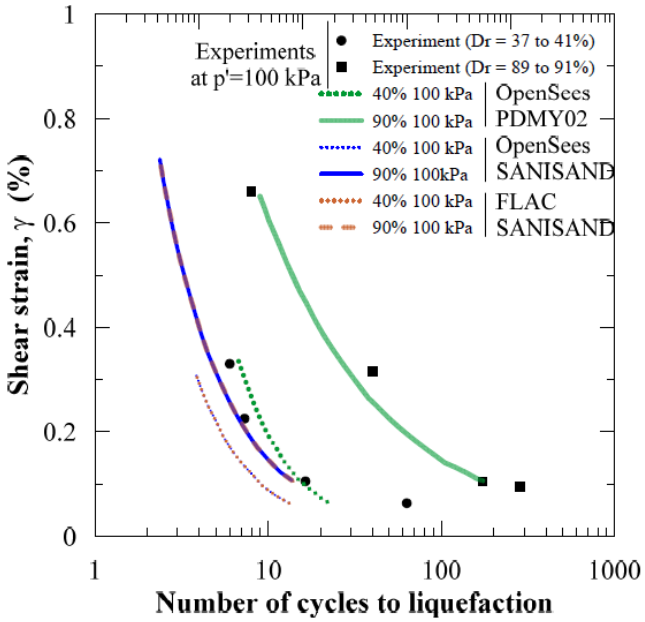

Figure 3.8 Relation between number of cycles required to achieve liquefaction ($r_u \approx 0.99$) and cyclic shear strain amplitude, γ, in numerical simulations and cyclic triaxial experiments on Ottawa sand in Calibration C.

3.5 Verification of Numerical Models

Prior to performing Class C predictions of the centrifuge test, the numerical frameworks were verified with closed-form solutions for the vertical propagation of shear waves through a homogeneous, linear-elastic soil medium (both dry and saturated). This verification step helped calibrate each numerical platform in terms of time integration coefficients, low strain Rayleigh damping values, number of elements, fixities and constrain handling, and simulation time step such that consistent results were obtained for a simple case for which a closed form exists. During this exercise, the low-strain shear modulus (G) of the soil column was assumed to be uniform = 62 MPa.

The models were excited at their base with a sine sweep (amplitude = 0.30*g*, frequencies ranging from 0.5 to 30 Hz). Teams 1 and 2 used a soil column with 25, 3D brickUP and SSPbrick elements in OpenSEES, respectively. Team 3 used 25, 4-nodes, quadrilateral, 2D elements in FLAC. Despite the uniform and linear-elastic soil properties assumed during verification, the maximum allowable element size was determined at each depth based on the small-strain Vs (Seed and Idriss 1970; Bardet et al. 1993; Menq 2003) of the soil profile and the maximum frequency content of the base motion Kobe-L (*e.g.*, conservatively taken as f_{max} = 10 Hz) in centrifuge. This was done to keep the mesh size consistent between the verification and validation exercises. The minimum wavelength ($\lambda_{min}=V_s/f_{max}$) was divided by 4 at each depth to obtain the maximum allowable element size ($h_{max}= \lambda_{min} /4$) required, which was further divided by a factor of C=4 to consider soil softening (*i.e.*, reduction in V_s) in the elasto-plastic model used later. Figure 3.9 presents the element discretization adopted by the modelers. The selected element size was judged acceptable through a sensitivity study of the elasto-plastic soil model performed by Team 1 (not shown).

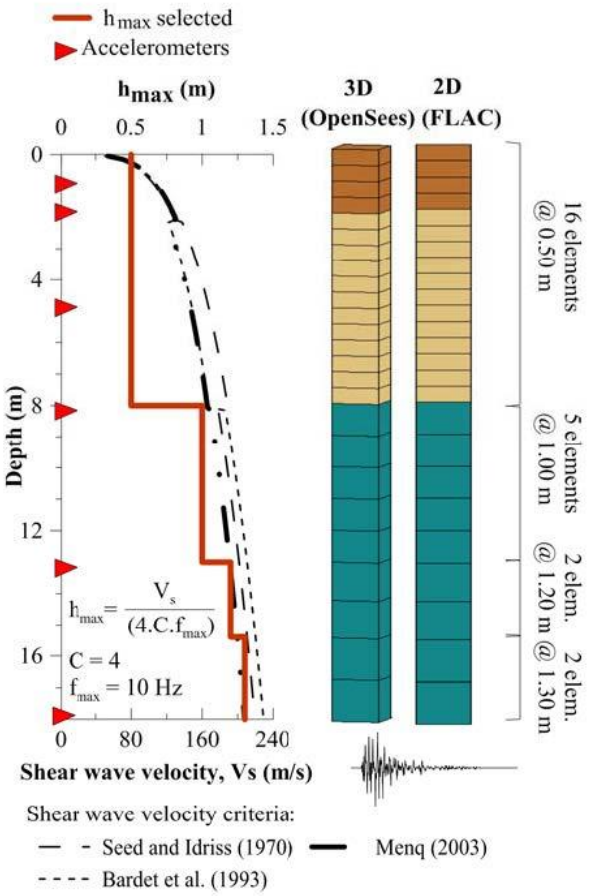

Figure 3.9 Mesh size criterion and distribution used in different simulations.

During verification, modelers agreed on consistent fixities, constraint conditions, integration solvers, small strain Rayleigh damping, and solver time steps to the extent possible between the two programs OpenSEES and FLAC to reduce epistemic uncertainty in the dynamic free-field analysis due to the use of different numerical platforms. The assigned fixities or boundary conditions forced the soil column to follow a shear beam mechanism and roughly reproduce the conditions in a flexible-shear-beam container. Therefore, nodes located at the same elevation were tied to move together in all directions. In OpenSEES kinematic constrains were applied using the Penalty method with a penalty parameter of $1x10^{15}$ by both Teams 1 and 2.

The Newmark integration method (Newmark 1959) with a gamma (γ) = 0.5 and beta (β) = 0.25 was used by Teams 1 and 2 in OpenSEES to limit any additional numerical damping. The

Rayleigh damping formulation used in OpenSEES considered a damping ratio (D) of 3% at frequencies = 2.8 and 13.8 Hz for a dry soil deposit, and frequencies = 2.5 and 12.3 Hz for the saturated deposit. These frequencies corresponded to the first and third modal frequencies of the soil deposit employed in the linear-elastic models [as recommended by Kwok et al. (2007)]. The central finite difference integration method with a local damping alpha (α) = 0.8 was used by Team 3 in FLAC. A Rayleight damping with D_{min} = 2.24% and center frequencies of 6.2 and 5.5 Hz for the dry and saturated soil deposits, respectively, was adopted by Team 3 to provide equivalent damping to OpenSEES.

In the finite element analyses, the selection of an appropriate time step increment Δt (*i.e.*, in this case $1x10^{-3}$ s) was based on recommendations by Tasiopoulou et al. (2015b) and was kept constant during the analysis. Team 3 used the same Δt as the other teams for the input motion. However, the analysis time step Δt was significantly smaller in FLAC, since it uses an explicit time-integration scheme that automatically reduces Δt to ensure numerical stability.

Figure 3.10 compares the analytical solution of the surface/base acceleration transfer functions to the numerical solutions for both dry and saturated columns. This comparison is valid in a linear system. The analytical solution was based on the elastic wave propagation theory for a uniform, damped soil underlaid by rigid bedrock, using Equations (1) and (2):

$$a_0 = 2D_{\min}\frac{\omega_1\omega_3}{\omega_1+\omega_3} \quad a_1 = 2D_{\min}\frac{1}{\omega_1+\omega_3} \tag{1}$$

where $\omega_1 = 2\pi f_1$, $\omega_3 = 2\pi f_3$ (f_1 and f_3 are the first and third modal frequencies of the soil);

$$TF = \frac{1}{\sqrt{\cos\left(\frac{\omega H}{V_s}\right)^2 + \left(\frac{a_0}{2\omega} + \frac{a_1 \omega}{2}\right)^2}} \quad (2)$$

where H=18 m and $V_s = \sqrt{G.g/\gamma}$, G=62 MPa, g=9.81 m/s^2 and γ = 15.30 and 19.33 kN/m^3 for dry and saturated sand. As shown in Figure 3.10, all the teams closely replicated the first three modal frequencies of the soil column and the amplitude of amplification expected at those modes (in the frequency range of interest). These comparisons ensured reliability and consistency among all numerical platforms.

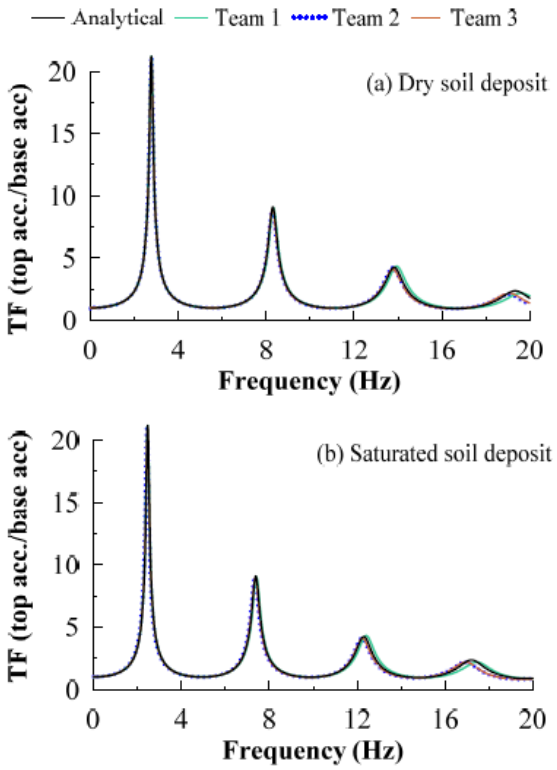

Figure 3.10 Analytical and numerically computed transfer function in a homogenous elastic soil for a dry and saturated soil deposit with low strain shear modulus = 62 MPa subjected to a sweep sine function with frequencies ranging from 0 to 30 Hz.

3.6 Class C Predictions of the Centrifuge Experiment

After verification under linear-elastic conditions, the three teams modeled the elasto-plastic soil response in the centrifuge. The column was defined by 25 elements as presented in Figure 3.9. Only the top nodes were set as pervious to allow upward flow, which did not exist in a linear-elastic model considered previously. Similar to the verification phase, a small-strain Rayleigh damping ratio of 3% at frequencies of 2.3 and 11.4 Hz (corresponding to the theoretical first and third, small-strain modal frequencies of the soil deposit) were considered in OpenSEES. An equivalent D_{min} of 2.2% at a frequency of 5.1 Hz was used in FLAC. The Δt used for the input motion and analysis was kept the same as those used during model verification.

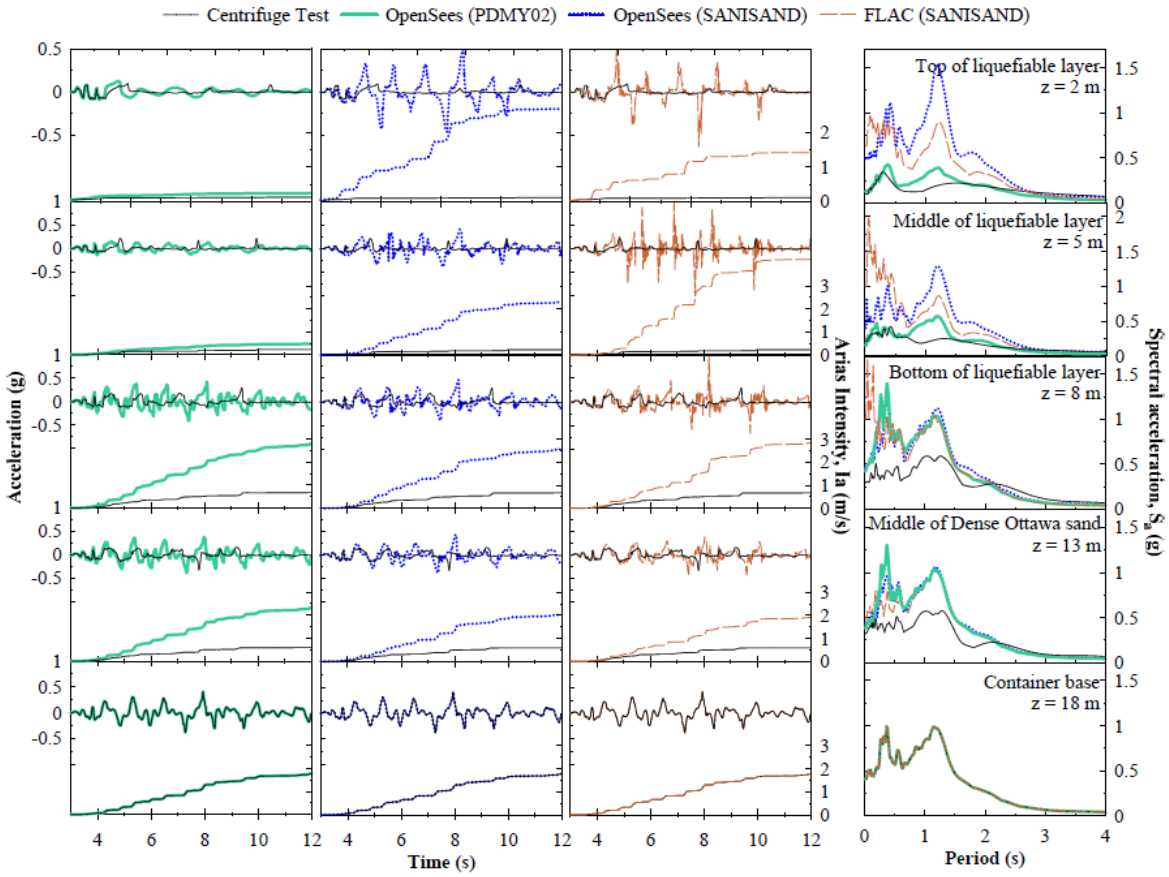

Figure 3.11 Experimentally measured and numerically computed (Class C) acceleration time histories, response spectra (5%-damped), and Arias Intensity time histories at different depths during the Kobe-L motion.

The acceleration time history recorded at the base of the container in the centrifuge (Figure 3.2) was applied as input to the rigid base of the numerical model. The numerical results were compared with the centrifuge measurements in terms of acceleration and Arias Intensity (I_a) time histories, 5%-damped acceleration response spectra (S_a), excess pore water pressure, and settlement time histories within different layers shown in Figure 3.11 through Figure 3.13. All models captured the first couple of cycles of acceleration at different depths. However, upon generation of large excess pore pressures, softening, and simultaneous densification in soil, the numerical predictions of acceleration diverged from those recorded in centrifuge. Despite their ability to better capture stress-strain and excess pore pressure generation patterns at an element level under undrained cyclic triaxial tests, the SANISAND model in both numerical platforms strongly over-predicted acceleration amplitudes at shorter periods (or higher frequencies) and showed excessive dilation tendencies (consistent with observations during monotonic triaxial tests at lower stresses). The PDMY02 model also overestimated accelerations within the dense layer of Ottawa sand (particularly at higher frequencies), but with its lower shear modulus and greater damping compared to SANISAND (Figure 3.3), it could better predict accelerations over time. This was also expected from observations during monotonic tests.

All models captured the magnitude and rate of excess pore pressure generation and net r_u values within the looser layer of Ottawa sand during strong shaking. However, they all underestimated the rate of pore pressure generation in the lower dense layer (particularly Teams 1 and 2 using OpenSEES) and overestimated the rate of dissipation after shaking in all layers. The PDMY02 model tended to overestimate the rate of pore pressure dissipation more than SANISAND, leading to poor predictions of net pore pressures in the dense layer during shaking

and in all layers after shaking. The excessive dilation tendencies of the SANISAND model were also apparent in the early parts of shaking as excessive drops in excess pore pressures.

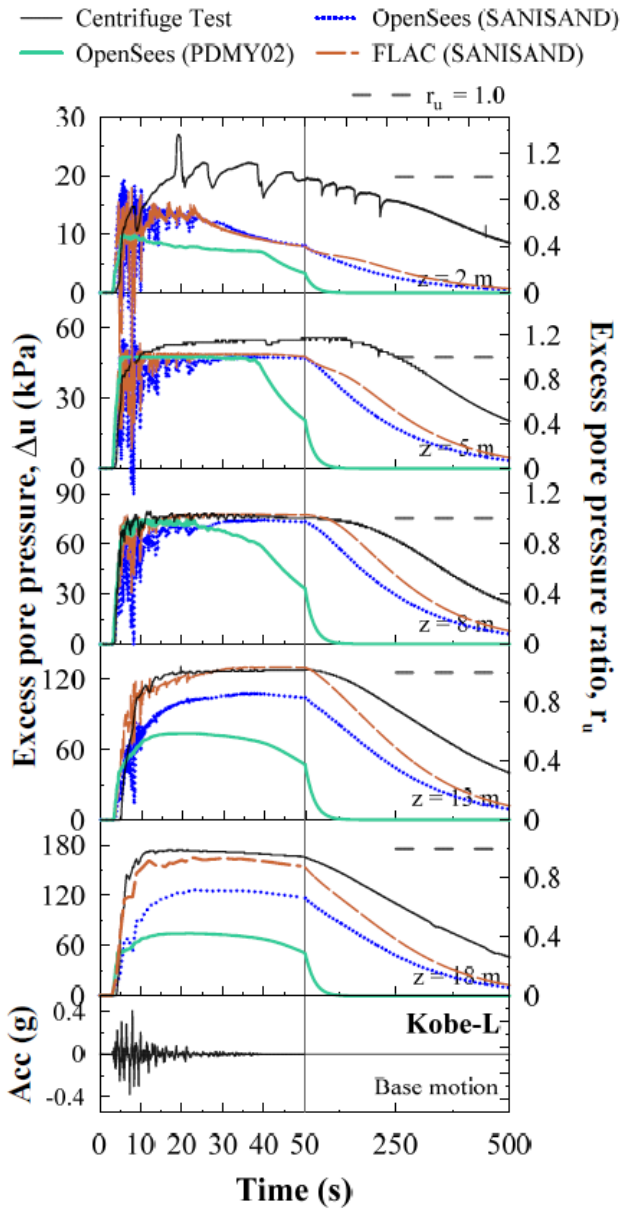

Figure 3.12 Experimentally measured and numerically computed (Class C) excess pore pressure time histories at different depths during the Kobe-L motion.

All numerical simulations highly underestimated the volumetric strains as observed experimentally, which are caused by consolidation, sedimentation, and partial drainage (Dashti et

al. 2010a). This is a well known problem of most numerical platforms and constitutive models (*e.g.*, Howell et al. 2015), which was also apparent in Figure 3.5 at an element level. Clearly all models underestimated volumetric settlements, particularly PDMY02 (Figure 3.13). One general approach that has been suggested by previous researchers to improve the prediction of volumetric settlements is to vary hydraulic conductivity (k) of the element as a function of time or r_u (*e.g.*, Shahir et al. 2012). In this study, however, the modelers decided to keep k constant, to fairly compare and evaluate the shortcomings of models.

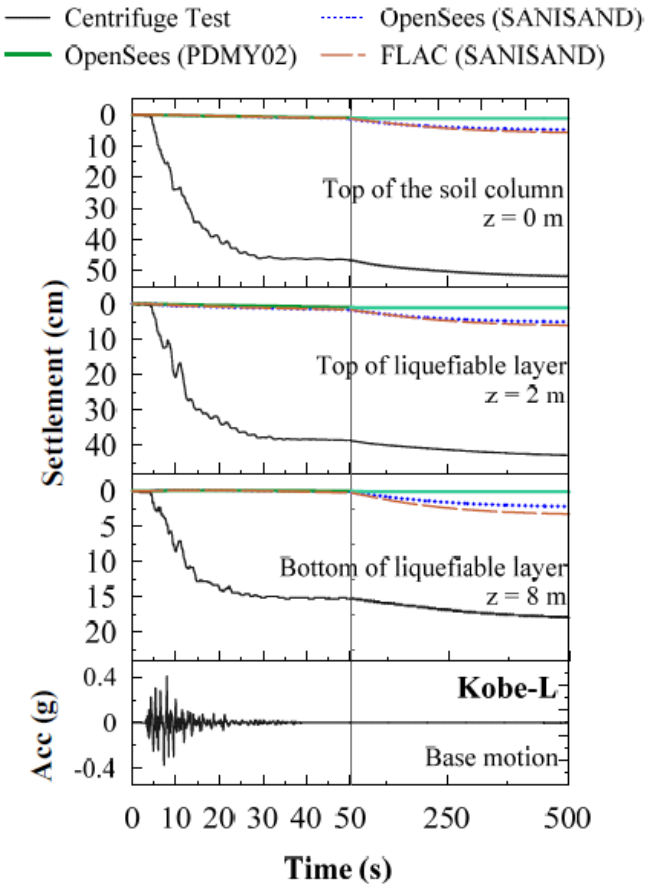

Figure 3.13 Experimentally measured and numerically computed (Class C) settlement time histories at different depths during the Kobe-L motion.

Using the linear interpolation of acceleration recordings in the centrifuge and displacement time histories (*i.e.*, double integration of accelerations), transient shear stress-strain time histories

were approximated following the procedure recommended by Zeghal and Elgamal (1998). The interpretted experimental results were subsequently compared with those numerically computed in Figure 3.14 at different depths. The numerical results included total strains (transient and permanent), whereas the experimental results only contained transient strains (no permanent deformation can be captured from accelerometer recordings alone). Despite the unfair comparison between numerical and experiemntal resutls in this case, Figure 3.14 intents to show the progression of shear stress and strain cycles over time. The numerical results, in this case, have the advantage of showing the accumuluation of strain in one direction, which experimental results do not. All numerical models indicated excessive regaining of shear stiffness, particularly in the dense layer, which is associated with an excessive dilation tendency (evident also during element test calibration). Within the loose layer, PDMY02 showed a more reasonable comparison with the experimental stress–strain response compared with SANISAND.

Figure 3.15 and Figure 3.16 quantify the percent (%) difference between the numerical and experimental results in terms of spectral accelerations, Arias Intensities, excess pore pressures, and settlements at different depths. A positive difference indicates an over-prediction of the experimental response, and vice versa. In general, all models overpredicted the spectral accelerations in periods less than approximately 2s as well as Arias Intensities. The PDMY02 predictions were the closest to experimental results in terms of accelerations. Yet, a peak difference of approximately 200% was still considered unacceptably high. Differences in the excess pore pressures were also significant (particularly within the dense layer and in the dissipation stage after strong shaking). The SANISAND model overall did significantly better than PDMY02 in their prediction of net excess pore pressures during strong shaking, with the exception of excessive momentary drops in excess pore pressures due to dilation. All numerical simulations

underestimated settlement by approximately 80 to 100%, which improved slightly over time after significant dissipation following shaking..

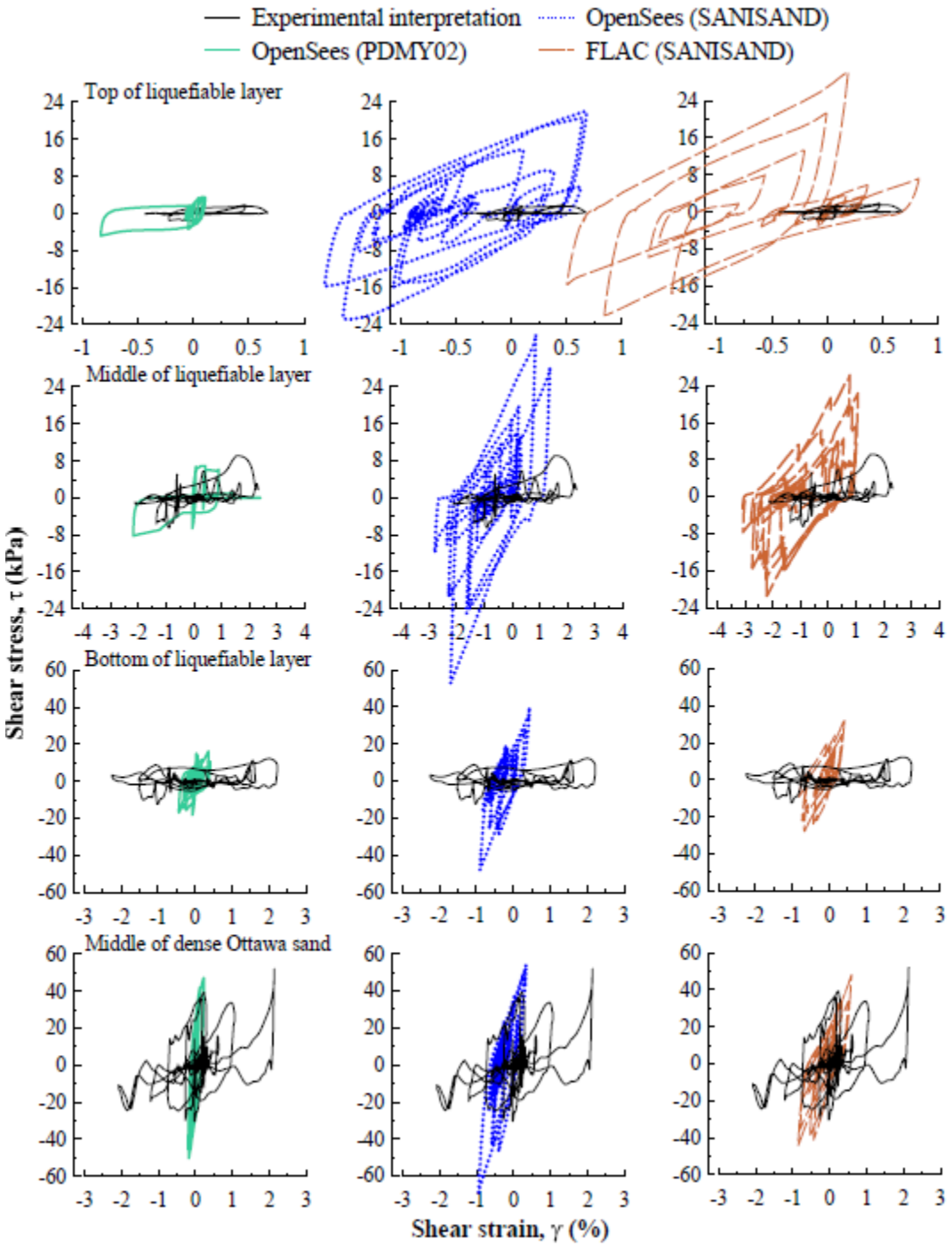

Figure 3.14 Experimentally interpreted and numerically computed (Class C) shear stress-shear strains at different depths during the Kobe-L motion.

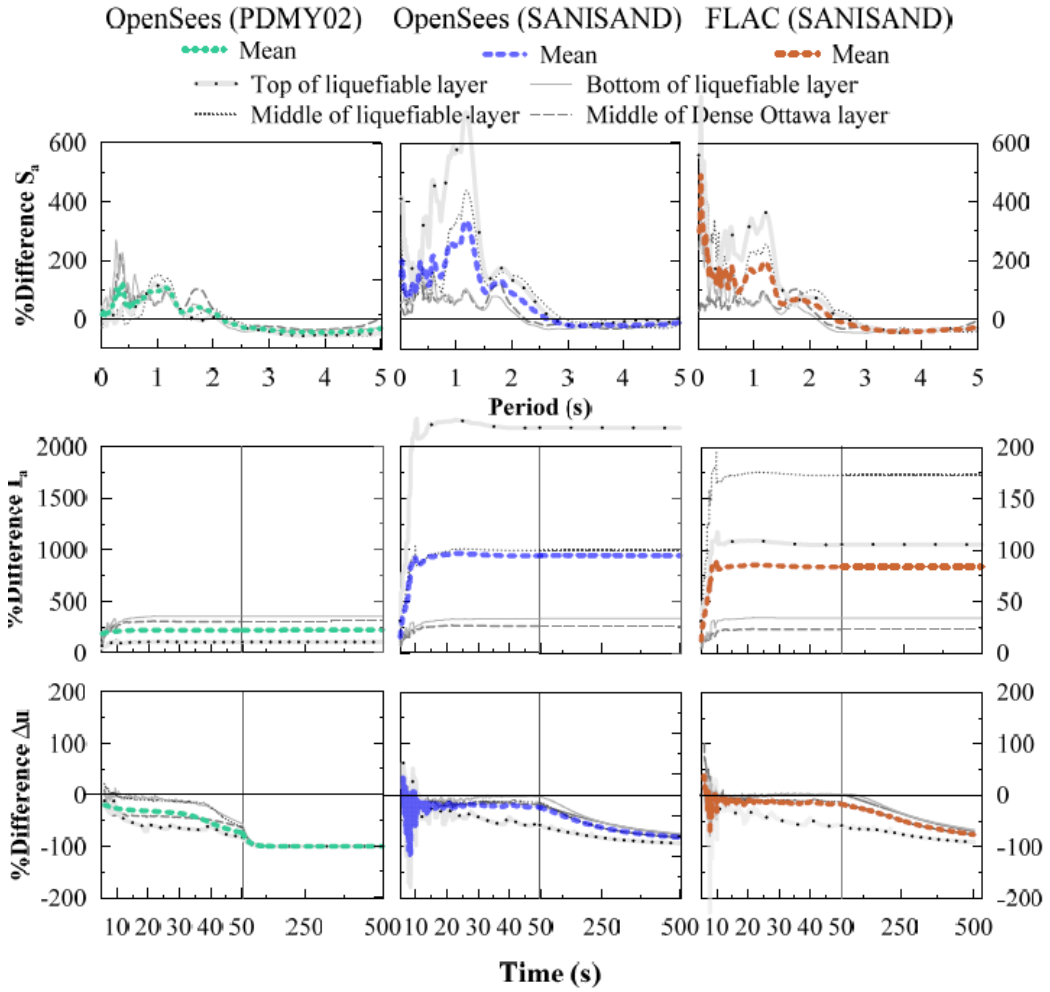

Figure 3.15% Difference between experimental and numerical (Class C) acceleration response spectra Sa (5%-damped), Arias Intensity, Ia, and excess pore pressures at different depths for each numerical simulation.

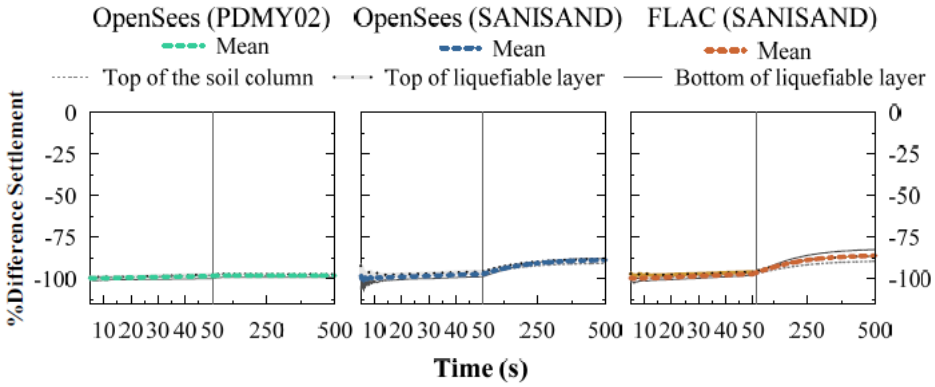

Figure 3.16% Difference between experimental and numerical (Class C) settlement time histories at different depths for each numerical simulation.

3.7 Second Calibration Phase

After comparison of the numerical simulation results with the centrifuge experiment and knowledge of model shortcomings, the teams proceeded to the second phase of soil model calibration (Calibration C1), to improve the predictions of both triaxial and centrifuge tests to the extent possible. The element type and computational platforms were not altered in this phase.

3.7.1 PDMY02 model parameter recalibration

Based on previous observations in Class C predictions, the PDMY02 model parameters were recalibrated for Ottawa sand, now prioritizing the stress-strain response and rate of excess pore pressure generation in triaxial tests as opposed to the number of cycles to liquefaction, particularly focusing on dense Ottawa sand. The PDMY02 parameters for Monterey sand were kept the same as for Calibration C.

In the recalibration process, Team 1 focused mostly on the cyclic response of dense Ottawa sand (*i.e.*, especially at larger shear strains of 0.315% and 0.66%), to improve the predicted pore pressures later in the centrifuge model. To capture the initial rate of excess pore pressure generation in dense sand in the triaxial tests, the number of cycles to liquefaction (r_u = 0.99) largely needed to be compromized. Knowing also that PDMY02 tends to strongly overestimate the coefficient of consolidation and rate of excess pore pressure dissipation it was now attempted to slightly overestimate the generation of excess pore pressures under undrained loading at an element level. The compressibility and hydraulic conductivity of the soil layers were not altered.

The recalibrated PDMY02 model parameters are shown in Table 3.3. To make the response of dense sand less dilative (more contractive), Team 1 sequentially reduced the low-strain maximum shear modulus at 1 atm ($G_{\max,s'_m=1atm}$) and modified the friction and phase transformation

angles within the range of what was expected empirically or measured experimentally, as well as the contraction and dilation parameters. Other parameters were adjusted to reduce the dilative tendency (*i.e.*, the space between the phase transformation envelope and the last yield surface), increase the accumulation of volumetric plastic strains, and generation of pore pressures. A similar approach was employed in the recalibration of loose Ottawa sand, although the changes were fewer than those needed in the dense layer. The model parameters were ensured to follow a logical trend for different soil relative densities. The implemented G/G_{max} curves in PDMY02 as well as the material damping ratio curves predicted by the model in Calibration C1 are shown in Figure 3.17, which did not change notably compared to Calibration C..

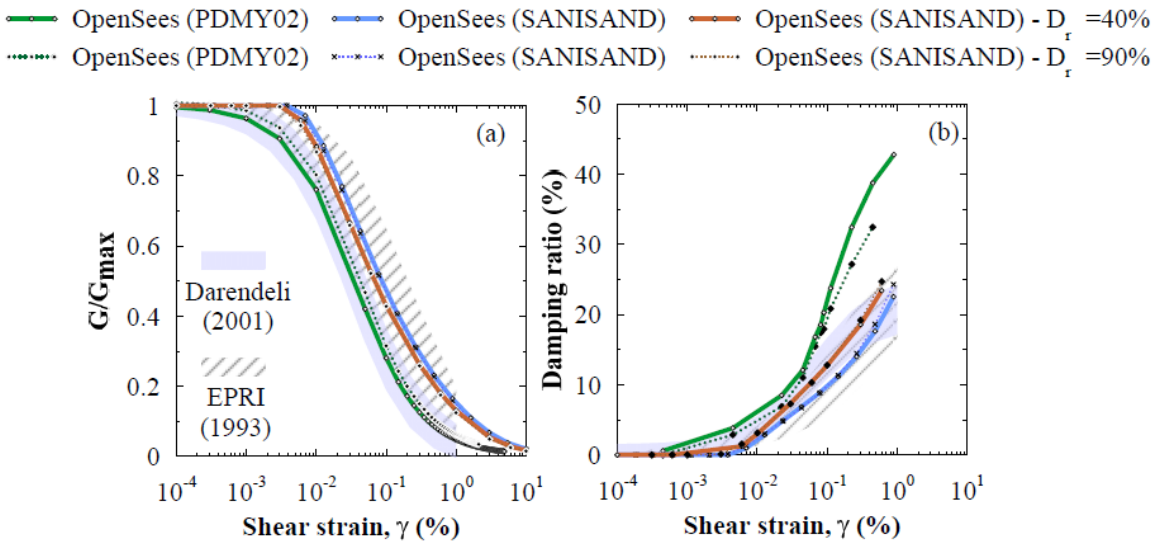

Figure 3.17 Comparison of model properties in Calibration C1: (a) shear modulus reduction curves (strength corrected) imposed on the PDMY02 and obtained from the default SANISAND constitutive models; (b) damping ratio curves obtained from the models.

3.7.2 SANISAND model parameter recalibration

Similar to the PDMY02 model, the SANISAND parameters showed excessive dilation during Class C predictions of the centrifuge model. As a result, accelerations were over-predicted, particularly at higher frequencies. This was also evident when comparing the response under

drained and undrained monotonic triaxial tests. The parameters A_0 and n^d were modified by the two teams (separately) to accumulate smaller positive volumetric strains and make the response more contractive. In order to better capture accelerations, the distance to the bounding surface controlled by the model parameter n^b was modified to reduce the plastic modulus to one that better represented the response of soft soil. The Monterey sand parameters were not changed. The modified SANISAND model parameters for Teams 2 and 3 are shown in Table 3.4. Figure 3.17 also shows a slight reduction in the predicted shear modulus and an increase in damping predicted by SANISAND both in OpenSEES and FLAC at larger strains compared to Calibration C.

3.7.3 Element level numerical and experimental comparisons (Calibration C1)

Numerical simulations were again compared to monotonic drained and undrained triaxial tests for loose and dense Ottawa sand (Appendix C). Team 1's results were similar between Calibrations C and C1 for loose Ottawa sand. Teams 2 and 3 using the bounding surface model, on the other hand, were able to increase contractive volumetric strains in loose sand, especially at low confining pressures that were poorly predicted previously. A significant reduction of dilation tendencies was achieved by all teams within the dense sand, even at the cost of sacrificing better match with drained triaxial tests. This led to better prediction of excess pore pressures under undrained loading (although PDMY02 still showed excessive dilation). Teams 2 and 3 focused mainly on the prediction of residual deviatoric stresses and strength rather than peak values, which made the response of dense sand less dilative. The SANISAND model improved its prediction of localized quasi-steady state (*e.g.*, at an axial strain of about 1-2%), especially for confining pressures $\leq$ 100 kPa.

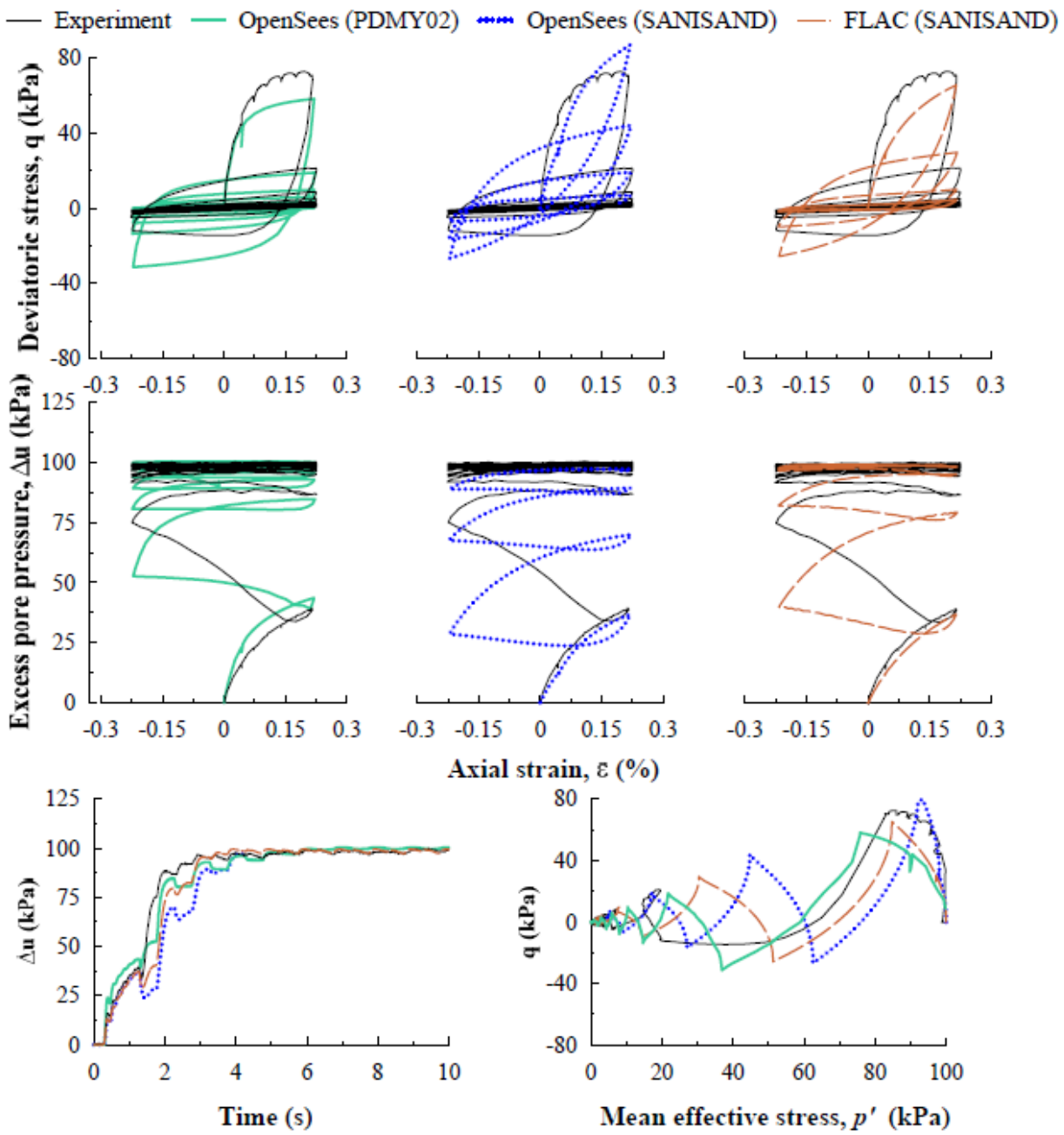

Figure 3.18 Comparison between experimental and numerical simulations (Calibration C1) for Ottawa sand F65 with D_r = 90% and a cyclic shear strain amplitude of 0.315% (or axial strain amplitude of 0.21%).

One representative cyclic undrained triaxial test for dense sand is shown in Figure 3.18. The excessive dilation predicted previously for dense sand, in particular with by PDMY02, was reduced. Since Team 1 sacrificed the number of cycles to liquefaction in Calibration C1, the rate

of excess pore pressure buildup was better captured now. Teams 2 and 3 also reduced the soil's dilative tendencies in Calibration C1. The experimental and numerical number of cycles to liquefaction are shown in Figure 3.19, indicating now a poor performance by all models. Despite using different elements and numerical platforms, and despite performing Calibration C1 independently (without communication between teams), the objectives and results were largely consistent between Teams 2 and 3. But the refined parameters by Team 2 (OpenSEES) predicted slightly larger shear stiffness and smaller damping compared to Team 3 (FLAC) as shown in Figure 3.17. This could influence acceleration predictions later.

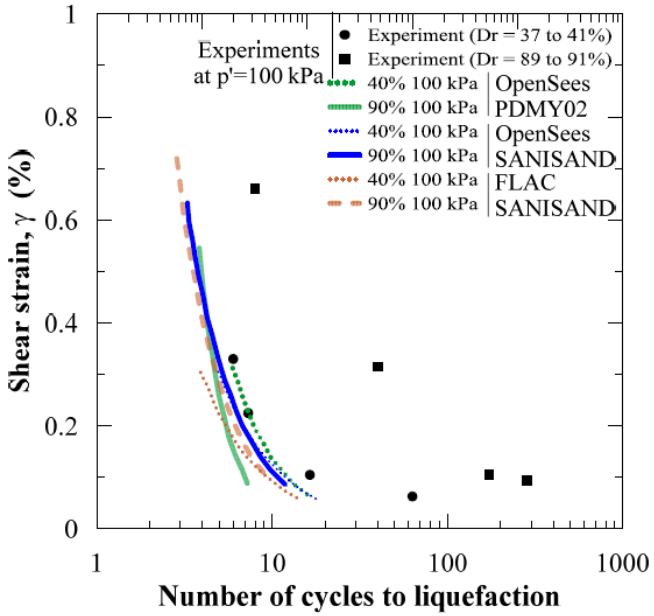

Figure 3.19 Relation between number of cycles required to achieve liquefaction (ru≈0.99) and cyclic shear strain amplitude, γ, in numerical simulations and cyclic triaxial tests on Ottawa sand F65 during Calibration C1.

3.8 Class C1 Predictions of the Centrifuge Experiment

Following Calibration C1, the three teams performed Class C1 predictions of the centrifuge test. Numerically computed and experimentally measured results are compared in Figure 3.20 through Figure 3.22. In general, all models showed significant improvements compared to the

Class C predictions. All the models now captured reasonably well the de-amplification of motions as shear waves travelled from the base to the surface of a softened soil deposit. The bounding surface plasticity model (SANISAND) showed notable improvements in its prediction of accelerations particularly at higher frequencies in both numerical platforms. Teams 1 and 2 using OpenSEES continued to slightly overestimate accelerations at higher frequencies (shorter periods) and Arias Intensities.

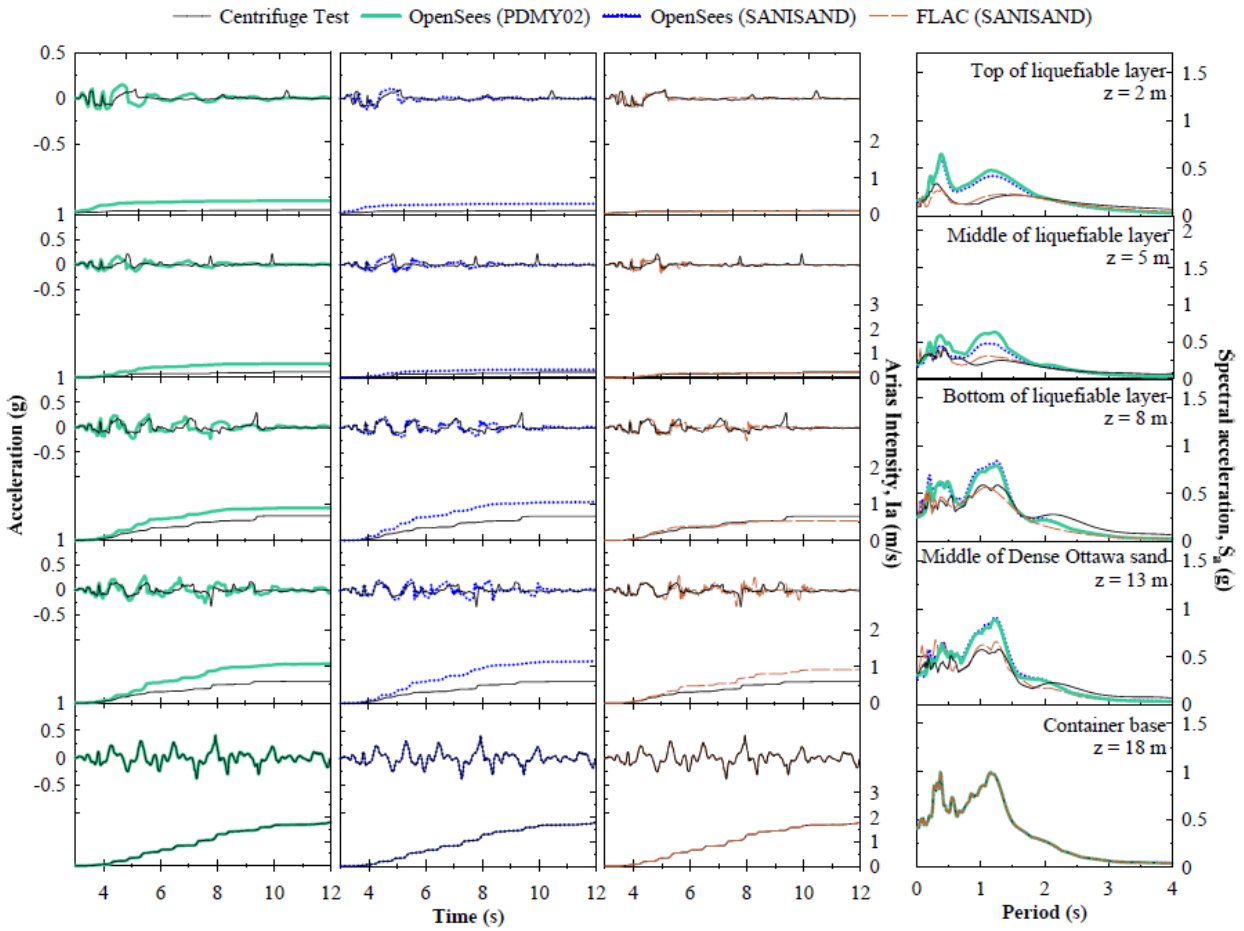

Figure 3.20 Experimentally measured and numerically simulated (Class C1) acceleration time histories, response spectra (5%-damped), and Arias Intensity time histories at different depths during the Kobe-L motion.

The PDMY02 model showed improvements in its prediction of peak excess pore pressures, particularly within the lower dense Ottawa sand layer after increasing its contractive tendencies

and prioritizing the rate of pore pressure generation at an element level. However, due to the model's significant underestimation of volumetric compressibility and subsequent overestimation of coefficient of consolidation, the rate of dissipation continued to be greatly overestimated. In a fully-coupled boundary value problem that allowed for simultaneous generation and redistribution of pore pressures (as opposed to a fully undrained response at an element level), additional dissipation of excess pore pressures was expected. The fast dissipation rate continued to reduce the net pore pressures predicted by PDMY02. This response can be improved if the modeler artificially reduces the hydraulic conductivity or increases the intrinsic coefficient of volumetric compressibility in the model (not adopted here, as this is not a fundamental change). The bounding surface model (SANISAND), however, captured the generation and dissipation rate of net excess pore pressures quite well, without any change in k over time indicating a more accurate volumetric response.

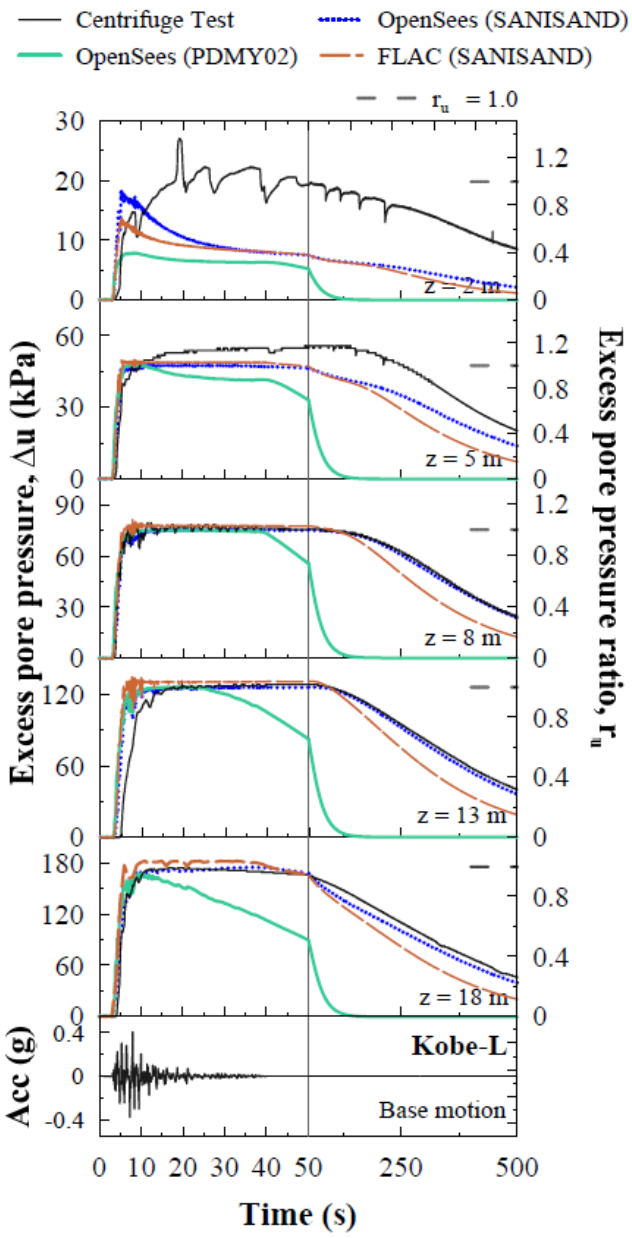

Figure 3.21 Experimentally measured and numerically simulated (Class C1) excess pore pressure time histories at different depths during the Kobe-L motion.

In terms of volumetric settlements, both Class C and Class C1 predictions showed unsatisfactory results (although the errors were slightly reduced in Class C1), emphasizing an important known deficiency of most continuum models in predicting volumetric deformations in a liquefied soil profile. This deficiency is partly associated with the constitutive models' weakness, but also partly with the type of elements used, the multiphase formulation implemented in each

platform, and most importantly the change in a few important soil properties (*e.g.*, pemeability and porosity) over time that are not captured numerically. Increasing soil's *k* may help improve the total volumetric settlements predicted (Shahir et al. 2012). But that may adversely affect the quality of excess pore pressure predictions and is not a fundamental improvement. Further, measuring settlement in soil experiemtnally involves a degree of uncertatinty due to the possible relative movement of the LVDT plates resting on softened soil as well as the possibility of flow along the container boundaries. This area is in need of further investigation in future research projects.

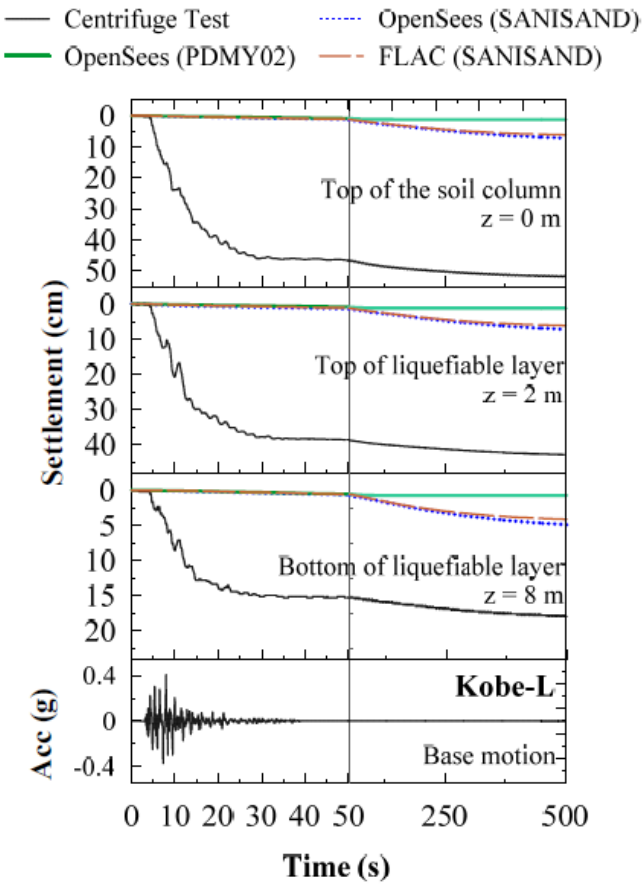

Figure 3.22 Experimentally measured and numerically computed (Class C1) settlement time histories at different depths during the Kobe-L motion.

Figure 3.23 shows the experimental interpretation of shear stress-strains at different depths (obtained from accelerometer recordings) compared to those predicted numerically. All numerical results showed a better match with centrifuge recordings during Class C1 predictions in terms of magnitude and shape of shear stresses and strains. The most drastic improvement was observed in SANISAND compared to their Class C predictions. These observations were consistent with Figure 3.20.

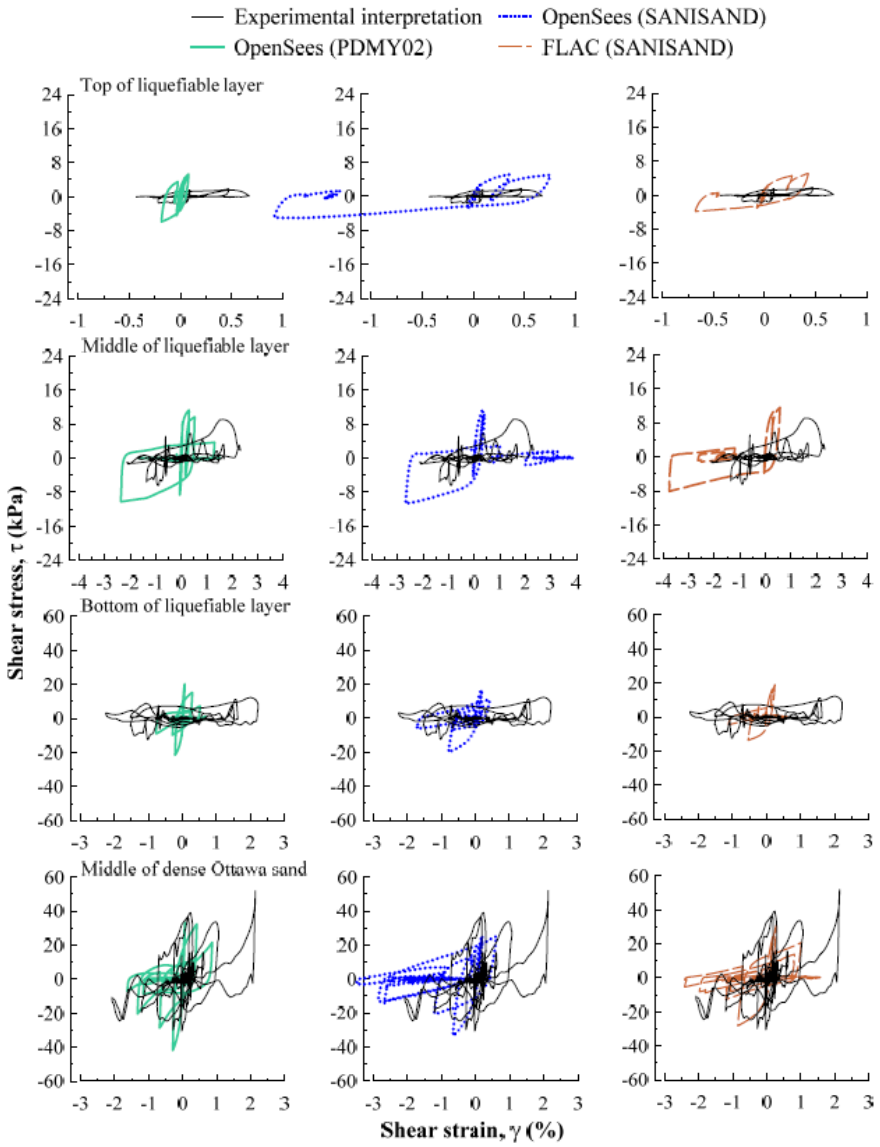

Figure 3.23 Experimentally interpreted and numerically computed (Class C1) shear stress-shear strains at different depths during the Kobe-L motion.

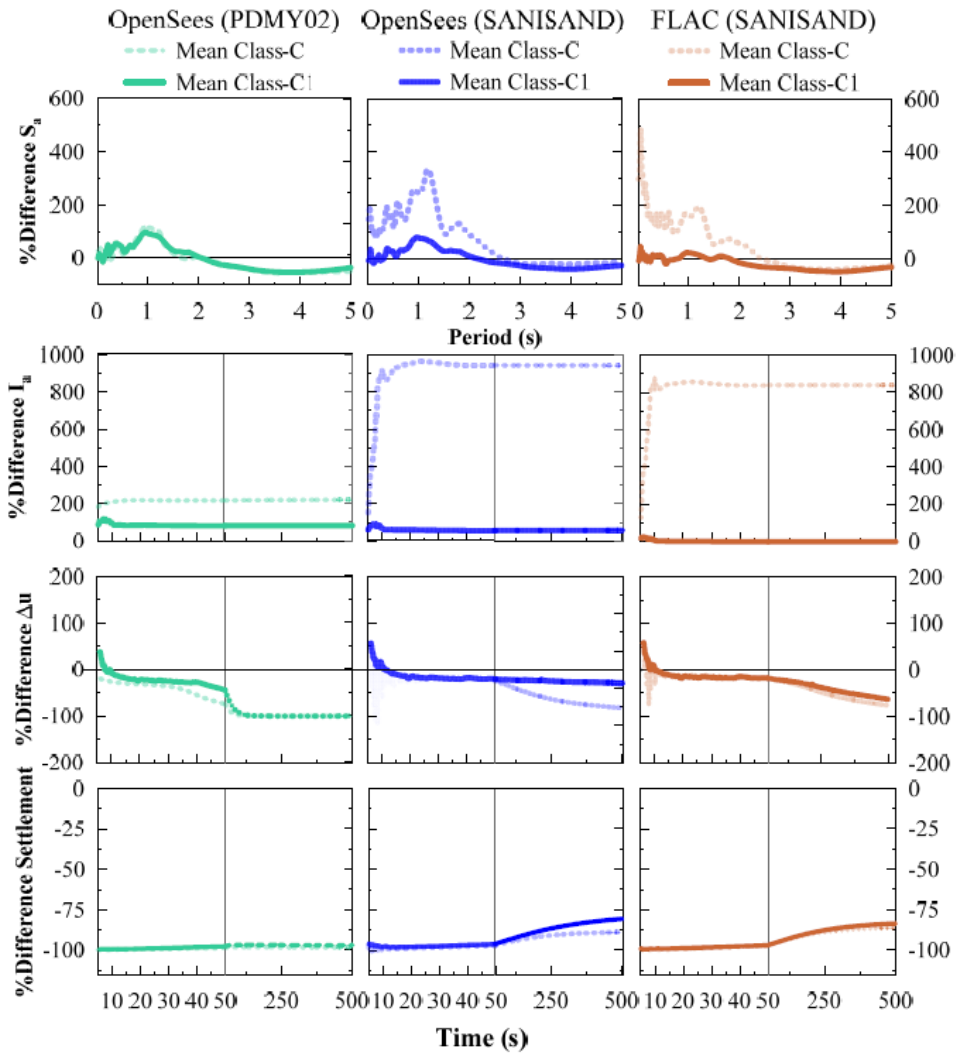

Figure 3.24 Comparison of mean % difference between numerical Class C and Class C1 simulations and experimental recordings in S_a, I_a, excess pore pressure, and settlement time histories at different depths for each constitutive model.

Figure 3.24 compares the mean values of % difference in various response parameters among different models during Class C and C1 predictions. Overall, the SANISAND model showed better predictions (smaller percent difference) in all parameters compared to PDMY02 after adjustments made in Calibration C1, particularly in terms of accelerations and excess pore pressures. Despite small differences due primarily to different numerical platforms and elements, the results of Teams 2 and 3 were consistent, and all models continued to largely underestimate

settlements. Although improved, the comparisons still point to the difficulty of simultaneaosly capturing accelerations, pore pressures, and settlements on level ground numerically.

CHAPTER 4

4 CAPABILITIES OF NUMERICAL SIMULATIONS TO CAPTURE THE PERFORMANCE OF INELASTIC STRUCTURES ON MITIGATED AND UNMITIGATED LIQUEFIABLE SOILS

This chapter presents a paper that will partly be submitted to a journal in February of 2019. It is co-authored by Jenny Ramirez, Shideh Dashti, Abbie Liel, Guido Camata, Massimo Petracca, and Yu-Wei Hwang.

4.1 Introduction

A number of liquefaction mitigation techniques have evolved over the past years, driven by damage to buildings and infrastructure due to seismically-induced soil liquefaction. These mitigation techniques, which include ground densification, soil reinforcement, grouting and mixing techniques, and enhanced drainage, aim to reduce settlement, tilt, and, hence, damage of shallow-founded structures. Yet, the effectiveness and efficacy of these techniques in achieving these goals near building and when the seismic performance of the entire soil-foundation-structure (SFS) system is considered remain unclear. In particular, the tradeoffs associated with different mitigation strategies which, on the one hand reduce a building's net settlement and possibly tilt, but on the other hand, amplify the seismic demand transferred to the superstructure, potentially increasing shaking-induced damage, are not well characterized. A better understanding of these

responses and interactions is required before we can realize the benefits of performance-based earthquake engineering in addressing and mitigating liquefaction and its consequences. Numerical modeling can provide important insights into these mechanisms of behavior, and the numerical simulation of alternative mitigation strategies is a critical component of performance-based frameworks. However, we first need to understand the capabilities of the existing numerical tools to capture the important phenomenon and demand parameters.

In this paper, we present the capabilities and limitations of state-of-the-art soil numerical models in capturing the response of inelastic structures founded on mitigated and unmitigated layered liquefiable soils as observed experimentally. Centrifuge experiments investigated the influence of mitigation on the response of inelastic, multiple-degree-of-freedom (MDOF) structural models on shallow foundations, and liquefiable soil profiles (Olarte et al. 2017, 2018a; Paramasivam et al. 2018). Two different mitigation techniques were evaluated: ground densification and enhanced drainage with prefabricated vertical drains (PVDs). Subsequently, three-dimensional (3D), nonlinear, solid-fluid, fully-coupled, effective stress, dynamic finite-element (FE) analyses of the centrifuge tests were performed in the OpenSEES platform using two constitutive models for soil. The soil models were first calibrated based on a large number of static and cyclic, drained and undrained triaxial tests and a free-field centrifuge test (previously detailed by Ramirez et al. 2017, 2018). The structural models and fuses were calibrated based on beam-column component tests and hammer impact tests (Olarte et al. 2017, 2018a). In this paper, these calibrated component models are combined to represent the dynamic response of the SFS system with and without mitigation. This paper explores the sensitivity of 3D, fully-coupled, nonlinear numerical predictions to various analysis parameters as well as their capabilities and limitations in capturing the response of highly nonlinear soil-foundation-structure systems.

4.2 Background

There are increasing documented examples of liquefaction damage after recent earthquakes (Ansal et al. 1999; GEER 2011). Yet, case history observations that document the performance of liquefaction mitigation strategies remain sparse, particularly near structures (*e.g.*, Watanabe 1966; Mitchell and Wentz 1991).

Alternatively, physical modeling can be used to generate experimental "case histories" under simpler and controlled conditions. Several researchers have performed shaking table tests at 1g, or under increased gravity in a geotechnical centrifuge, to evaluate the seismic performance of buildings on unmitigated liquefiable soil deposits (*e.g.*, Yoshimi and Tokimatsu 1977; Liu and Dobry 1997; Hausler 2002; Adalier et al. 1998; Dashti at al. 2010a, 2010b; Mitrani and Madabhushi 2013; Jones 2013; Chandra and Gueguen 2017). A smaller but growing number of experimental studies have examined the response of model structures on mitigated soils (*e.g.*, Hausler 2002; Takemura et al. 2009; Kuriki et al. 2012; Rasouli et al. 2015; Olarte et al. 2017, 2018a, 2018b; Paramasivam et al. 2018, 2019). The more recent of these incorporated physical models with realistic dynamic properties that are capable of damage to characterize soil-foundation-mitigation-structure interaction (SFS) interaction on liquefiable sites (Olarte et al. 2017, 2018a; Paramasivam et al. 2018). These experimental studies generally showed that ground densification, soil reinforcement, and vertical drains can reduce settlement of shallow-founded structures. However, Olarte et al. (2018a) showed that the force and acceleration demand on the superstructure can be amplified by increasing stiffness of the underlying soil through reinforcement or densification. Likewise, Paramasivam et al. (2018) found that PVDs amplify the seismic demand transferred to the superstructure, which can amplify flexural drifts and damageability. This increase in flexural drifts has the second order effect of further increasing

moment demands about the foundation (*i.e.*, P-Δ effects), which could in turn amplify tilt. Such experiments improve our understanding of the potential tradeoffs associated with liquefaction mitigation. They also provide the data required to calibrate and validate advanced numerical tools, which can in turn be used to study more realistic conditions and variations in parameters.

Fully-coupled, nonlinear, effective-stress, dynamic numerical modeling is a powerful tool to assess the response of liquefiable soil deposits and their effects on buildings for a range of soil, structural, and ground motion characteristics. Over the past few decades, a number of nonlinear, elasto-plastic soil constitutive models have been developed and implemented in both finite-element and finite-difference platforms for modeling the response of liquefiable soil deposits and their effects on buildings. A few examples include: the UBCSAND model (Puebla et al. 1997); the pressure-dependent-multiyield surface (PDMY02) model (Elgamal et al. 2002 and Yang et al. 2008); the bounding surface SANISAND model and its variations (Dafalias and Manzari 2004); and the stress-ratio controlled, critical state compatible PM4SAND model (Boulanger and Ziotopoulou 2015).

Ramirez et al. (2018) investigated PDMY02 and SANISAND, showing that these models predict the accelerations and excess pore pressures in a layered liquefiable soil profile in the far-field (without a structure) relatively well. However, the models and a continuum framework were unable to capture volumetric strains due to sedimentation, which tend to govern settlements in the far-field, particularly in thicker deposits. As a result, far-field settlements were underestimated by up to 100%. The key difference in the models in terms of results was the dissipation of excess pore pressures. The PDMY02 model predicted a greater rate of excess pore pressure dissipation due to the model's significant overestimation of coefficient of volumetric compressibility. Ramirez et al. (2018) demonstrated the importance of soil model calibration not only based on the number

of cycles to trigger liquefaction, but also the time histories of shear stress, strain, and pore pressure generation at an element level. They also showed the value of access to a more realistic boundary value problem with simultaneous cyclic generation and dissipation of pore pressures during soil model calibration. Ramirez et al. (2018) did not evaluate the numerical prediction of soil-structure interaction nor the effectiveness of liquefaction mitigation techniques.

A number of prior researchers have studied the dynamic interactions between softened ground and structures using advanced soil models, but simple representations of the superstructure. For example, Popescu et al. (2006) carried out a plain-strain analysis of structures (modeled as a rigid foundation) on liquefiable soils (modeled with a multi-yield constitutive model). More recently, other researchers (*e.g.*, Lopez-Caballero and Farahmand-Razavi 2008; Dashti and Bray 2013; Karimi and Dashti 2016a,b; Luque and Bray 2017) numerically represented the building as linear-elastic, single degree-of-freedom (SDOF) systems on a nonlinear soil domain. The studies generally showed it critical to model the building's inertial response (*e.g.*, mass, height, stiffness) in addition to foundation's properties to evaluate its influence on soil deformations. Thus, these were a notable improvement to prior models with rigid foundations. These models' use of elastic SDOF structures was justified on unmitigated soil deposits, because the superstructure typically behaves elastically, while damage is dominated by foundation tilt and settlement on softened ground. Karimi and Dashti (2016a, 2016b) also showed the importance of modeling the system in 3D to capture the 3D nature of shear deformations and flow patterns below foundations that are not long in one direction.

When mitigation techniques are employed, nonlinearity and damage in the superstructure may play an important role in the performance of the overall soil-foundation-structure (SFS) system, which could not be studied in prior elastic or rigid model buildings. Simultaneous

modeling of soil and structure's nonlinear response and interactions, however, requires careful calibration, validation, and knowledge of the underlying sensitivities, limitations, and capabilities, prior to use in practice or a parametric study.

4.3 Centrifuge Testing Program

4.3.1 Overview

A number of centrifuge experiments has recently been completed at the University of Colorado Boulder's 5.5 m-radius, 400 g-ton centrifuge facility (Ko 1988) to evaluate soil-structure interaction on liquefiable soils with different mitigation techniques (Olarte et al. 2017, 2018a, 2018b; Paramasivam et al. 2018, 2019). Seven of these tests are described in Table 4.1, and are the focus of this paper. The goal of these tests was to evaluate the influence of mitigation techniques on the seismic performance of SFS systems. The tests varied the thickness of the liquefiable deposit, the embedment depth of the foundation, the key dynamic properties of the structures (*i.e.*, contact pressure, modal frequencies, force-deformation behavior, yield capacity), and the type of mitigation. In this paper, we focus only on the cases in these tests involving no mitigation, densification, and prefabricated vertical drains (PVDs). Elevation and plan view drawings of selected tests that were later numerically simulated, and their instrumentation layouts, are shown in Figure 4.1.

All experiments included two separate model structures with different mitigation techniques, with the exception of the test that modeled only far-field conditions without structures. The two model structures had a center-to-center distance of 3.5 times foundation width to reduce their interaction. However, some interaction was still expected between the two building models and with the container boundaries, particularly during strong levels of shaking. Hence, the entire soil-foundation-structure system in centrifuge was modeled together in the numerical simulations.

Table 4.1 Centrifuge testing program at the University of Colorado Boulder

Test ID	Structure or Far-Field ID	Soil Profile[a]	Mitigation Technique	Reference
$FF_{DR\text{-}DS\text{-}6}$	$FF_{DR\text{-}6}$ $FF_{DS\text{-}6}$	2	PVDs Densification	Kirkwood and Dashti 2019
$A1_{NM\text{-}DS\text{-}4}$	$A1_{NM\text{-}4}$ $A1_{DS\text{-}4}$	1	None Densification	Olarte et al. 2017
$A1_{DR\text{-}SW\text{-}4}$	$A1_{DR\text{-}4}$ $A1_{SW4}$[b]	1	PVDs Structural walls	Olarte et al. 2017
$A2_{NM\text{-}DS\text{-}6}$	$A2_{NM\text{-}6}$ $A2_{DS\text{-}6}$	2	None Densification	Olarte et al. 2018a
$A2_{DR\text{-}SW\text{-}6}$	$A2_{DR\text{-}6}$ $A2_{SW\text{-}6}$[b]	2	PVDs Structural walls	Paramasivam et al. 2018
$B_{NM\text{-}DR\text{-}6}$	$B_{NM\text{-}6}$ $B_{DR\text{-}6}$	2	None PVDs	Paramasivam et al. 2018
$B_{DS\text{-}DSL\text{-}6}$	$B_{DS\text{-}6}$ $B_{DSLB\text{-}6}$[b]	2	Densification Dens. +Latex Barrier	Olarte et al. 2018b

[a]The name of each test first specifies the structure type (*e.g.*, Structures A1, A2, B, or FF for far-field conditions). The subscript in the test name identifies first the type of mitigation strategy employed around that structure (NM for no-mitigation, DS for densification, SW for in-ground structural walls, DR for enhanced drainage, and DS-LB for densification and latex barrier), followed by the thickness of the looser Ottawa sand layer (4 or 6 m) in a given test.[b]These tests were not evaluated numerically.

The elevation-view drawings of different tests and their instrumentation layouts are shown in Figure 4.1. Test $FF_{DR\text{-}DS\text{-}6}$ represented Soil Profile 2 (liquefiable layer thickness, H_{liq} = 6 m) under far-field conditions, without any structure, but with two mitigation techniques: 1) PVDs or drains ($FF_{DR\text{-}6}$) and ground densification ($FF_{DS\text{-}6}$). Test $A1_{NM\text{-}DS\text{-}4}$ represented Soil Profile 1 (H_{liq} = 4 m) and contained two identical Structure A1s: one with no mitigation ($A1_{NM\text{-}4}$) and one on densified ground ($A1_{DS\text{-}4}$). Using the same building and soil profile, Test $A1_{DR\text{-}SW\text{-}4}$ considered PVDs around Structure $A1_{DR\text{-}4}$ and structural walls around $A1_{SW\text{-}4}$ (not evaluated in this paper). The other tests modeled Structure A2 or B with the same mitigation techniques on Soil Profile 2.

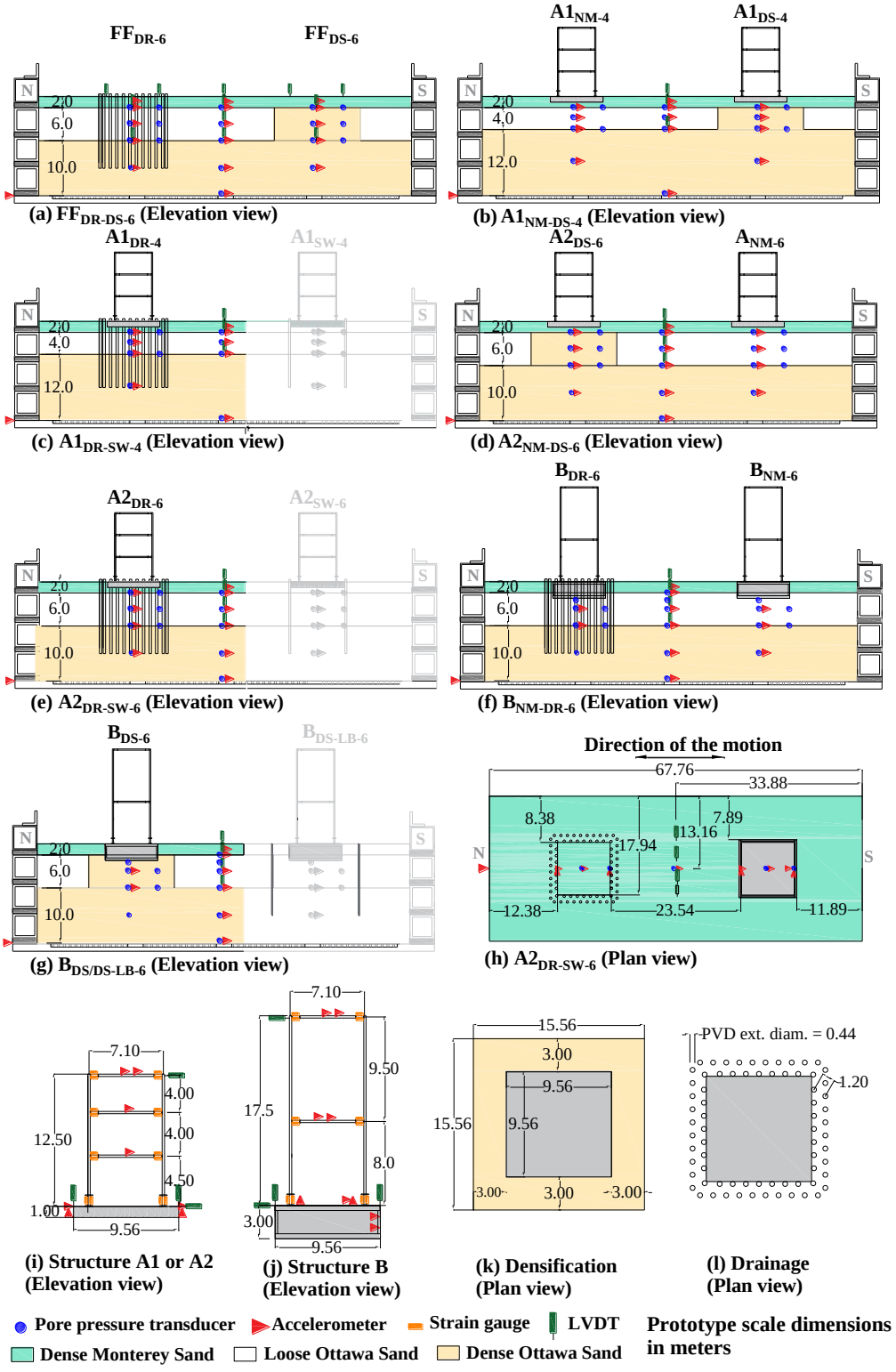

Figure 4.1 Configuration and instrumentation layout of the centrifuge experiments. (All units are in prototype scale meters.)

4.3.2 Soil properties

The lowest layer of the soil specimen was prepared by dry pluviating a dense layer of Ottawa sand F65 (D_{50} = 0.15 mm, Cu = 1.56, e_{min} = 0.53, e_{max} = 0.81) with an initial D_r of approximately 90% with a thickness of 10 m (Soil Profile 1) or 12 m (Soil Profile 2). Subsequently, the same material with a $D_r \approx 40\%$ was dry pluviated as the liquefiable layer with a thickness of 4 or 6 m (Profiles 1 or 2, respectively). Finally, 2 m of Monterey 0/30 sand (D_{50} = 0.40 mm, Cu= 1.3, e_{min} = 0.54, e_{max} = 0.84) (Dashti et al. 2010a) was dry pluviated to attain a $D_r \approx 90\%$. This layer provided a coarse, draining, and non-liquefiable crust. The initial soil properties of each layer are summarized in Table 4.2 (described by Olarte et al. 2017). An automated soil pluviation system (Kirkwood and Dashti 2018) was employed to improve the uniformity and repeatability of soil properties across the container. An extensive set of triaxial data (drained/undrained and monotonic/cyclic under different strain levels) was also performed to characterize the stress-strain response of Ottawa sand F65 at the same relative densities, these specimens were prepared in a similar manner as the centrifuge tests (Ramirez et al. 2017,2018). The soil deposit was prepared inside a Flexible-Shear-Beam (FSB) container, constructed of aluminum and rubber frames, to reduce boundary effects (Paramasivam 2018).

Table 4.2 Initial soil properties in the centrifuge experiments

Layer/ D_r	**Void ratio (e)**	**Sat. unit weight, γ_{sat} (kN/m^3)**	**Hydraulic conductivity, *k*(m/s)**
Monterey Sand (0/30)/ 90%	0.57	19.81	5.30×10^{-4}
Ottawa Sand (F65)/ 40%	0.70	19.05	1.41×10^{-4}
Ottawa Sand (F65)/ 90%	0.56	19.89	1.19×10^{-4}

A solution of methylcellulose in water (Stewart et al. 1998) with a viscosity 70 times that of water was used to saturate the soil specimens under vacuum with an automated saturation

technique (Olarte et al. 2017). Subsequently, the models were spun to a nominal centrifugal acceleration of 70 g. All units and simulations presented in this paper are in prototype scale, unless indicated otherwise.

4.3.3 Structural properties

Two potentially inelastic, MDOF, steel, moment-resisting frame structures were modeled in centrifuge. Figure 4.1i and Figure 4.1j show Structures A and B along with their dimensions in prototype scale, and Table 4.3 summarizes the key properties.

Structure A (A1 and A2) represented the key properties of a 3-story, steel, moment-resisting frame structure (simplified with 3-DOFs), and Structure B represented a 9-story structure (simplified with 2-DOFs). Due to restrictions associated with the container size, overhead limitations, and practicality, both structures were limited to one-bay, but they followed modern U.S seismic design codes (*i.e.*, following AISC-360 2010 and ASCE-7 2010). Structures A1 and A2 were designed for a site with S_s = 2.4g and S_1 = 0.84g, while Structure B was designed for a lower demand of S_s = 1.25g and S_1 = 0.40g. Structure A rested on a 1 m-thick mat foundation, and Structure B on a 1-story basement with an embedment depth of 3 m. Footing areas of both structures were similar, resulting in a larger static bearing pressure for the taller Structure B. The mat and basement foundations were constructed using aluminum to simulate the approximate unit weight of reinforced concrete. As a result of the taller structure (longer fundamental period), and lower design base shear, Structure B was both more flexible and weaker than Structure A; it was also heavier.

Both structures were assembled with steel grade A992 beam and column sections. Potential inelastic behavior was designed to occur at the column base and beam ends, in reduced section areas called “fuses”. The prototype 3-story Structure A was designed with two different fuse

materials, steel grade A992 and nickel grade N200/201 fuses for Structures A1 and A2, respectively, that had the same thickness (0.33 m). A thinner nickel fuse (0.22 m) was designed for Structure B.

Table 4.3 Foundation and structural properties in the centrifuge experiments (in prototype scale)

Description	**Structure**		**Structure B**
	A1	**A2**	
Foundation size (m)[(a)]	9.56 x 9.56		9.56 x 9.56
Foundation embedment (m)	1		3
Foundation contact pressure (kPa)[(b)]	76		187
Fuse material	Steel	Nickel	Nickel
Fuse cross section (m x m)	0.532 x 0.33	0.532 x 0.33	0.532 x 0.22
Fuse end cross section (m x m)	1.11 x 0.33	1.11 x 0.33	1.11 x 0.33
Young's modulus of fuse (MPa)	2.05×10^5 [(c)]	1.37×10^5 [(d)]	1.37×10^5 [(d)]
Base shear strength/weight[(e)]	1.48	0.74	0.042

[(a)]Designed based on the constraints of centrifuge model container
[(b)]Includes the pressure from basement self-weight
[(c)]Strength obtained from the manufacturer data sheet
[(d)]Obtained from the beam-column component tests
[(e)]Ratio of yield base shear, estimated from nonlinear pushover analyses (OpenSEES), to the above-ground structural weight

The fixed-base natural periods and damping properties of the structures were measured after fabrication and assembly through free-vibration impact tests (see Table 4.3). The moment-rotation (M-θ) behavior of steel and nickel fuse sections was characterized under monotonic and cyclic loading, using beam-column component tests (Olarte et al. 2017, 2018a). Tensile tests were also performed to characterize the yield stress of the different fuses (key results also provided in Table 4.3).

4.3.4 Mitigation properties

The mitigation techniques evaluated in this study are: 1) ground densification and 2) enhanced drainage with PVDs. Olarte et al. (2017, 2018a) and Paramasivam et al. (2018) provided additional details on the design criteria and construction procedures for each of these mitigation techniques, with summary information provided in Table 4.4.

In each test with ground densification (Olarte et al. 2017, 2018a), the entire thickness of loose Ottawa sand was dry pluviated to a dense state (D_r = 90%) under the foundation. The lateral

extension of densification beyond the foundation footprint was selected as 3 m (Figure 4.1j), based on JGS (1996) recommendations. The main objectives of this mitigation approach were to increase the soil's resistance to rapid generation of excess pore pressures and the soil's shear stiffness, in order to reduce the foundation's settlement. Note, however, that by dry pluviating dense sand around the foundation, these experiments did not attempt to alter the soil fabric. Hence, they did not mimic typical vibration-based densification methods expected in the field.

The second mitigation procedure (Paramasivam et al. 2018), PVDs, were used to limit the extent and duration of excess of pore pressures in the soil below by enhancing drainage without significant reinforcement. PVDs were placed vertically around the perimeter of the foundation. This arrangement was selected around the perimeter (instead of a more common matrix configuration extending under the foundation), to simulate conditions appropriate for retrofit of existing structures. The model PVDs extended in elevation from the surface of the soil to the middle of dense Ottawa sand, and were placed in a triangular pattern with a center-to-center spacing of 1.2 m in prototype units (Figure 4.1l). These model PVDs were made of soft santoprene rubber tubes that had an inner and outer radius of 11.1 and 22.2 cm, respectively, in prototype scale. Orifice holes were drilled along the length of the tube to provide radial drainage, and the tube was wrapped with a geotextile to avoid clogging due to fines from the surrounding soil. These specifications were based on Pestana et al. (1997), to achieve a maximum excess pore pressure ratio, r_u, of 0.6 within the drain's radius of influence. However, because drains were only placed around the foundation's perimeter, a greater r_u was possible under the footing.

Table 4.4 Mitigation properties in the centrifuge experiments

Properties	**Design in centrifuge**
Ground densification (DS)	
Material	Ottawa sand F65
Lateral extension (m)	3
Relative Density (%)	~ 90
Prefabricated vertical drains (DR)	
Material: drain pipe	Santoprene
Material: geotextile	Polyester woven
Internal pipe radius (m)	0.11
Depth of treatment (m) [(a)]	12 or 13
Drain pattern	triangular
Center to center spacing (m)	1.2
Longitudinal hydraulic conductivity inside drain pipe (m/s)	3.33×10^{-2}

[(a)] Soil Profile 1 or 2

In an effort to investigate the drainage properties of a model PVD, constant head permeability tests were carried out by Paramasivam (2018) at different gradients at 1g, using both water and viscous fluid. The fluid flow inside the model PVD was characterized using the non-dimensional Reynold's number (R). The Reynold's number of the viscous fluid flow at 1g ($R_{viscous-scaled}$) was obtained as 0.40 to 0.70. Following the scaling laws proposed by Vytiniotis and Whittle (2017), R in prototype scale was estimated to range from 1960 to 3430 ($R_{viscous-prototype}=70^2 R_{viscous-scaled}$). This result indicated that flow inside the drains in centrifuge was either laminar or in a transition regime. From the R values obtained experimentally, the velocity of flow, *v*, inside the PVD was computed as 1 to 1.5 cm/s at the gradient, *i*, of 0.30. Therefore, the average longitudinal hydraulic conductivity inside the drain was computed using Darcy's law as 3.33 cm/s ($k = v/i$). This approximation of longitudinal permeability was later adopted in the numerical simulations.

4.3.5 Instrumentation and Ground Motions

Each test was instrumented with accelerometers, pore pressure transducers, linear variable displacement transducers (LVDTs), and strain gauges (Figure 4.1). Accelerations, pore water pressures, and vertical displacements were measured within soil under each structure (referred to

as “near-field”) and at a location farthest from the two structures and container boundaries (referred to as “far-field”). Instruments were placed at the boundaries between soil layers and their mid-depth. Accelerations were also recorded on the foundation and different levels of each structure. For structures like A, the transient lateral displacements were computed by double integrating the lateral accelerations on each level (no permanent deformation could be captured in this way) except for Structure B, which was instrumented with LVDTs at the roof and foundation levels. Strain gauges were placed in a half-bridge configuration on both sides of column and beam fuses.

Each model specimen was subjected to a series of 1D horizontal earthquake motions applied to the container base in flight, using the 1D servo-hydraulic shake table mounted on the centrifuge platform. The selected earthquake motions covered a range of amplitudes (L: low, M: Moderate, H: High), frequency contents, and durations (detailed by Olarte et al. 2017, 2018a and Paramasivam et al. 2018). These motions were identified as Joshua, Kobe, and Northridge. The first minor motion (identified as Joshua-L), which did not induce any excess pore pressures or settlement, corresponded to a scaled and modified version of the M_w = 7.3 1992 Landers earthquake recorded at the Joshua Tree station. The goal of applying this motion was to characterize the systems’ response at low strains. The first major motion was referred to as Kobe-L, and corresponded to a scaled version of the north-south, fault normal, horizontal component of the M_w = 6.9 1995 Kobe, Japan earthquake recorded at the Takatori station. This paper mainly focuses primarily on results from Kobe-L. Due to the greater uncertainty in initial soil properties and geometry after Kobe-L, the results of the consecutive motions were not numerically evaluated. Figure 4.2 shows the acceleration time histories, acceleration response spectra (5%-damped), and Arias Intensity time histories of the Joshua-L and Kobe-L motions (average and variation among

different tests). For each numerical model, we applied the motion recorded at the centrifuge experiment of the corresponding test.

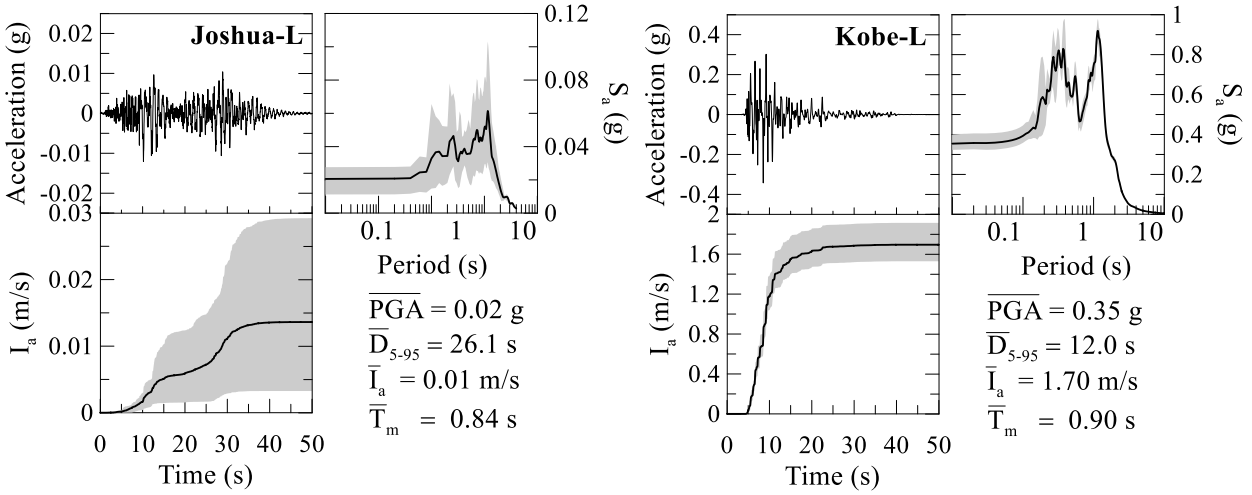

$\overline{PGA}$: mean peak ground acceleration; $\overline{D}_{5-95}$: mean significant duration; $\bar{I}_a$: mean Arias Intensity; $\overline{T}_m$: mean period among the motions considered

Figure 4.2 Mean acceleration time histories, as well as the mean, maximum, and minimum over all tests in acceleration response spectra (5%) and Arias Intensity time histories of the base motions recorded among different centrifuge experiments during the Joshua-L and Kobe-L motions.

4.4 Numerical Simulation

Our goal was to evaluate the predictive capability and practicality of multi-yield and bounding-surface based soil constitutive models, when combined with inelastic nonlinear structural models in a 3D finite element framework analyses. The simulations were conducted in the object-oriented, open-source, OpenSEES platform (Mazzoni et al. 2006). Due to the size of the numerical models, a parallel version of OpenSEES (OpenSEESMP version 3.0.0 rev 6692; McKenna et al. 2000, McKenna and et al. 2010) was used on the Summit supercomputer[2] at the University of Colorado Boulder. The presented simulations can be classified as Class-C1

[2] A Linux cluster with CPU Intel Xeon E5-2680 v3 at 2.50Hz (2CPUs/node, 24 cores/node). Memory: 2133 MT/s, Dual Rank, x4 Data width RDIMM, and 4.84 GB/core

predictions (Lambe 1973), meaning the modeler had access to the centrifuge results during calibration.

4.4.1 Model geometry, elements, and materials

Figure 4.3 through Figure 4.5 show the mesh configuration and numerical model details for three representative centrifuge tests ($FF_{DR\text{-}DS\text{-}6}$, $A1_{NM\text{-}DS\text{-}4}$, and $B_{NM\text{-}DR\text{-}6}$). All numerical models considered only half of the corresponding physical models across the container width to increase computational efficiency: response of centrifuge models was symmetric in the out-of-plane direction (perpendicular to the shaking direction).

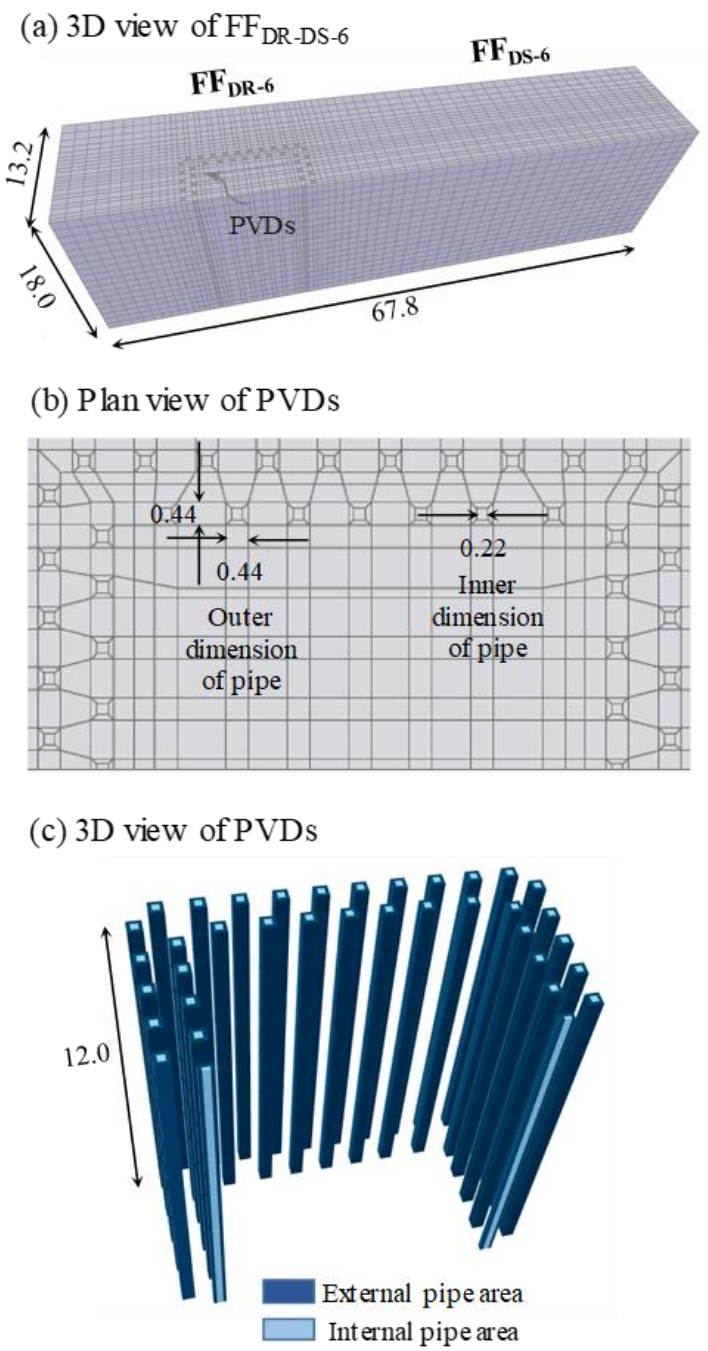

Figure 4.3 Schematic drawings showing the numerical modeling of Test $FF_{DS-DR-6}$: (a) 3D view of the model showing half of the container width based on symmetry; (b) plan view mesh configuration around drains; and (c) 3D view of drain pipes. (Note: all dimensions are in prototype scale in meters.)

(a) 3D view of $A1_{NM-DS-4}$

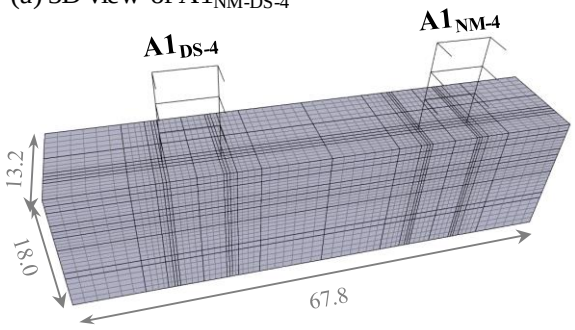

(b) 3D view of densified areas

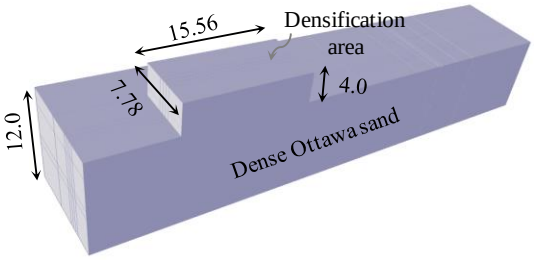

(c) Detail of Structure A1 and its foundation

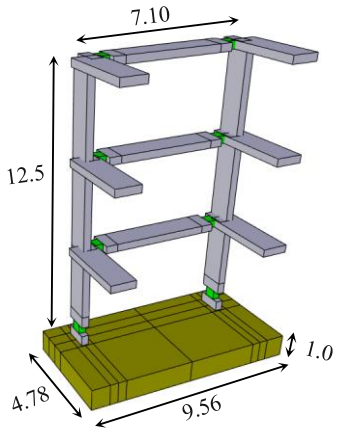

(d) Detail of structural fuse

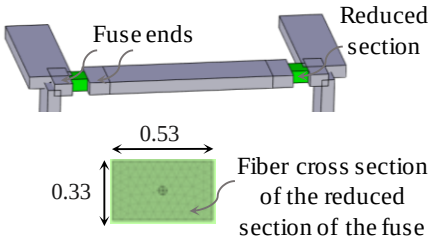

Figure 4.4 (a) Schematic drawings showing the numerical modeling of Test $A1_{NM-DS-4}$, (b) 3D view of the model showing the densified areas; and (c) 3D view of Structure A1 and its foundation (Note: all dimensions are in prototype scale in meters.)

(a) 3D view of $B_{NM\text{-}DR\text{-}6}$

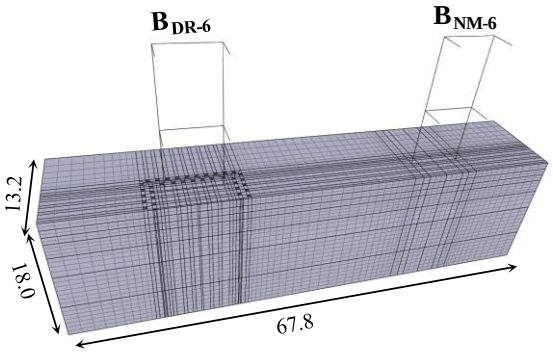

(b) Detail of Structure B and its basement

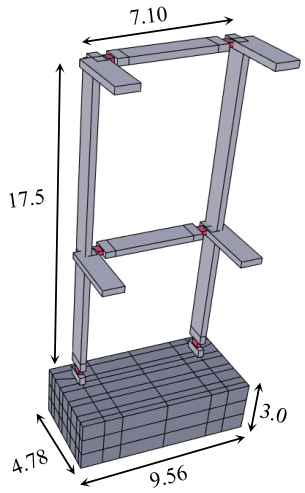

(c) Detail of structural fuse

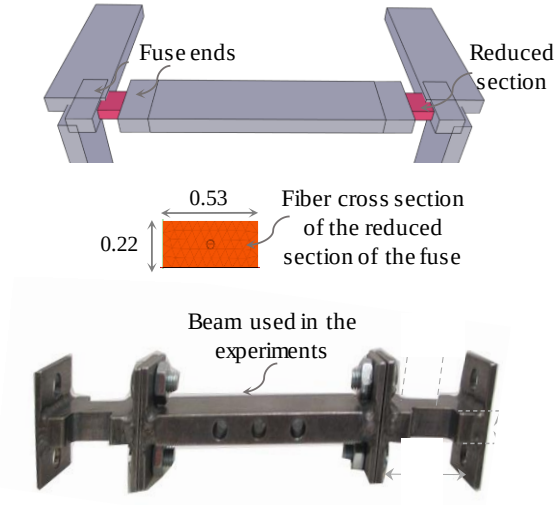

Figure 4.5 (a) Schematic drawings showing the numerical model of Test $B_{NM\text{-}DR\text{-}6}$; (b) 3D view of Structure B and its basement showing half of the structure width based on symmetry; and (c) detail of the structural fuse (Note: all dimensions are in prototype scale in meters.)

4.4.1.1 Soil modeling

Two soil constitutive models were considered: 1) the pressure dependent multi-yield surface, version 2 (PDMY02) (Elgamal et al. 2002 and Yang et al. 2008); and 2) the bounding surface, simple ANIsotropic critical-state based, SANISAND model (with the model tag in OpenSEES of ManzariDafalias; Dafalias and Manzari 2004). Both models include functionalities to represent cyclic response of pressure dependent materials. PDMY02 is based on multiple yield criteria defined by a number of open conical-shaped yield surfaces with a common apex at the origin of the principal stress space; these cones are of different sizes to form the hardening zone (Yang and Elgamal 2000). The multi-yield approach allows the user to introduce the G/G_{max} curves to specify evolution of the plastic moduli. For each relative density, the user needs to specify the contraction and dilation parameters based on a reference effective confining pressure. SANISAND is formulated within the framework of critical state soil mechanics using bounding surface plasticity. This framework is particularly attractive because the user only needs one set of parameters for a certain material, regardless of its density or confining pressure. In both models, the user needs to define the small-strain Rayleigh damping, due to the inability of the models to dissipate energy at small strains. More details are given in the next section.

Prior to performing numerical simulations of the entire soil-foundation-structure (SFS) system, soil parameters were systematically calibrated using a set of fully drained and undrained, monotonic and cyclic triaxial tests and a more realistic boundary-value problem (free-field centrifuge test, with no structure or mitigation present) as previously detailed by Ramirez et al. (2018). Table 4.5 and Table 4.6 summarize the parameters obtained for each constitutive model to achieve these objectives above.

Table 4.5 Soil model parameters for the PDMY02 constitutive model, obtained in Ramirez et al. (2018)

Description	PDMY02		
	Monterey sand	Ottawa sand	
Relative density, D_r (%)	85	40	90
Ref. effective confining pressure, $p_r^{'}$ (kPa)	101	101	101
Pressure dependence coeff., d	0.5	0.5	0.5
Octahedral reference low-strain shear modulus, G_{ref} (MPa)	133.3	108.5	130
Triaxial peak friction angle, $\phi_p^{'}$ (°)	42.0	32.0	40.8
Phase transformation angle, ϕ_{PT} (°)	32.0	27.5	28.0
Control shear-induced volumetric change, contraction tendency and overburden effect, c1, c2 and c3	0.014	0.070	0.045
	2.0	4.0	1.5
	0.15	0.95	0.50
Reflect dilatation tendency, stress history and overburden stress, d1, d2 and d3	0.36	0.01	0.03
	3.0	3.0	3.0
	0.005	0.00	0.00
Number of yield surfaces	20[(a)]	99[(b)]	44[(b)]

[(a)]Automatic yield surfaces; [(b)]user defined yield surfaces

Table 4.6 Soil model parameters for the SANISAND constitutive model, obtained in Ramirez et al. (2018)

Description	SANISAND	
	Monterey sand	**Ottawa sand**
Elasticity		
Elastic material constant, G_0	130	100
Poisson's ratio, ν	0.05	0.05
Critical state stress		
Critical state stress ratio, M	1.27	1.26
Ratio of critical state stress ratio in extension and compression, c	0.712	0.73
State line constant, λ_c	0.02	0.0287
Void ratio at p=0, e_0	0.858	0.78
State line constant, ξ	0.69	0.70
Yield surface constant, m	0.02	0.02
Plastic modulus		
h_0	8.50	5.0
c_h	0.968	0.968
n^b	1.05	0.64
Dilatancy		
A_0	0.60	0.45
n^d	2.50	0.50
Fabric-dilatancy tensor parameters		
z_{max}	4.00	11.0
c_z	50.0	500

The saturated soil was modeled as a two-phase material based on Biot (1941). All soil nodes had 4-DOFs, three for displacement in the 3D orthogonal space and one for fluid pressure. 3D 8-node, hexahedral soil-fluid, fully-coupled, brickUP (Yang et al. 2008) and SSPbrickUP (McGann et al. 2015) elements were used with the PDMY02 and SANISAND models, respectively. Both brickUP and SSPbrickUP (Stabilized Single Integration Point brickUP) use standard linear shape functions. However, the volumetric integrals are performed using a single integration (Gauss) point on SSPbrickUP, as opposed to 8 points in brickUP. For a high-order accuracy, the brickUP element was initially used for both soil constitutive models, using up to 10

processors in parallel. Despite better predictions of settlement when using SANISAND, the models were more computationally expensive and impractical, even with a supercomputer. The reasons are discussed in more detail later. Hence, for computational efficiency, the SSPbrickUP element was employed with SANISAND. To ensure accuracy equivalent to a higher order element, a pressure field stabilization scheme (McGann et al. 2015) was activated with $\alpha=15x10^{-5}$, as previously used by Ramirez et al. (2018).

Element dimensions in elevation within the soil domain (Figure 4.6) was determined at each depth based on the soil's small-strain shear wave velocity, Vs, obtained empirically (Seed and Idriss 1970; Bardet et al. 1993; Menq 2003), and the maximum frequency content of the achieved base motions, f_{max} (*i.e.*, f_{max} = 10 Hz, in prototype scale, after filtering). The minimum wavelength ($\lambda_{min}=V_s/f_{max}$) was divided by 4 to obtain the maximum element size required to allow for shear waves of f_{max} to vertically propagate through soil, which was further divided by a constant C, to account for soil's softening at larger shear strains (*i.e.*, reduction of effective Vs) and excess pore pressure generation. Therefore, $h_{max} = \lambda_{min}/(4C)$, where C was selected as 4 through sensitivity analyses in a single soil column (far-field conditions). The selected mesh dimensions were always smaller than the maximum allowed size (h_{max}).

The mesh size in plan view depended on the foundation footprint and the mitigation configuration. A finer mesh was used near the buildings compared to the far-field, to better capture the larger shear strains around the foundation edges and to facilitate modeling of mitigation techniques (Figure 4.3 to Figure 4.5). The soil mesh around the foundation was defined through a sensitivity analysis (not presented here for brevity). The maximum element size was determined when the foundation settlement and tilt was no longer sensitive to reductions in mesh size. Towards the boundaries of the domain, the soil mesh was made gradually coarser. The aspect ratio of

elements was limited to 1:3 except in areas where PVDs were used (maximum of 1:10 at the bottom of the container next to PVDs) (See Figure 4.3).

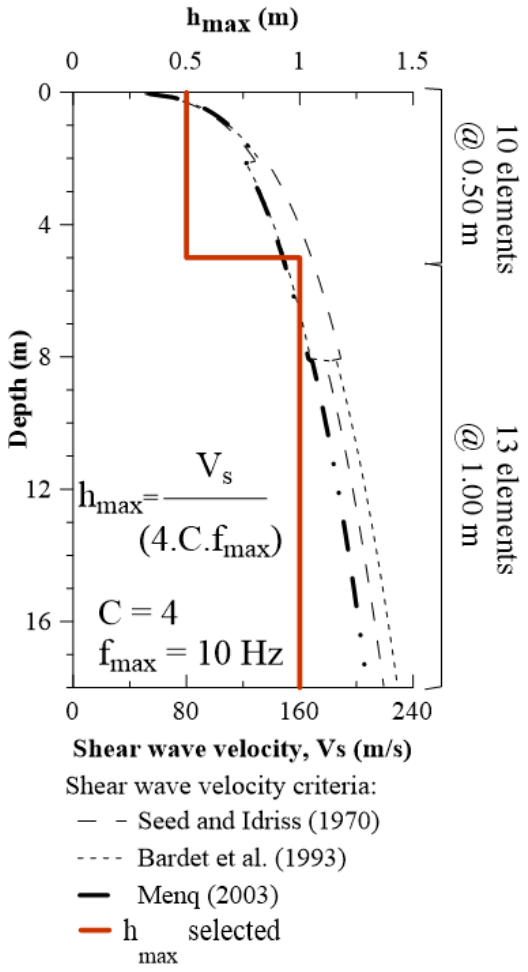

Figure 4.6 Mesh size selection criteria and distribution with depth in relation to the estimated shear wave velocity profile.

4.4.1.2 Structure modeling

Beams and columns were modeled using elastic beam-column elements. The fuse ends were likewise represented by elastic beam-column elements. The reduced section of fuses was modeled with nonlinear beam-column, displacement-based, elements that were discretized into fiber sections. The stress-strain behavior of the fibers was represented by the Giuffre-Menegotto-Pinto uniaxial steel material (Giuffre and Pinto 1970) (model tag Steel02 in OpenSEES), which

combines linear kinematic and isotropic strain hardening. Although the Steel02 material was developed to simulate the stress-strain response of steel, this material also captured the isotropic strain hardening behavior observed for nickel (used in fuses of Structures A2 and B) with modified yield strength. Although the Steel02 material did not capture buckling, it was considered appropriate for all simulations presented here because no buckling was observed in the experiments. All analyses used the P-Δ coordinate transformation to consider second-order geometric nonlinear effects.

The key parameters of the structural materials are the stiffness (Young's modulus) and expected yield stress, reported in Table 4.7. The Young's modulus (E) of the beam-column elements was selected as 2.05×10^5 MPa, obtained from the manufacturer. The Young's modulus of the elastic beam-column elements representing fuse ends was corrected to represent not only the material stiffness, but the additional flexibility from the plate-fuse welding connection stiffness and the bolted connection between the fuse and beam/columns. After an extensive calibration (not presented here for brevity), the value adopted corresponded to 9.0×10^4 MPa (*i.e.*, approximately 2/3 of the nickel Young's Modulus). The Young's modulus of the nickel reduced fuse section was 1.37×10^5 MPa, determined experimentally through coupon tests. The magnitude of the bending strains in fuses was strongly influenced by the yield capacity of the nonlinear elements. This yield capacity corresponded to the intersection of both the post-yield and initial elastic tangent.

Subsequently, numerical models of each fixed-base structure were created, and the buildings' modal response and damping characteristics were checked against the hammer impact test results. The fixed-base natural periods obtained numerically were in good agreement with the experimental results (Table 4.7).

A Rayleigh damping formulation was employed for the superstructure. The experimental small-strain damping ratios of 0.8% and 1.2% (obtained from hammer tests) were considered for Structures A and B, respectively.

Table 4.7 Summary of the model parameters for structural elements

Description	A1	A2	B
▪*Beams and Columns (elastic)*			
Elastic properties (MPa)	$E = 2.05x10^5$		
▪*Fuse ends (elastic beam)*			
Young Modulus, E (MPa)[(a)]	$E = 9.0x10^4$		
▪*Fuse (Displacement-based fiber elements) - Giuffre-Menegotto-Pinto parameters*			
Expected yield strength, *fy* (MPa)[(b)]	345	180	180
Young Modulus, E (MPa)	$2.05x10^5$	$1.37x10^{5(c)}$	$1.37x10^{5(c)}$
Strain-hardening ratio, b_{rat}	0.020	0.025	0.025
▪Modal Periods (s)			
Fixed-base natural periods from simulations	0.56; 0.16[(d)]		2.8; 0.72
Fixed-base natural periods from experiments[(e)]	0.57; 0.15		2.9; 0.74

b_{rat}=ratio between post-yield tangent and initial elastic tangent
[(a)]Considering the flexibility in the bolted beam-plate connection
[(b)]Stress that corresponds to the intersection of the post-yield tangent and initial elastic tangent
[(c)]Obtained from beam-column tests
[(d)]Mean numerical values between Structures A1 and A2
[(e)]Mean experimental values

4.4.1.3 Foundation modeling

The foundations were modeled with SSPbrick elements for computational advantages using a linear elastic material (model tag ElasticIsotropic in OpenSEES). Due to incompatibility between the number of DOFs at each node in foundation (3-DOFs) and superstructure (6-DOFs) elements, beam-type rigid links were placed to connect the foundation to the column base. These rigid links were connected to the foundation using the master/slave command.

4.4.1.4 Mitigation modeling

Two different liquefaction mitigation techniques were modeled near buildings, representing those used in centrifuge as closely as possible. Ground densification was numerically

simulated by replacing the properties of loose Ottawa sand F65 with dense sand in the area of interest (Table 4.2 and Figure 4.1k). The element type or size was not altered.

A number of prior studies have investigated different ways of modeling PVDs in coupled flow-deformation analyses. For instance, Vytiniotis and Whittle (2017) developed PVD elements and a constitutive model in OpenSEES, which can simulate laminar and turbulent pipe flow regimes in 2D. Howell at al. (2015) simulated PVDs using a 3D finite-element unit cell model. The pore pressures were held at their hydrostatic levels along the vertical center line of the drain, representing a perfect (infinitely permeable) drain. However, this approach would overestimate the rate of drainage in PVDs used in centrifuge.

In this study, the PVDs were numerically constructed in a grid pattern to represent the physical area and position of each drain (see Figure 4.3). 3D drains were modeled with 8-node, fully-coupled brickUP and SSPbrickUP elements (for PDMY02 and SANISAND soil models, respectively). Different properties were assigned to for the perforated (santoprene) elements and the internal (drain) areas of the mesh (Figure 4.3). The horizontal flow of the perforated tube was governed by the hydraulic conductivity of the soil around it. Therefore, the horizontal hydraulic conductivity of all the PVD elements was assigned that of the soil around drains. The vertical hydraulic conductivity of the santoprene area was greatly reduced to limit vertical flow in the pipes' external section. The elements representing the internal drain area were assigned a vertical hydraulic conductivity equal to the drain's longitudinal permeability, 3.33×10^{-2} m/s in prototype scale, as determined experimentally (Paramasivam 2018).

4.4.1.5 Boundary and loading conditions

As shown in Figure 4.7, each numerical model's bottom boundary was fixed both in horizontal and vertical directions to simulate a rigid base, consistent with the centrifuge conditions.

All nodes surrounding the soil medium on the base and sides were set as impervious to represent the container, and the symmetry conditions. In addition, nodes at the symmetric face and its parallel face were restricted for out-of-plane displacement (perpendicular to shaking). The lateral boundary nodes located at the same elevation were tied to move together in both horizontal directions (*i.e.*, using the master/slave technique with the equalDOF option in OpenSEES), to roughly reproduce the boundary conditions provided by the Flexible-Shear-Beam container in centrifuge. Displacement of structure nodes at the symmetry face was likewise restricted from out-of-plane movements, and the rotations were constrained around two axes: (i) the vertical axis,and (ii) the horizontal axis parallel to direction of shaking. Rigid floor diaphragms were used to assure proper distribution of seismic forces to all lateral force resisting elements per floor in the structure.

Superstructure gravity loads were applied at the top of column. This approach underestimates loads and bending strains on fuses under gravity loads (because loads at that position do not impose initial strains on fuses). However, this approach is sufficient for simulating seismic soil-structure interaction and dynamic strains in beams and columns. The foundation weight was applied as a body force in the SSPbrick elements. Once numerical models reached static equilibrium, they were excited at the base nodes with the acceleration time history recorded at the base of the container in each centrifuge test.

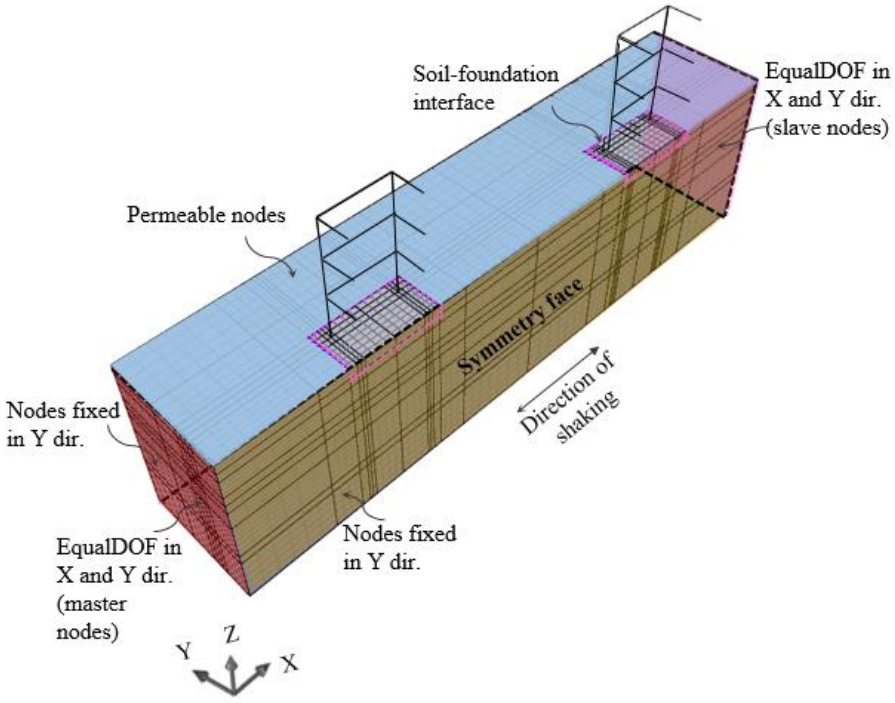

Figure 4.7 Schematic representation of boundary conditions.

4.4.1.6 Analysis parameters and processing

Analysis parameters include definitions of solution algorithm, integrator, constraint-handlers, mapping between the degrees-of-freedom (DOF) at the nodes (or DOF Numberer), system of equations solver, and convergence tests. These analysis parameters provide flexibility in the performance of the analysis and allow the analyst to carefully monitor and control convergence.

To compute the equilibrium of systems that involve soil elements, a transient analysis with a large pseudo-time step (*e.g.*, 500 seconds) was required to allow for the equilibrium of pore pressure (Vytiniotis 2012) during the static stage. For computational efficiency, all simulations used an implicit time integration technique (as recommended by Wang and Sitar 2006), namely the Newmark integration method. All transient dynamic analyses were performed using the

Newmark parameters γ =0.5 and β =0.25, to limit any additional numerical damping (Newmark 1959). Different values for γ and β were evaluated in a 1D site response in the next section.

Due to the size of all numerical models, the parallel OpenSEESMP was used. OpenSEESMP uses the MUltifrontal Massively Parallel Sparse direct solver (MUMPS) that distributes the models in different partitions, which are solved by every processor (or partitions) simultaneously. The mapping between equation numbers and DOFs were constructed by the Reverse Cuthill-McKee numbering scheme (Cuthill and McKee 1969). The presence of a large number of DOFs required either the Constraint Penalty method or the Transformation method to effectively enforce the boundary conditions of all multi-constrained nodes. All simulations used a single- multi-constraint parameter (αS and αM) of $1x10^{18}$ using the Constraint Penalty to ensure an adequate kinematic constraint of all DOFs (as suggested by Cook et al. 2002). A sensitivity analysis of the constraint handler conditions is included in the next section. A nonlinear Newton with Line Search algorithm (Crisfield 1991) was needed and used to solve the equilibrium equations for cases with zerolengthcontact3D element between the soil and foundation (described below). To speed up the simulations that did not include zerolengthcontact3D elements, the Krylov-Newton algorithm (Scott and Fenves 2006) was chosen (as used by Barbosa et al. 2012). In order to store and solve the sparse system of equations of the SFS systems in a time efficient fashion, the system Mumps –ICNTL14 was required and used (as suggested by Rahmani 2014). To check the convergence at each time step, the Norm Displacement Increment Test was used, as it is required when using the Constraint Penalty method (Mazzoni et al. 2006).

To limit the computational time, a tolerance on displacement of 2 cm was used. This tolerance was considered satisfactory, as it is slightly smaller than what is considered acceptable settlement in design (about 2.5 cm) and smaller than the standard deviation (about 30 cm) of

liquefaction-induced foundation settlement based on the semi-empirical procedure proposed by Bullock et al. (2018). This parameter had limited to no effects on seismic site response, as presented and discussed in the next section. The integration method guaranteed unconditional stability, so the time step (Δt) at each increment was controlled by the model convergence. In particular, Δt was reduced when convergence was not achieved in the previous iteration. Small changes in Δt were not expected to influence the soil response (Wang and Sitar 2011).

Pre- and post-processing of the models were carried out in the Scientific ToolKit for OpenSEES, STKO version 1.0.0, developed by Petracca et al. (2017). During the preparation of this paper, version 3 of the PDMY model became available (Khosravifar et al. 2018), but version 2 had already been used for our simulations. A stable release of SANISAND in OpenSEES was only accessible in version 2.5.0, which was employed for the simulations. Appendix D shows the computational time and memory required for the analyses presented in this section.

4.5 Key Factors Controlling the Numerical Response

During preliminary comparisons of numerical results with centrifuge recordings, a number of factors were shown to control the global response of the soil-foundation-structure system: a) soil small-strain Rayleigh damping characteristics and Newmark integration parameters; b) type and characteristics of the soil constitutive model and (more importantly) the element; and c) type and properties of the soil-foundation interface. This section describes investigations into each of these key factors and justifies the selection of final values and modeling approaches for comparison with all the centrifuge results.

4.5.1 Influence of soil small-strain damping and analysis parameters on seismic site response

To evaluate the sensitivity of seismic site response in a layered liquefiable soil deposit (primarily in terms of pore pressures and accelerations) to soil small-strain damping assumptions, a series of dynamic, nonlinear, finite-element analyses were performed on a single soil column using the same geometry, motions, and soil constitutive model parameters for PDMY02 and SANISAND as described above in the previous sections. Modeling a single soil column allowed for an extended sensitivity analysis, which was not possible for the larger SFS system. Variations in other analysis parameters were also considered, which were found to be significantly less influential and hence not shown.

The soil small-strain Rayleigh damping coefficient and frequencies evaluated are shown in Table 4.8. The analysis parameters evaluated were: the parameters for the transient integrator method (*i.e.*, Newmark-method), type of constraint-handler, the tolerance for convergence, and analysis time increment. Other analysis parameters or conditions (*e.g.*, the mapping between equation numbers and degrees-of-freedom, constraint method to enforce the boundary conditions, system of equation solver, and solution algorithm) were applied as detailed in the previous section and kept constant, to ensure a converging solution for the larger soil-foundation-structure systems. With the parameters considered, each damping characteristics or parameter were varied independently in a sensitivity analysis, while others were kept constant with the values previously defined. Figure 4.8 summarizes the variations in the parameters considered.

4.5.1.1 Damping ranges and analysis parameters considered

The primary goal of assigning a small-strain Rayleigh damping coefficient to soil is to adequately capture its damping at small-strains, provide numerical stability, and avoid high

frequency noise, without overdamping its nonlinear and hysteresis response at larger strains. As described in Table 4.8 and Figure 4.8 the Rayleigh damping coefficient (D) was varied from 0 to 7%, reflecting a range that is typical in practice and research (Phillips et al. 2012; Tsai et al. 2014; Karimi and Dashti 2016b). The two frequencies assigned to Rayleigh damping were also varied as follows: 1) using the site's first and third mode, small-strain fundamental frequencies, as recommended by Kwok et al. (2007) (*i.e.,* $f_{1,3}$ = 2.4 and 12.3 Hz, where f_1 and f_3 were determined empirically by Ramirez et al. 2018); 2) replacing f_1 with the smaller, strain-compatible fundamental frequency of the liquefiable site (f_{liq} = 0.4 Hz determined from experimental transfer functions by Olarte et al. 2018a and Paramasivam et al. 2018a); 3) the frequency range of interest for earthquake loading (f_{min} = 0.01 or 0.1, and f_{max} = 20.0 or 25.0 Hz, which limited the extent and contribution of Rayleigh damping across a wider range of frequencies than other cases. In cases 1 through 5 described in Table 4.8, we varied the small-strain Rayleigh damping from 0 to 7%, while the corresponding frequencies were kept at $f_{1,3}$. In cases 6 through 9, the frequencies were varied, now considering f_{liq} or $f_{min,max}$ with a constant D = 4%.

The Newmark parameters for the dynamic analyses were set as values that ensured unconditional stability for the larger soil-foundation-structure system (γ = 0.5 and β = 0.25; Newmark 1959). We also considered cases when a small numerical damping was added (γ =0.60 and β = 0.30), as recommended by Vytiniotis (2012) and Kamalzare (2016). Constraint types and convergence tolerance values were varied based on the ranges recommended in the OpenSEES manual (Mazzoni et al. 2006) and by Kamalzare (2016) to ensure the boundary conditions are enforced properly for the SFS models. The minimum (Δt) selected was $1x10^{-3}$ s, as indicated by Ramirez et al. (2018). However, to balance the numerical stability and computational cost (particularly for the large SFS models), a maximum time step of and $5x10^{-3}$ s was also considered

based on the recommendation of Tasiopoulou et al. (2015b). Since the simulations were performed using an implicit integration method, the stability was mainly controlled by the convergence tolerance (discussed in more detail in the previous section), as opposed to the analysis time increment (Δt).

Table 4.8 Variation of damping and other analysis parameters considered in 1D site response sensitivity analyses

Analysis parameter	Used by Ramirez et al. (2018)	Case No.	Variation
Rayleigh damping	D = 3% f_1 = 2.4, f_3 = 12.3 Hz f_1 and f_3 represent the 1st and 3rd modal frequencies in the small-strain regime	*1* *2* *3* *4* *5* *6* *7* *8* *9*	No Rayleigh damping D = 1% at f_1, f_3 D = 3% at f_1, f_3 D = 5% at f_1, f_3 D = 7% at f_1, f_3 D = 4% at f_{liq}, f_3 D = 4% at 0.1, f_3 D = 4% at 0.1, 25 Hz D = 4% at 0.01, 25 Hz
Newmark parameters	$\gamma = 0.500$, $\beta = 0.250$	*10* *11*	$\gamma = 0.50$, $\beta = 0.25$ $\gamma = 0.60$, $\beta = 0.30$
Constraint types	Penalty method: αS, αM = $1x10^{15}$,$1x10^{15}$	 *12* *13* *14* *15*	Penalty method: $\alpha S = 1x10^{12}$ $\alpha M = 1x10^{12}$ $\alpha S = 1x10^{15}$ $\alpha M = 1x10^{15}$ $\alpha S = 1x10^{18}$ $\alpha M = 1x10^{18}$ Transformation method
Tolerance	$1x10^{-4}$	*16 - 19*	$1x10^{-5}$, $1x10^{-4}$, $1x10^{-3}$, $1x10^{-2}$
Time step	$1x10^{-3}$	*20* *21*	$1x10^{-3}$ s $5x10^{-3}$ s

D = small-strain damping ratio
$f_{1,3}$ = first and third modal frequencies of the soil column at small strains (2.4 and 12.3, respectively)
f_{liq} = strain compatible fundamental frequency of the liquefied soil column, $f_{liq} \approx 0.4$ Hz during the Kobe-L motion obtained from the transfer function of accelerations at the surface and base of the far-field soil column experimentally.
αS = factor on single-point constraint
αM = factor on multi-point constraint

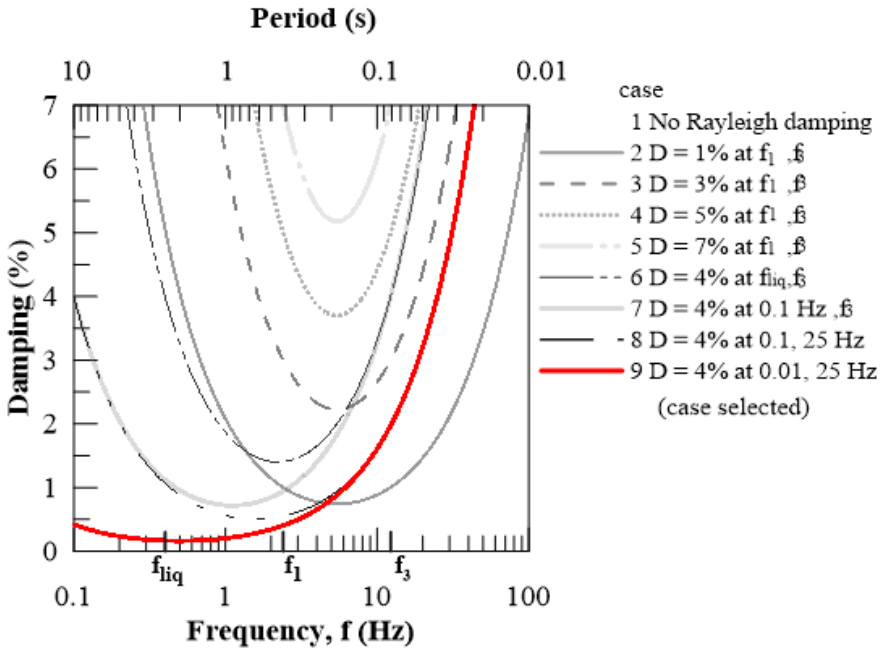

Figure 4.8 Frequency response of soil small-strain Rayleigh damping coefficients for soil for cases considered in Table 4.8.

4.5.1.2 Sensitivity of seismic site response

Representative results of these sensitivity analyses for the 1D soil column are shown in tornado diagrams of Figure 4.9 in terms of PGA at the middle of dense and loose Ottawa sand layers for both soil constitutive models and the two motions of interest (Joshua-L and Kobe-L). The predicted accelerations (particularly the PGAs) were, in general, highly sensitive to the value and frequency dependence of small-strain Rayleigh damping, particularly in the deeper layer of dense Ottawa sand and for the PDMY02 model. Other analysis parameters were comparatively less influential.

To separate the influence of Rayleigh damping from material or hysteretic damping in soil, the low-intensity motion (Joshua-L) was considered first. When Rayleigh damping was set to zero, PGAs were highly overestimated particularly with PDMY02. This comparison showed that including some damping is necessary for energy dissipation at low strains, when one cannot rely on material damping. At larger strains (*e.g.*, the more intense Kobe-L motion), although material

damping was expected to be the primary source of energy dissipation in soil, Rayleigh damping was still necessary to damp out the spurious noise at higher frequencies, particularly at greater depths.

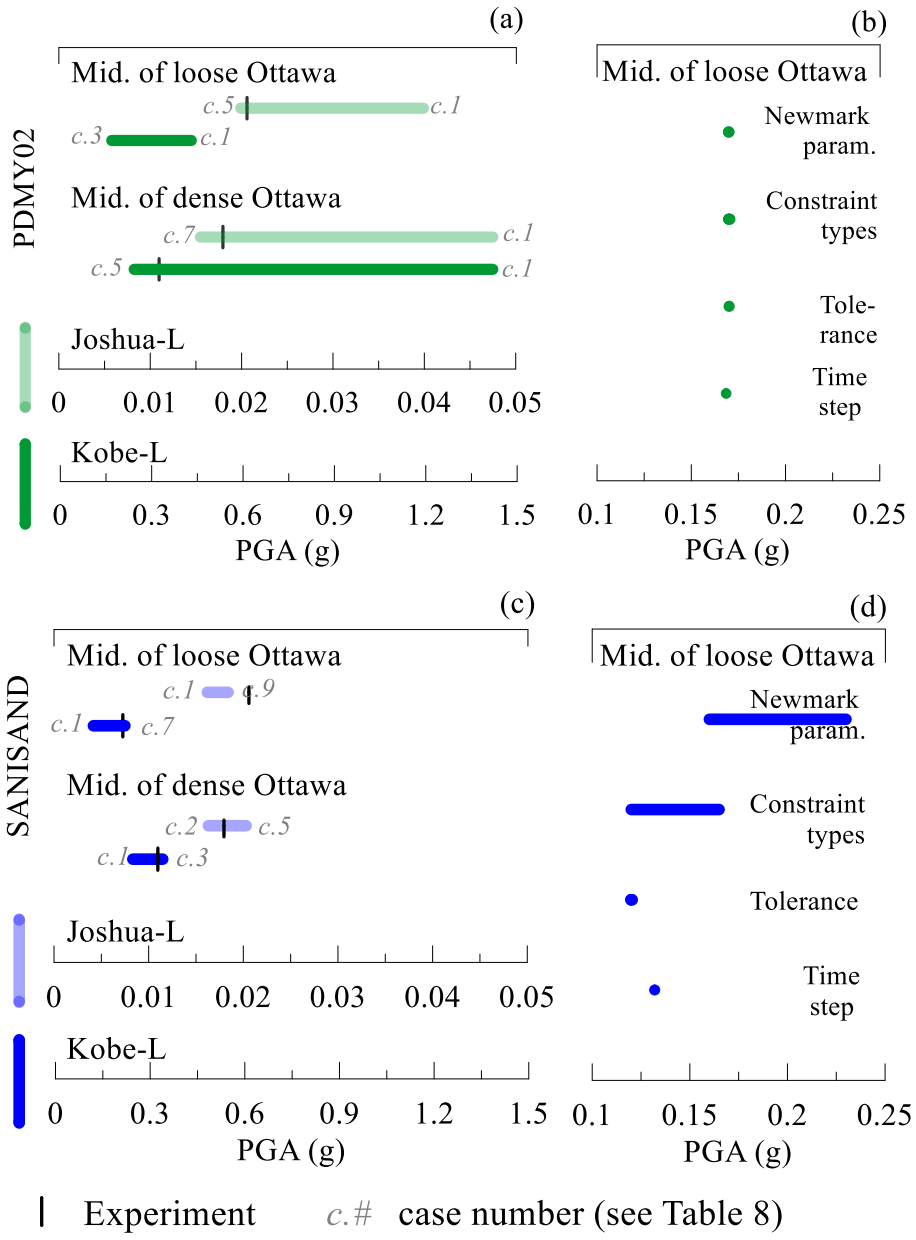

Figure 4.9 Tornado diagrams showing the sensitivity of PGA predicted in the middle of the dense and loose Ottawa sand layers in a single soil column to variations in: (a),(c) small-strain Rayleigh damping in soil during two ground motions of varying intensity (Joshua-L and Kobe-L); and (b),(d) other analysis parameters during Kobe-L, when using two soil constitutive models PDMY02 and SANISAND.

To evaluate the influence of small-strain Rayleigh damping on accelerations at greater periods, Figure 4.10 compares the simulated acceleration response spectra from three representative cases (*i.e.*, cases 1, 5, and 9) with centrifuge results in a free-field test closest to the response of a single soil column (Ramirez et al. 2018). Results are shown at the middle of the loose Ottawa sand layer during Kobe-L. The predicted spectral accelerations near the motion's predominant period ($T_p \approx 1.2$ s, where there was significant spectral energy input to the system) was highly sensitive to the characteristics of small-strain Rayleigh damping, particularly when using PDMY02. Case 1 (no Rayleigh damping) amplified the predicted accelerations at periods near 0 sec (hence the PGA), which could lead to numerical instability when modeling the larger SFS system. Yet, it led to better predictions of accelerations at greater periods, particularly near the motion's T_p. Conversely, overdamped systems (*e.g.*, Case 5 with D = 7% at f_1 and f_3) better predicted the low-period accelerations, while strongly amplifying accelerations at greater periods and the motion's T_p. Numerical results from Case 9 (D = 4% at 0.01 and 25 Hz) appeared to compare reasonably well with experimental measurements for the range of periods (or frequencies) of interest. These patterns cannot be explained based on the damping frequencies shown in Figure 4.8 alone. Instead, they signify more complex interactions between the characteristics of the assigned small-strain damping, wave propagation through a highly nonlinear and nonstationary soil profile, and the strain- and frequency-dependent nature of hysteresis damping provided by the constitutive models that should be considered.

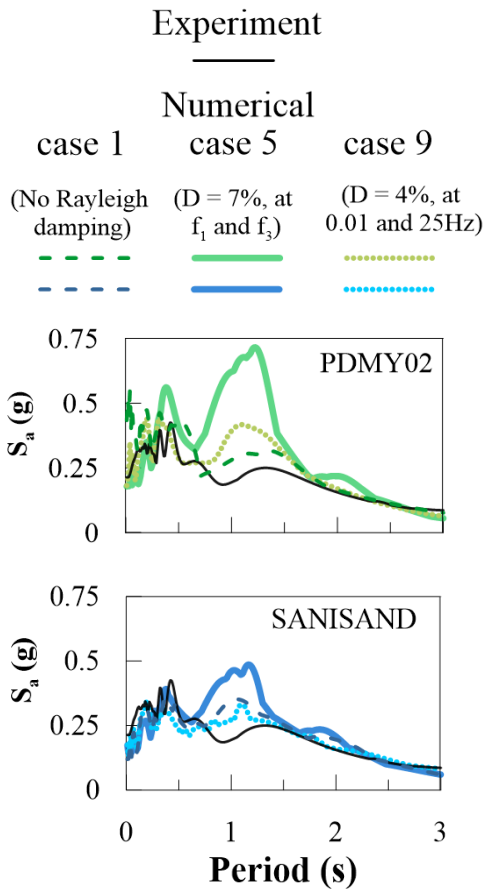

Figure 4.10 Comparison of the numerical response spectra (5%-damped) for some of the damping cases considered in Table 4.8 with the experimental results in the middle of the liquefiable layer in the free-field during Kobe-L.

The error in the numerical predictions of both acceleration and pore pressure time histories (with respect to the experimental measurements) for each damping case was quantified by Total Normalized Prediction Error (TNPE), the definition of which is detailed in Table 4.9. This error term combines error in two different quantities (X), 1) acceleration time histories; and 2) excess pore pressure time histories, at the middle of loose and dense Ottawa sand layers. Settlement time histories were not considered in this sensitivity evaluation, because Ramirez et al. (2018) previously showed the general inadequacy of these numerical predictions in capturing volumetric strains in liquefiable deposits. The TNPE was computed as follows. Initially, a sum of the squared error $\sum \tilde{X}^2$ was computed over time using Equation 1 (Steps 1 and 2 of Table 4.9) for each

response parameter of interest. The mean squared error term (MSE, Table 4.9) divides $\sum \tilde{X}^2$ by the number of points in time and was evaluated for each quantity at the same two representative depths within the soil column. The Normalized Prediction Error (NPE) was then calculated through a normalization of each MSE by the square of the peak value of the same experimental parameter at the corresponding depth, as suggested by Baiser and Glacer (2000) and used by Dashti et al. (2012). Finally, the TNPE combined the errors in the two response parameters by summing the normalized prediction errors for each quantity.

Table 4.9 Definitions of error in numerical predictions with respect to centrifuge measurements (after Baiser and Glacer 2000)

Step 1. $\tilde{X}^2$ was computed for each moment in the time domain using Eq. 1 for each depth* and quantity of interest X†. $$\tilde{X}^2=\left[X_{numerical}-X_{experiment}\right]^2 \quad \text{(eq. 1)}$$
Step 2. $\sum_{i=1}^{N} \tilde{X}^2$ sums the error over the entire time domain.
Step 3. The mean squared error (MSE) was evaluated as $\sum_{i=1}^{N} \tilde{X}^2$ divided by the number of points (N) used in step 2. $$MSE=\frac{\sum_{i=1}^{N} \tilde{X}^2}{N} \quad \text{(eq. 2)}$$
Step 4. The normalized prediction error (NPE) was computed as MSE normalized by the maximum squared experimental value of X. $$NPE=\frac{MSE}{\max\left(X_{experiment}\right)^2} \quad \text{(eq. 3)}$$
Step 5. Steps 1 through 4 were repeated for two representative depths within the soil column (middle of loose and dense Ottawa sand layers) and for two quantities of acceleration and pore pressure.
Step 6. The total normalized prediction error was the sum of all the NPE computed at step 5.

*Middle of loose and dense layers of Ottawa sand.
†acceleration and excess pore pressure time histories.

Figure 4.11 quantifies the TNPE for each case and constitutive model, showing the contribution of each NPE in acceleration and excess pore pressure time histories at two representative depths. Excess pore pressure and acceleration time histories contributed approximately equally to the total error, though excess pore pressures were relatively insensitive to the characteristics of small-strain Rayleigh damping. These plots confirm that site response analyses with PDMY02 were more sensitive to small-strain damping, likely because SANISAND provided greater hysteresis damping at larger strains. When no small-strain damping was used (Case 1), the error in accelerations (particularly at high frequencies) were greater in the deeper dense Ottawa sand layer, due to the reflection of high frequency waves from the model's base. On the other hand, when excessive damping was employed (*e.g.*, Case 5), greater errors in acceleration were observed within the upper looser Ottawa sand layer that was already experiencing significant nonlinearity and hysteresis damping. The Rayleigh damping formulation that reduced the total error (TPNE) in both acceleration and pore pressure time histories reasonably in both constitutive models corresponded to Case 9, with D = 4% and $f_{min,max}$ = 0.01 and 25 Hz, which was adopted in the remaining simulations. These results suggest that a small-strain damping should be applied to a wide frequency range, which is different from what many practitioners commonly do, to avoid excessive damping within the frequency range of interest for earthquake applications.

Among the analysis parameters investigated, the Newmark integration method ranked second in importance, especially when SSPbrickUP elements were used with SANISAND (comparing Figure 4.9b and Figure 4.9d). As this element was developed with an efficient temporal single-point integration method, the Newmark β coefficients larger than 0.25 produced instability and numerical noise, affecting the predicted accelerations and pore pressures. Hence, values of γ = 0.50 and β = 0.25 were judged adequate in these simulations, to limit additional numerical

damping and ensure stability. Other analysis parameters had less influence on soil response in terms of acceleration and pore pressure.

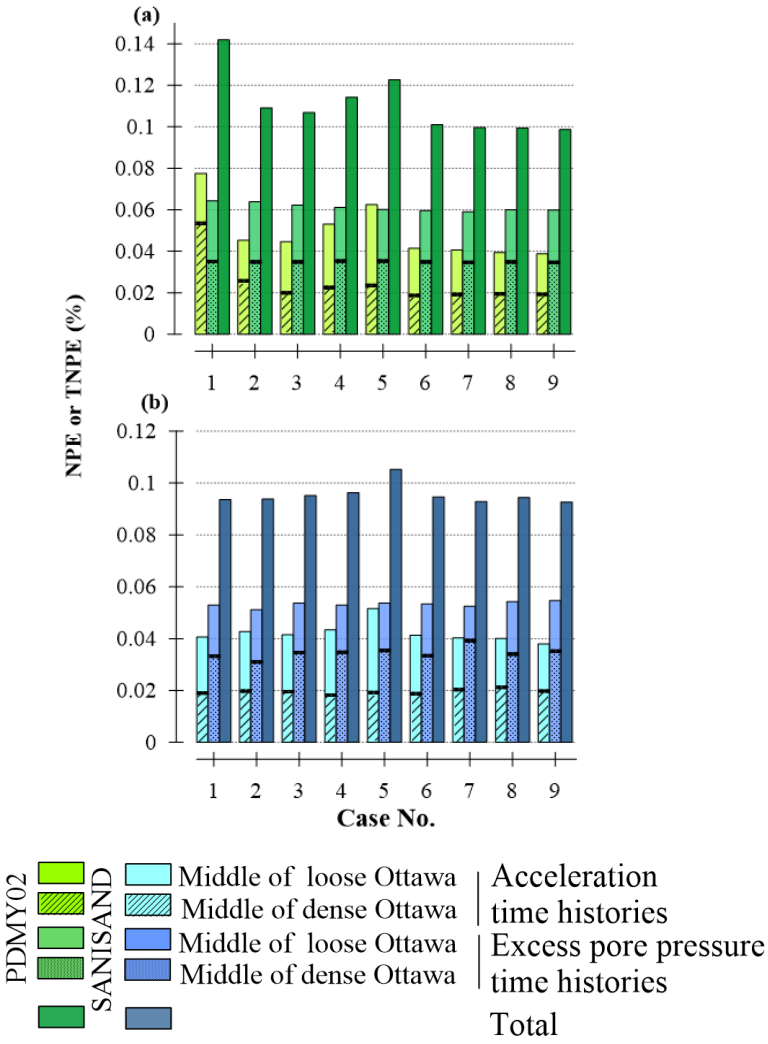

Figure 4.11 Total Normalized Prediction Error (TNPE) and Normalized Prediction Error (NPE) for numerically predicted free-field site response analyses during Kobe-L with: a) PDMY02; and b) SANISAND constitutive models with respect to centrifuge measurements for damping cases considered in Table 4.8 and Figure 4.8.

4.5.2 Effects of constitutive model and element choice on seismic response in the far- and near-field

To evaluate the influence of soil constitutive model type and characteristics on seismic response of the SFS system, the authors simulated two representative centrifuge tests with both PDMY02 and SANISAND, using the brickUP and SSPbrickUP elements, respectively. Despite

the simultaneous change in both soil constitutive model and element type, these combinations intended to improve computation efficiency, as shown later in this section. Initially, we compared the results in terms of horizontal accelerations, excess pore pressures, and settlements in the far-field with no structures but with two mitigation techniques present (*i.e.*, $FF_{DS\text{-}6}$ and $FF_{DR\text{-}6}$). Subsequently, the near-field seismic response was evaluated in terms of foundation's average settlement and tilt as well as accelerations and pore pressures below the structures and strains within the superstructure.

The acceleration, excess pore pressure, and settlement time histories and response spectra (5%-damped) of the numerical and experimental results in the far-field are compared in Figure 4.12. Results are presented in the middle of the densified zone ($FF_{DS\text{-}6}$) and in the middle of the PVD zone ($FF_{DR\text{-}6}$) at two representative depths (middle of loose and dense Ottawa sand layers). Overall, both numerical models captured relatively well the acceleration spikes due to dilation at large strain within the densified and drained zones. PDMY02 simulated the low-period (high-frequency) accelerations better than SANISAND, showing that PDMY02 had a higher dilative tendency under the presence of mitigation (with no structure). PDMY02 also better predicted accelerations near the motion's predominant period (T_p) of around 1.2 s.

Overall, both soil models provided good estimates of excess pore pressures during shaking. However, the PDMY02 model strongly underestimates the coefficient of volumetric compressibility, leading to an overestimation of the rate of excess pore pressure dissipation (Howell et al. 2015; Karimi and Dashti 2016b; Ramirez et al. 2018). This led to a poor prediction of net pore pressures after strong shaking in comparison with the experiment or the SANISAND model. Both constitutive models underestimated the volumetric settlements (*e.g.*, sedimentation) in mitigated far-field soils by approximately 60% to 100%, which was in line with observations of

other researchers in the absence of structures (Karimi and Dashti 2016b; Kamalzare 2016; Ramirez et al. 2018).

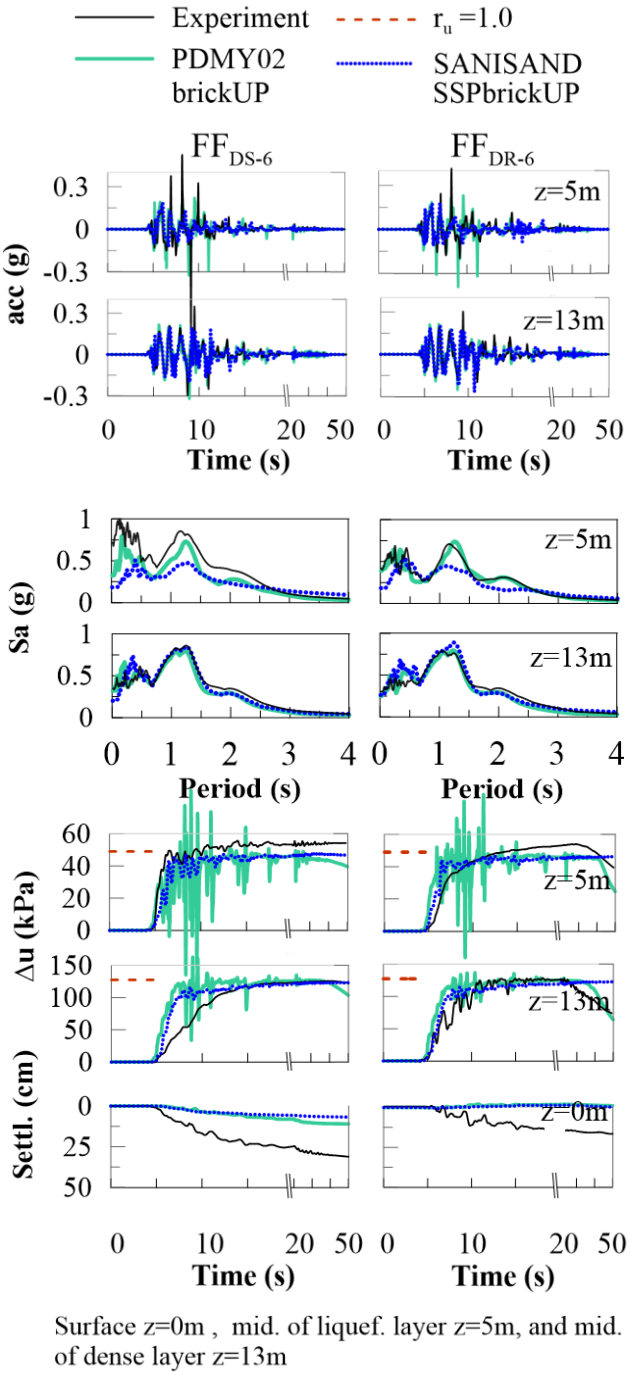

Figure 4.12 Effects of soil constitutive model and element type on acceleration, excess pore pressure, and settlement time histories and response spectra (5%-damped) in the middle of the loose and dense Ottawa sand layers in the far-field (FF_{DS-6} and FF_{DR-6}) during Kobe-L.

Figure 4.13 compares the numerical results with the experimental measurements under the center of Structures $A2_{NM-6}$ and $A2_{DS-6}$ (near-field). Note that for the purpose of comparing the constitutive models alone, these simulations considered a master and slave (in terms of displacement), node-to-node, connection (equalDOF) between the soil and foundation. The interface condition is discussed in more detail later. In general, the numerical models showed relatively good agreement with experimental acceleration time histories and response spectra in the near-field. However, both models at times overestimate the low-period accelerations near 0.2 to 0.5 s), particularly under the unmitigated structures at shallow depths and in thicker soil profiles (see Appendix E). SANISAND, in particular, predicted larger dilation cycles and high frequency (low period) spikes in acceleration below the foundation in loose Ottawa sand in comparison with PDMY02 and the experiments, which increased the required analysis time to ensure convergence. Moreover, note that SANISAND required a longer computational time compared to PDMY02, despite using low-order elements (SSPbrickUP) (see Appendix D). SANISAND updates the state parameter in soil at every time step, which in itself, leads to a notably slower simulation process than PDMY02. Further, the applied static and dynamic stresses from the building increased the stress state beyond the soil's bounding surface or dilatancy limit, which in turn, extended the trial-and-error convergence procedure used at every stress-ratio increment. In the presence of mitigation techniques (*e.g.*, below Structure $A2_{DS-6}$), the induced shear strains were restrained such that the model's dilation tendency and corresponding acceleration spikes at low periods were also controlled and comparisons of accelerations were significantly improved.

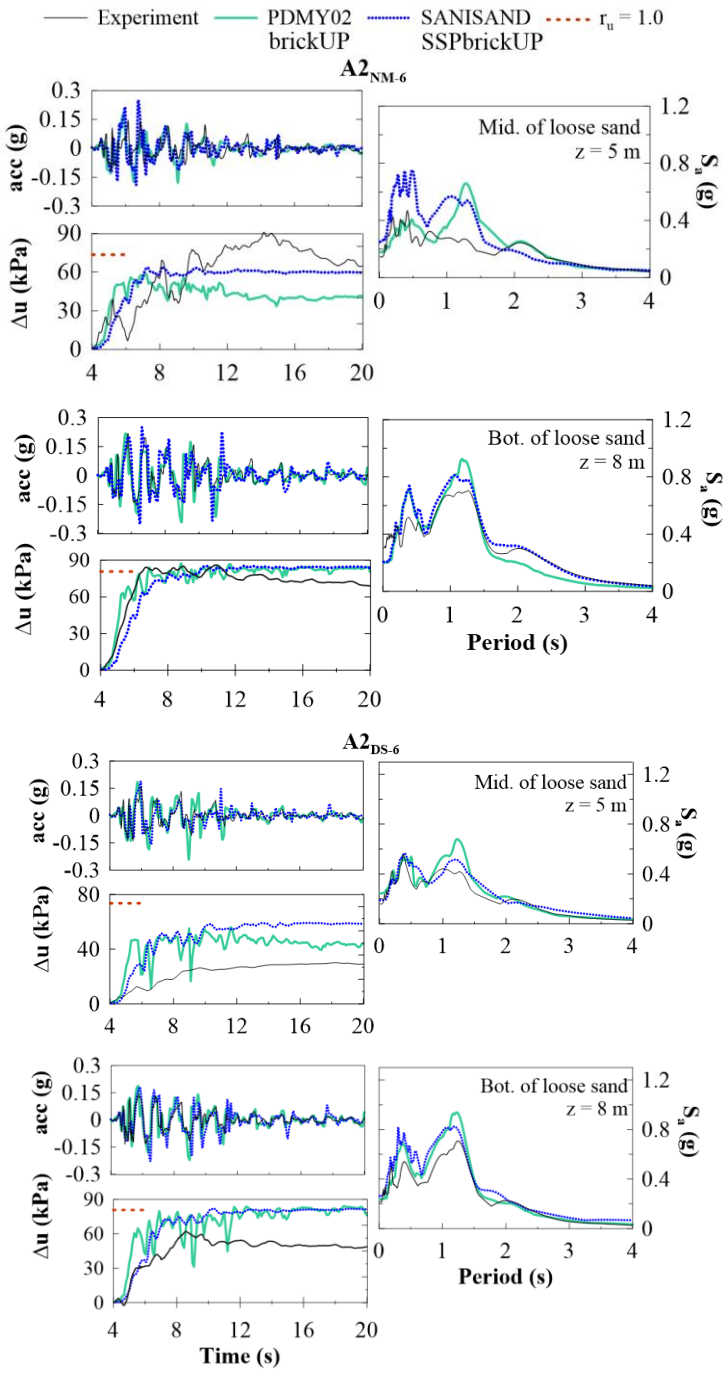

Figure 4.13 Effects of soil constitutive model and element type on acceleration and excess pore pressure time histories and acceleration response spectra (5%-damped) under the center of Structures $A2_{NM-6}$ and $A2_{DS-6}$ in the middle of the loose and dense Ottawa sand layers during Kobe-L.

In the experiments of unmitigated systems, a significant degree of de-amplification was observed in accelerations from the container base toward the foundation near the motion's

predominant period (*i.e.*, T_p of approximately 1.2 s), mainly within the looser layer of Ottawa sand. This degree of de-amplification was not observed in the far-field, nor under the mitigated structures. We hypothesize that the accumulation of large shear strains underneath the unmitigated structures (*e.g.*, $A2_{NM\text{-}6}$) increased the soil's damping of accelerations across a range of periods, particularly near T_p, where there was significant seismic energy input to the system. This de-amplification was not effectively captured by either of the numerical models. Both constitutive models roughly captured the rate of pore pressure generation under the unmitigated structures, but they tended to overestimate pore pressures in the mitigated cases. Hence, they did not effectively capture the reduction in the degree of soil softening below structures improved with densification. PDMY02 continued to over-estimate the rate of dissipation in all cases, which became evident after strong shaking (around 12 sec).

The numerically-simulated average foundation settlement and tilt time histories together with column bending strain time histories of Structures $A2_{NM\text{-}6}$ and $A2_{DS\text{-}6}$ are compared with the corresponding experimental measurements in Figure 4.14. Predictions of average foundation settlement (during shaking) were quite similar in models with PDMY02-brickUP and SANISAND-SSPbrickUP with a relatively high error with respect to the experiments. It was initially unclear whether this error was attributed to the constitutive model or the element type (detailed later in this section). The foundation rotation or tilt was, on the other hand, strongly influenced by the soil constitutive model and element type combination. Simulations with SANISAND-SSPbrickUP experienced slightly greater transient transverse rotations. However, models with PMDY02-brickUP better predicted the accumulation of permanent tilt. The foundation permanent tilt predictions with SANISAND-SSPbrickUP were near zero in all cases,

regardless of changes in various analysis parameters, constitutive model parameters, foundation-soil interface conditions, or analysis time steps.

To investigate the influence of element type on predicted foundation settlement and tilt, the unmitigated Structure A2 was next simulated with both constitutive models and element types (results shown in Figure 4.14). The prediction of settlement was generally better when using brickUP compared to SSPbrickUP with both constitutive models. Moreover, the accumulation of permanent differential settlements under the building's inertial load on a uniformly layered deposit could not be predicted when using the SSPbrickUP elements, regardless of the constitutive model. This single-point element averages out the excess pore pressure distribution and degree contraction and dilation underneath the foundation edges, reducing the accumulation of asymmetric shear and volumetric that lead to foundation's permanent foundation tilt. This problem was partly resolved when using brickUP. To match the accuracy of a higher-order element (*e.g.*, brickUP), one could refine the mesh below the foundation. However, this would increase the computational time even further (mainly an issue with SANISAND), affecting the practicality of the simulations.

The best results in terms of foundation settlement were obtained with the SANISAND-brickUP combination. In general, keeping the elements the same, SANISAND predicted larger foundation average settlements compared to PDMY02 (closer to those measured experimentally), due to its ability to better predict excess pore pressures, degree of soil softening, and the resulting volumetric and deviatoric strains during and immediately after shaking. The remaining error between the SANISAND-brickUP predicted average foundation settlement and experimental results was due to sedimentation, which could not be captured in finite elements. Note, however, that simulation of these models with the SANISAND-brickUP combination took approximately 25 times longer than PDMY02-brickUP (see Appendix D), making it impractical particularly when

mitigation techniques are introduced. In order to speed up the simulations, the authors also used SANISAND with both elements simultaneously: (i) brickUP elements for the two upper layers of loose Ottawa sand and Monterey sand where most of the shear strains were concentrated; and (ii) SSPbrickUP for the lower dense Ottawa sand layer. However, the analysis time continued to be impractical and the settlement predictions degraded. Additional research is needed to optimize the analysis time and element type(s) appropriate for this constitutive model. Figure 4.14 also indicated that PDMY02 with the higher order brickUP element provided slightly better predictions of foundation tilt and notably better predictions of column bending strains (likely due to improved predictions of low-period transverse and rotational accelerations about the foundation compared to other models), hence the deformation demand on the superstructure.

Despite significantly improved predictions of average settlement with SANISAND-brickUP, given the similar or worse predictions of foundation rotation, column strains, and low-period foundation accelerations compared to PDMY02-brickUP and the significantly longer required analysis time deeming it impractical, the latter model and element type combination was adopted for further analyses and comparisons with the centrifuge experimental database.

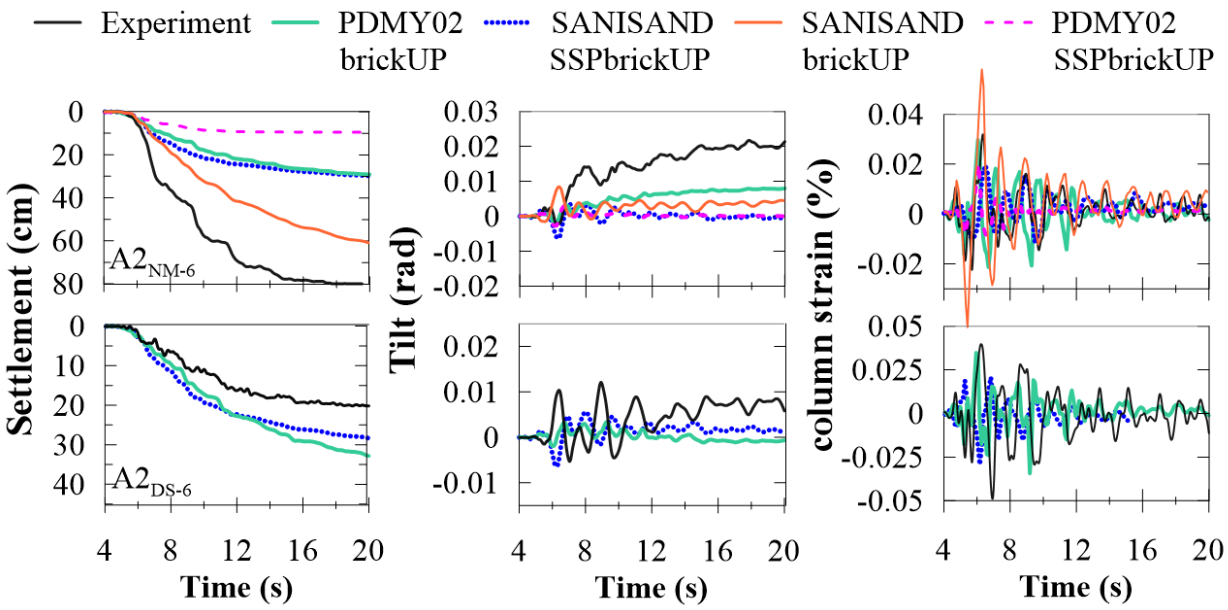

Figure 4.14 Effect of soil constitutive model and the element type on foundation average settlement, tilt, and column strain time histories of Structure $A2_{NM-6}$ and $A2_{DS-6}$ during Kobe-L.

4.5.3 Influence of the soil-foundation interface on the near-field response

Three types of soil-foundation interface conditions were considered to evaluate their effects on the numerical prediction of foundation settlement and tilt: a) a widely known nonlinear, zero-length, q-z and p-y springs at the bottom and lateral sides of the foundation, respectively; b) a more simplistic soil/foundation multi-point full connection (equalDOF through the master/slave connection); and c) a more complex zero-length, node-to-node frictional 3D contact elements. Figure 4.15 shows a schematic representation of these three soil-foundation interface conditions considered.

In the first condition, the bottom foundation-soil interface was represented with nonlinear q-z springs (tagged as QzSimple1 in OpenSEES) as a combination of elastic ($q\text{-}z^e$), plastic ($q\text{-}z^p$), and gap ($q\text{-}z^g$) components in series (Boulanger et al. 1999), as shown in Figure 4.15a. These springs were initially developed for piles, but a number of researchers have previously used them to model the soil interface with shallow foundations (*e.g.*, Deng et al. 2010; Liu and Hutchinson 2018). Likewise, the lateral soil-foundation interface condition was expressed by nonlinear p-y

springs (tagged as PySimple1 in OpenSEES), which also consisted of elastic (p-y^e), plastic (p-y^p), and gap (p-y^g) components (Boulanger et al. 1999).

Despite reasonably good predictions of foundation settlement when using these zero-length springs, the nonlinearity underneath the foundation was mainly controlled by the springs as opposed to the soil, which was not realistic because it allowed a slight penetration of the foundation elements into soil. Subsequently, the zero-length springs at the foundation base were made stiff enough in z-direction to avoid penetration, as presented by Liu and Hutchinson (2018). This led to a response similar to that of the attached soil-foundation condition (equalDOF), discussed below next.

In the second condition (Figure 4.15b), the foundation base was attached to the soil in all directions using a master/slave (equalDOF) option, with the soil functioning as master. Foundation nodes at the lateral perimeter of the footing were only attached to the soil in the horizontal direction to allow for relative settlement between soil and foundation in the vertical direction around the perimeter. This condition did not allow for separation or relative sliding. It was therefore, expected to slightly restrain the foundation's rocking tendency and damping in soil.

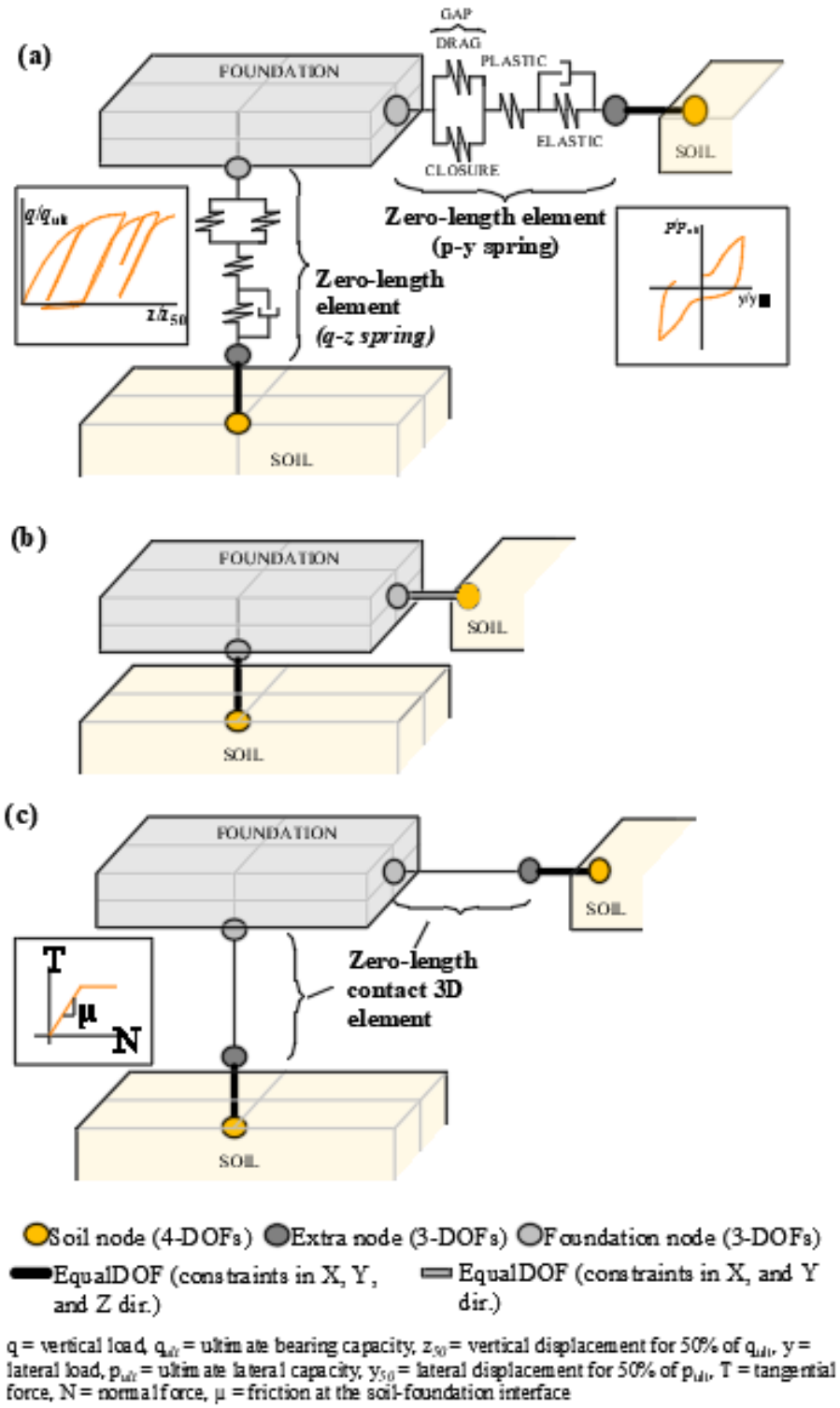

q = vertical load, q_{ult} = ultimate bearing capacity, z_{50} = vertical displacement for 50% of q_{ult}, y = lateral load, p_{ult} = ultimate lateral capacity, y_{50} = lateral displacement for 50% of p_{ult}, T = tangential force, N = normal force, μ = friction at the soil-foundation interface

Figure 4.15 Schematic representation of the three different soil-foundation interface models evaluated in this paper: (a) nonlinear, zero-length, q-z and p-y springs; (b) equalDOF through master/slave connection; and (c) zero-length, node-to-node frictional 3D contact elements.

In the third condition, zero-length, node-to-node, frictional, 3D contact elements (with a model tag of zeroLengthContact3D in OpenSEES) were used (see Figure 4.15c). These elements were implemented in OpenSEES by Wang and Sitar (2004) and correspond to a modified version of the continuum-based implicit formulation proposed by Laursen and Simo (1993). Along the soil-foundation connection, these contact elements were defined by penalty constraints (K_n, K_t) in the normal and tangential direction, cohesion ($c_{s\text{-}f}$), and friction angle ($\phi_{s\text{-}f}$). For the cases presented in this study, the penalty constraints in the normal and tangential direction were chosen as $K_n=1x10^8$ and $K_t=1x10^4$, respectively. The normal constraint penalty was large enough to avoid penetration in the normal direction. The non-penetration condition is usually defined by a minimum distance (or gap) function between the contacting surfaces (Wriggers and Zavarise 2004; Laursen and Simo 1993). This allowed to model the interface between soil and foundation in a more realistic fashion. The penalty constraint in the tangential or shear direction was selected to ensure stability and allow relative displacement between soil and foundation simultaneously. These contact elements follow a Mohr-Coulomb strength law in the tangential direction ($T=\phi_{s\text{-}f.N}+c_{s\text{-}f}$), defined by the interface friction angle ($\phi_{s\text{-}f}$) and the reaction force in the normal direction (N). The interface friction angle between the foundation and soil was set as 29° (70% of the peak friction angle of Monterey sand to avoid bearing capacity failure), and cohesion was set as zero. Since the zero-length contact elements are a discrete boundary (node-to-node) between the soil and foundation, the solution of SFS problems with these interface elements became computationally more expensive. This has been also identified by other researchers (*e.g.,* Wang and Sitar 2004). Other continuum soil-foundation interface types (*e.g.,* node-to-surface or surface-to-surface contact element) have been developed (Petek 2006), but they can only be used in static problems.

Figure 4.16 compares the experimental and numerical time histories of foundation average settlement, tilt, and column strains for two different unmitigated structures (*i.e.*, $A2_{NM-6}$ and B_{NM-6}) during Kobe-L using the PDMY02-brickUP model and two interface conditions: equalDOF and zero-length 3D contact elements. Figure 4.17 shows the deformed mesh and shear strain contours around Structures $A2_{NM-6}$ and B_{NM-6} for the two different interface conditions compared to the photographs taken during centrifuge model excavation. The settlement predictions were generally poor on the soil profile with a relatively thick liquefiable layer (*i.e.*, 6 m). This was partially due to the model's underprediction of net excess pore pressures within loose Ottawa sand during and immediately after strong shaking, and partially due to the continuum framework's inability to capture the contribution of sedimentation to volumetric strains. For the structure with greater inertia and deeper foundation (Structure B), the presence of zero-length contact elements slightly increased the relative movement of the foundation and soil elements, while allowing for the accumulation of marginally greater differential shear strains in soil below the foundation. Based on these observations, the final simulations of the SFMS systems with the PDMY02 model included zero-length contact elements.

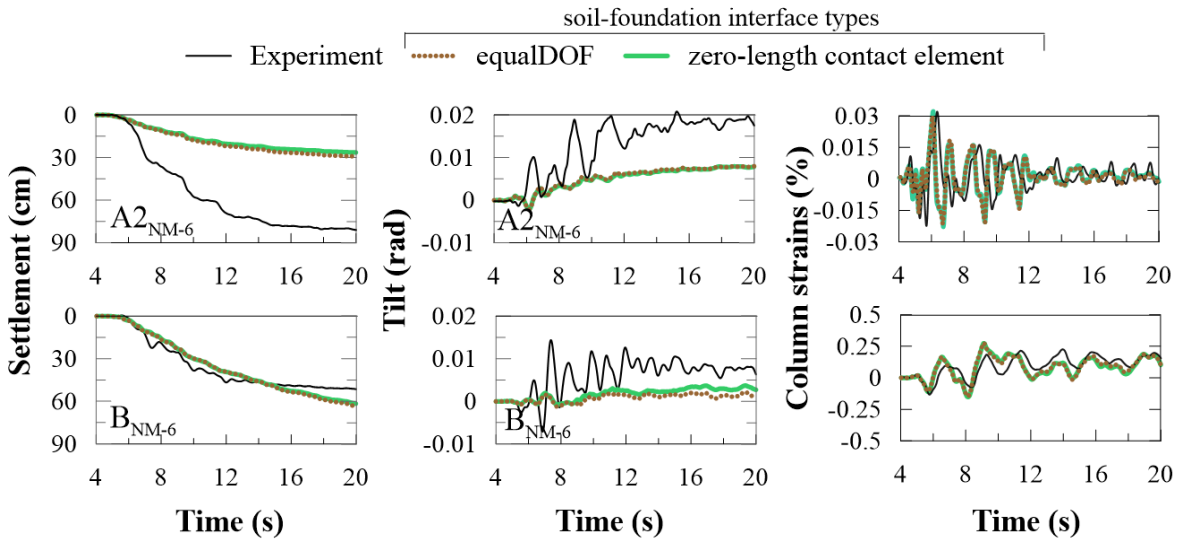

Figure 4.16 Effect of soil-foundation interface condition on the average settlement and tilt of two representative unmitigated structures ($A2_{NM-6}$ and B_{NM-6}) during Kobe-L.

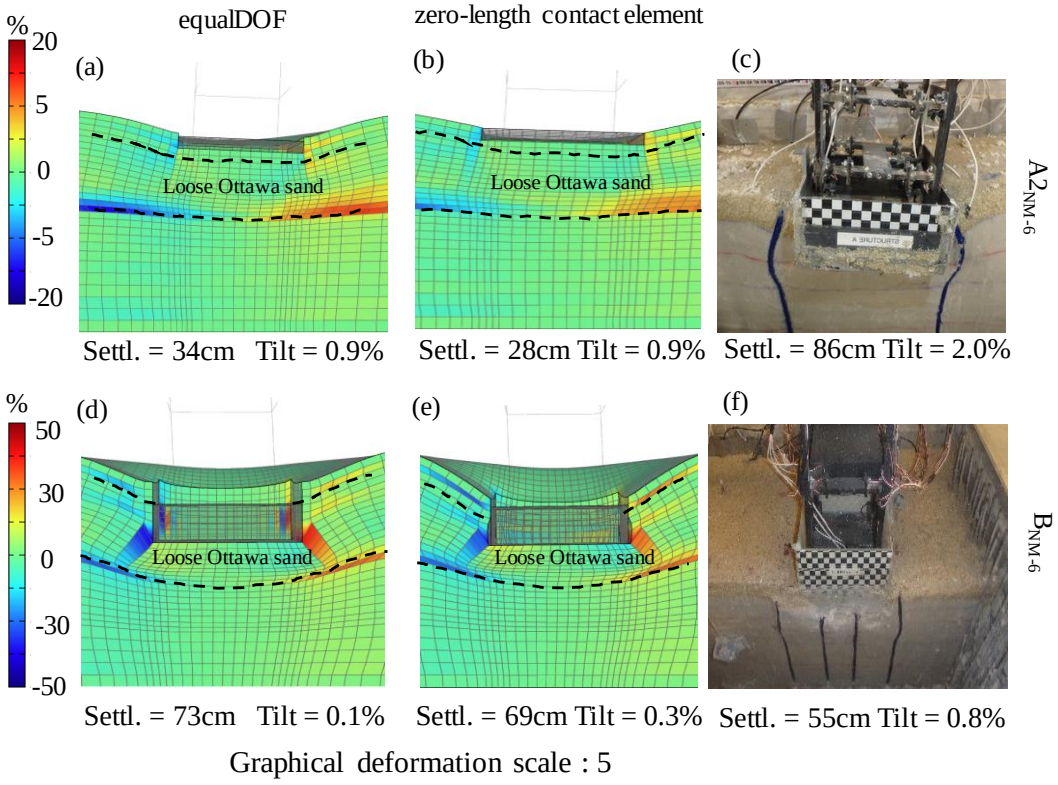

Figure 4.17 Deformed mesh indicating the numerically simulated shear strain of Structure $A2_{NM-6}$ and B_{NM-6} during Kobe-L using (a),(d) the equalDOF connection, and (b),(e) the zero-length contact element; and (c),(f) experimental deformation of the structures after a series of earthquakes. The values of residual settlement and tilt below each figure are those obtained after Kobe-L.

4.6 Comparison of Numerical Results with Experimental Measurements

In this section, the numerically-simulated response of the SFS system with the PDMY02 constitutive model, brickUP elements, and the zero-length contact elements is compared with centrifuge measurement. We compare the results in terms of horizontal accelerations, excess pore pressures, and settlements in the near-field. In addition, the response of each structure and foundation is assessed in terms of acceleration demand, settlement, tilt, roof drift, and strains on column and beam fuses. Figure 4.18 compares all the numerical and experimental results for Structure $A2_{DR\text{-}6}$, as a representative example. The remaining cases are provided in Appendix E. To quantify the differences between the numerical and experimental data, we use the percent (%) difference, taken as [numerical – experimental]/experimental. In these results, a positive value indicates the simulations over-predict the experimental response, and a negative value indicates under-prediction. We also use q-q (quantile-quantile or 1:1) plots and time history plots for a direct comparison of all results.

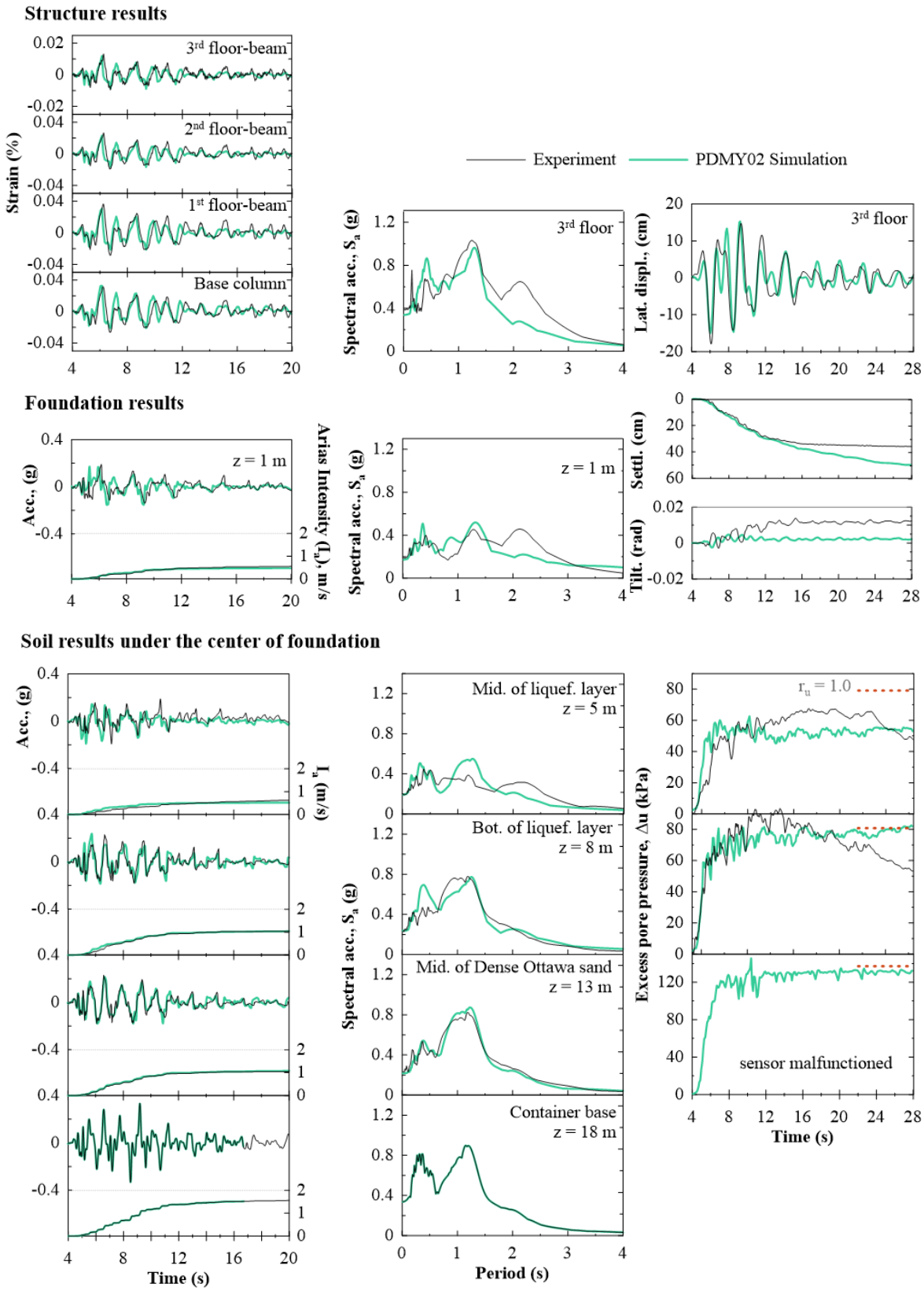

Figure 4.18 Comparison of numerical and experimental results for Structure A2DR-6.

4.6.1 Soil response in the near-field

In Figure 4.19 through Figure 4.21, the numerical results for accelerations and excess pore pressure time histories and response spectra are compared with the experimental measurements under the center of all structures. Figure 4.22 and Figure 4.23 compare the numerical and experimental profiles of peak ground accelerations (PGA) and the percent difference in spectral accelerations at various depths.

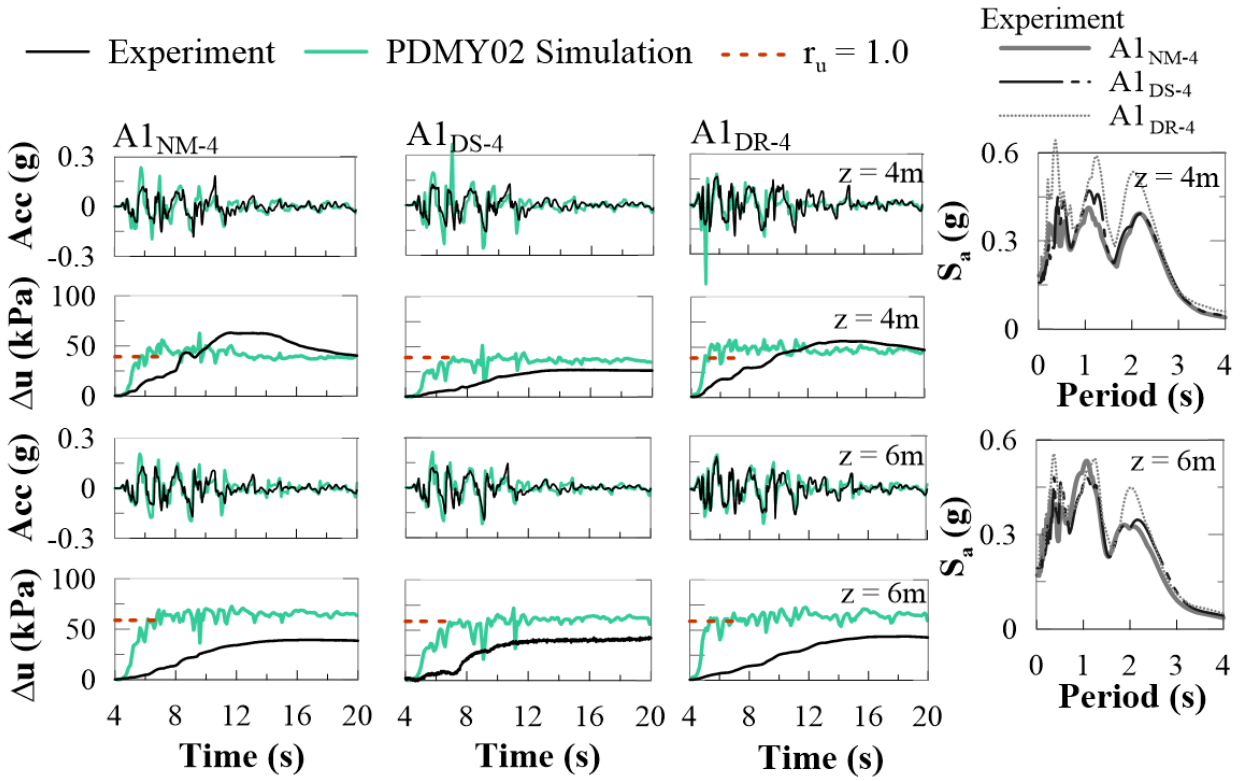

Figure 4.19 Comparison of numerical and experimental results under the center of structures like A1 in terms of: acceleration and excess pore pressure time histories and response spectra, in the middle and bottom of loose Ottawa sand.

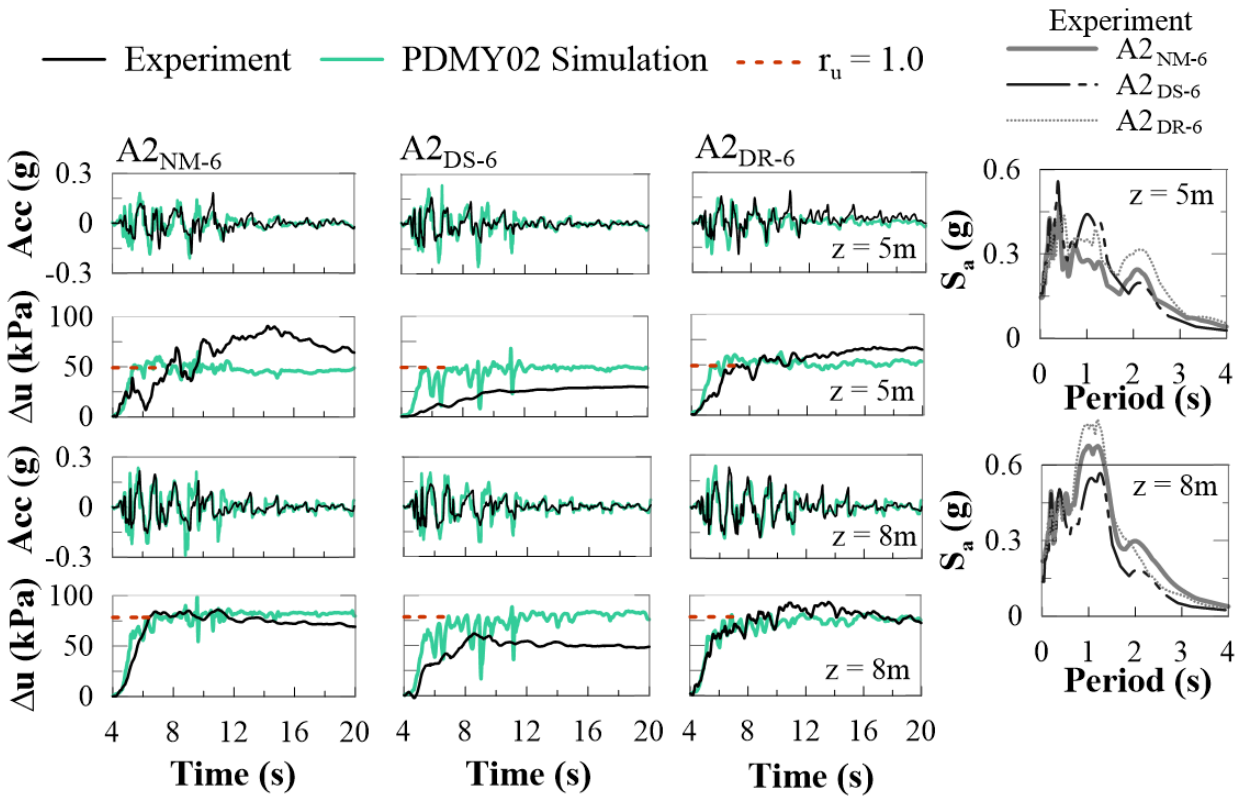

Figure 4.20 Comparison of numerical and experimental results under the center of structures like A2 in terms of: acceleration and excess pore pressure time histories and response spectra, in the middle and bottom of loose Ottawa sand.

The numerical results showed that, in general, the peak values of pore pressures underneath the buildings were well captured by the simulations (maximum error of 55%), particularly at shallower depths. However, the numerical simulations typically overestimated the initial rate of excess pore pressure build up below the lighter structures like A (Figure 4.19 and Figure 4.20). They also did not capture the extend of reduction in pore pressures below structures mitigated with densification (consistent with prior observations in the far-field). Larger numerical pore pressures resulted in more extensive soil softening (reduction in mean effective stress) and larger shear strains in each cycle of loading compared to the experiments, which in turn led to larger dilation-induced acceleration spikes affecting spectral accelerations at lower periods (higher frequencies). The greater confining pressure below the heavier structures like B reduced the soil's dilation

tendencies in the model and experiment, resulting in slightly better predictions of the rate of pore pressure build up and of accelerations (Figure 4.21).

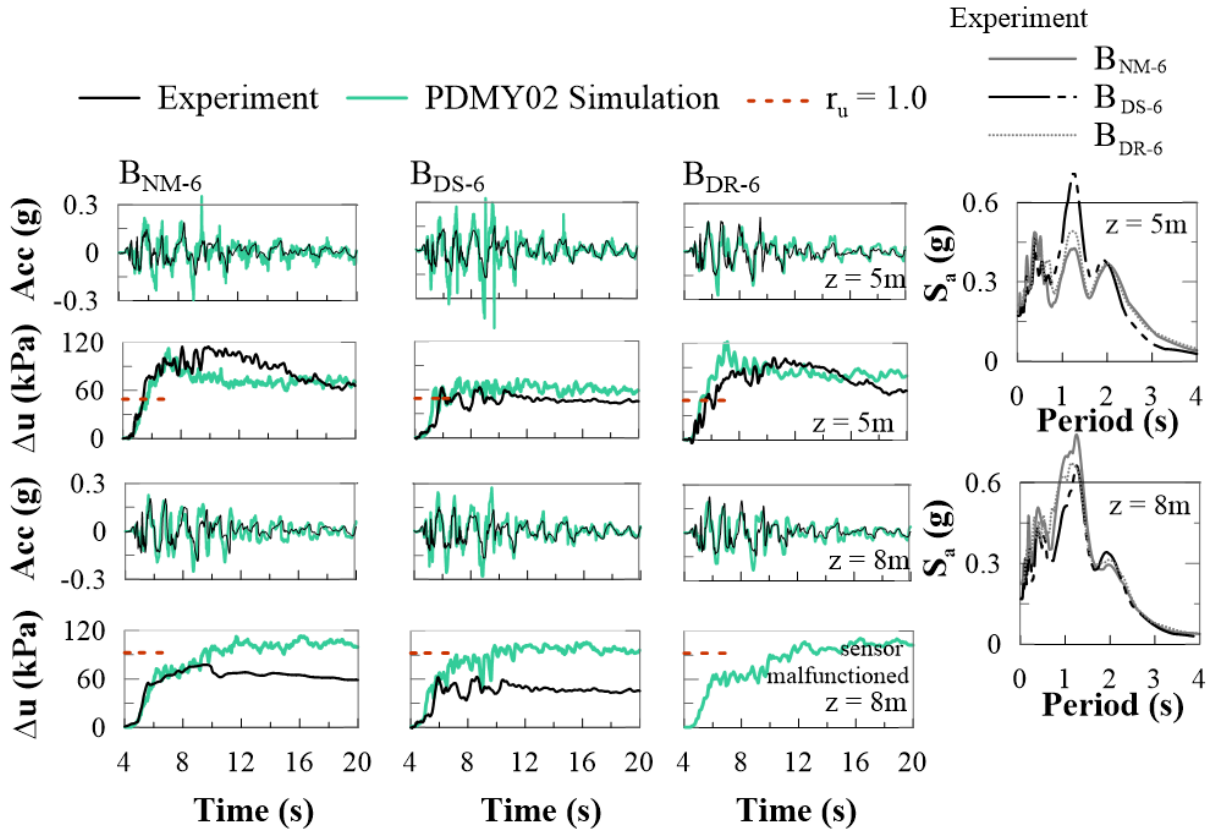

Figure 4.21 Comparison of numerical and experimental results under the center of structures like B in terms of: acceleration and excess pore pressure time histories, and response spectra, in the middle and bottom of loose Ottawa sand.

Although the PGA values (and spectral accelerations at periods below about 1.5 s) were generally predicted well below the foundation, they were sometimes overestimated at shallow depths, particularly in profiles with a thicker liquefiable layer and greater soil nonlinearity and strain accumulation. This effect can be observed in some of the simulations' overestimation of PGAs (Figure 4.22 and Figure 4.23). For example, a difference of up to +150% was observed in PGA below Structure $A2_{NM-6}$. .The presence of 3D zero-length contact elements contributed to the larger accelerations predicted near T= 0 and 1.2 s (the motion's T_p), observed previously in Figure

4.13. The interface elements added a fictitious stiffness in and around the soil-foundation contact area, amplifying particularly the PGA in soil at depths near the foundation.

In the experiments, densification limited the generation of excess pore pressure and softening under the structure (Olarte et al. 2018a). When densification was employed (*e.g.*, $A1_{DS-4}$ and $A2_{DS-6}$ in Figure 4.19 and Figure 4.20), the numerical models did not effectively capture the drop in peak excess pore pressures relative to the unmitigated cases, and excess pore pressures were over-predicted. The initial calibration of soil properties for dense Ottawa sand attempted to increase soil's contractive behavior to better match the predicted pore pressures in the free-field centrifuge test, as detailed by Ramirez et al. (2018). The response with the same model parameters under the static and seismic stresses of the foundation, considering the whole SFS system, appeared to be too contractive.

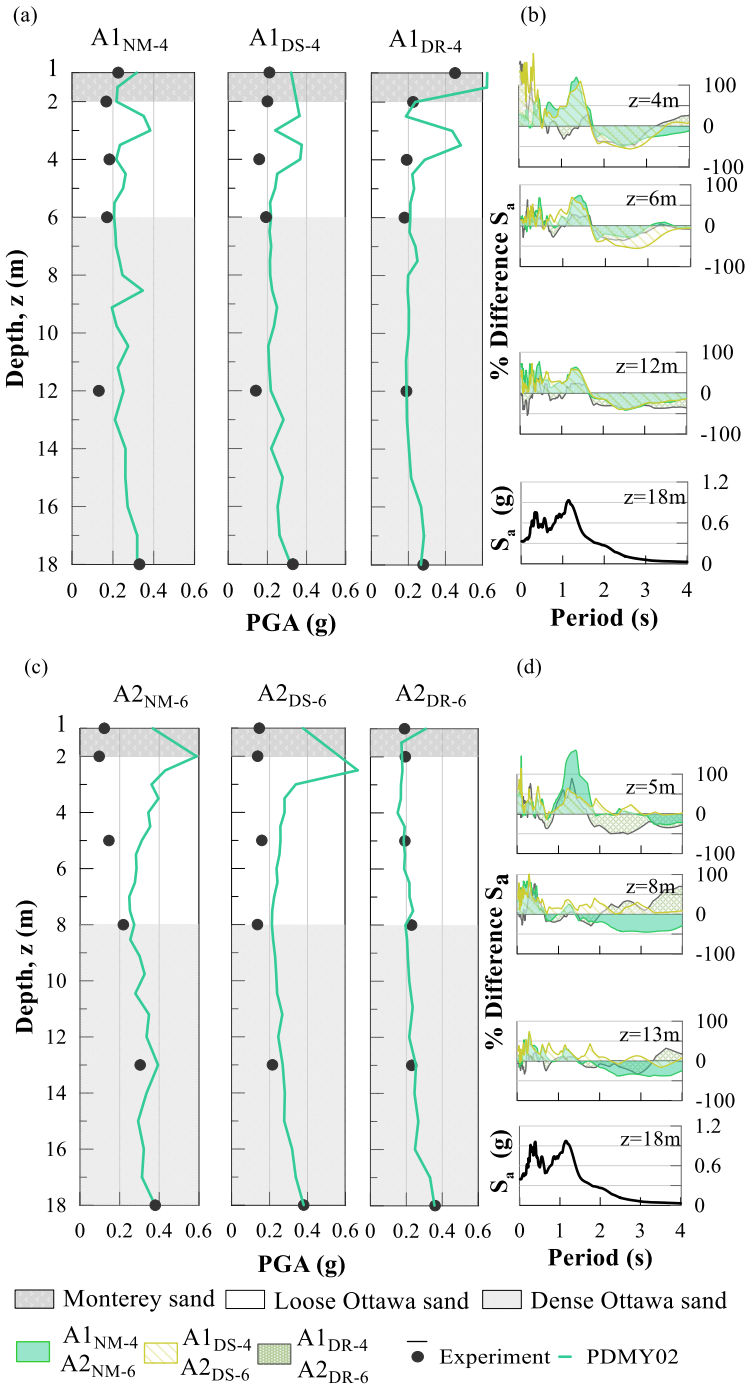

Figure 4.22 Comparison of numerical and experimental results for (a),(c) PGA versus depth under the center of Structures A1 and A2; and (b),(d) response spectra of base motion and percent difference between the numerical and experimental results in acceleration response spectra at selected depths.

The presence of PVDs around each structure in centrifuge (Paramasivam et al. 2018) typically slightly amplified accelerations at periods below 1.5 s below structures (Figure 4.19 and Figure 4.20) by increasing the rate of pore pressure dissipation, particularly near the edges of the foundation (within the drains' radius of influence). The numerical models could typically capture this behavior well, particularly in tests with a thicker liquefiable deposit (*i.e.*, 6 m), as detailed in Appendix E, Figure 4.20, and Figure 4.21. The simulations with PDMY02 continued to overestimate the rate of pore pressure dissipation, which became apparent after strong shaking (Appendix E). As described by other researchers (Howell et al. 2015; Karimi and Dashti 2016b; Ramirez et. al. 2017, 2018), the faster rate of pore pressure dissipation in PDMY02 results from its underestimation of volumetric compressibility.

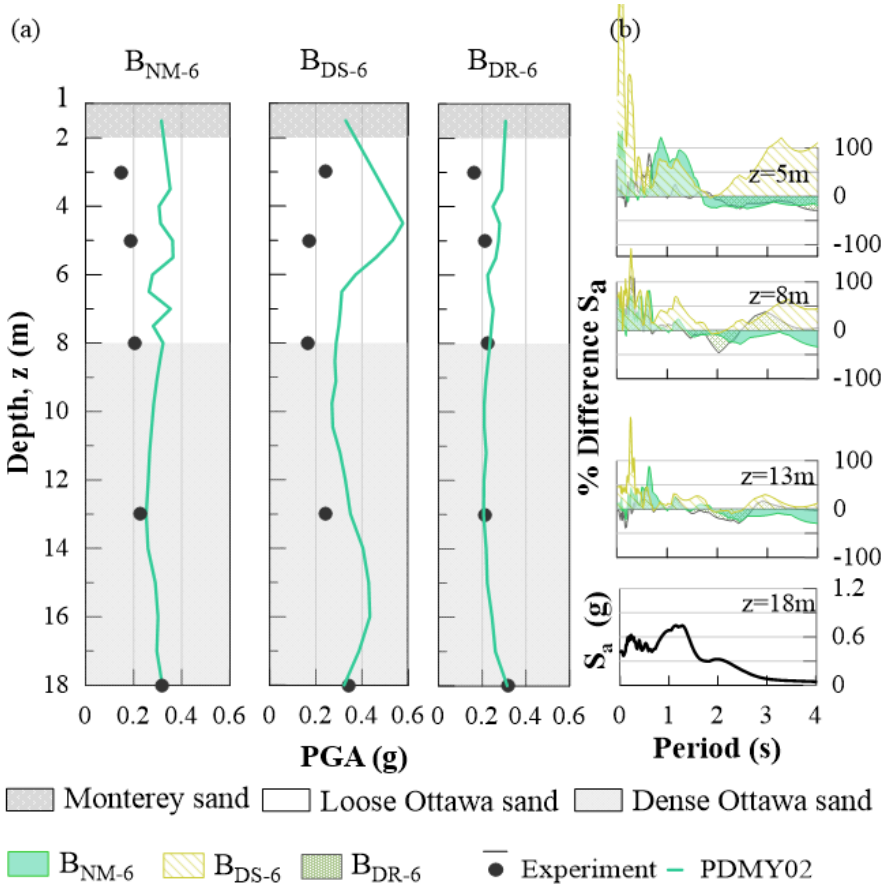

Figure 4.23 Comparison of numerical and experimental results for (a) PGA versus depth under the center of Structures B; and (b) response spectra of base motion and percent difference between the numerical and experimental results in acceleration response spectra at selected depths.

4.6.2 Response of the foundation

Figure 4.24 compares the numerical and experimental results in terms of the time histories of average foundation settlement and tilt as well as column bending strain for different structures. Permanent settlement and tilt are examined for numerical and experimental models in Figure 4.25.

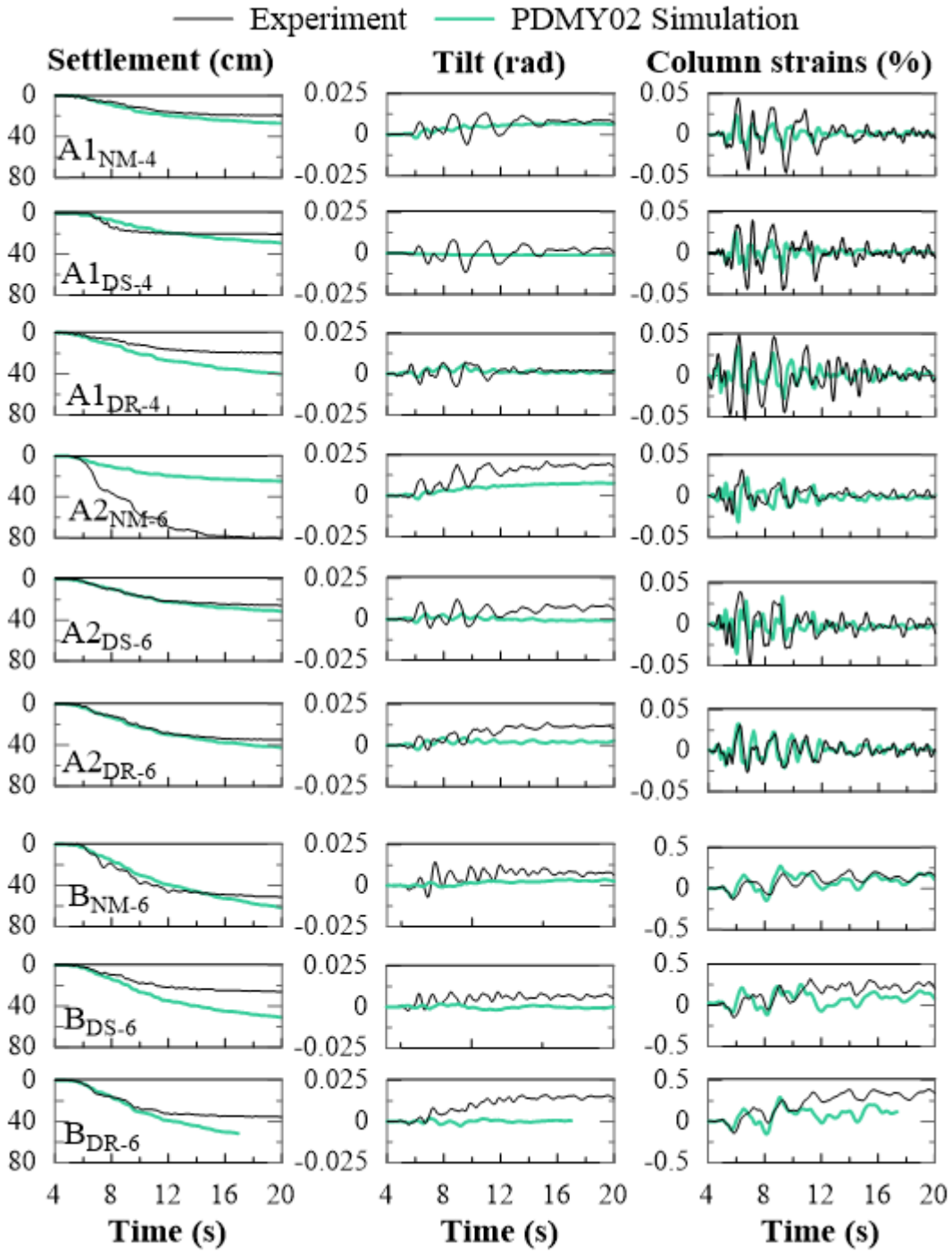

Figure 4.24 Comparison of experimental results for all structures in terms of: average settlement, tilt, and column bending strains. Note: Structure B_{DR-6} could not be for more than 10 seconds of motion due to the limitation of computational time in the supercomputer.

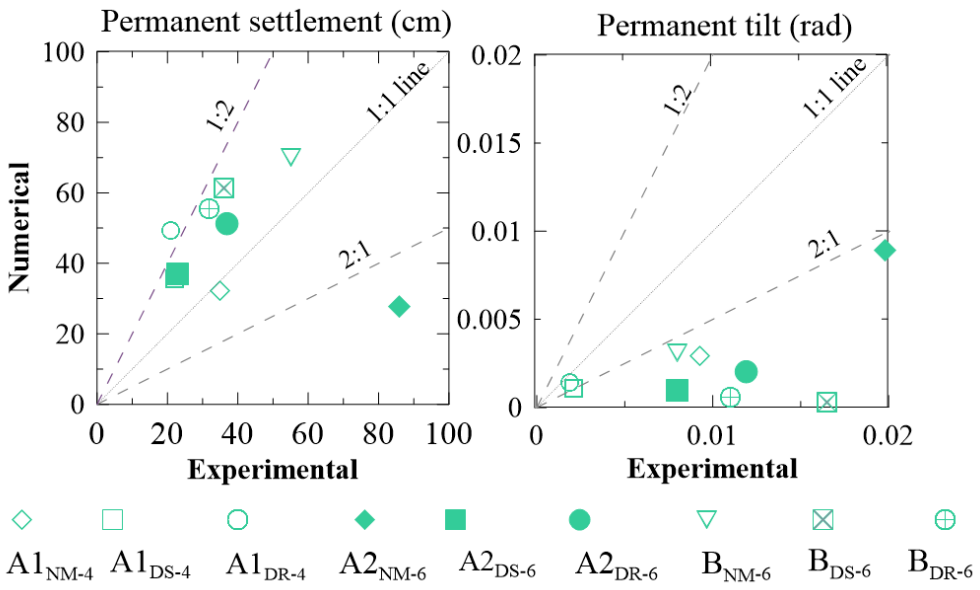

Figure 4.25 Comparison of the numerical and experimental results for all structures in terms of: (a) permanent settlement; and (b) permanent tilt of the foundations.

In the centrifuge, the foundation settlement increased notably with increasing thickness of the looser layer of Ottawa sand, primarily due to the contribution of larger volumetric strains (*e.g.*, sedimentation). Without mitigation, the heavier and taller Structure B settled less than Structure A, mainly because of its greater embedment and smaller thickness of loose Ottawa sand below its basement. Application of ground densification and PVDs slightly reduced the foundation's average settlement for both Structures A and B. The influence of mitigation on permanent tilt depended on the structure's strength and inertial response. For example, use of drains typically reduced tilt of lighter and stronger structures like A. However, it amplified the seismic demand transferred to the superstructure, which in the case of weaker and heavier structures like B led to greater permanent drifts that amplified the moment about the foundation and its permanent rotation. Not all these trends were captured numerically, as explored in more detail next.

In general, the numerical models (and a continuum framework) were not able to accurately capture the influence of liquefiable layer thickness on settlement, because they were unable to predict the important contribution of sedimentation to volumetric strains. This shortcoming led to

similar numerical predictions of settlement (about 30 cm) for the two unmitigated Structures $A1_{NM-4}$ and $A2_{NM-6}$, while the corresponding experimental values ranged from about 20 cm to 80 cm, respectively. The quality of settlement predictions notably improved for structures on thinner liquefiable layers (*e.g.*, 4 m instead of 6 m), when any form of mitigation was employed, or for heavier and more deeply embedded structures (like B) that limited the extent of softening (in terms of r_u) below the foundation. In all these cases, the contribution of sedimentation to volumetric strains was reduced by the changes to the SFS system, accounting for the improved numerical predictions.

Figure 4.25 shows that permanent foundation tilt was always underestimated, with errors ranging from +70 to -130%. The predictions generally improved for cases without mitigation. Use of contact elements between the soil and foundation slightly helped improve the predicted residual tilt, for the heavier and more deeply embedded, unmitigated Structure B_{NM-6}. Nevertheless, the soil was modeled as a continuum and the soil-foundation elements were connected in a node-to-node fashion, while in reality, a large number of soil particles interact with and move around the solid foundation in 3D during shaking. Modeling the soil at the grain scale is expected to better capture the accumulation of localized and asymmetric plastic strains under the foundation's dynamic compression and extension cycles. However, this approach is not practical for the problem under consideration and the available computational capabilities. As a result, the presented finite element analyses were not able to fully capture the cumulative foundation rotations, and often largely underestimated tilt compared to the experimental observations (particularly for buildings with mitigation). This shortcoming must be considered in the numerical simulations of liquefaction mitigation strategies.

4.6.3 Response of the superstructure

In general, experimentally, mitigation had the effect of increasing demands on the superstructure in terms of story flexural drifts, beam and column strains, and floor/roof accelerations, though the significance and magnitude of this increase depended on the mitigation and force-deformation characteristics of the structures (Olarte et al. 2017, 2018a, and Paramasivam et al. 2018). For Structures A1 and A2, for example, which responded elastically, the mitigations modestly increased the flexural drift, beam and column strains, and roof accelerations, particularly when the motion resonated with the building's fundamental mode. However, mitigation of the weaker, more flexible Structure B had the effect of drastically increasing nonlinear response and damage in the superstructures, as well as rotation of the foundation.

As defined by Gelagoti et al. (2012) and Karimi and Dashti (2016b), the rocking drift (Δu_r) and the flexural drift (Δu_f) contribute to the total drift on structures (see Figure 4.26). In the absence of horizontal LVDTs on the roof of Structure A, the experimental transient displacements at the roof and floor levels were obtained by integrating from acceleration measurements from accelerometers. For comparison, the numerical total drifts for structures like A were filtered to provide only transient displacements. When considering structures like B that experienced permanent flexure, the total displacement (transient and permanent) was experimentally obtained directly from LVDTs and used to compute the experimental total drift. A similar approach was used to obtain the numerical total drift, which considered the total lateral displacements computed at the building's roof. The numerical peak total drifts, as well as the maximum dynamic bending strains on the column and roof beam fuses, were then compared with the corresponding experimental results in Figure 4.27. In computing strains, we consider only the dynamic contribution to the strains in both experiments and simulations.

The total numerical drifts typically compared well with the experimental results (Figure 4.27a). This outcome is possible despite relatively worse predictions of tilt. The most relevant comparison is for Structure B, where LVDTs enabled measurement of transient and permanent drift. For Structure B, we underestimated tilt (rocking) by more than 150%, while overestimating bending strains by more than 70% (for reasons described below). Total drift depends on both of these underlying factors. In this case, these sources of error in effect canceled each other, leading to reasonable estimates of total drift. For structures like A, we could only compare transient drifts from accelerometer recordings. Hence, the comparisons are subject to error due particularly to the exclusion of permanent rocking drifts. The reliability of these estimates is expected to improve in cases with smaller permanent tilt (*e.g.*, Structure A1 on mitigated ground).

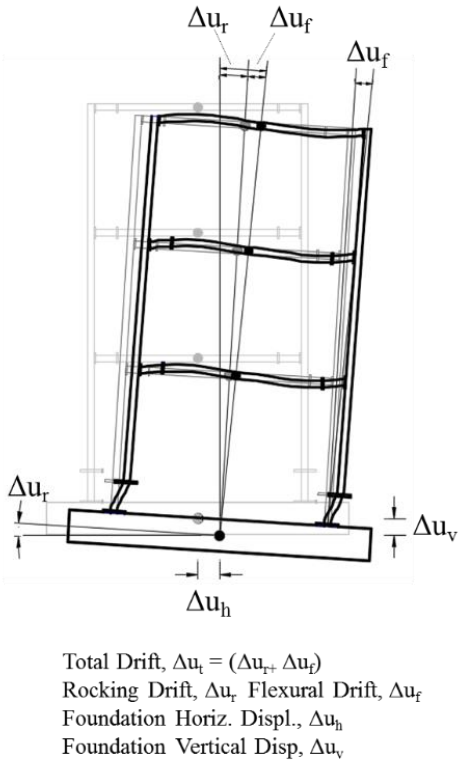

Figure 4.26 Schematic representation of total drift (Δu_t), rocking drift (Δu_r), and flexural roof drift (Δu_f) in a representative structure.

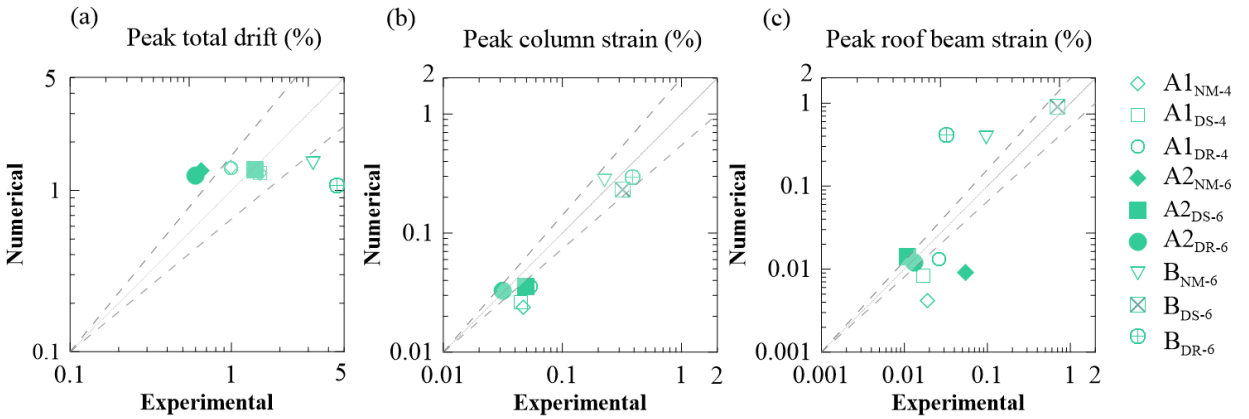

Figure 4.27 Comparison of numerical and experimental results for all structures in terms of: (a) peak total drifts; (b) peak column strains; and (c) peak roof beam strains.

Roof beam strains were generally underestimated for structures like A and overestimated for structures like B, as observed in Figure 4.27c. In particular, the results seem to indicate that beam strains for Structure A1 are the most underestimated, very slightly underestimated for A2, and then overestimated for B. The same trend was observed for column strains (Figure 4.27b). When calibrating the properties of nickel fuses in Structures A2 and B, the team decreased the Young's modulus to reflect the flexibility in the connection as well as the material itself. This led to an overestimation of bending strains especially for the taller, heavier, and weaker Structure B that experienced large strain demands. In contrast, during the calibration of steel fuses in Structure A1, we used the material Young's modulus directly, overestimating the stiffness of the connection. The larger errors observed in beam strains compared to column strains likely stemmed from the discrepancies between the numerical and physical models of structures. For instance, in the physical models, the gravity load from each floor mass was applied in the middle of the corresponding beam, and beam bending was restrained by the stiffness of a central mass. Yet in the numerical models, the load was applied at the top of the columns, and the physical dimensions of the floor mass were not represented. Hence, the beams were free to bend. These differences affected the dynamic contribution of the structure's mass to strains as well as the stiffness and

displaced shape of the beams, much more so than columns. Despite these differences, however, the numerical prediction of structural deformations better compared with centrifuge measurements compared to those in soil (*e.g.*, in terms of settlement and tilt).

Figure 4.28 compares the numerically computed and experimentally measured roof acceleration time histories and response spectra for different structures. The numerical peak spectral accelerations on the roof agreed relatively well with the experimental results (within 100%). The best comparisons were observed for structures like B ($B_{DS\text{-}6}$ and $B_{DR\text{-}6}$) and $A2_{DR\text{-}6}$, where reasonably good predictions of excess pore pressure and foundation accelerations were observed. In addition, the greater nonlinearity in the Structures like B damped out a greater range of frequencies, including near $T_{p,}$ with the result of producing a better match between experiment and numerical. Any errors in predicting foundation accelerations (*e.g.*, the de-amplification of motion near a T_p of about 1.2 s in the experiment that was not captured well in the models) also affected the predicted roof accelerations, particularly near the unmitigated, lighter structure on the thicker liquefiable layer ($A2_{NM\text{-}6}$). Low-period roof spectral accelerations were also overestimated by the numerical model in cases with densification, because the overestimation of these accelerations below the foundation were transmitted to the structure.

Taken together, these results imply that reliable predictions of structure's response and damage potential are possible, despite possible challenges in capturing the settlement and rotation of the foundation in some cases

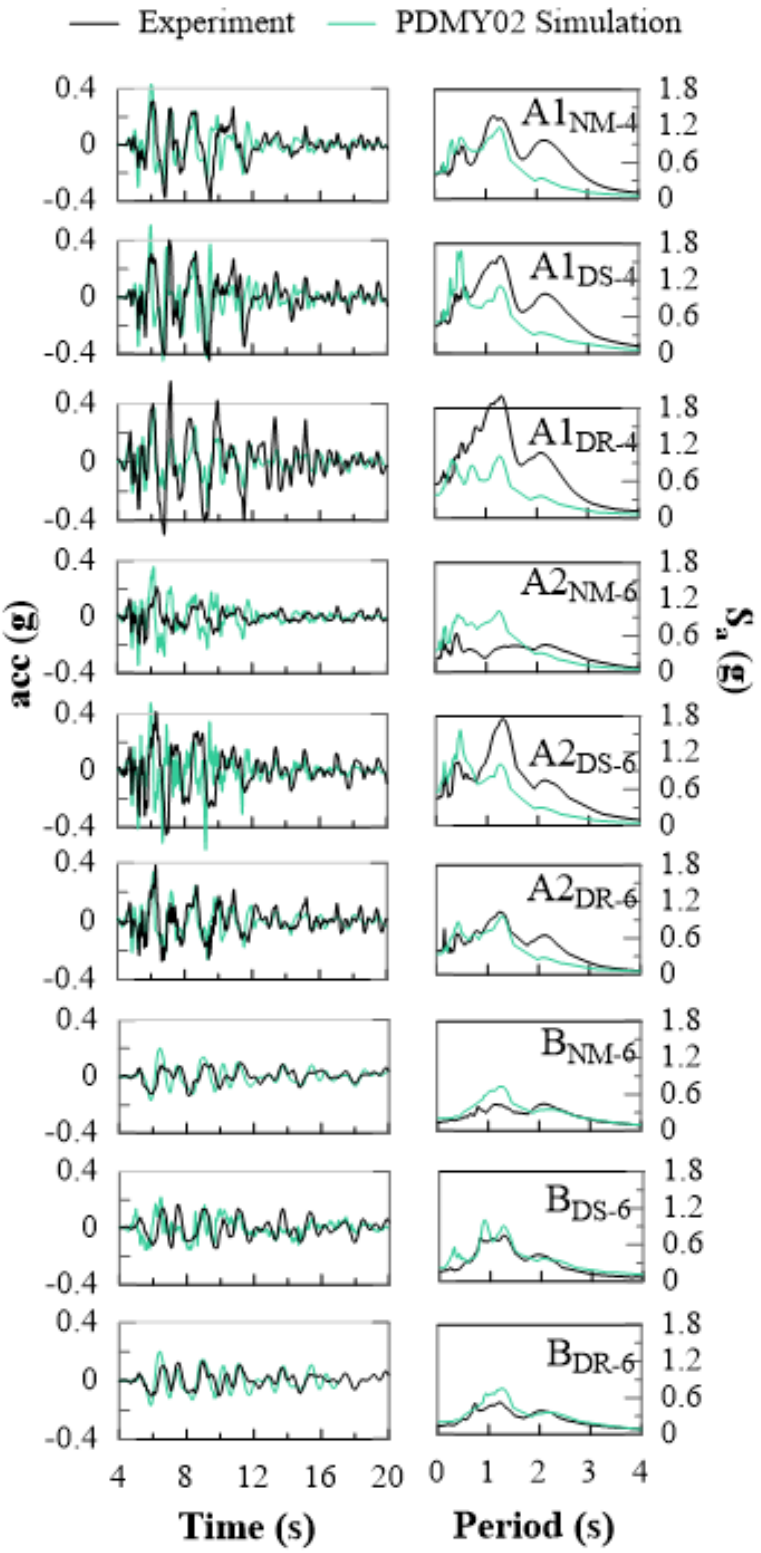

Figure 4.28 Comparison of numerical and experimental results for all structures in terms of roof acceleration time histories and their response spectra Sa (5% damped).

CHAPTER 5

5 CONCLUSIONS AND FUTURE RESEARCH RECOMMENDATIONS

5.1 Overview

This dissertation validates 3D fully-coupled, effective stress, nonlinear, dynamic numerical simulations with centrifuge experiments that involved potentially inelastic, multi-degree-of-freedom shallow-founded structures in the presence of two common mitigation techniques. This study aimed to provide: 1) insight into the capabilities, limitations, and practicality of advance numerical tools in reliably predicting seismic site response, soil-structure interaction, and key demand parameters quantifying structural performance (*e.g.*, foundation settlement and tilt, roof drift and acceleration demands on the superstructure); 2) observations about the modeling uncertainties of simulations involving soil-foundation-mitigation-structure systems; 3) recommendations for future modeling development and improvements of numerical tools; and 4) validated numerical simulations that can be used for future numerical parametric studies or employed in design.

5.2 Summary and Key Findings

5.2.1 Evaluation of different numerical tools in predicting seismic site response in the free-field

The results from two numerical platforms and two constitutive models were systematically compared regarding their capability to capture free-field volumetric settlements, accelerations, and excess pore pressures in a layered saturated level liquefiable soil deposit under 1D horizontal

earthquake shaking as observed in a centrifuge test. One team of collaborating researchers (Team 1) used the multi-yield PDMY02 soil model implemented in OpenSEES. Two other teams (Teams 2 and 3) used the bounding surface SANISAND model implemented in OpenSEES and FLAC, respectively. All teams conducted their first phase of calibration (Calibration C) based on the results of the same set of monotonic and cyclic fully drained and undrained triaxial tests in a consistent manner. At this stage, the teams had no access to centrifuge experimental results. The calibration goals and priorities of the three teams were not the same. Team 1 prioritized capturing the number of cycles to liquefaction while capturing other response parameters at the element level to the extent possible. Teams 2 and 3 focused on capturing the stress–strain response and generation of excess pore pressures as observed particularly in the undrained cyclic triaxial tests over a range of strains, while accounting for the critical-state parameters roughly estimated from monotonic tests. After calibration and model verification, all teams performed Class C predictions of site performance in the centrifuge model during one earthquake motion. The PDMY02 model greatly over-predicted the rate of excess pore-pressure dissipation observed in the centrifuge, which led to poor predictions of net pore pressures, particularly in dense sand. Its predictions of accelerations were reasonable. The bounding surface model (SANISAND) in both OpenSEES and FLAC also overestimated the rate of pore-pressure dissipation, but not as severely as PDMY02, due to the model's greater inherent volumetric compressibility. Its excessive dilative tendencies and smaller material damping evident in monotonic triaxial tests, however, led to the prediction of excessively large acceleration spikes. None of the models could predict volumetric settlements well. The Class C predictions indicated that calibration based on small element tests do not necessarily lead to a successful prediction of seismic site response in the centrifuge, regardless of the type of computational platform, constitutive model, or user's calibration methodology.

The three teams carried out Calibration C1 followed by Class C1 predictions of the centrifuge test. All models reduced their dilation tendencies in loose and particularly dense Ottawa sand, even at the cost of slightly sacrificing the quality of predictions in fully drained or undrained element tests at certain strain levels or sacrificing the number of cycles to liquefaction (*e.g.*, previously prioritized by PDMY02). The recalibration of SANISAND also attempted to increase material damping slightly. Although the results were improved in terms of accelerations and peak pore pressures in all models, PDMY02 continued to overestimate the rate of dissipation. The improved Class C1 predictions, however, showed that setting number of cycles to trigger liquefaction for a large range of strains or stresses as a priority during calibration (often the only data available in practice from empirical observations) may not only be ineffective, it can at times jeopardize the model's ability to reliably predict the rate of pore-pressure generation and accelerations, particularly in denser sands.

In general, the results and comparisons presented in this study point to the importance of including a more realistic boundary value problem (*e.g.*, centrifuge testing) capable of simultaneous generation and dissipation of excess pore pressures during realistic earthquake motions when possible for model calibration. The calibration of soil models only based on a range of fully drained and undrained element tests under monotonic or sinusoidal cyclic loading did not yield acceptable results when blindly predicting seismic site performance in centrifuge. The centrifuge results were valuable in identifying the shortcomings of each model and helped improve their predictive capabilities in terms of accelerations and excess pore pressures. All models, however, continued to perform poorly in terms of volumetric settlements. This deficiency was expected to be associated with the weakness of constitutive models, type of element, the multiphase formulation implemented in each platform, and the change in soil properties over time

(*e.g.*, permeability and porosity) that were not captured numerically. This is an area in need of investigation and improvement in future generations of liquefaction computational and experimental modeling.

Despite obtaining satisfactory results with SANISAND in the finite difference platform FLAC, simulations were considerably more time consuming and computationally expensive compared to OpenSEES, even for a single soil column. Therefore, the finite difference tool was not further explored for the simulations of the larger SFS systems.

5.2.2 Evaluation of 3D numerical simulations in predicting the response of inelastic structures on mitigated and unmitigated liquefiable soils

In this study, we evaluated the limitations and capabilities of 3D, solid-fluid, fully-coupled, nonlinear, dynamic finite element simulations in predicting the seismic response of potentially inelastic, multi-degree-of-freedom, shallow-founded structures on layered soil profile sand mitigated with densification and PVDs, through comparison with seven centrifuge experiments. The numerical simulations of the soil-foundation-structure (SFS) systems were performed in OpenSEES using two state-of-the-art soil constitutive models (PDMY02 and SANISAND) for soil and nonlinear beam elements with fiber sections and P-Δ geometric transformations for the structure. Details of the calibration of soil models have been published previously by Ramirez et al. 2018)

We first evaluated the influence of three critical modeling decisions on seismic site and SFS system response: 1) magnitude and formulation of small-strain damping; 2) choice of the constitutive model and element type; and 3) method of modeling the soil-foundation interface. A sensitivity analysis showed that the horizontal accelerations at lower periods (and hence, the PGA) were highly sensitive to the magnitude and frequency characteristics of small-strain Rayleigh

damping in soil, particularly with the multi-yield surface soil constitutive model (PDMY02). These results highlighted the complex influence of small-strain damping on material's stress-strain response, hysteresis damping, and predicted accelerations. A small-strain damping of 4% at a frequency range exceeding those of interest in earthquake engineering (0.01 to 25 Hz) was shown to improve the predicted accelerations and avoid excessive over- or under-damping across the frequency range of interest.

Subsequently, simulations were carried out to compare the capabilities of the PDMY02 and SANISAND soil constitutive models with two element types of brickUP and SSPbrickUP against representative centrifuge tests. Both constitutive models predicted reasonably well the response in the far-field in terms of accelerations and excess pore pressure, while highly underestimated settlements. The differences between constitutive models and element types became more apparent below the structures. SSPbrickUP elements, with their lower order and single integration point, averaged the distribution of pore pressures below the foundation and did not capture the localized accumulation of plastic strains, hence its permanent settlement and tilt. SANISAND together with brickUP led to notably better predictions of foundation's permanent settlement compared to PDMY02-brickUP, due to improved predictions of excess pore pressures and degree of softening in the soil below the foundation. This constitutive model and element type combination, however, required 25 times the analysis time of PDMY02-brickUP, making it impractical. Staying with brickUP, due to SANISAND's similar or slightly worse predictions of foundation tilt, low-period accelerations, and column strains as well as its unreasonably long analysis time, PDMY02 was selected for further simulations. Additional research is needed to optimize the analysis time and appropriate element type(s) that would allow use of SANISAND when modeling large SFS systems.

The use of a node-to-node full connection (equalDOF or master/slave condition) constrained the foundation's relative movement with respect to soil. Use of a more complex 3D zero-length contact elements slightly improved the relative movements, but did not notably affect average foundation settlements and tilt compared to cases with an equalDOF connection.

After an initial investigation of model sensitivities and selection of small-strain soil damping, constitutive model, element type, and contact element conditions, the numerical simulations were compared with all available experimental results. Despite better predictions of accelerations in the near-field (compared to the far-field), the numerical simulations overestimated low-period accelerations (affecting the PGA) near the foundation. This was affected by the presence of contact element, which added a fictitious stiffness in and around the soil-foundation contact area. In addition, the models were not able to effectively capture the drop in excess pore pressures below structures mitigated with densification, indicating an excessively contractive soil response.

Foundation settlements were generally predicted within a factor of 2, except when the volumetric strains due to sedimentation became significant (*e.g.*, Structure $A2_{NM\text{-}6}$), where the factor was larger (about 3). The quality of the numerical predications improved for the more deeply embedded and heavier structure or tests with mitigation strategies. For the more deeply embedded and heavier structure, the greater confining pressure and embedment of the structure limited the extend of softening below the foundation, net excess pore pressure ratio, r_u, and the contribution of sedimentation of total volumetric strains below the foundation, which, in turn, reduced the total settlement and improved the quality of the numerical predictions.

The residual foundation tilts were generally underestimated. The predictions worsened for cases with mitigation. Column and roof beam bending strains and maximum roof spectral

accelerations were captured reasonably well in all structures. Hence, the performance of mitigated and unmitigated nonlinear structures and their damage potential could be reasonably predicted, despite possible shortcomings and a large error in capturing settlement and tilt of their foundation.

These results suggest that more work is needed to improve modeling capabilities of the cyclic softening in dense sand, volumetric strains in loose, saturated granular soils, and accumulation of localized and asymmetric plastic strains below the foundation. However, numerical modeling of soil-foundation-structure systems characterized either by a relatively thin liquefiable layer or by a form of mitigation were shown to sufficiently capture, in gross terms, the system's performance in terms of deformations and damage potential (with the exception of foundation tilt).

5.3 Limitations and Future Research Recommendations

The Class-C1 simulations presented in the first phase of this dissertation concluded that incorporation of a more realistic boundary value problem (*e.g.*, a centrifuge test) during calibration, as opposed to only relying on fully-drained or undrained element tests, can significantly improve the predictive capabilities of both soil constitutive models considered (*i.e.*, PDMY02 and SANISAND) for seismic site response and therefore, seismic response of soil-structure systems. However, in practice, centrifuge tests are rarely conducted and practitioners have more access to traditional elements tests or simply the number of cycles to trigger liquefaction at different stress levels based on prior case histories (*e.g.*, Youd et al. 2001). Hence, it is critical to either improve the existing constitutive models or develop a more practical calibration routine that simultaneously captures response at multiple scales in terms of triggering of liquefaction in the field, rate of pore pressure generation and stress-strain response at an element level, as well as pore pressures and accelerations in a site response analysis.

- Despite significant advances in constitutive modeling for capturing liquefaction consequences, we show in this dissertation that capturing volumetric strains (particularly due to sedimentation) is still not possible in a continuum framework, with the existing state-of-the art models and platforms. This shortcoming may be acceptable when predicting performance on relatively thin liquefiable layers of clean sand or on densified ground. This is because the contribution of sedimentation to total settlements is proportional to layer thickness. But when predicting response of light structures on thicker liquefiable deposits, where we expect a large degree of softening and liquefaction in a thicker profile, the inability of our numerical models to capture sedimentation can lead to significant errors in predicting total settlement below the foundation. Future research in dynamic poromechanics using the finite element method (FEM) coupled with discrete element method and computational fluid dynamics (DEM-CFD) multiscale modeling is anticipated to help improve our predictive capabilities in the future.
- The numerical and experimental results presented in this dissertation are limited to one soil type (*e.g.*, a clean silica sand without fines) and a simple soil stratigraphy (*e.g.*, level ground with uniform layers). Future experimental studies should include sand with varying fines contents (*e.g.*, less than 15%), interlayering (variations in permeability), and stratigraphic variations (changes in layer thickness or ground slope), which are all expected to influence the consequences of liquefaction, the contribution of different mechanisms of deformation (*e.g.*, shear, volumetric, and ejecta), and the effectiveness of mitigation techniques (*e.g.*, PVDs). More realistic site conditions in future experimental studies will help reveal the strengths and limitations of the numerical tools in capturing more complexities in the presence of static shear stresses, permeability variations, and formation of a water lens and ejecta.

- Due to restrictions associated with container size and constructability, the model structures tested in centrifuge were designed to capture the most important features of the target prototype structures (3- and 9-story single frame structure). Certain properties of the structures (particularly the 9-story) were not captured due to space limitations. Additional centrifuge tests that consider different properties, dimensions, and configurations for structures and their foundations are needed.
- Based on the calibrated and validated numerical tools developed in this dissertation, a preliminary parametric study can be initiated to investigate the influence of different liquefaction mitigation techniques (*e.g.*, densification or drainage) on the performance and damage potential of the soil-foundation-structure systems. The generated numerical data can enable evaluation of the key demand parameters (*e.g.*, foundation settlement, tilt, peak roof drift, column strain) for a range of ground motions, soil profiles, structure types, and mitigation strategies, with the goal of developing a performance-based mitigation design procedure.
- Motivated by the configuration of urban environments, further investigation is required to evaluate the influence of liquefaction mitigation strategies on the performance of structure-soil-structure systems. Future experimental and numerical models should consider the presence of adjacent structures, with and without remediation strategies. This will provide insights into the capabilities of numerical models in predicting the performance of structures in isolation and when adjacent to other building(s) and their interaction with liquefaction mitigation techniques.

REFERENCES

Adalier, K., A.W. Elgamal., and G.R. Martin. 1998. "Foundation liquefaction counter-measures for earth embankments." J. Geotech. Geoenviron. Eng., 124,6, 500–517.

AISC, Specification for structural Steel Buildings (ANSI/AISC 360). 2010. American Institute of Steel Construction, Chicago, IL.

Alawaji, H., S. S. Runesson, and K. Axelsso. 1992. "Implicit integration in soil plasticity under mixed control from drained and undrained response." Int. J. Numer. Anal. Method Geomech. 16 (10): 737–756. https://doi.org/10.1002/nag.1610161004.

Andrade, J. E., A. M. Ramos, and A. Lizcano. 2013. "Criterion for flow liquefaction instability. Acta Geotech. 8 (5): 525–535. https://doi.org/10.1007/s11440-013-0223-x.

Andrianopoulos, K. I. 2006. "Numerical modeling of static and dynamic behavior of elastoplastic soils." Doctorate Thesis, Department of Geotechnical Engineering, School of Civil Engineering, National Technical University of Athens (in Greek).

Andrianopoulos K. I., A. G. Papadimitriou, and G. D. Bouckovalas. 2010a. "Bounding surface plasticity model for the seismic liquefaction analysis of geostructures." Soil Dynamics and Earthquake Eng. 30(10): 895–911, http://dx.doi.org/10. 1016/j.soildyn.2010.04.001.

Andrianopoulos K. I., A. G. Papadimitriou, and G. D. Bouckovalas. 2010b." Explicit integration of bounding surface model for the analysis of earthquake soil liquefaction." International Journal for Numerical and Analytical Methods in Geomechanics. 34(15): 1586–1614, http://dx.doi.org/10.1002/nag.875.

Ansal,A., N. Abrahamson, J. P. Bardet, A. Barka, M. B. Baturay, B. M. Berilgen, R. Boulanger, J. Bray, O. Cetin, L. Cluff, T. Durgunoglu, D. Erten, M. Erdik, D. Frost, I. M. Idriss, T. Karadayilar, A. Kaya, W. Lettis, J. Martin, J. Mitchell, G. Olgun, T. O'Rouke, W. Paige, E. Rathje, C. Roblee, R. Sancio, W. Savage, R. Seed, P. Somerville, J. Stewart, B. Sunman, B. Swan, S. Toprak, D. Ural, M. Yashinski, T. Yilmaz, and L. Youd. 1999. "Initial geoetechnical observations of the August 17,1999, Kocaeli earthquake." A report of the Turkey-US geotechnical earthquake engineering reconnaissance team.

Arulanandan, K., and R. F. Scott. 1993. "Verification of numerical procedures for the analysis of soil liquefaction problems. Vol. 1: Experimental results and numerical predictions." In Proc., Int. Conf. on the Verification of Numerical Procedures for the Analysis of Soil Liquefaction Problems. Rotterdam, Netherlands: A.A. Balkema.

Arulanandan K., and R. F. Scott. 1994. "Verification of numerical procedures for the analysis of soil liquefaction problems. Vol. 2: Experimental results and numerical predictions." In

Proc., Int. Conf. on the Verification of Numerical Procedures for the Analysis of Soil Liquefaction Problems. Rotterdam, Netherlands: A.A. Balkema.

API, American Petroleum Institute. 1987. "Recommended Practice for Planning, Designing and Constructing Fixed Offshore Platforms API Recommended Practice 2A (RP2A)." Seventeenth Edition, April 1..

ASCE. American Society of Civil Engineers. 2010. "Minimum design loads for buildings and other structures (ASCE7)." ASCE/SEI7, Reston, VA.

ASTM. 2000. Standard test methods for minimum index density and unit weight of soils and calculation of relative density. ASTM D4254-00. West Conshohocken, PA: ASTM.

ASTM. 2006. Standard test methods for maximum index density and unit weight of soils using a vibratory table. ASTM D4253-06. West Conshohocken, PA: ASTM.

ASTM. 2007. Standard test method for particle-size analysis of soils.

ASTM D422-07. West Conshohocken, PA: ASTM.

ASTM. 2011a. Method for consolidated drained triaxial compression test for soils. ASTM D7181-11. West Conshohocken, PA: ASTM.

ASTM. 2011b. Standard test methods for consolidated undrained triaxial compression test for cohesive soils. ASTM D4767-11. West Conshohocken, PA: ASTM.

ASTM. 2013. Standard test method for load controlled cyclic triaxial strength of soils. ASTM D5311/D5311M-13. West Conshohocken, PA: ASTM.

Baiser, L. G., and S. D. Glaser. 2000. "Consistency of ground-motion estimates made using system identification." Bulletin of the Seismological Society of America, 90(4), 993–1009.

Barbosa, A. R., Mason, H. B., and Romney, K. 2012. "SSI-Bridge: Soil-bridge interaction during long-duration earthquake." Final project report No. 2012-S-OSU-0008 for Pacific Northwest Transportation Consortium (PacTrans) USDOT University Transportation Center for Federal Region 10, University of Washington.

Bardet, J. P., and W. Choucair. 1991. "A linearized integration technique for incremental constitutive equations." Int. J. Numer. Anal. Methods Geomech. 15 (1): 1–19. https://doi.org/10.1002/nag.1610150102.

Bardet, J. P., Q. Huang, and S. W. Chi. 1993. "Numerical prediction for model no 1." In Proc., Int. Conf. on the Verification of Numerical Procedures for the Analysis of Soil Liquefaction Problems, edited by K. Arulanandan and R. F. Scott, 67–86. Rotterdam, Netherlands: A.A. Balkema.

Barrero, A. R. 2019. "Multi-scale modeling of the response of granular soils under cyclic shearing." Ph.D. thesis, Dept. of Civil Engineering, Univ. of British Columbia.

Beaty, M., and P. M. Byrne. 1998. "An effective stress model for predicting liquefaction behavior of sand." In Vol. 1 of Geotechnical Earthquake Engineering and Soil Dynamics III, 766–777. Reston, VA: ASCE.

Biot, M. A. 1941. "General theory of three-dimensional consolidation." J. Appl. Phys. 12 (2): 155–164. https://doi.org/10.1063/1.1712886.

Boulanger, R. W., C. J. Curras, B. L. Kutter, D. W. Wilson, and A. Abghari. 1999. "Seismic soil-pile-structure interaction experiments and analyses." Journal of Geotechnical and Geoenvironmental Engineering, 125(9), 750–759.

Boulanger, R.W., and K. Ziotopoulou. 2015. "PM4Sand (Version 3): A sand plasticity model for earthquake engineering applications." Rep. No. UCD/CGM-15/01. Davis, CA: Center for Geotechnical Modeling, Univ. of California.

BTL Committee. 1998. "Research report for liquefaction and lateral spreading during the Hyogoken Nanbu earthquake, liquefaction and lateral spreading countermeasure committee for building foundations/" (BTL Committee), March (in Japanese).

Bullock, Z., Z. Karimi, S. Dashti, K. Poter, A. B. Liel, and W. Franke. 2018. "A physics-informed semi-empirical probabilistic model for settlement of shallow-founded structures on liquefiable ground." Geotechnique https://doi.org/10.1680/jgeot.17.P.174.

Byrne, P. 1991. "A cyclic shear-volume coupling and pore-pressure model for sand." In Proc., 2nd Int. Conf. on Recent Advances in Geotechnical Earthquake Engineering and Soil Dynamics, 47–55. Alexandria, VA: National Science Foundation.

Chandra, J., and P. Gueguen. 2017. "Nonlinear response of soil-structure systems using dynamic centrifuge experiments." Journal of Earthquake Engineering, https://doi.org/10.1080/13632469.2017.1398692.

Cook, R. D., D. S. Malkus, M. E. Plesha, and R. J. Witt. 2002. "Concepts and applications of finite element analsyis." 4th Ed. John Wiley & Sons, Inc.

Cooke, H. G., and J. K. Mitchell. 1999. "Guide to remedial measures for liquefaction mitigation at existing highway bridge sites." Technical Report MCEER-99-015, Multidisciplinary Center for Earthquake Engineering Research, Buffalo, NY, 176 pp.

Crisfield, M. A. 1991. "Nonlinear Finite Element Analysis of Solids and Structures. Volume 1: Essentials." Wiley.

Cubrinovski, M., and I. McCahon. 2012. "Short term recovery project 7: CBD foundation damage." Natural Hazards Research Platform, Univ. of Canterbury, Christchurch, New Zealand.

Cuthill, E., and J. McKee. 1969. "Reducing the bandwidth of sparse symmetric matrices." In Proc. 24th Nat. Conf. ACM, pages 157-172.

Dafalias Y. F., and L. R. Herrmann. 1980. "Bounding surface formulation of soil plasticity." Soil Mechanics – Transient and Cyclic Loads, G. Pande and O. C. Zienkiewicz, eds., John Wiley and Sons, Inc. , London, 253-282.

Dafalias, Y. F., and M. T. Manzari. 2004. "Simple plasticity sand model accounting for fabric change effects." J. Eng. Mech. 130 (6): 622–634. https://doi.org/10.1061/(ASCE)0733-9399(2004)130:6(622).

Dafalias, Y. F., and M. Taiebat. 2016. “Sanisand-z: Zero elastic range sand plasticity model.” Géotechnique 66 (12): 999–1013. https://doi.org/10.1680/jgeot.15.P.271.

Darendeli, M. B. 2001. “Development of a new family of normalized modulus reduction and material damping curves.” Ph.D. dissertation, Dept. of Civil, Architectural and Environmental Engineering, Univ. of Texas at Austin.

Dashti, S., J. D. Bray, J. M. Pestana, M. R. Riemer, and D. Wilson. 2010a. “Centrifuge testing to evaluate and mitigate liquefaction-induced building settlement mechanisms.” J. Geotech. Geoenviron Eng. 136 (7):918–929. https://doi.org/10.1061/(ASCE)GT.1943-5606.0000179.

Dashti, S., J. D. Bray, J.M. Pestana, M.R. Riemer, and D. Wilson. 2010b. “Mechanisms of seismically-induced settlement of buildings with shallow foundations on liquefiable soil.” J. Geotech. Geoenviron. Eng., 10.1061/(ASCE)GT.1943-5606.0000179, 151–164.

Dashti, S., J. D. Bray, J. Reilly, S. Glaser, A. Bayen, and E. Mari. 2012. “Evaluating the reliability of mobile phone as seismic monitoring instruments.” Earthquake Spectra, Vol. 30, No. 2, 721-742.

Dashti, S., and Bray, J. D. 2013. “Numerical simulation of building response on liquefiable sand.” J. Geotech. Geoenviron. Eng., 10.1061/(ASCE)GT.1943-5606.0000853, 1235–1249.

Deng, L., B. L. Kutter, S. Kunnath, and T. B. Algie. 2010. “Performance of bridge systems with nonlinear soil-footing-structure interactions.” Soil-Foundation-Structure Interaction – Orense, Chouw & Pender (eds). Taylor and Francis Group, London, ISBN 978-0-415-60040-8

Detournay, E., and A. D. Cheng. 1993. “Fundamentals of poroelasticity.” In Chap. 5, Vol. 2 of Comprehensive rock engineering, 113–171. Oxford, UK: Pergamon Press.

Drnevich, V. P., and F. E. Richart Jr. 1970. “Dynamic prestraining of dry sands.” J. Soil Mech. Found. Div. 96 (SM2): 453–469.

Duncan, J.M. and Chang, C.M. 1970. “Nonlinear analysis of stress and strain in soils.” Journal of Soil Mechanics and Foundations Division, ASCE, 96(SM5), 1629-1653.

Ekstrom, L. T., and K. Ziotopoulou. 2017. “Seismic response of liquefiable sloping ground: Validation of class B predictions against the LEAP centrifuge tests.” In Proc., Geotechnical Frontier 2017, GSP 281. Roseville, MN: Industrial Fabrics Association International.

Elgamal, A., E. Parra, Z. Yang, R. Dobry, and M. Zeghal. 1998. “Liquefaction constitutive model.” In Proc., Int. Workshop on the Physics and Mechanics of Soil Liquefaction, edited by P. Lade. Baltimore: A.A. Balkema.

Elgamal, A., Z. Yang, and E. Parra. 2002. “Computational modeling of cyclic mobility and post-liquefaction site response.” Soil Dyn. Earthquake Eng. 22 (4): 259–271. https://doi.org/10.1016/S0267-7261(02)00022-2.

EPRI, Electric Power Research Institute. 1993. Guidelines for determining design basis ground motions. Final Rep. No. TR-102293, Palo Alto, CA.

Finn, W. D. L., M. Yogendrakumar, and N. Yoshida. 1986. TARA-3: A program to compute the seismic response of 2-D embankments and soil–structure interaction systems to seismic loadings. Vancouver, BC, Canada: Dept. of Civil Engineering, Univ. of British Columbia.

Fudo Construction Co, Ltd., 1995. "1995 Hyogoken Nambu earthquake preliminary research report." Fudo Construction Co. Ltd., March (in Japanese).

GEER, Geotechnical Earthquake Engineering Reconnaissance. 2011. "Geotechnical Reconnaissance of the 2011 Christuchurch, New Zealand earthquake." Editors M. Cubrinovski, R. A. Green, L. Wotherspoon.

Gelagoti, F., Kourkoulis, R., Anastasopoulos, I., and Gazetas, G. 2012. "Rocking isolation of low-rise frame structures founded on isolated footings." Earthquake Eng. Struct. Dyn., 41(7), 1177–1197.

Ghaboussi, J. and H. Momen. 1982. "Modeling and analysis of cyclic behavior of sands." G. N. Pande and O. C. Zienkiewicz (eds), Soil Mechanics-Transient and Cyclic Loads, Wiley, New York, 313-342.

Ghofrani, A., and P. Arduino. 2016. "Prediction of LEAP centrifuge tests results using a pressure-dependent bounding surface constitutive model." Soil Dyn. Earthquake Eng., in press. https://doi.org/10.1016/j.soildyn.2016.12.001.

Giuffrè, A., and P. E. Pinto. 1970. "Il comportamento del cemento armato per sollecitazioni cicliche di forte intensità." Giornale del Genio Civile, 5(1): 391-408.

Hamada, M., R. Isoyama, and K. Wakamatsu. 1995. "The 1995 Hyogoken Nanbu (Kobe) earthquake, liquefaction ground displacement and soil condition in Hanshin area." Association for development of earthquake prediction, Japan.

Hardin, B. O. 1965. "Dynamic versus static shear modulus for dry sand." Mater. Res. Stand. 5 (5): 232–235.

Hardin, B. O., and V. P. Drnevich. 1972. "Shear modulus and damping in soils: Design equations and curves." J. Soil Mech. Found. Div.98 (SM 7): 667–692.

Hashash, Y. M. A., S. Dashti, M. I. Romero, M. Ghayoomi, and M. Musgrove. 2015. "Evaluation of 1-D seismic site response modeling of sand using centrifuge experiments." Soil Dyn. Earthquake Eng.78: 18–31.

Hashash, Y. M. A., and D. Park. 2001. "Nonlinear one-dimensional seismic ground motion propagation in the Mississippi embayment." Eng. Geol. 62 (1–3): 185–206. https://doi.org/10.1016/S0013-7952(01)00061-8.

Hausler, E.A. 2002. "Influence of ground improvement on settlement and liquefaction: a study based on field case history evidence and dynamic geotechnical centrifuge tests." Ph.D. dissertation. Berkeley, University of California.

Head, K. H. 1998. "Manual of soil laboratory testing." Vol. 3 of Effective stress tests. 2nd Ed. Hoboken, NJ: Wiley.

Howell, R., E. M. Rathje, and R. W. Boulanger. 2015. "Evaluation of simulation models of lateral spread sites treated with prefabricated vertical drains." J. Geotech. Geoenviron. Eng. 141 (1): 04014076. https://doi .org/10.1061/(ASCE)GT.1943-5606.0001185.

Idriss, I. M., and R. W. Boulanger. 2008. "Soil liquefaction during earthquakes." Monograph MNO-12. Earthquake Engineering Research Institute, Oakland, CA, 261 pp.

Ishihara, K. 1985. "Stability of natural deposits during earthquakes." Proc. of the 11th International Conf. on Soil Mechanics and Foundation Engineering, San Francisco, 1:321-376.

JGS, Japanese Geotechnical Society. 1996. "Remedial measures against soil liquefaction." Rotterdam: A.A. Balkema.

Jones, K. C. 2013. "Dynamic soil-structure analysis of structures in dense urban environments." Ph.D. Thesis. University of California Berkeley.

Kamalzare, S. 2016. "Performance of columnar reinforced ground during seismic excitation." Doctoral Thesis. Virginia Polytechnic Institute and State University.

Kammerer, A., J. Wu, M. Riemer, J. Pestana, and R. Seed. 2004. "Anew multi-directional simple shear testing database." In Proc., 13th World Conf. on Earthquake Engineering. Ottawa: Canadian Association for Earthquake Engineering.

Karimi, Z., and S. Dashti. 2016a. "Numerical and centrifuge modeling of seismic soil-foundation-structure interaction on liquefiable ground." J. Geotech. Geoenviron. Eng. 142 (1): 04015061. https://doi.org/10.1061/(ASCE)GT.1943-5606.0001346.

Karimi, Z., and S. Dashti. 2016b. "Seismic performance of shallow founded structures on liquefiable ground: Validation of numerical simulations using centrifuge experiments." J. Geotech. Geoenviron. Eng. 142 (6):04016011. https://doi.org/10.1061/(ASCE)GT.1943-5606.0001479.

Khosravifar, A., A. Elgamal, J. Lu, and J. Li. 2018. "A 3D model for earthquake-induced liquefaction triggering and post-liquefaction response.". Soil Dyn. And Earthquake Eng. 110: 43-52. https://doi.org/10.1016/j.soildyn.2018.04.008.

Kirkwood, P., and S. Dashti. 2018. "A centrifuge study of seismic structure-soil- structure interaction on liquefiable ground and implications for design in dense urban areas." Earthquake Spectra, in press. https://doi.org/10.1193/052417EQS095M.

Kirkwood, P., and S. Dashti. 2019. "Influence of prefabricated vertical drains on the seismic performance of similar neighbouring structures founded on liquefiable deposits." Geotechnique https://doi.org/10.1680/jgeot.17.P.077.

Ko, H. Y. 1988. "The Colorado centrifuge facility." In Proc., Centrifuge 88, edited by J. F. Corte, 73–75. Rotterdam, Netherlands: A.A. Balkema.

Kramer, S., and P. Arduino. 1999. "Constitutive modeling of cyclic mobility and implications for site response." In Vol. 3 of Proc., 2nd Int. Conf. Earthquake Geotechnical Engineering, edited by P. S. Sêco e Pinto, 1029–1034. Rotterdam, Netherlands: A.A. Balkema.

Kuriki, A. S. Tamura, Y. Zhou, and K. Tokimatsu. 2012. “Centrifugal model tests of liquefaction countermeasure for existing houses.” Proc. 47th J.G.S. Conf. .Hachinohe, Japan, 1497-1498

Kutter, B. L., T. J. Carey, T. Hashimoto, M. T. Manzari, A. Vasko, M. Zeghal, and R. J. Armstrong. 2015. “LEAP database for verification, validation, and calibration of codes for simulation of liquefaction.” In Proc., 6th Int. Conf. on Earthquake Geotechnical Engineering. Christchurch, New Zealand: International Society for Soil Mechanics and Geotechnical Engineering.

Kwok, A. O. L., J. P. Stewart, Y. M. A. Hashash, N. Matasovic, R. Pyke, Z. Wang, and Z. Yang. 2007. “Use of exact solutions of wave propagation problems to guide implementation of nonlinear seismic ground response analysis procedures.” J. Geotech. Eng. 133 (11): 1385–1398.

Lade, P. V. 1977. “Elasto-plastic stress-strain theory for cohesionless soil with curved yield surfaces.” Int. J. Solids Structures, Vol 13, pp. 1019-1035.

Lambe, T.W. 1973. “Predictions in soil engineering.” 13th Rankine Lecture, Geotechnique, 23(2): 149-202. https://doi.org/10.1680/geot.1973.23.2.151.

Laursen, T. A. and J. C. Simo. 1993. “A Continuum-based Finite Element Formulation for the Implicit Solution of Multibody, Large Deformation Frictional Contact Problems.” Int. J. Numer. Methods Eng, 36, 3451-3485.

Li, X. S., and Y. Wang. 1998. “Linear representation of steady-state line for sand.” J. Geotech. Geoenviron. Eng. 124 (12): 1215–1217. https://doi.org/10.1061/(ASCE)1090-0241(1998)124:12(1215).

Li, X. S., and Y. F. Dafalias. 2012. “Anisotropic critical state theory: Role of fabric.” J. Eng. Mech. 138 (3): 263–275. https://doi.org/10.1061/(ASCE)EM.1943-7889.0000324.

Liu, L., and R. Dobry. 1997. “Seismic response of shallow foundation on liquefiable sand.” J. Geotech. Geoenviron. Eng., 123_6_, 557–567.

Liu, W., and T. C. Hutchinson. 2018. “Numerical investigation of stone columns as a method for improving the performance of rocking foundation systems.” Soil Dynamics and Earthquake Engineering. 106:60-69. https://doi.org/10.1016/j.soildyn.2017.10.015.

Lopez-Caballero, F., and Farahmand-Razavi, A. M. 2008. “Numerical simulation of liquefaction effects on seismic SSI.” Soil Dyn. Earthquake Eng., 28(2), 85–98.

Luque, R., and J. D. Bray. 2017. “Dynamic analyses of two buildings founded on liquefiable soils during the Canterbury earthquake sequence.” J. Geotech. Geoenviron. Eng. 143(9). DOI: 10.1061/(ASCE)GT.1943-5606.0001736

Manzari, M. T., and K. Arulanandan. 1993. “Numerical predictions for model no. 1.” In Verification of numerical procedures for the analysis of soil liquefaction problems, edited by K. Arulanandan and R. F. Scott, 179–185. Rotterdam, Netherlands: A.A. Balkema.

Manzari, M. T., and Y. F. Dafalias. 1997. “A critical state two-surface plasticity model for sands.” Géotechnique 47 (2): 255–272. https://doi.org/10.1680/geot.1997.47.2.255.

Matasovic, N., and M. Vucetic. 1993. "Cyclic characterization of liquefiable sands." J. Geotech. Eng. 119 (11): 1805–1822. https://doi.org/10.1061/(ASCE)0733-9410(1993)119:11(1805).

Mazzoni, S., F. McKenna, M. Scott, and G. Fenves. 2006. "Open system for earthquake engineering simulation user command-language." Berkeley, CA: Network for Earthquake Engineering Simulations.

McGann, C. R., P. Arduino, and P. Mackenzie-Helnwein. 2015. "A stabilized single-point finite element formulation for three-dimensional dynamic analysis of saturated soils." Comput. Geotech. 66: 126–141. https://doi.org/10.1016/j.compgeo.2015.01.002.

McKenna, F., G. L. Fenves., M. H. Scott, and B. Jeremic. 2000. "Open system for earthquake engineering simulation (opensees)." Technical Report Pacific Earthquake Engineering Research Center, University of California Berkeley.

McKenna, F., M. H. Scott, and G. L. Fenves. 2010. "Nonlinear finite-element analysis software architecture using object composition." Journal of Computing in Civil Engineering. DOI: 10.1061/_ASCE_CP.1943-5487.0000002

Menq, F. Y. 2003. "Dynamic properties of sandy and gravelly soils." Ph.D. dissertation, Dept. of Civil, Architectural and Environmental Engineering, Univ. of Texas at Austin.

Mitchell, J. K., and F. J. Wentz. 1991. "Performance on improved ground during the Loma Prieta earthquake." University of California, Berkeley, Earthquake Engineering Research Center Report No. UCB/EERC-91/12, October.

Mitrani, H., and S. P. G. Madabhushi. 2013. "Geomembrane containment walls for liquefaction remediation". Proceedings of the Institution of Civil Engineers: Ground Improvement, 166. pp. 9-20. ISSN 1755-0750.

Mroz, Z., V. A. Norris, and O. C. Zienkiewicz. 1981. "An anisotropic, critical state model for soils subjects to cyclic loading." Geotechnique, London, England, 31(4), 451-469.

Nakakita, Y., and Y. Watanabe. 1981. "Soil stabilization by preloading in Kobe Port Island." Proc. 9th Intl. Cong. On Soil Mechanics and Foundation Engineering, Tokyo, 611-622.

Newmark, N. M. 1959. "A method of computation for structural dynamics." J. Eng. Mech. Div. 85 (3): 67–94.

Olarte, J., B. Paramasivam, S. Dashti, A. Liel, and J. Zannin. 2017. "Centrifuge modeling of mitigation-soil-foundation-structure interaction on liquefiable ground." Soil Dyn. Earthquake Eng. 97: 304–323. https://doi.org/10.1016/j.soildyn.2017.03.014.

Olarte, J., S. Dashti, and A. Liel. 2018a. "Can ground densification improve seismic performance of the soil-foundation-structure system on liquefiable soils." Earth. Eng. Struct. Dyn. : 1–19. https://doi: 10.1002/eqe.3012.

Olarte, J., S. Dashti, A. Liel, and B. Paramasivam. 2018b. "Effects of drainage control on densification as a liquefaction mitigation technique." Soil Dynamics and Earthquake Engineering. 110:21-231 https://doi.org/10.1016/j.soildyn.2018.03.018.

Papadimitriou, A. G., G. D. Bouckovalas, and Y. F. Dafalias. 2001. “Plasticity model for sand under small and large cyclic strains.” Journal of Geotechnical and Geoenvironmental Engineering, ASCE, 127, no. 11, 973-983.

Papadimitriou, A. G., and G. D. Bouckovalas. 2002. “Plasticity model for a sand under small and large cyclic strains: a multiaxial formulation.” Soil Dynamics and Earthquake Engineering 22:191-204.

Park, S., and Byrne, P. 2004. “Practical constitutive model for soil liquefaction, in ‘Proc., 9th Int. Symp. On Numerical Models in Geomechanics (NUMOG IX)’, CRC Press, Boca Raton, FL, pp. 181–186.

Paramasivam, B. 2018. “Influence of traditional and innovative liquefaction mitigation strategies on the performance of soil-structure systems, considering soil heterogeneity”. Ph.D. Thesis. University of Colorado Boulder.

Paramasivam, B., S. Dashti, A. Liel. 2018. “Influence of prefabricated vertical drains on the seismic performance of structures founded on liquefiable soils”. J. Geotech. Geoenvirom. Eng. 144(10):04018070. https://ascelibrary.org/doi/abs/10.1061/(ASCE)GT.1943-5606.0001950

Paramasivam, B., S. Dashti, and A. Liel. 2019. “Impact of spatial variations in permeability of liquefiable deposits on the seismic performance of structures and effectiveness of drains”. J. Geotech. Geoenvirom. Eng., (Accepted)

Parra, E. 1996. “Numerical modeling of liquefaction and lateral ground deformation including cyclic mobility and dilation response in soil system.” Ph.D. thesis. Dept. of Civil Engineering, Rensselaer Polytechnic Institute.

Pestana, J. M., C. E. Hunt, and R. R. Goughnour. 1997. “FEQDrain: A finite element computer program for the analysis of the earthquake generation and dissipation of pore water pressure in layered sand deposits with vertical drains.”. Earthquake Engineering Research Center, Report No. EERC 97-15.

Petracca, M., F. Candeloro, and G. Camata. 2017. “STKO user manual.” ASDEA Software Technology, Pescara Italy.

Phillips, C., Y. M. A. Hashash, S. M. Olson, and M. R. Muszynski. 2012. “Significance of small strain damping and dilation parameters in numerical modeling of free-field lateral spreading centrifuge tests.” Soil Dyn Earthq Eng 2012;42:161–76. http://dx.doi.org/10.1016/j.soildyn.2012.06.001.

Popescu, R., and J. H. Prevost. 1993. “Centrifuge validation of a numerical model for dynamic soil liquefaction.” Soil Dynamics and Earthquake Engineering 12:73-90 DOI: 10.1016/0267-7261(93)90047-U.

Popescu, R., and J. H. Prevost. 1995a. “Comparison between VELACS numerical ‘class A’' predictions and centrifuge experimental soil test results.” Soil Dynamics and Earthquake Eng., 14(2):79-92.

Popescu, R., J. H. Prevost, G. Deodatis, and P. Chakrabortty. 2006. "Dynamics of nonlinear porous media with applications to soil liquefaction." Soil Dynamics and Earthquake Engineering 26:648-665.

Prevost, J. H. 1978. "Plasticity Theory for soil stress-strain behavior." Journal Eng. Mech. Div. ASCE, Vol. 104, No. EM5. 1177-1194.

Prevost, J. H. 1985. "A simple plasticity theory for frictional cohesionless soils." Soil Dyn. Earthquake Eng. 4 (1): 9–17. https://doi.org/10.1016/0261-7277(85)90030-0.

Puebla, H., P. M. Byrne, and R. Philips. 1997. "Analysis of CANLEX liquefaction embankments: Prototype and centrifuge models." Can. Geotech. J., 34(5), 641–657.

Rahmani, A. 2014. "Three dimensional nonlinear analysis of dynamic soil-pile-structure interaction for bridge systems under earthquake shakings." Ph. D. Thesis. The University of British Columbia.

Ramirez, J., A. R. Barrero, L. Chen, A. Ghofrani, S. Dashti, M. Taiebat, and P. Arduino. 2017. "Seismic performance of a layered liquefiable site: Validation of numerical simulations using centrifuge modeling." In Geotechnical Frontiers 2017, Geotechnical Special Publication 281 Reston, VA: ASCE.

Ramirez, J., A. R. Barrero, L. Chen, A. Ghofrani, S. Dashti, M. Taiebat, and P. Arduino. 2018. "Site response in a layered liquefiable deposit: Evaluation of different numerical tools and methodologies with centrifuge experimental results." ". J. Geotech. Geoenvirom. Eng. 144(10):04018073. https://doi.org/10.1061/(ASCE)GT.1943-5606.0001947.

Rasouli, R. T. Akima, V. Awad, S. Tan, and I. Towhata. 2015. "3-D Experiments on performance of mitigation against liquefaction-induced subsidence of surface structures." International Symposium on earthquake Engineering, JAEE, Vol2.

Seed, H. B., and I. M. Idriss. 1970. "Soil moduli and damping factors for dynamic response analyses." Technical Rep. No. EERRC-70-10, Berkeley, CA: Univ. of California.

Seed, R. B., K. O. Cetin., R. E. S. Moss, A. M. Kammerer, J. Wu, J. M. Pestana, M. F. Riemer, R. B. Sancio, J. D. Bray, R. E. Kayen, and A. Faris. 2003. "Recent advances in soil liquefaction engineering: A unified and consistent framework." 26th Annual ASCE Los Angeles Geotechnical Spring Seminar, ASCE.

Scott, M. H., and G. L. Fenves. 2006. "Plastic hinge integration methods for force-based-beam-column elements." J. of Structural Eng. ASCE. https://doi.org/0.1061/_ASCE_0733-9445_2006_132:2_244.

Shahir, H., A. Pak, M. Taibeat, and B. Jeremic. 2012. "Evaluation of variation of permeability in liquefiable soil under earthquake loading." Comput. Geotech. 40: 74–88. https://doi.org/10.1016/j.compgeo.2011.10.003.

Shibata, T., F. Oka, and Y. Ozawa. 1996. "Characteristics of ground deformation due to liquefaction." Soils and Foundations, Special issue on the geotechnical aspects of the January 17 1995 Hyogoken-Nambu earthquake, January, 65-79.

Skempton, A.W. 1954. "The pore-pressure coefficients A and B." Géotechnique 4 (4): 143–147.

Stewart, D. P., Y. R. Chen, and B. L. Kutter. 1998. "Experience with the use of methylcellulose as a viscous pore fluid in centrifuge models. Geotech. Test. J. 21 (4): 365–369. https://doi.org/10.1520/GTJ11376J.

Taiebat, M., and Y. F. Dafalias. 2008. "SANISAND: Simple anisotropic sand plasticity model." Int. J. Numer. Anal. Methods Geomech. 32 (8): 915–948. https://doi.org/10.1002/nag.651.

Taiebat, M., H. Shahir, and A. Pak. 2007. "Study of pore pressure variation during liquefaction using two constitutive models for sand." Soil Dyn. Earthquake Eng. 27 (1): 60–72. https://doi.org/10.1016/j.soildyn.2006.03.004.

Taiebat, M., Y. F. Dafalias, A. M. Kaynia, and Z. Cheng. 2010. "Propagation of seismic waves through liquefied soils." Soil Dyn. Earthquake Eng. 30 (4): 236–257. https://doi.org/10.1016/j.soildyn.2009.11.003.

Takemura, J., R. Igarashi, N. komatsumoto, and M. Okamura. 2009. "Soil desaturation by ground water lowering as a liquefaction countermeasure." Int. J. Physical Modelling in Geotechnics.

Tasiopoulou, P., N. Gerolymos, and G. Gazetas. 2015a "Class A prediction for seismic centrifuge modeling of multi-block quaywall: Undrained (PLAXIS) versus coupled (FLAC) effective stress analysis." In Proc., 5th ECCOMAS Thematic Conf. on Computational Methods in Structural Dynamics and Earthquake Engineering. Barcelona, Spain: European Community on Computational Methods in Applied Sciences.

Tasiopoulou, P., M. Taiebat, N. Tafazzoli, and B. Jeremic. 2015b. "Solution verification procedures for modeling and simulation of fully coupled porous media: Static and dynamic behavior." Coupled Syst. Mech. 4 (1): 67–98. https://doi.org/10.12989/csm.2015.4.1.067.

Tsai, C-C., D. Park, and C-W Chen. 2014. "Selection of the optimal frequencies of viscous damping formulation in nonlinear time-domain site response analysis." Soil Dynamics and Earthquake Engineering. 67:353-358. http://dx.doi.org/10.1016/j.soildyn.2014.10.026.

Tsegaye, A. 2010. "Plaxis liquefaction model. Report no. 1." PLAXIS knowledge base.

Valanis, K. C. 1982. "An endochronic geomechanical model for soils." IUTAM Conference of Deformation and Failuer of Granular Materials. Delft. Vermeer and Luger Delft (eds), Balkema, pp. 159-165.

Vytiniotis, A. 2012. "Contributions to the analysis and mitigation of liquefaction in loose sand slopes." Ph.D. Thesis. Massachusetts Institute Technology.

Vytiniotis A., and A. J. Whittle. 2017. "Analysis of PV drains for mitigation of seismically-induced ground deformations in sand slopes." Journal of Geotechnical and Geoenvironmental Engineering, 10.1061/(ASCE)GT.1943-5606.0001722.

Wang, G. and N. Sitar. 2004. "Numerical analysis of piles in elasto-plastic soils under axial loading." 17th ASCE Engineering Mechanics Conf. University of Delaware, Newark, DE, June 13-16.

Wang, G. and N. Sitar. 2006. “Nonlinear analysis of a oisl-drilled pier system under static and dynamic axial loading.” Technical Report Pacific Earthquake Engineering Research Center, University of California Berkeley.

Wang, G., and N. Sitar. 2011. “Static and dynamic axial response of drilled piers. II: Numerical simulation.” Journal of Geotechnical and Geoenvironmental Engineering. DOI: 10.1061/(ASCE)GT.1943-5606.0000548.

Watanabe, T. 1966. “Damage to oil refinery plans and a building on compacted ground by the Niigata earthquake and their restoration.” Soil and Foundation, Vol. VI, No.2. The Japanese Society of Soil Mechanics and Foundation Engineering, March, 86-99.

Wriggers, P., and G. Zavarise. 2004. “Chapter 6. Computational contact mechanics.” Encyclopedia of Computational Mechanics, Ed. By Erwin Stein, Rene de Borst and Thomas J. R. Hughes, Vol. : Solids and Structures.

Wotherspoon, L. M., R. P. Orense, M. Jacka, R. A. Green, B. R. Cox, and C. M. Wood. 2014. “Seismic performance of improved ground sites during the 2010-2011 Canterbury earthquake sequence.” Earthquake Spectra, Vol. 30, No. 1, pages 111-129. Earthquake Engineering Research Institute

Yang, Z., and A. Elgamal. 2000. Numerical modeling of earthquake site response including dilation and liquefaction. Structural Systems Research Project Rep. No. SSRP-2000/01. San Diego: Dept. of Structural Engineering, Univ. of California.

Yang, Z., A. Elgamal, and E. Parra. 2003. “Computational model for cyclic mobility and associated shear deformation.” J. Geotech. Geoenviron. Eng. 129 (11): 1119–1127. https://doi.org/10.1061/(ASCE)1090-0241(2003)129:12(1119).

Yang, Z., J. Lu, and A. Elgamal. 2008. OpenSees soil models and solid fluid fully coupled elements: User’s manual. San Diego: Dept. of Structural Engineering, Univ. of California.

Yasuda, S. K. Ishihara, K. Harada, and N. Shinkawa. 1996. “Effects of soil improvement on ground subsidence due to liquefaction.” Soil and Foundations, Special issue on the geotechnical aspects of the January 17 1995 Hyogoken-Nambu earthquake, January, 99-107.

Youd, T., I. Idriss, R. Andrus, I. Arango, G. Castro, J. Christian, R. Dobry., W. Finn, J. L. Harder, M. Hynes, K. Ishihara, J. Koester, S. Liao, W. III Marcuson, G. Martin, J. Mitchell, Y. Moriwaki, M. Power, P. Robertson, R. Seed, and K. II. Stokoe. 2001. “Liquefaction resistance of soils: Summary report from the 1996 NCEER and 1998 NCEER/NSF workshops on evaluation of liquefaction resistance of soils.” J. Geotech. Geoenviron. Eng. 127, 817–833.

Yoshimi, Y., and K. Tokimatsu. 1977. “Settlement of buildings on saturated sand during earthquakes.” Soils Foundations, 17(1), 23–38.

Zeghal, M., and A. Elgamal. 1998. “Analyses of site liquefaction using downhole array seismic records.” In Proc., 11th World Conf. on Earthquake Engineering. Oxford, UK: Elsevier.

Zienkiewicz, O. C., and T. Shiomi. 1984. “Dynamic behavior of saturated porous media, the generalized Biot formulation and its numerical solution.” Int. J. Numer. Methods Geomech. 8 (1): 71–96. https://doi.org/10.1002/nag.1610080106.

Ziotopoulou, K. 2016. “Seismic response of liquefiable sloping ground: Class A and C numerical predictions of centrifuge model responses.” Soil Dyn. Earthquake Eng., in press. https://doi.org/10.1016/j.soildyn.2017.01.038.

APPENDIX A

Appendices A, B, and C show the data and results concerned with the calibration of soil parameters shown in Chapter 3.

Table A1. Summary of soil sample properties in drained and undrained triaxial tests

Isotropically Consolidated Monotonic Drained Triaxial Tests						
No.	$\sigma_c^{'}$ **(kPa)**	$e_{A.C}$	γ_{dry} **(kN/m³)**	γ_{sat} **(kN/m³)**	**D_r (%)**	ϕ_p
1	100	0.699	19.34	15.30	40	32.3
2	200	0.702	19.32	15.28	39	32.4
3	300	0.697	19.35	15.32	40	32.0
4	100	0.557	20.21	16.70	90	42.1
5	200	0.551	20.25	16.777	92	41.8
6	300	0.549	20.26	16.79	93	41.5
7	100	0.646	19.65	15.80	59	36.1
8	200	0.640	19.68	15.85	61	35.4
9	300	0.635	19.71	15.90	62	34.8
Isotropically Consolidated Monotonic Undrained Triaxial Tests						
No.	$\sigma_c^{'}$ **(kPa)**	$e_{A.C}$	γ_{dry} **(kN/m³)**	γ_{sat} **(kN/m³)**	**D_r (%)**	ϕ_{PT}
5	50	0.704	19.31	15.25	38	25.1-31.2
3	100	0.695	19.36	15.34	41	28.3-29.3
4	200	0.694	19.37	15.35	41	28.8-30.4
6	50	0.559	20.19	16.67	89	22.2-25.3
7	100	0.558	20.20	16.68	90	23.1-28.5
8	200	0.553	20.23	16.74	92	22.7-28.4
9	50	0.647	19.64	15.79	58	25.1-28.5
10	100	0.639	19.68	15.86	61	24.5-30.0
11	200	0.634	19.71	15.91	63	25.5-29.6

Isotropically Consolidated Cyclic Undrained Triaxial Tests					
No.	$\sigma_c^{'}$ **(kPa)**	ε **(%)**	γ **(%)**	**N_{cycles} (r_u≈0.99)**	**D_r (%)**
2	100	0.070	0.105	20	37
3	100	0.150	0.225	7	37
4	100	0.220	0.330	3	38
8	100	0.042	0.063	38	41
1	100	0.070	0.105	200	91
5	100	0.440	0.660	7	89
6	100	0.063	0.095	285	90
7	100	0.210	0.315	40	90
9	100	0.070	0.105	40	59
10	100	0.140	0.210	23	58
11	100	0.225	0.338	10	61
12	100	0.290	0.435	6	57

$\sigma_c^{'}$: isotropic consolidation stress; $e_{A.C}$: void ratio after consolidation; γ_{dry}: dry unit weight; γ_{sat}: saturated unit weight; D_r: relative density; ϕ_p: peak friction angle; ϕ_{PT}: phase transformation angle; ε: axial strain ; γ: shear strain.

APPENDIX B

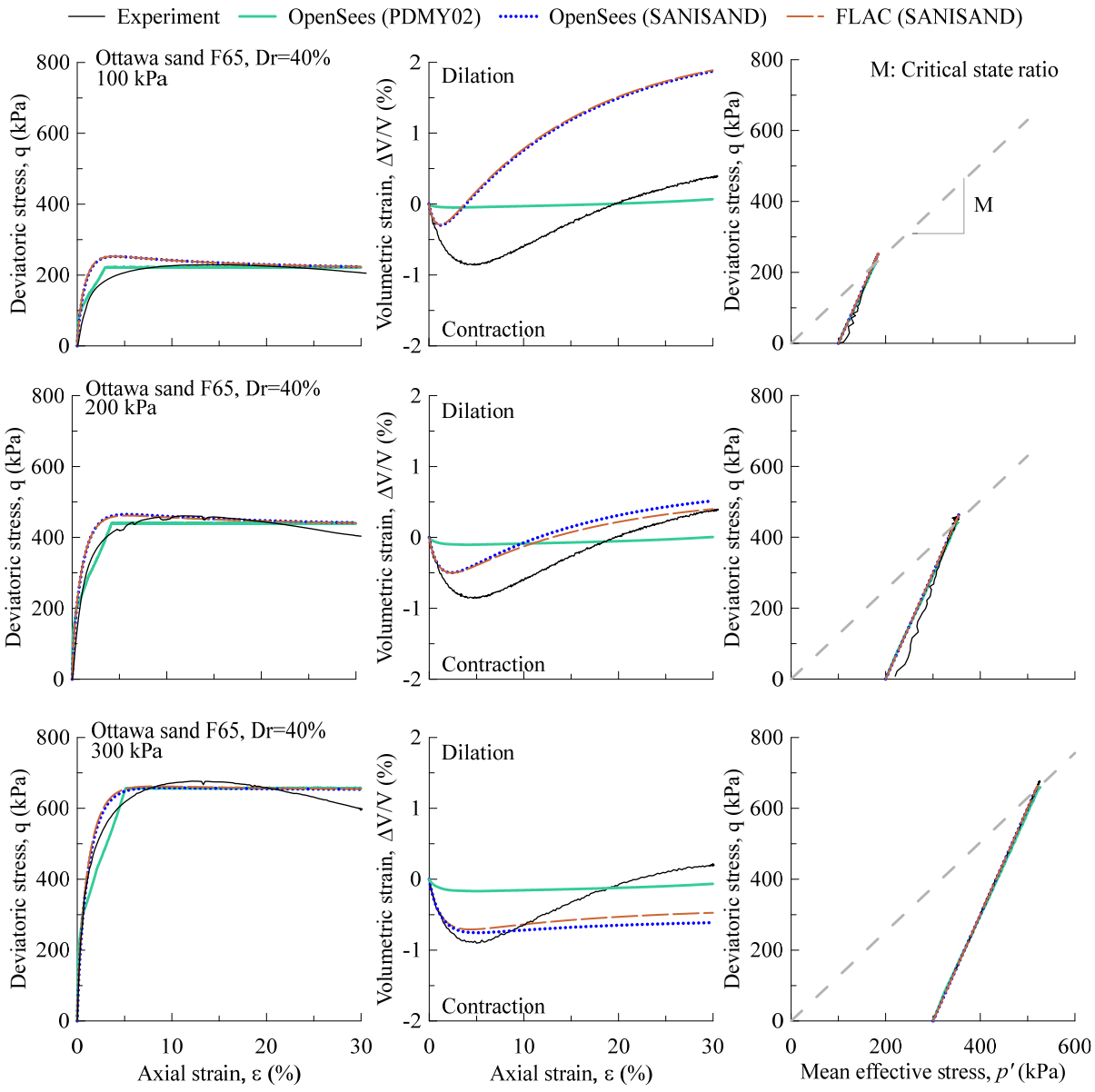

Figure B1. Comparison between experimental monotonic drained triaxial tests and numerical (Calibration C) simulated response for Ottawa sand F65 (D_r = 40%)

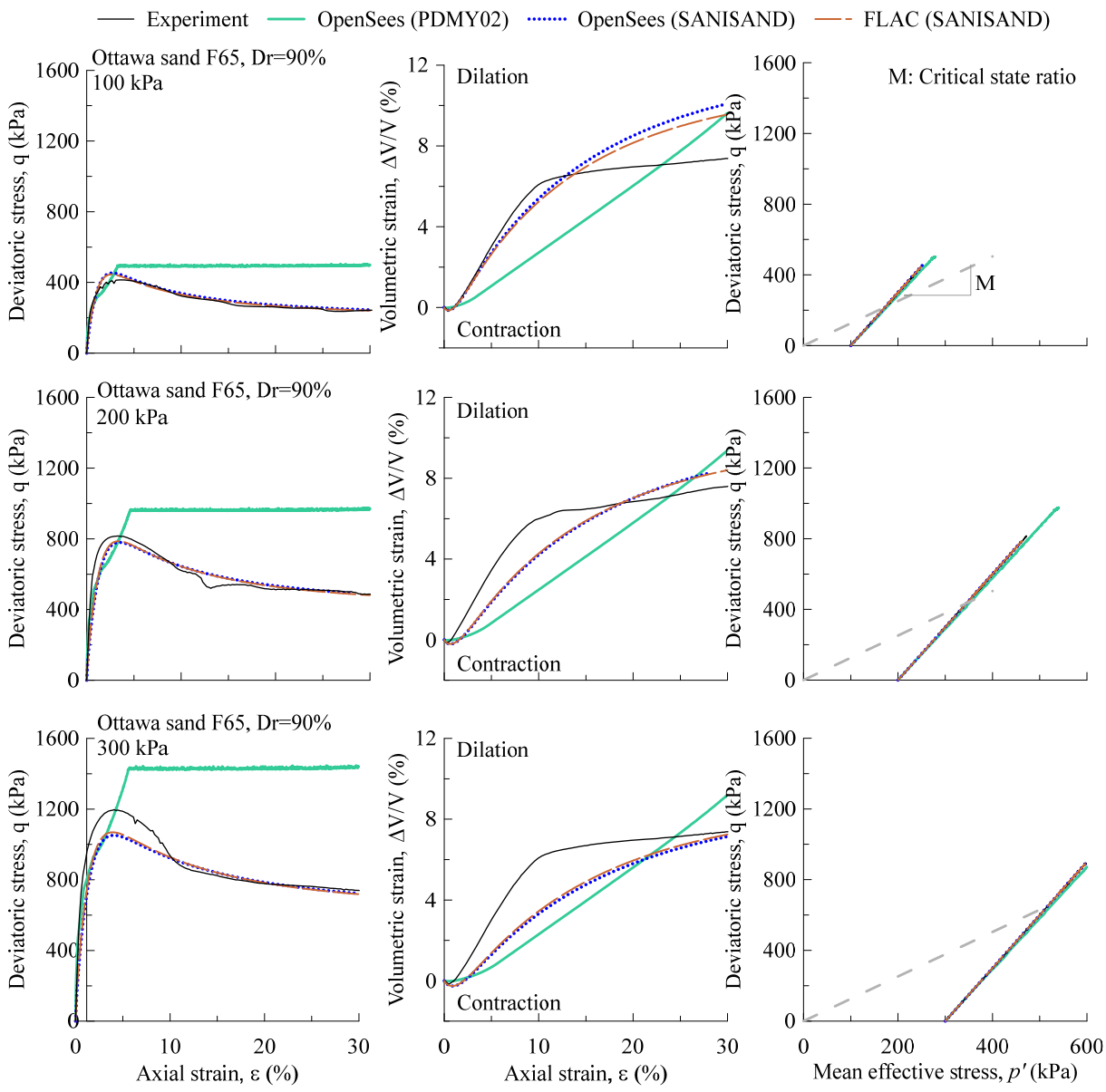

Figure B2. Comparison between experimental monotonic drained triaxial tests and numerical (Calibration C) simulated response for Ottawa sand F65 (D_r = 90%)

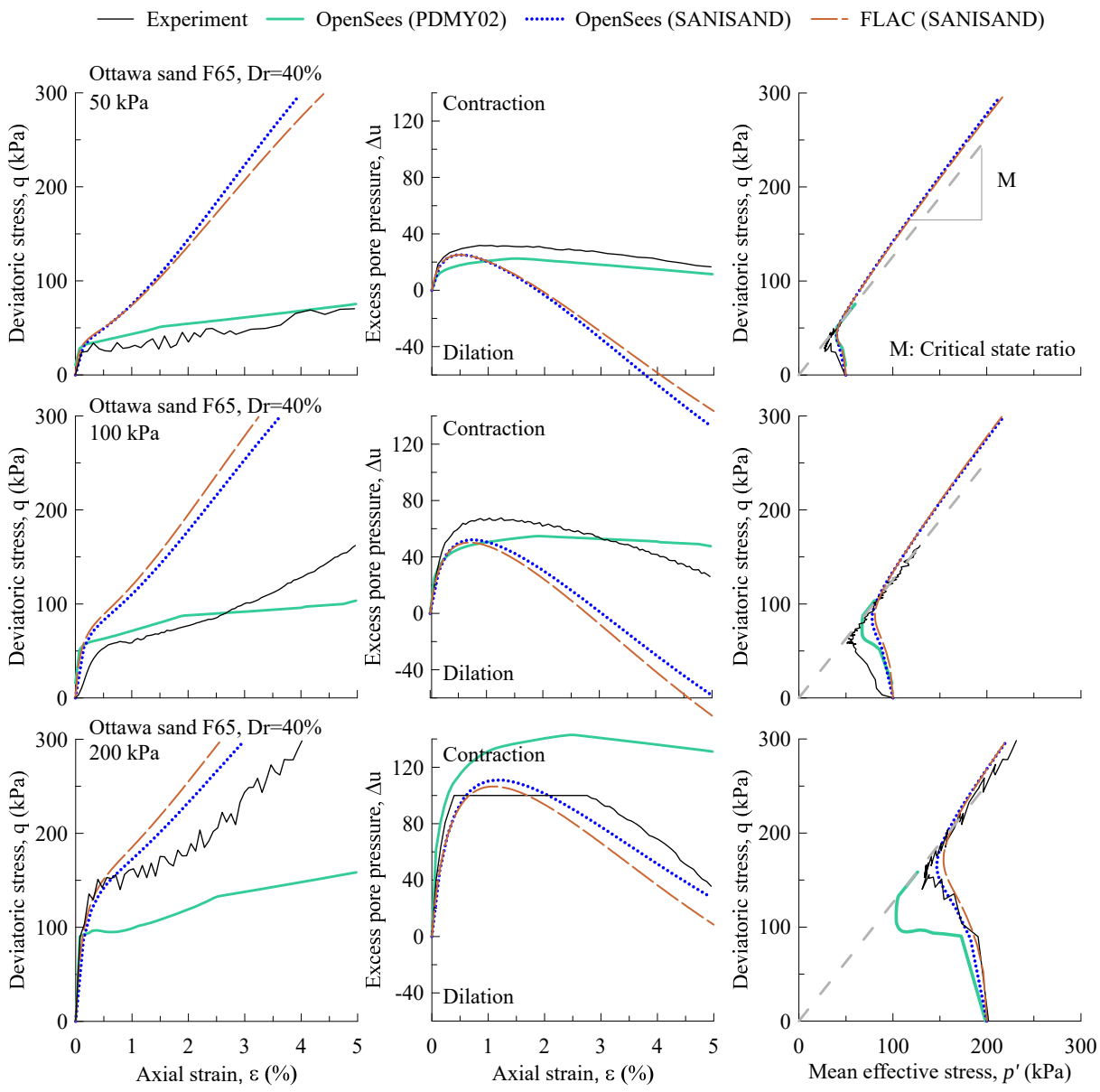

Figure B3. Comparison between experimental monotonic undrained triaxial tests and numerical (Calibration C) simulated response for loose Ottawa sand F65 (D_r = 40%)

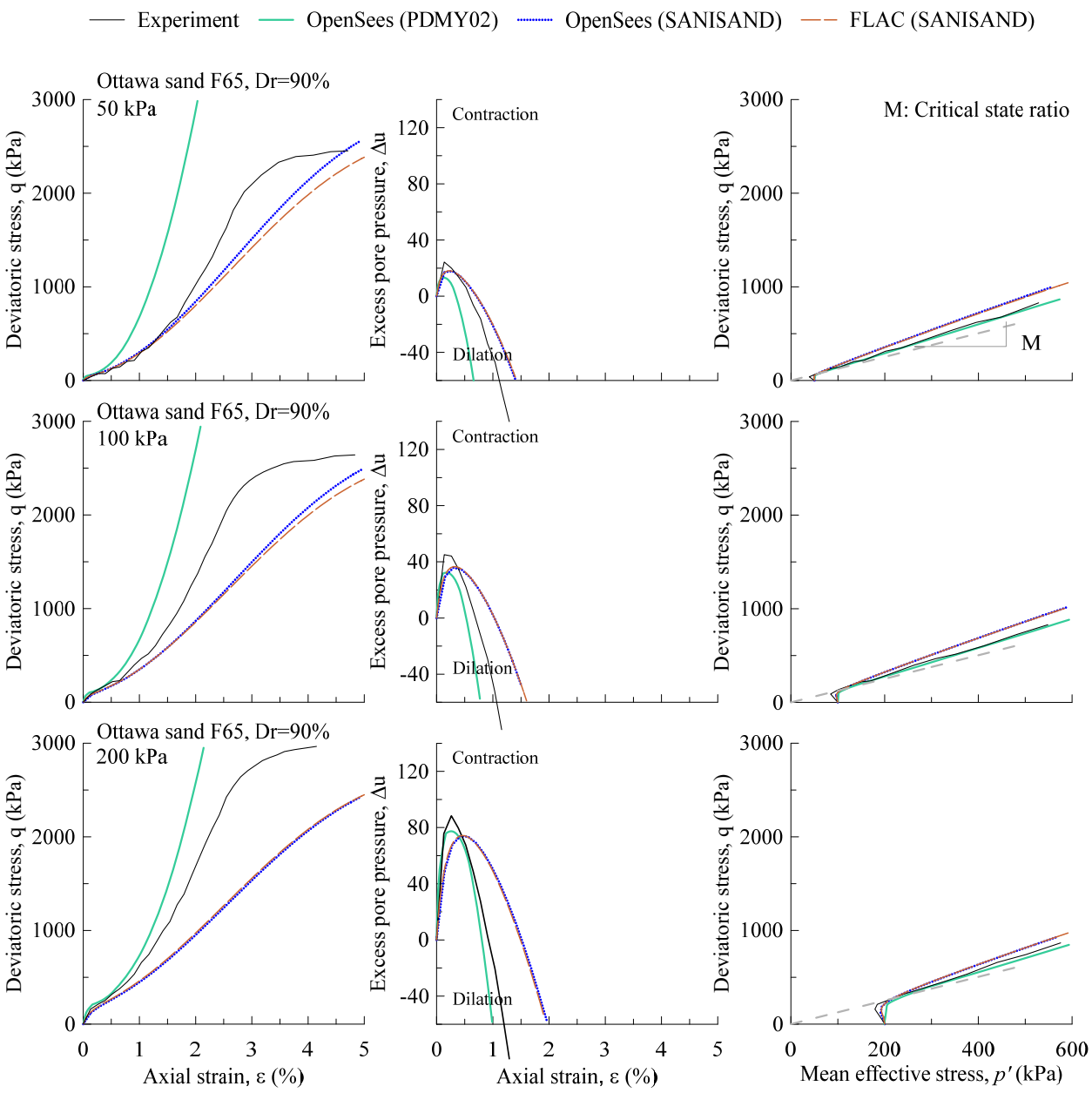

Figure B4. Comparison between experimental monotonic undrained triaxial tests and numerical (Calibration C) simulated response for dense Ottawa sand F65 (D_r = 90%)

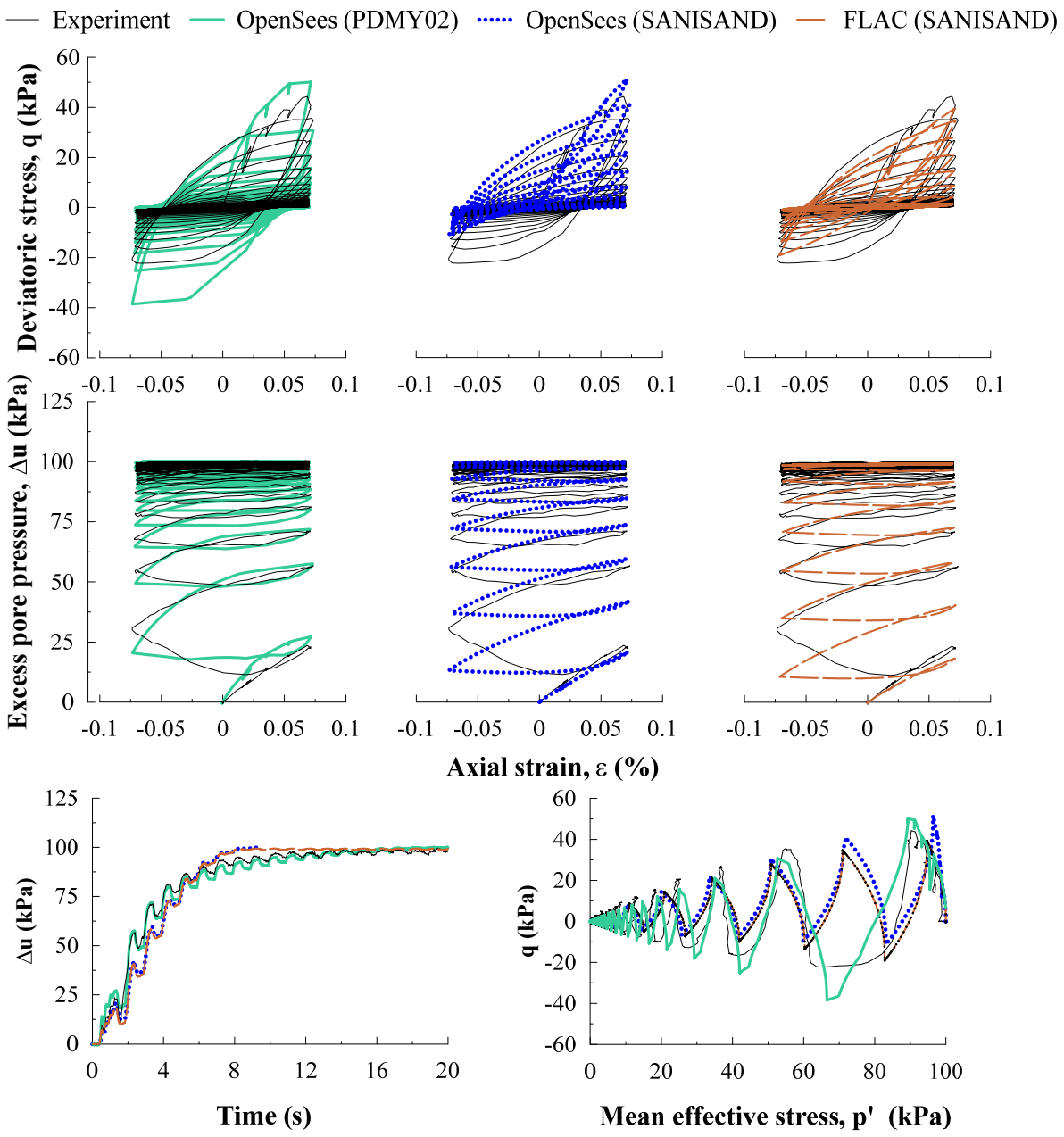

Figure B5. Comparison between experimental and numerical simulated (Calibration C) response for Ottawa sand F65 with D_r = 40% and a cyclic shear strain amplitude of 0.105% or axial strain amplitude of 0.070%

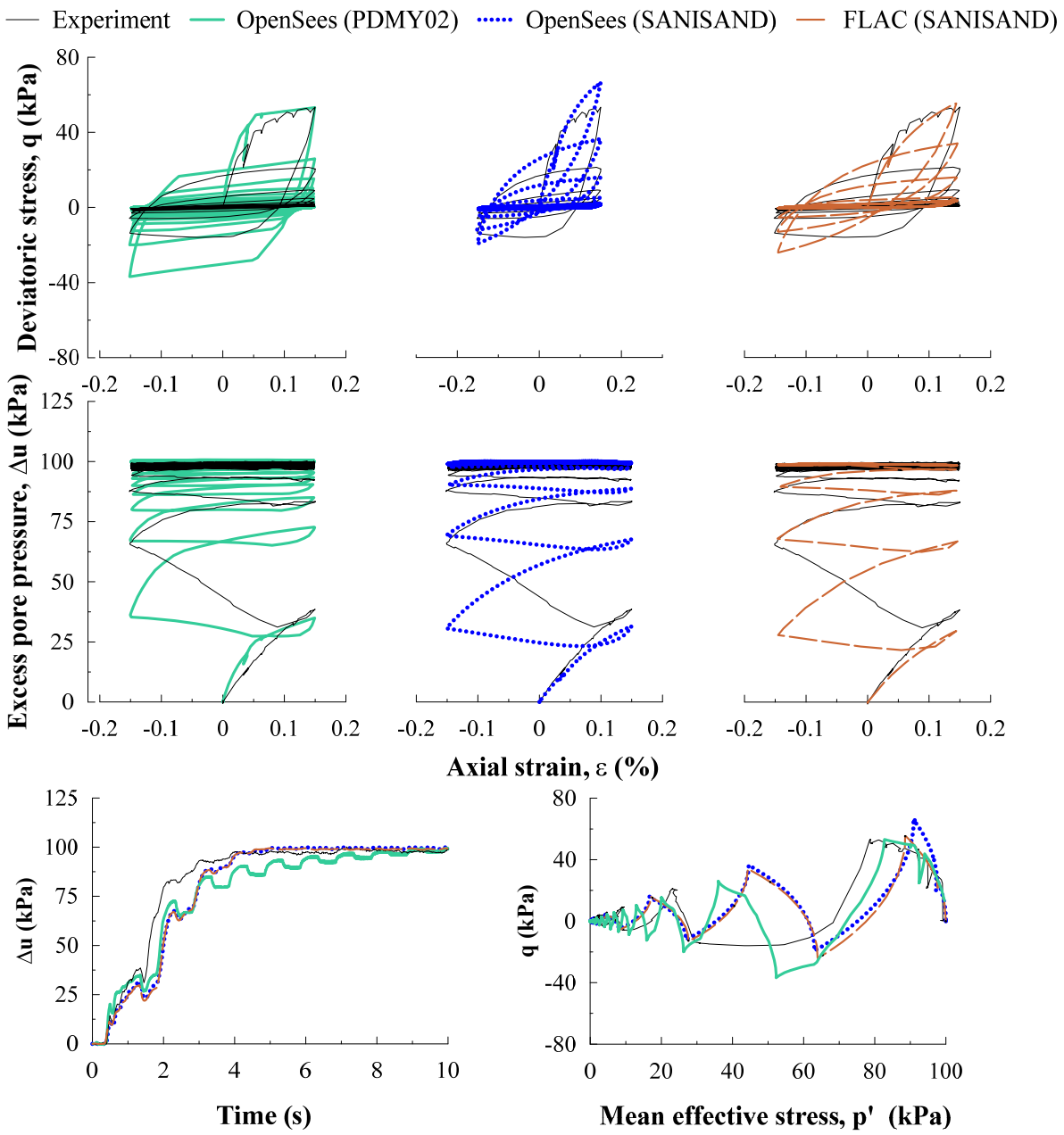

Figure B6. Comparison between experimental and numerical simulated (Calibration C) response for Ottawa sand F65 with D_r = 40% and a cyclic shear strain amplitude of 0.225% or axial strain amplitude of 0.15%

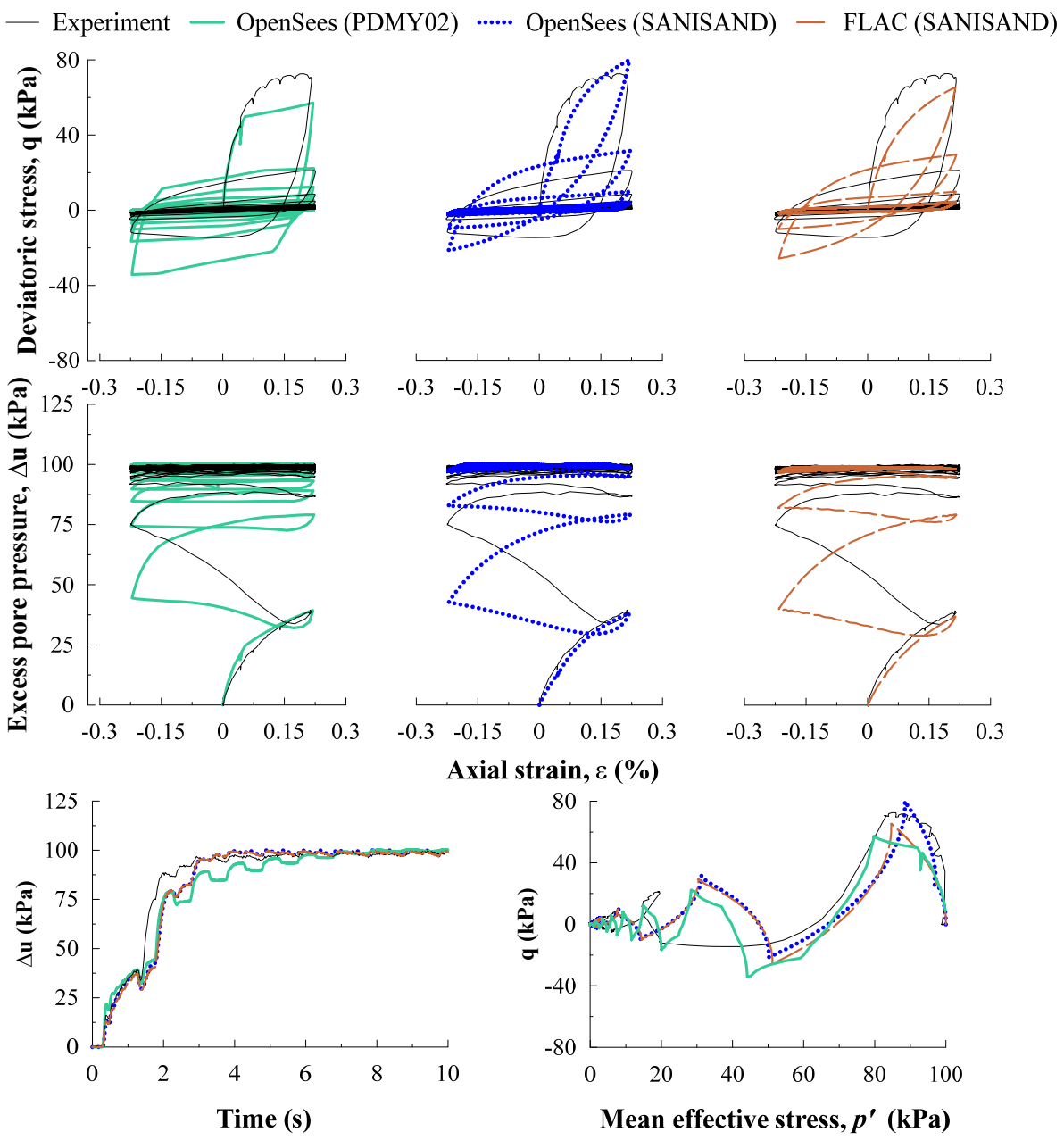

Figure B7. Comparison between experimental and numerical simulated (Calibration C) response for Ottawa sand F65 with D_r = 40% and a cyclic shear strain amplitude of 0.33% or axial strain amplitude of 0.22%

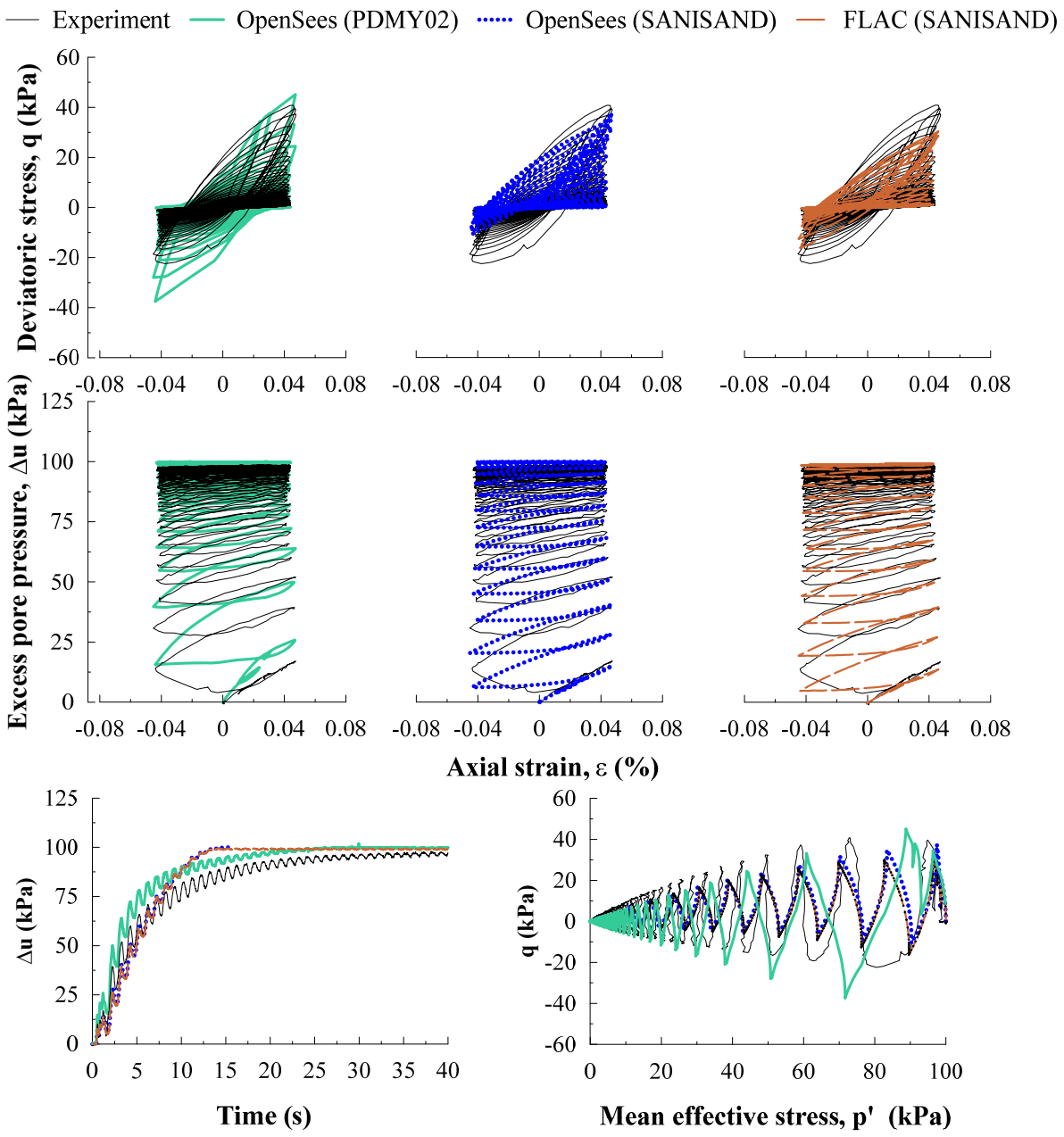

Figure B8. Comparison between experimental and numerical simulated (Calibration C) response for Ottawa sand F65 with D_r = 40% and a cyclic shear strain amplitude of 0.063% or axial strain amplitude of 0.042%

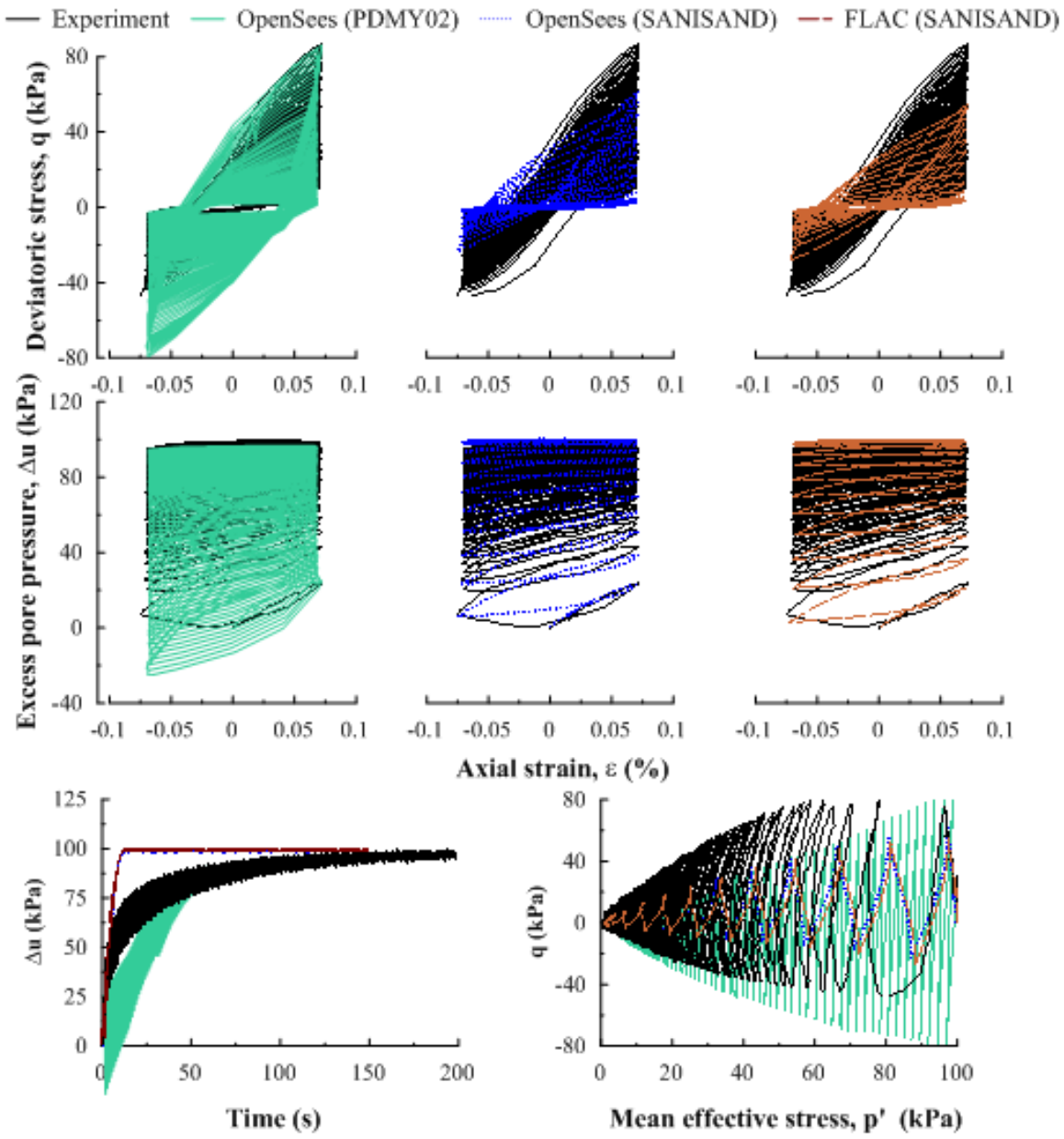

Figure B9. Comparison between experimental and numerical simulated (Calibration C) response for Ottawa sand F65 with D_r = 90% and a cyclic shear strain amplitude of 0.105% or axial strain amplitude of 0.070%

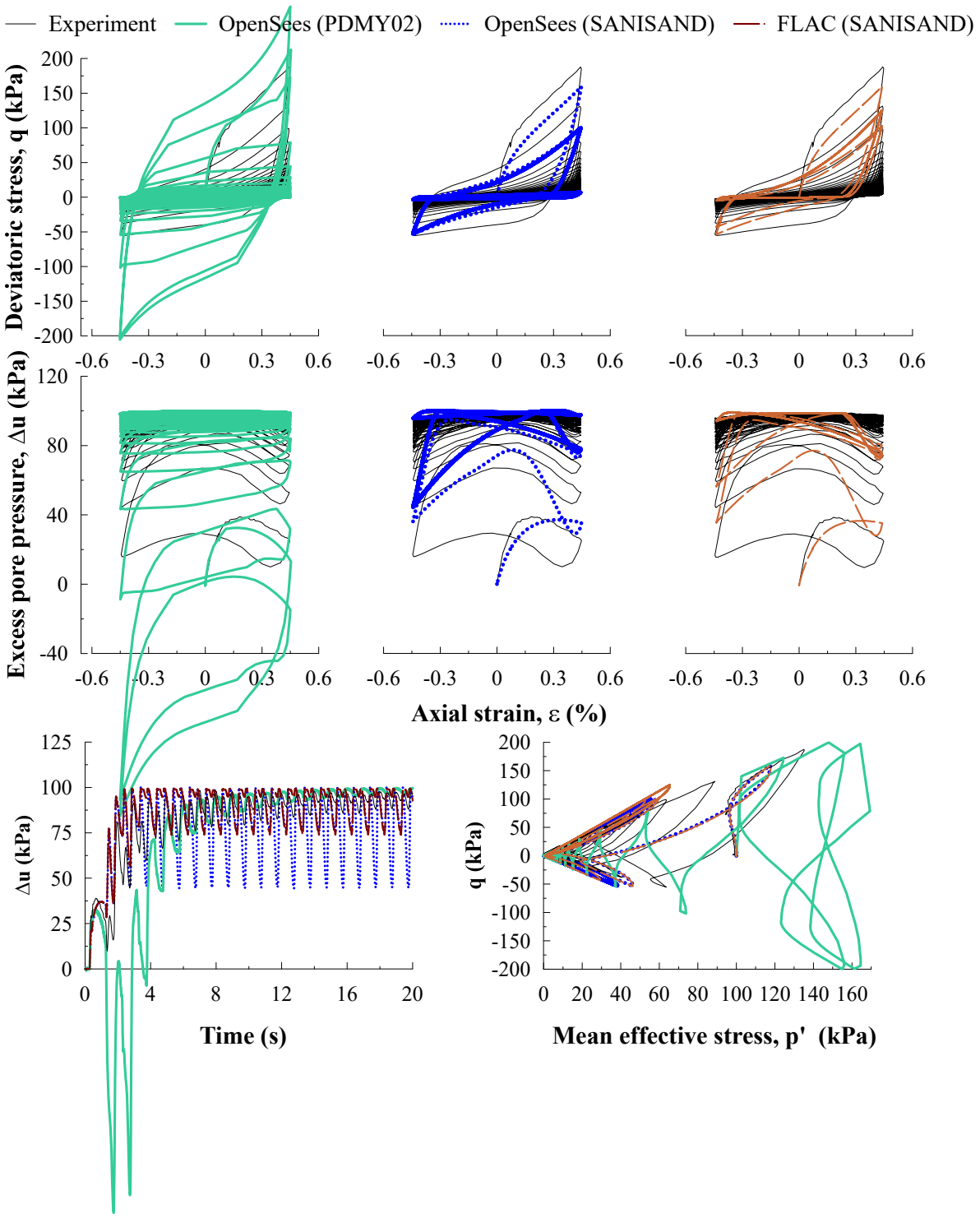

Figure B10. Comparison between experimental and numerical simulated (Calibration C) response for Ottawa sand F65 with D_r = 90% and a cyclic shear strain amplitude of 0.66% or axial strain amplitude of 0.44%

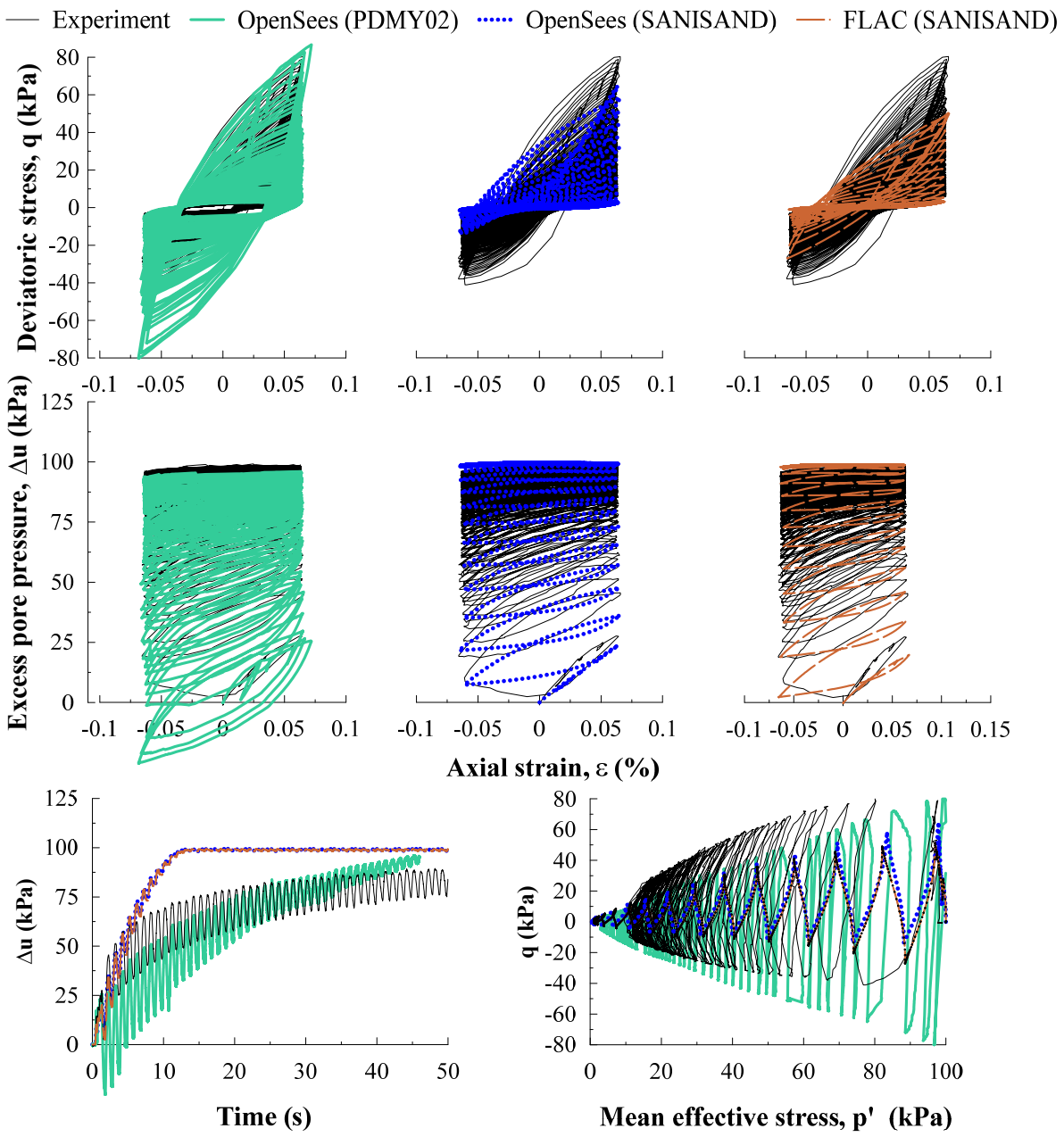

Figure B11. Comparison between experimental and numerical simulated (Calibration C) response for Ottawa sand F65 with D_r = 90% and a cyclic shear strain amplitude of 0.095% or axial strain amplitude of 0.063%

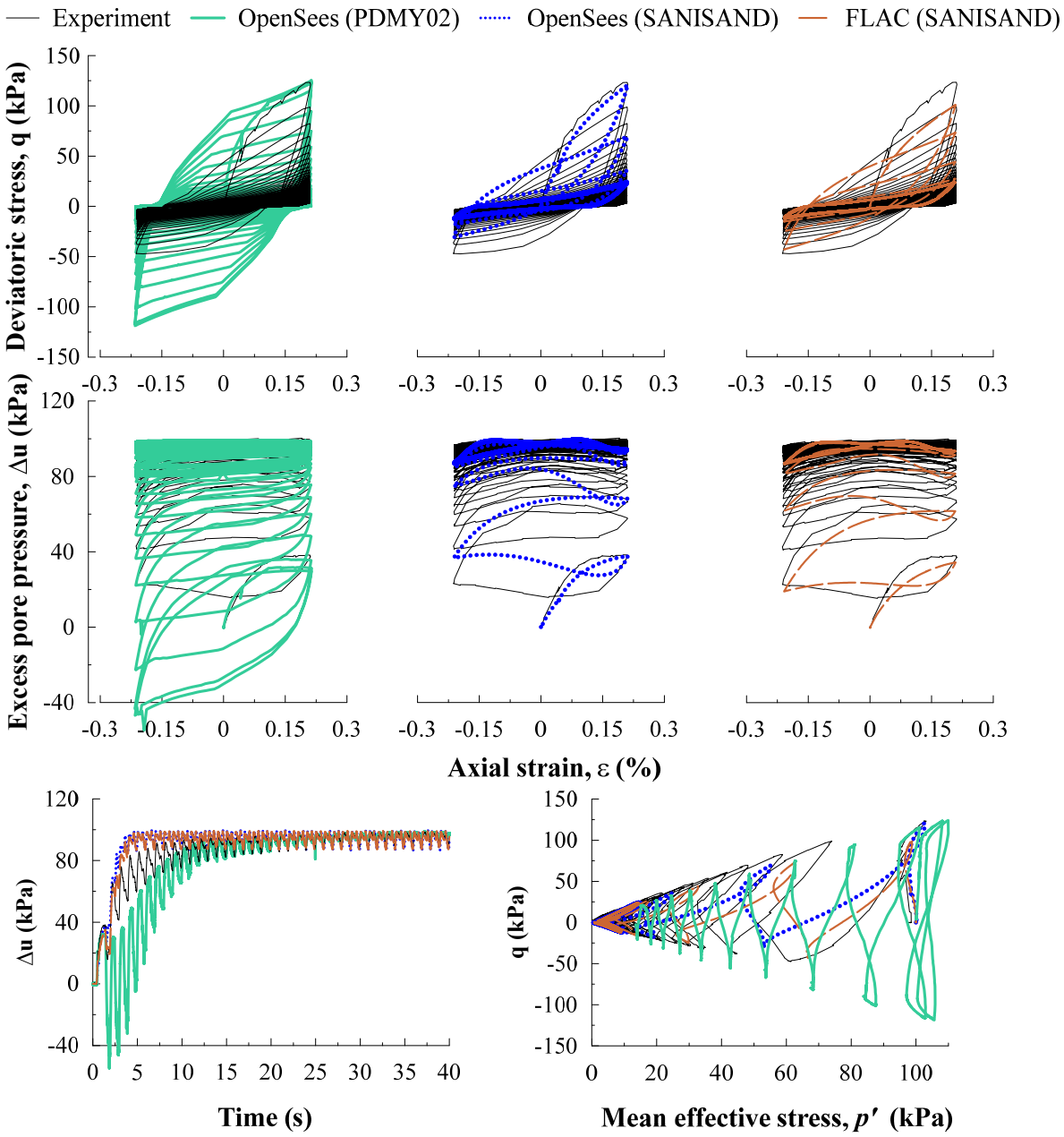

Figure B12. Comparison between experimental and numerical simulated (Calibration C) response for Ottawa sand F65 with D_r = 90% and a cyclic shear strain amplitude of 0.315% or axial strain amplitude of 0.21%

APPENDIX C

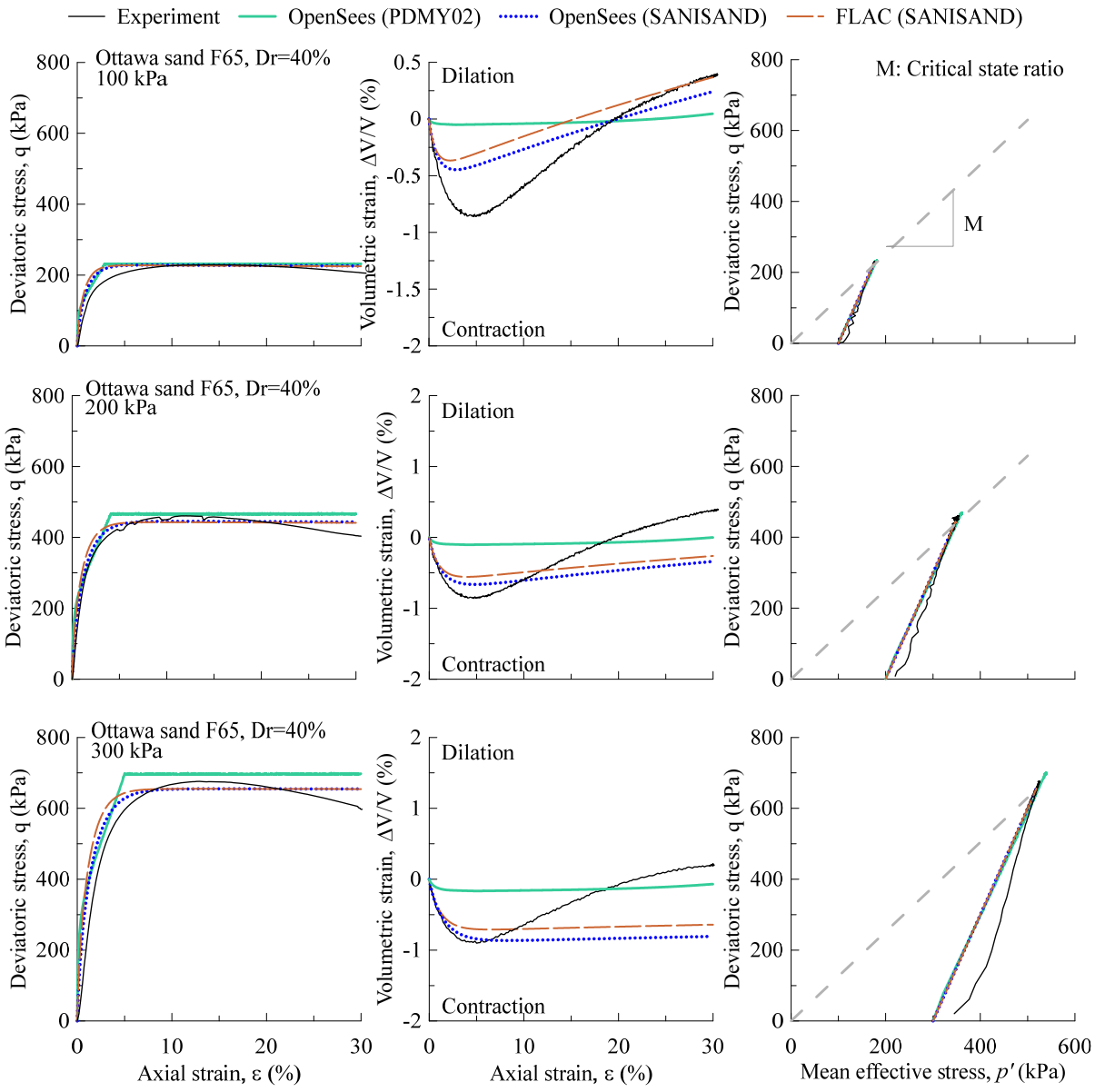

Figure C1. Comparison between experimental monotonic drained triaxial tests and numerical (Calibration C1) simulated response for Ottawa sand F65 (D_r = 40%)

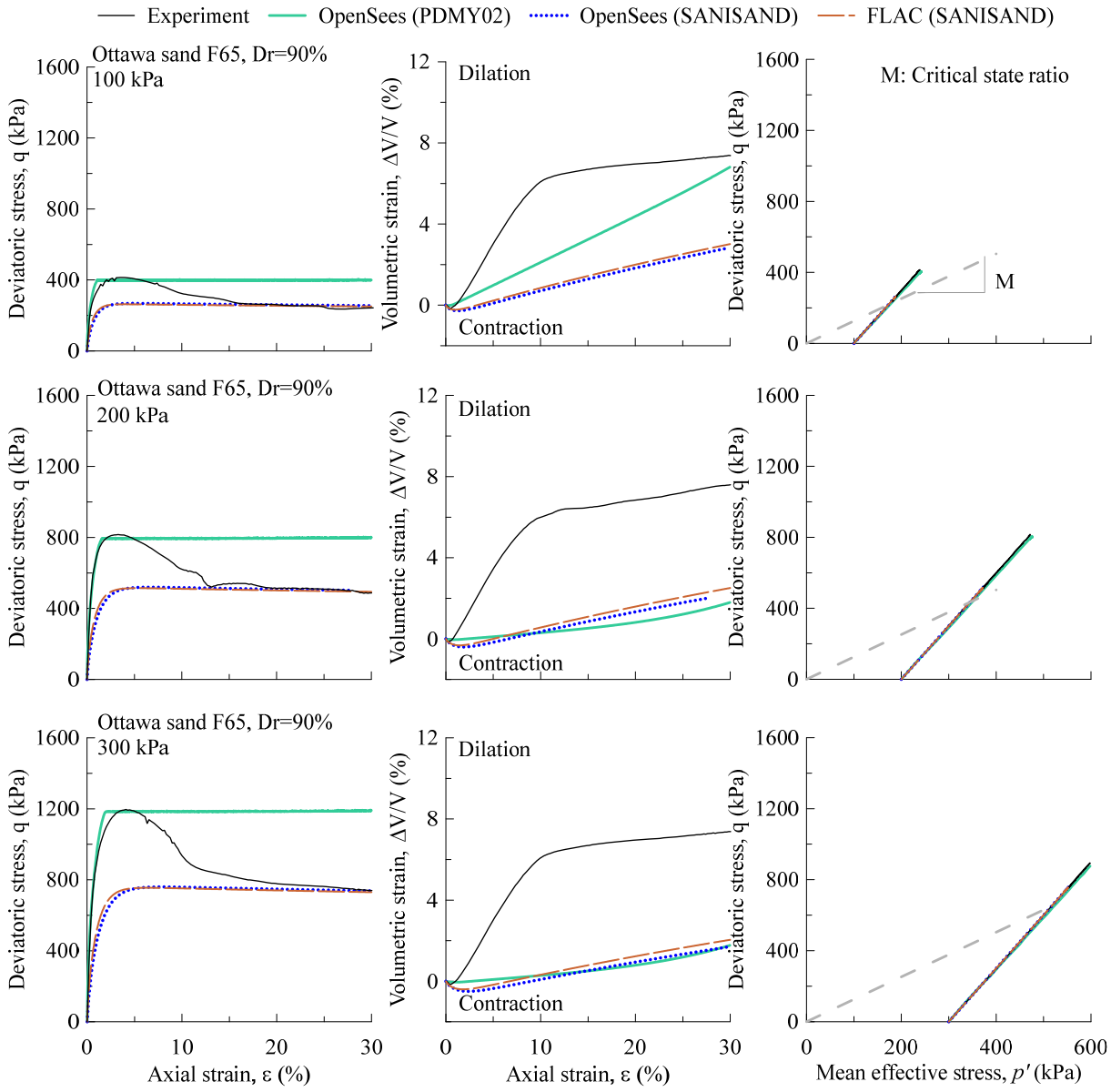

Figure C2. Comparison between experimental monotonic drained triaxial tests and numerical (Calibration C1) simulated response for Ottawa sand F65 (D_r = 90%)

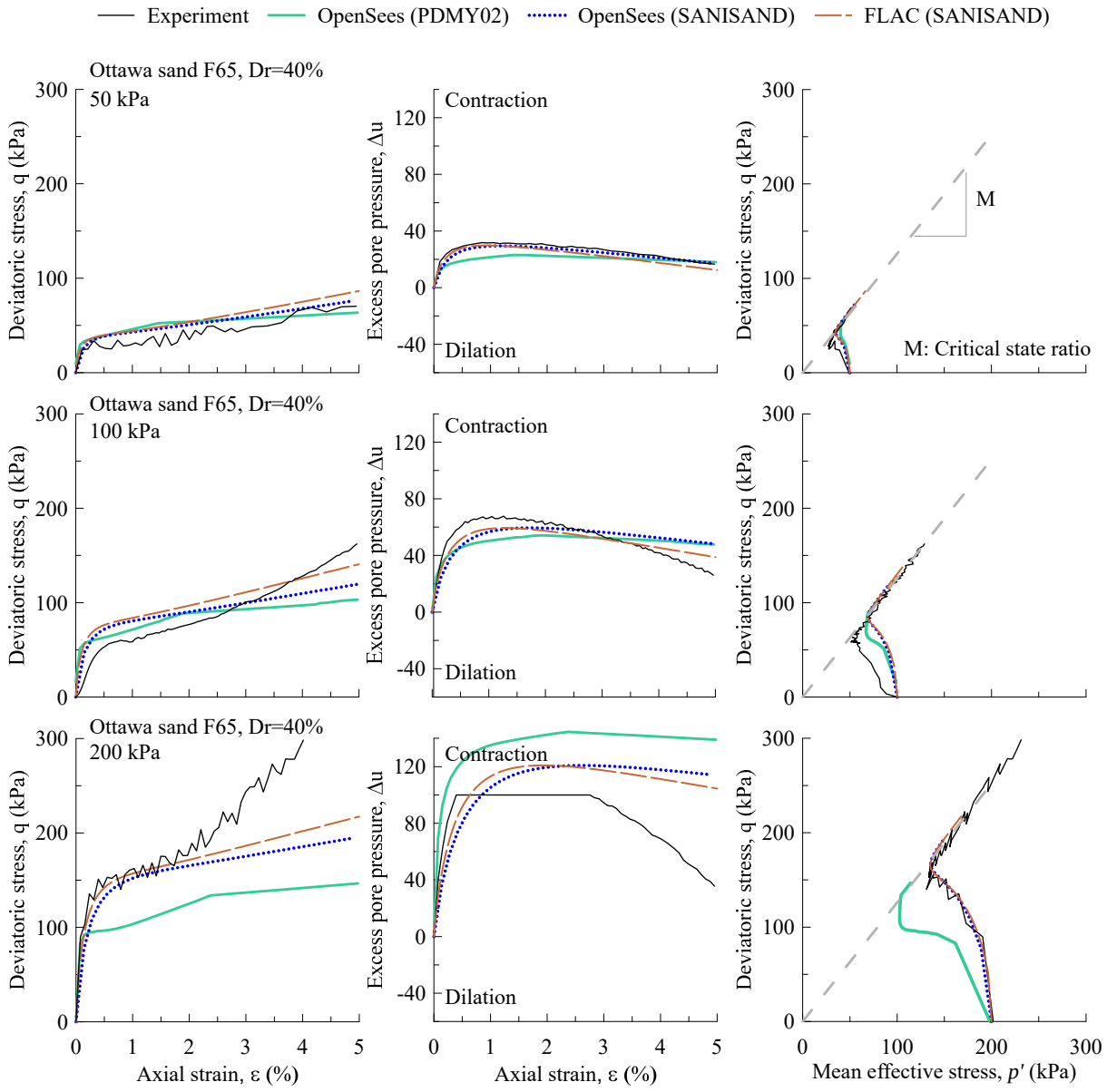

Figure C3. Comparison between experimental monotonic undrained triaxial tests and numerical (Calibration C1) simulated response for loose Ottawa sand F65 (D_r = 40%)

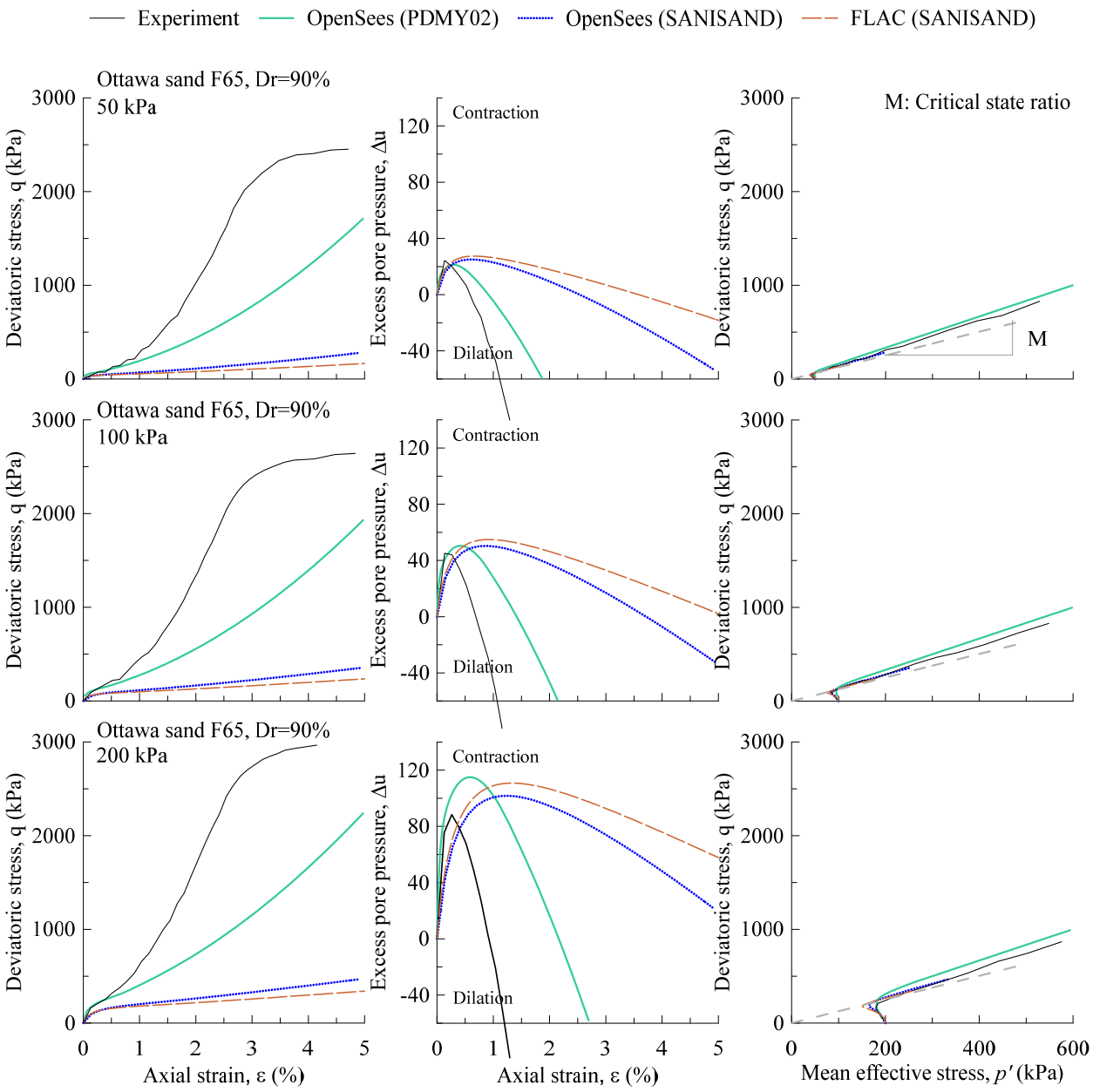

Figure C4. Comparison between experimental monotonic undrained triaxial tests and numerical (Calibration C1) simulated response for dense Ottawa sand F65 (D_r = 90%)

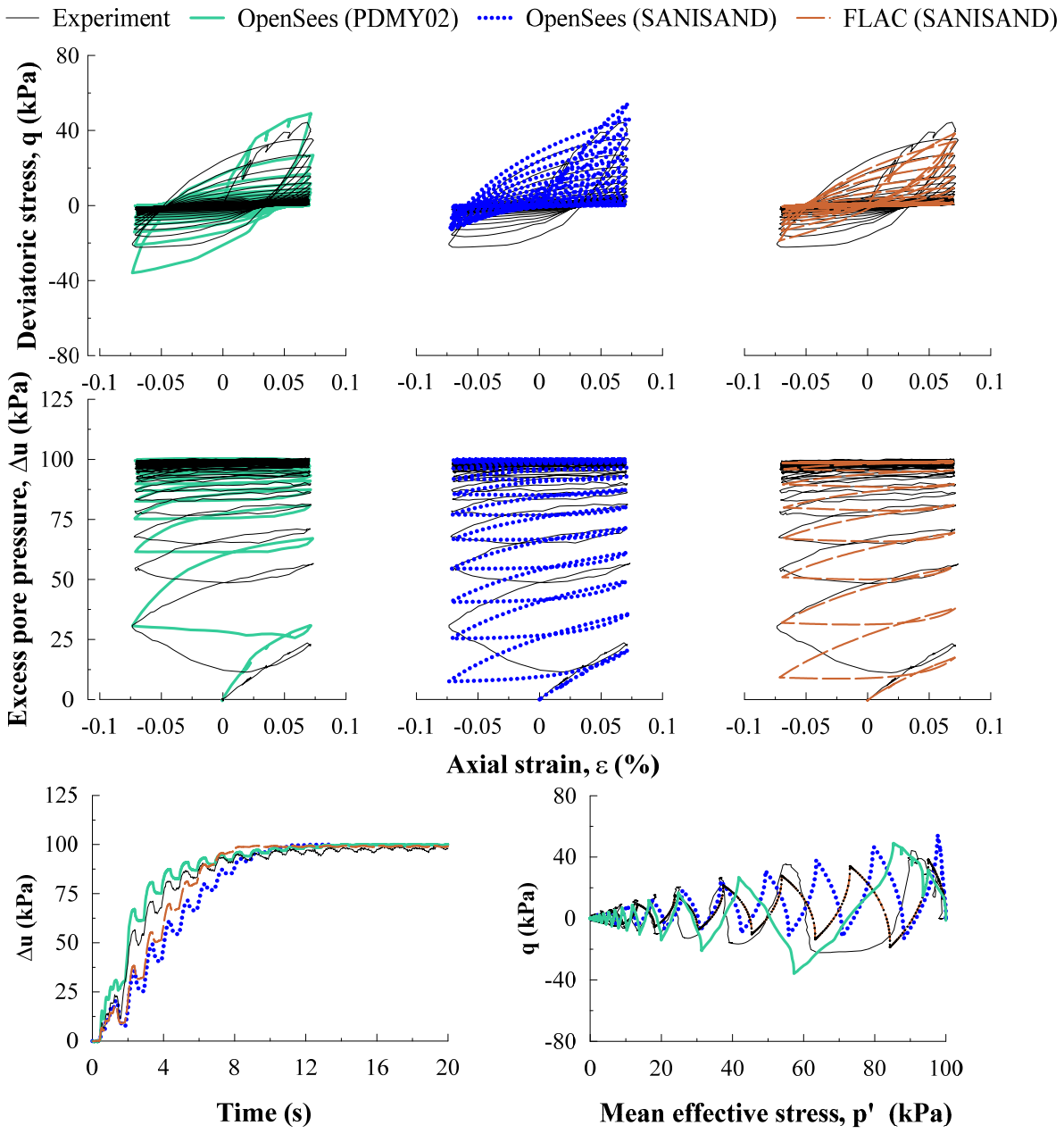

Figure C5. Comparison between experimental and numerical simulated (Calibration C1) response for Ottawa sand F65 with D_r = 40% and a cyclic shear strain amplitude of 0.105% or axial strain amplitude of 0.070%

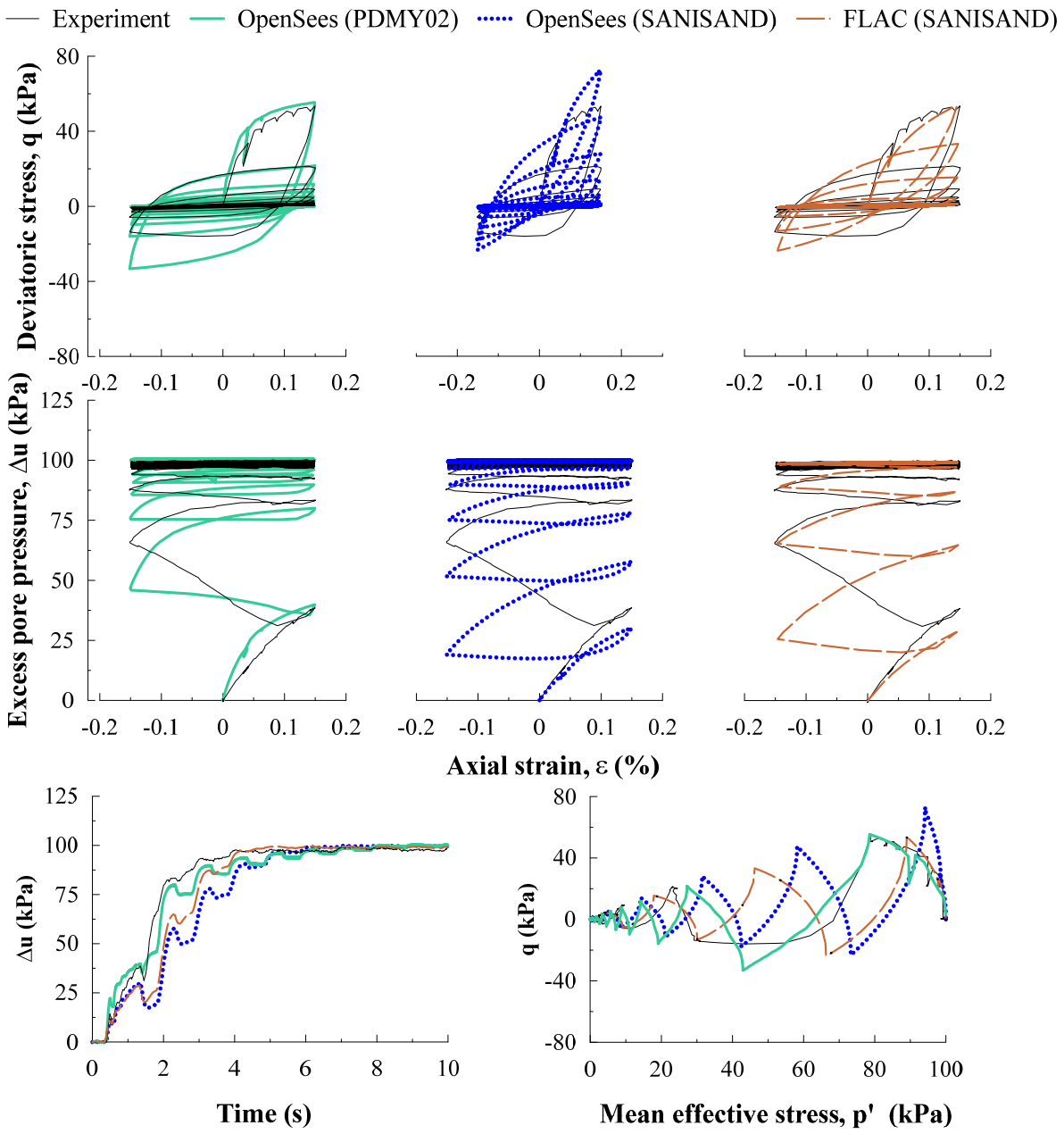

Figure C6. Comparison between experimental and numerical simulated (Calibration C1) response for Ottawa sand F65 with D_r = 40% and a cyclic shear strain amplitude of 0.225% or axial strain amplitude of 0.15%

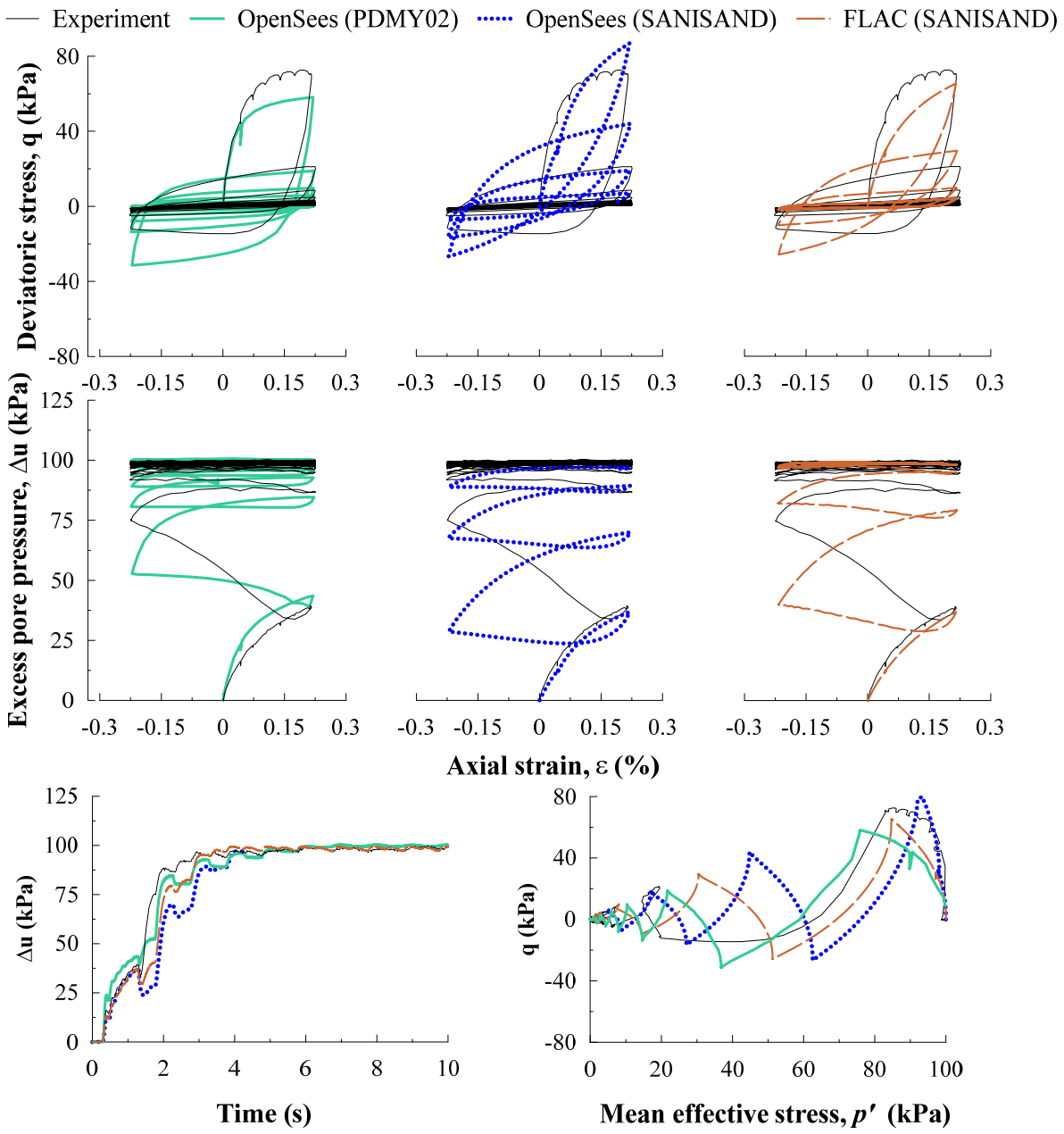

Figure C7. Comparison between experimental and numerical simulated (Calibration C1) response for Ottawa sand F65 with D_r = 40% and a cyclic shear strain amplitude of 0.33% or axial strain amplitude of 0.22%

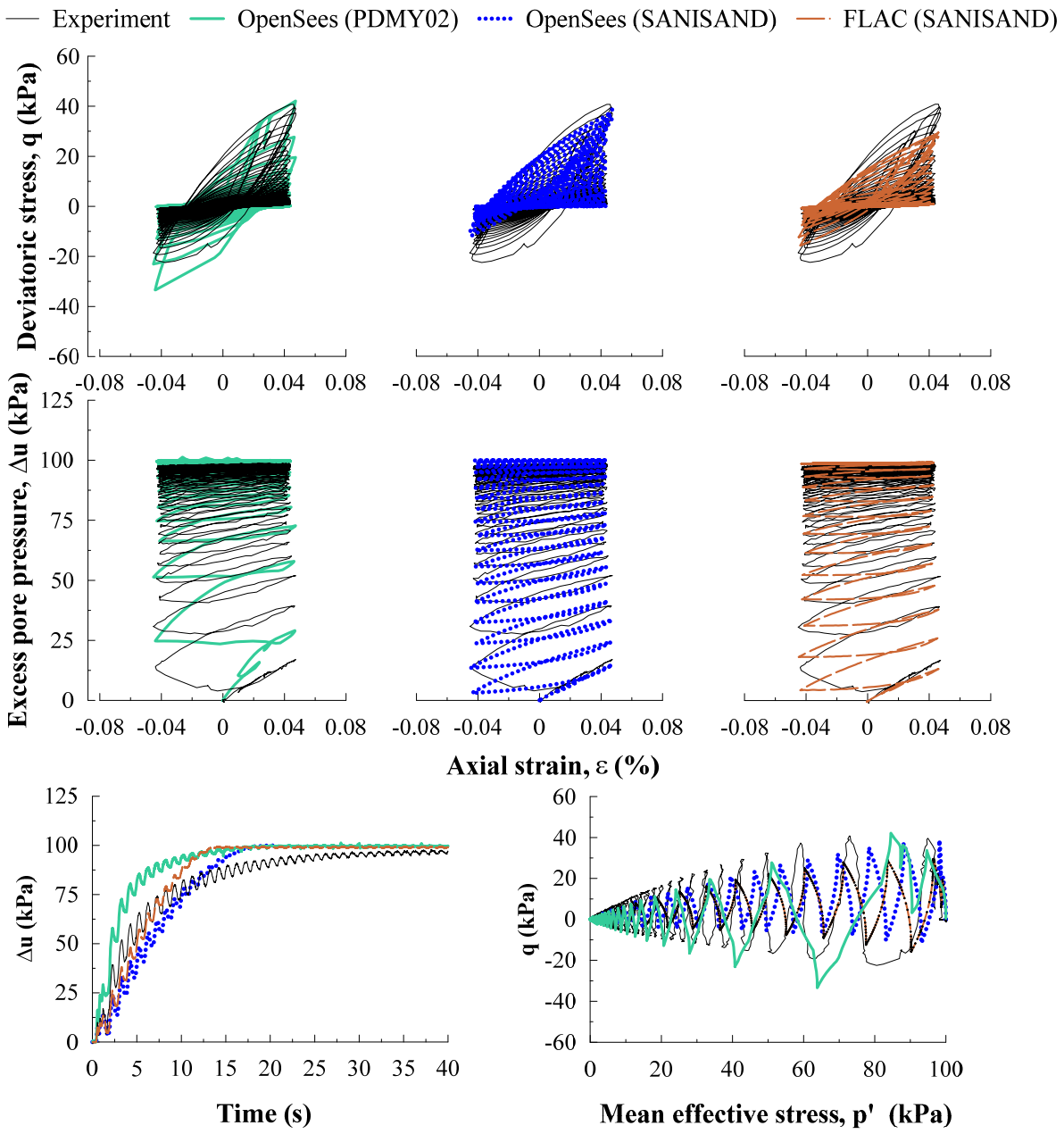

Figure C8. Comparison between experimental and numerical simulated (Calibration C1) response for Ottawa sand F65 with D_r = 40% and a cyclic shear strain amplitude of 0.063% or axial strain amplitude of 0.042%

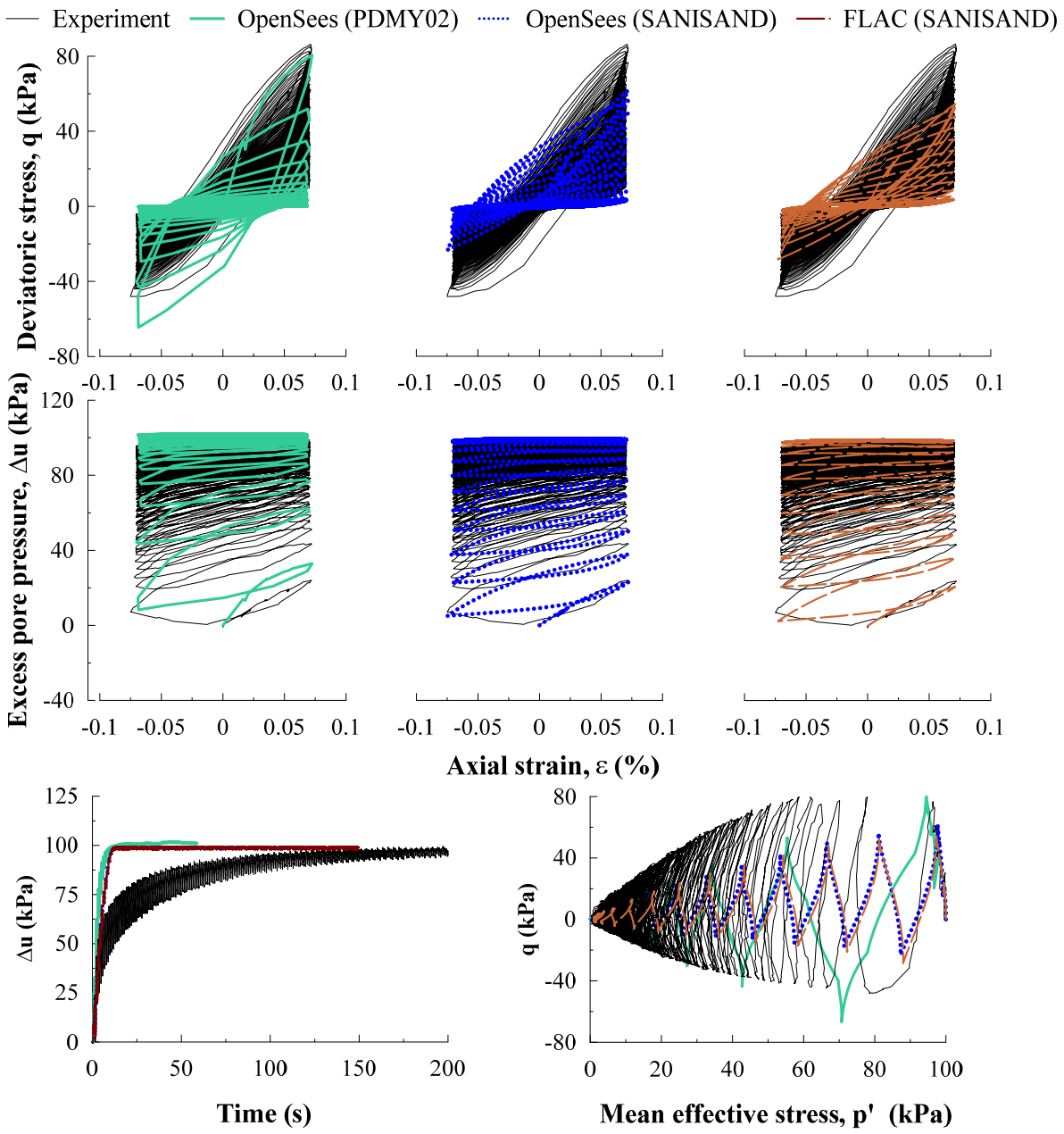

Figure C9. Comparison between experimental and numerical simulated (Calibration C1) response for Ottawa sand F65 with D_r = 90% and a cyclic shear strain amplitude of 0.105% or axial strain amplitude of 0.070%

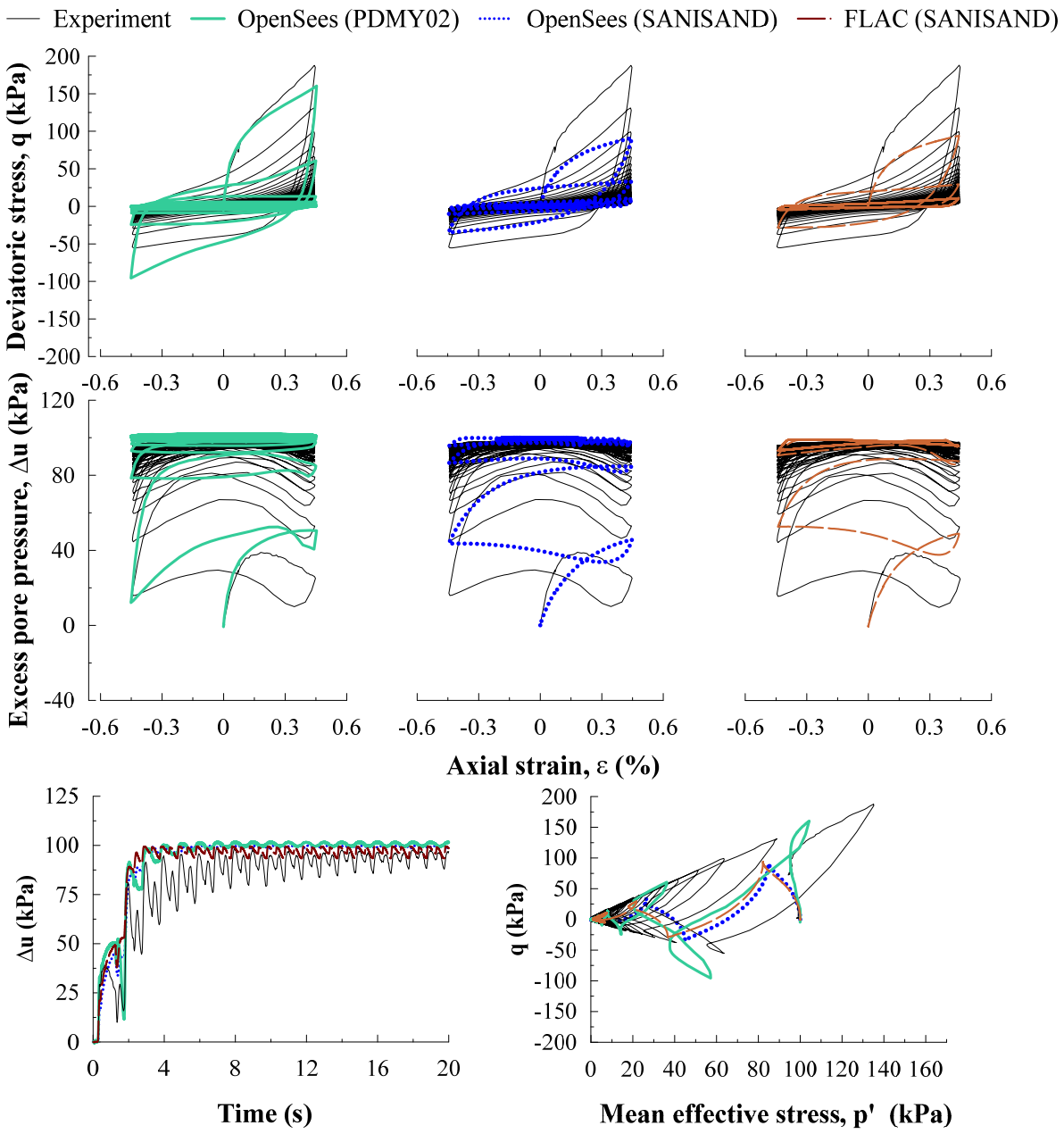

Figure C10. Comparison between experimental and numerical simulated (Calibration C1) response for Ottawa sand F65 with D_r = 90% and a cyclic shear strain amplitude of 0.66% or axial strain amplitude of 0.44%

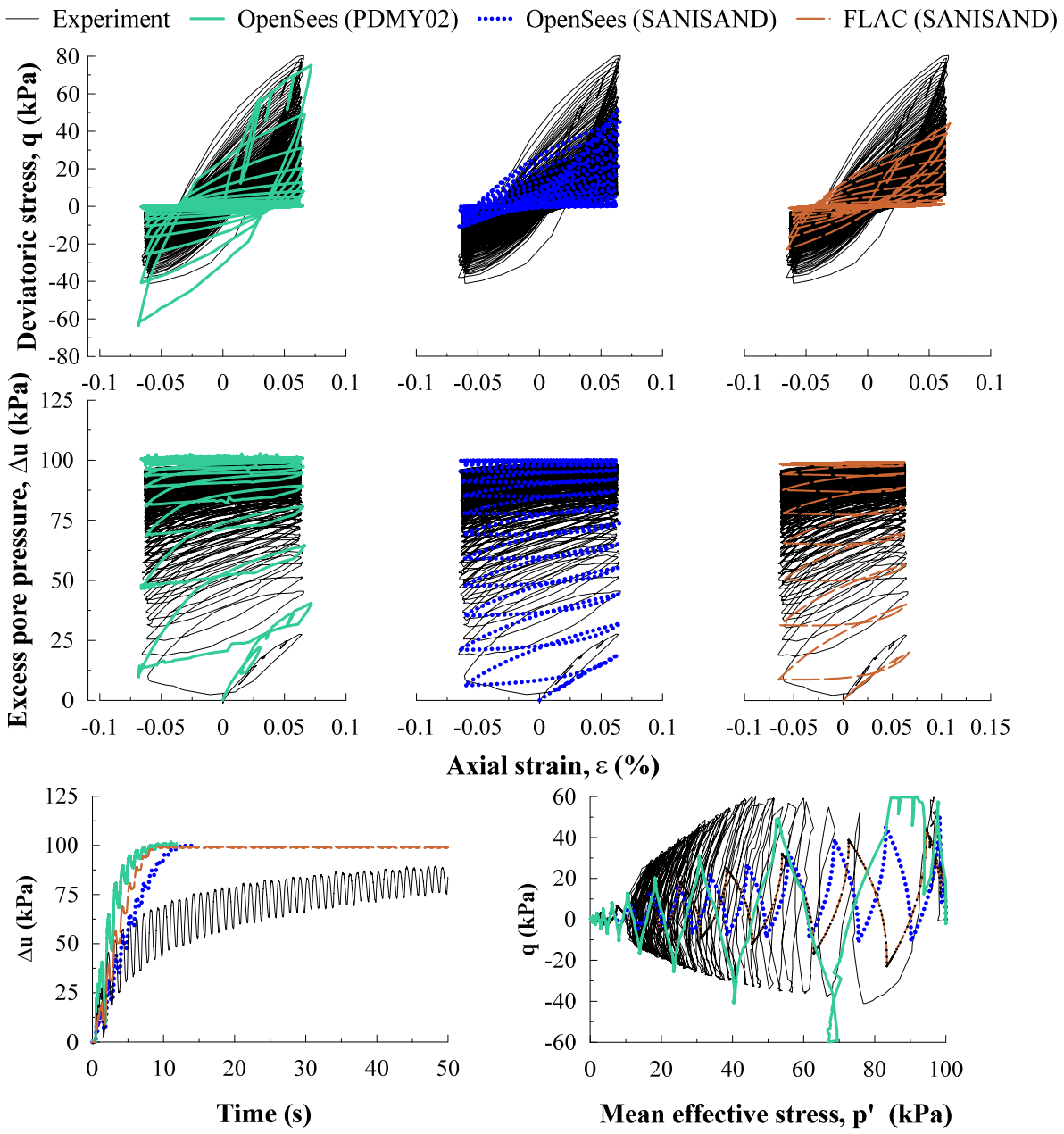

Figure C11. Comparison between experimental and numerical simulated (Calibration C1) response for Ottawa sand F65 with D_r = 90% and a cyclic shear strain amplitude of 0.095% or axial strain amplitude of 0.063%

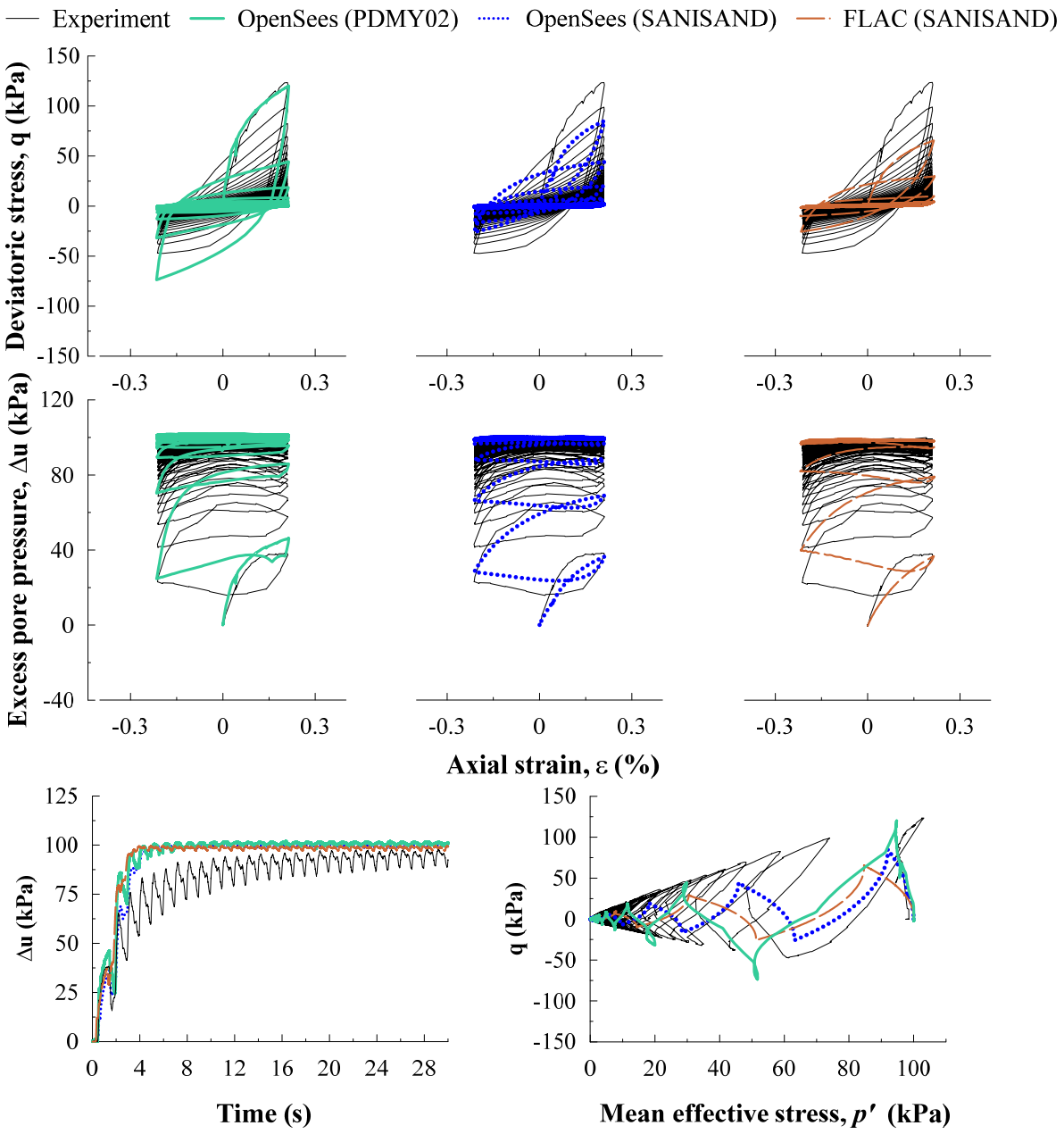

Figure C12. Comparison between experimental and numerical simulated (Calibration C1) response for Ottawa sand F65 with D_r = 90% and a cyclic shear strain amplitude of 0.315% or axial strain amplitude of 0.21%

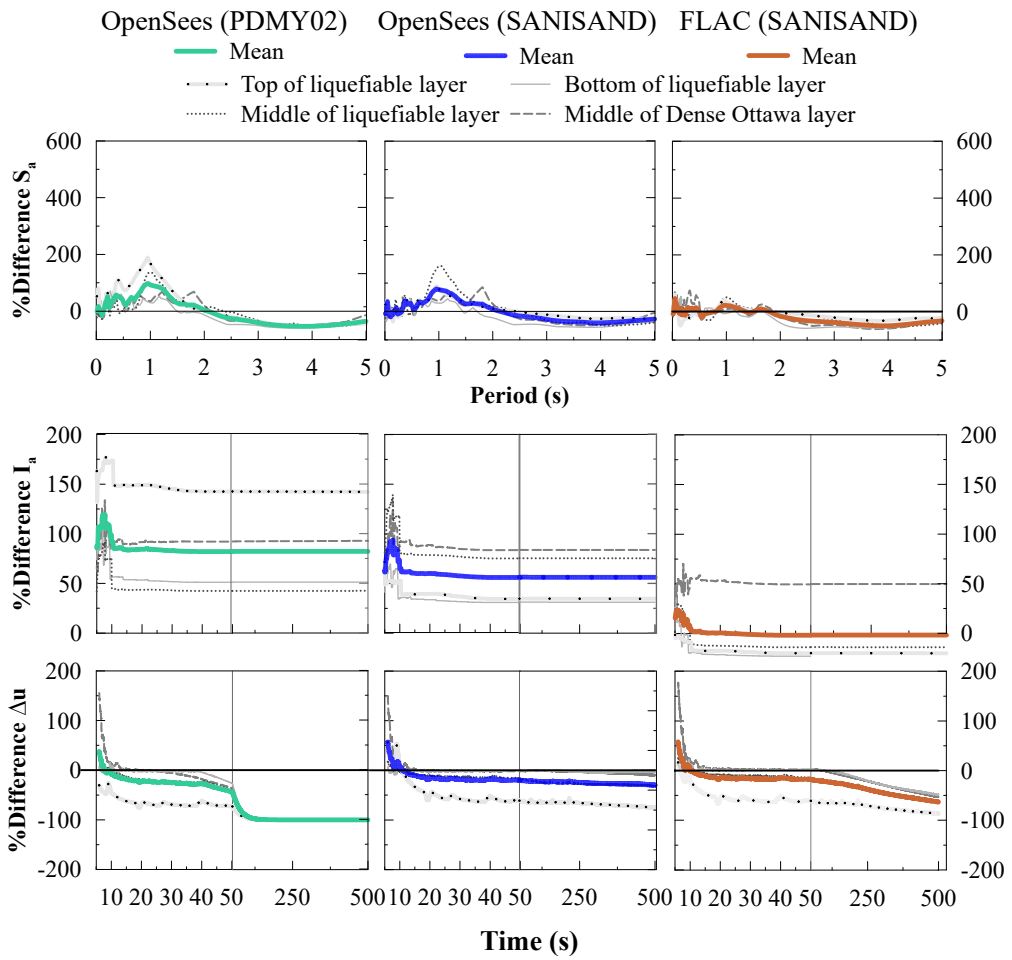

Figure C13. Percent difference between experimental and numerical (Class-C1) Response Spectra Sa (5%-damped), Arias Intensity, I_a, and excess pore pressure at different depths for each constitutive model

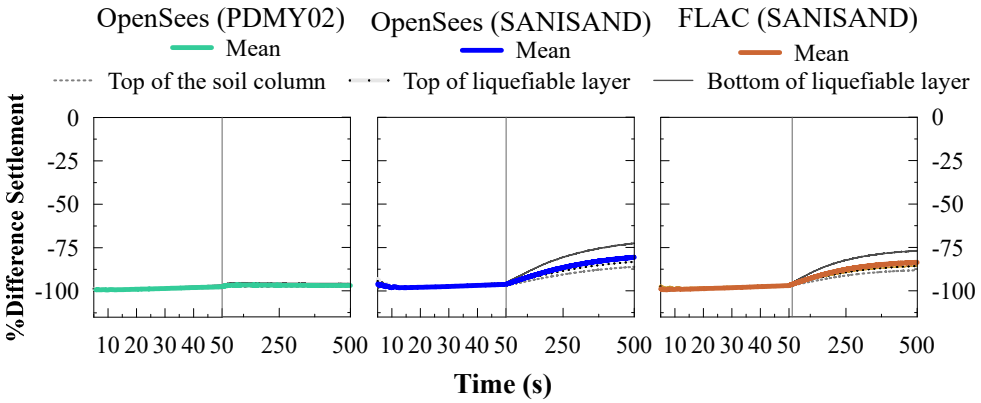

Figure C14. Percent difference between experimental and numerical (Class-C1) settlement time histories at different depths for each constitutive model

APPENDIX D

This appendix shows the computational time and memory for all simulations presented in Chapter 4.

.

Table D1. Summary of both computational time and memory for all simulations

Test	No. of cores	CPU time (h)	Core times CPUtime (h)	Soil models	Elements	Soil-foundation interface
$FF_{DS\text{-}DR\text{-}6}$	6	11	66	PDMY02	brickUP	N.A.
$FF_{DS\text{-}DR\text{-}6}$	1	64	64	SANISAND	SSPbrickUP	N.A.
$A2_{NM\text{-}DS\text{-}6}$	10	14	140	PDMY02	brickUP	equalDOF
$A2_{NM\text{-}DS\text{-}6}$	8	24	192	SANISAND	SSPbrickUP	
$A2_{NM\text{-}6}$	1	34	34	PDMY02	brickUP	equalDOF
$A2_{NM\text{-}6}$	1	34	34	SANISAND	SSPbrickUP	
$A2_{NM\text{-}6}$	8	110	880	SANISAND	brickUP	
$A2_{NM\text{-}6}$	1	19	19	PDMY02	SSPbrickUP	
$A2_{NM\text{-}6}$	1	592	592	SANISAND	SSPbrickUP/brickUP	
$A1_{NM\text{-}DS\text{-}4}$	8	42	336	PDMY02	brickUP	Zero-length contact element
$A1_{DR\text{-}SW\text{-}4}$	8	47	376			
$A2_{NM\text{-}DS\text{-}6}$	10	41	410			
$A2_{DR\text{-}SW\text{-}6}$	8	41	328			
$B_{NM\text{-}DR\text{-}6}$	10	168	1680			
$B_{DS\text{-}DSL\text{-}6}$	8	168	1344			

All simulations were performed using an Intel Xeon E5-2680 v3 Linux cluster with 2.50GHz that has 2 CPUs/node, 24 cores/node, and 4.84 GB per cores. Each model considered an input motion of 6000-steps (30-second motion with 0.005 seconds of time increment). For time efficiency, a user-defined algorithm was included to update the analysis time step at each time increment.

APPENDIX E

This appendix shows the numerical and experimental results of soil-foundation-(mitigation)-structure systems discussed in Chapter 4.

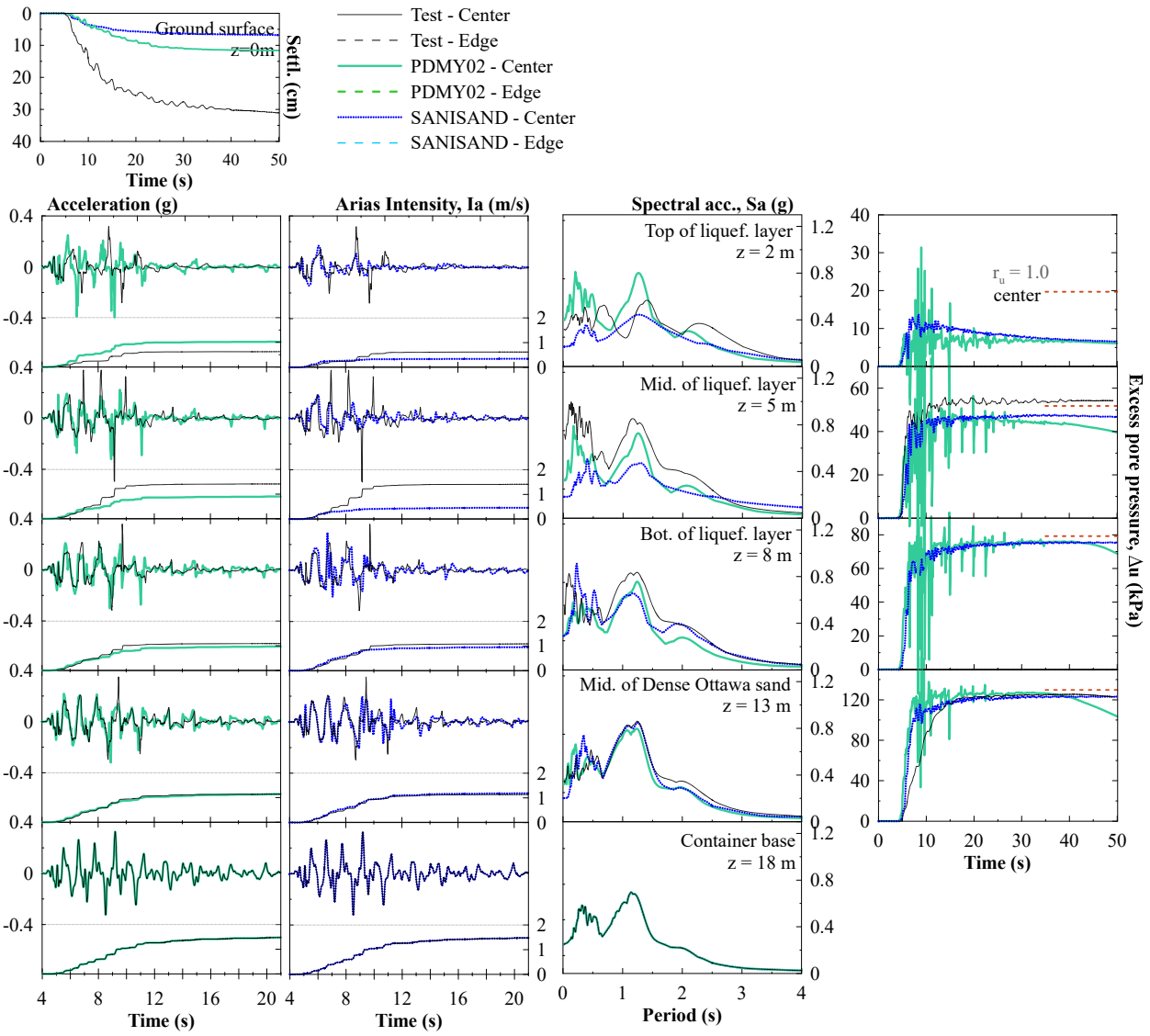

Figure E.1 Comparison of numerical and experimental results for FF_{DS-6}

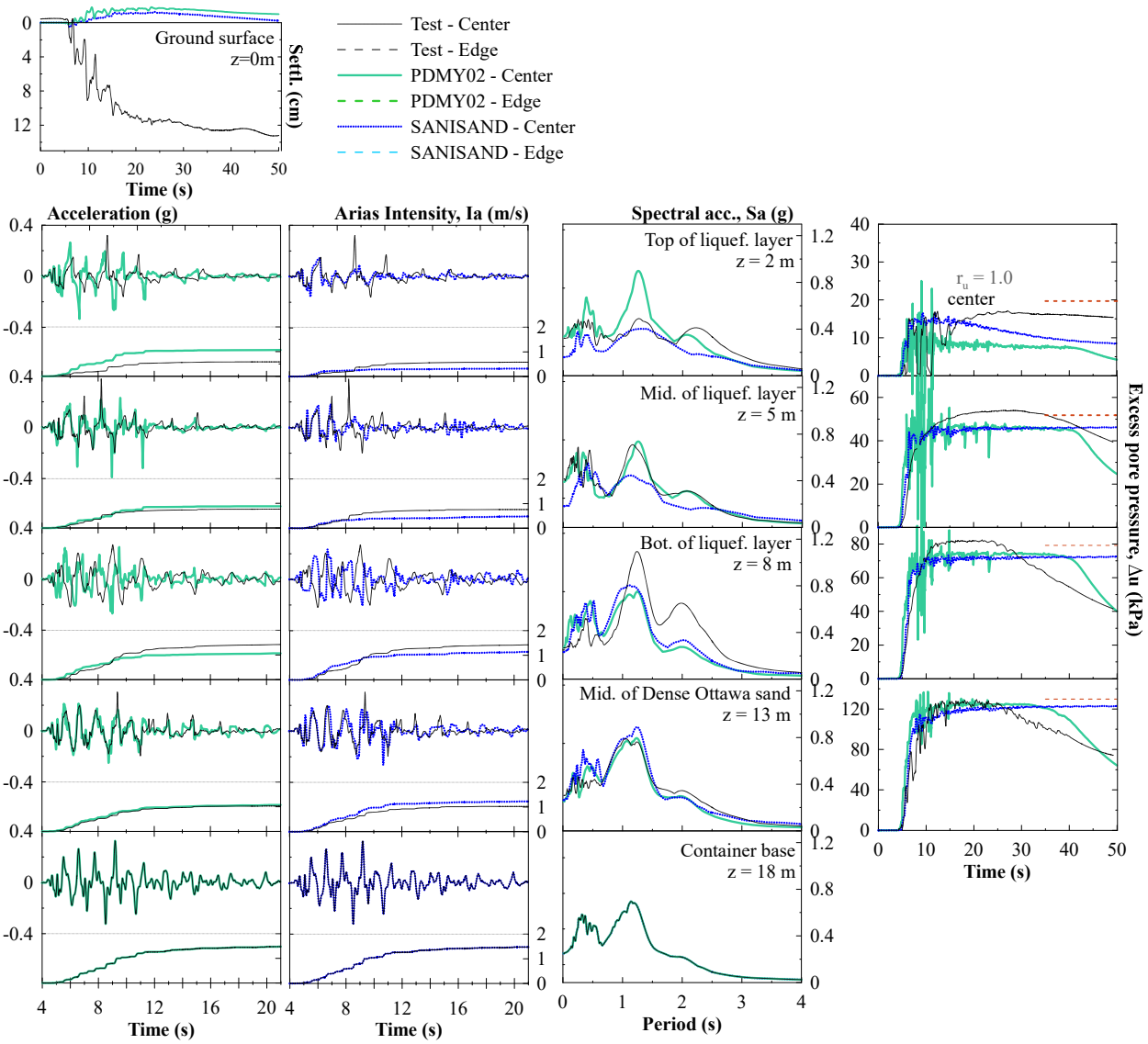

Figure E.2 Comparison of numerical and experimental results for $FF_{DR\text{-}6}$

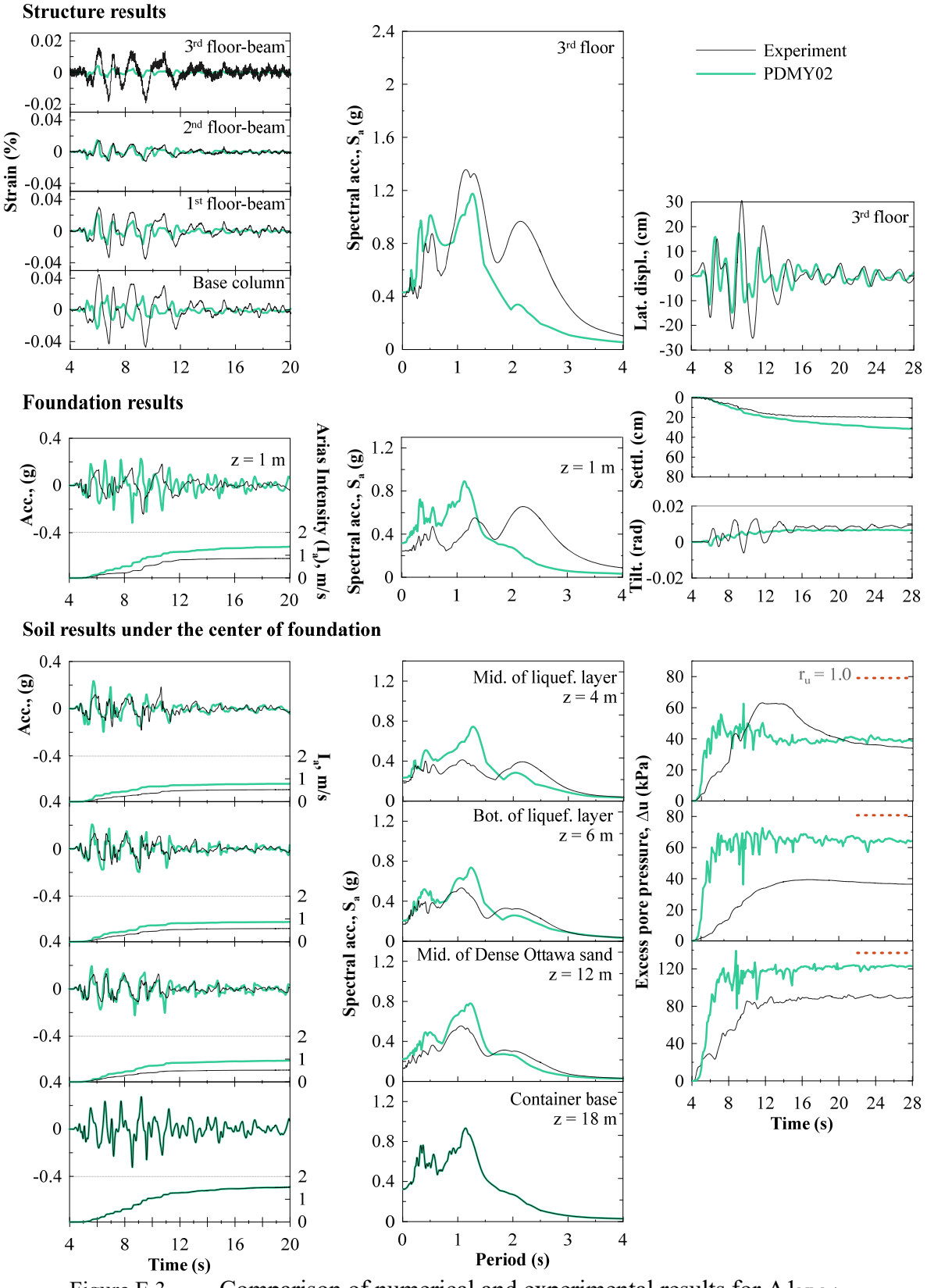

Figure E.3 Comparison of numerical and experimental results for A1$_{NM-4}$

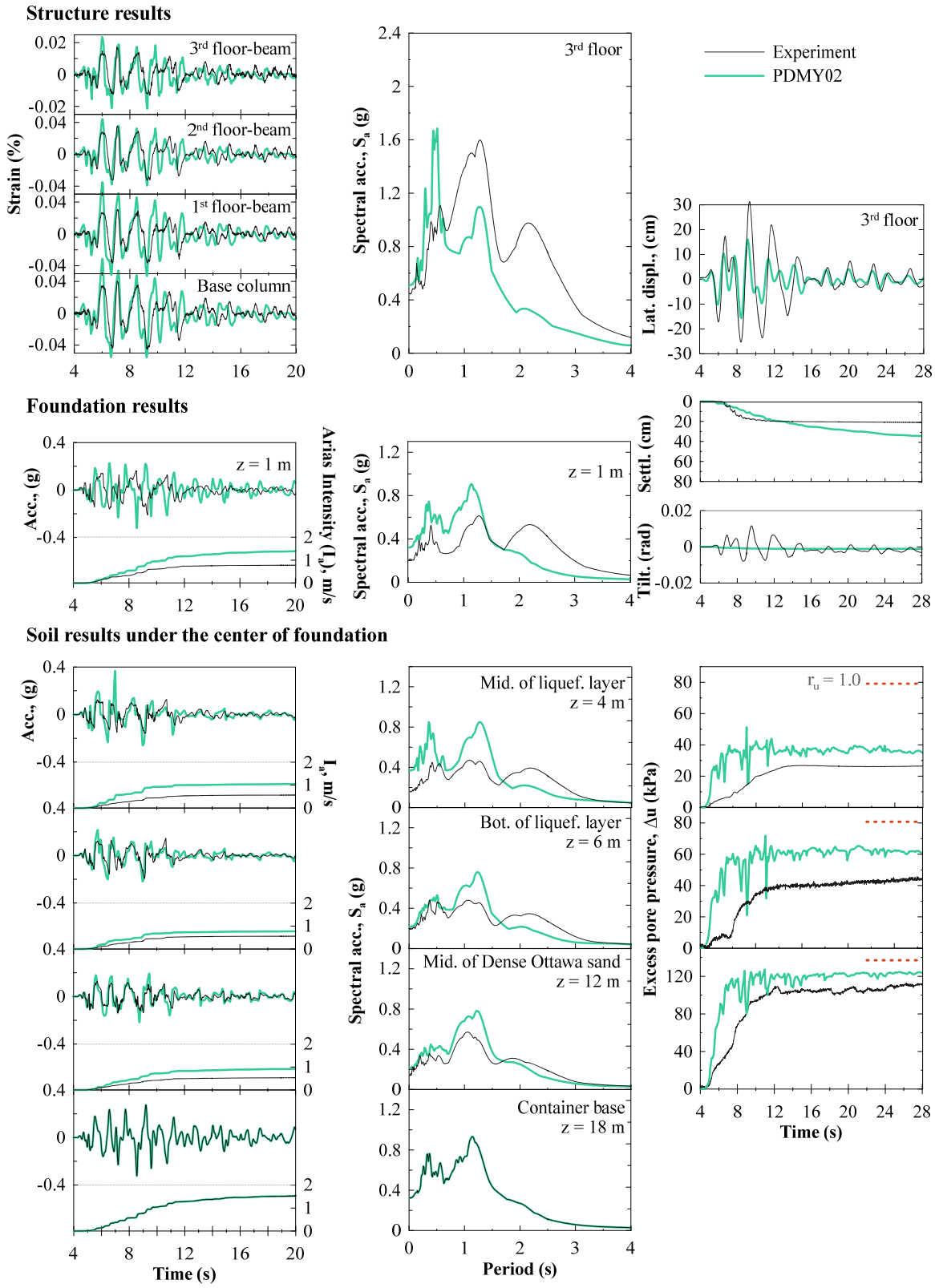

Figure E.4 Comparison of numerical and experimental results for $A1_{DS-4}$

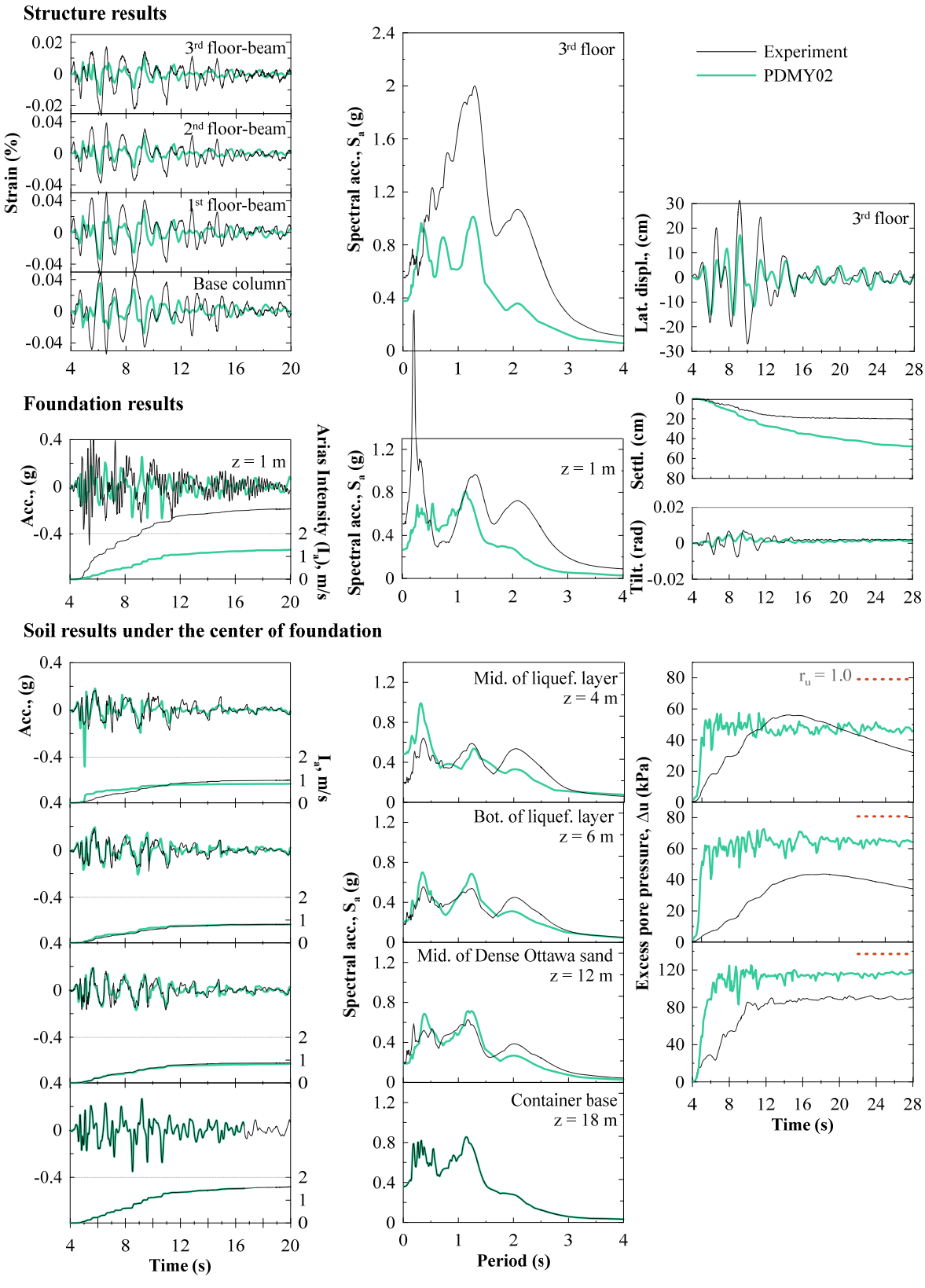

Figure E.5 Comparison of numerical and experimental results for A1$_{DR-4}$

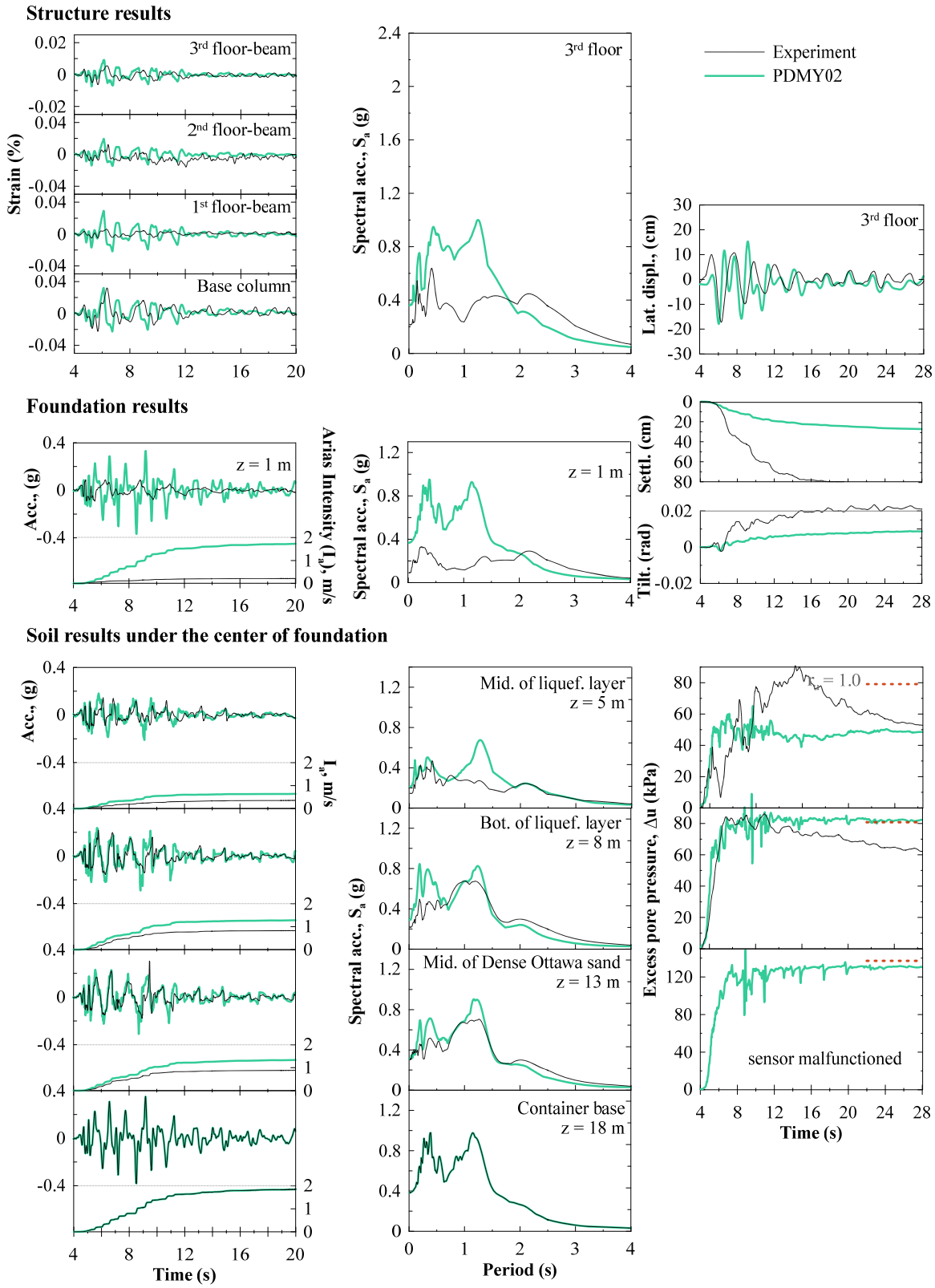

Figure E.6 Comparison of numerical and experimental results for $A2_{NM-6}$

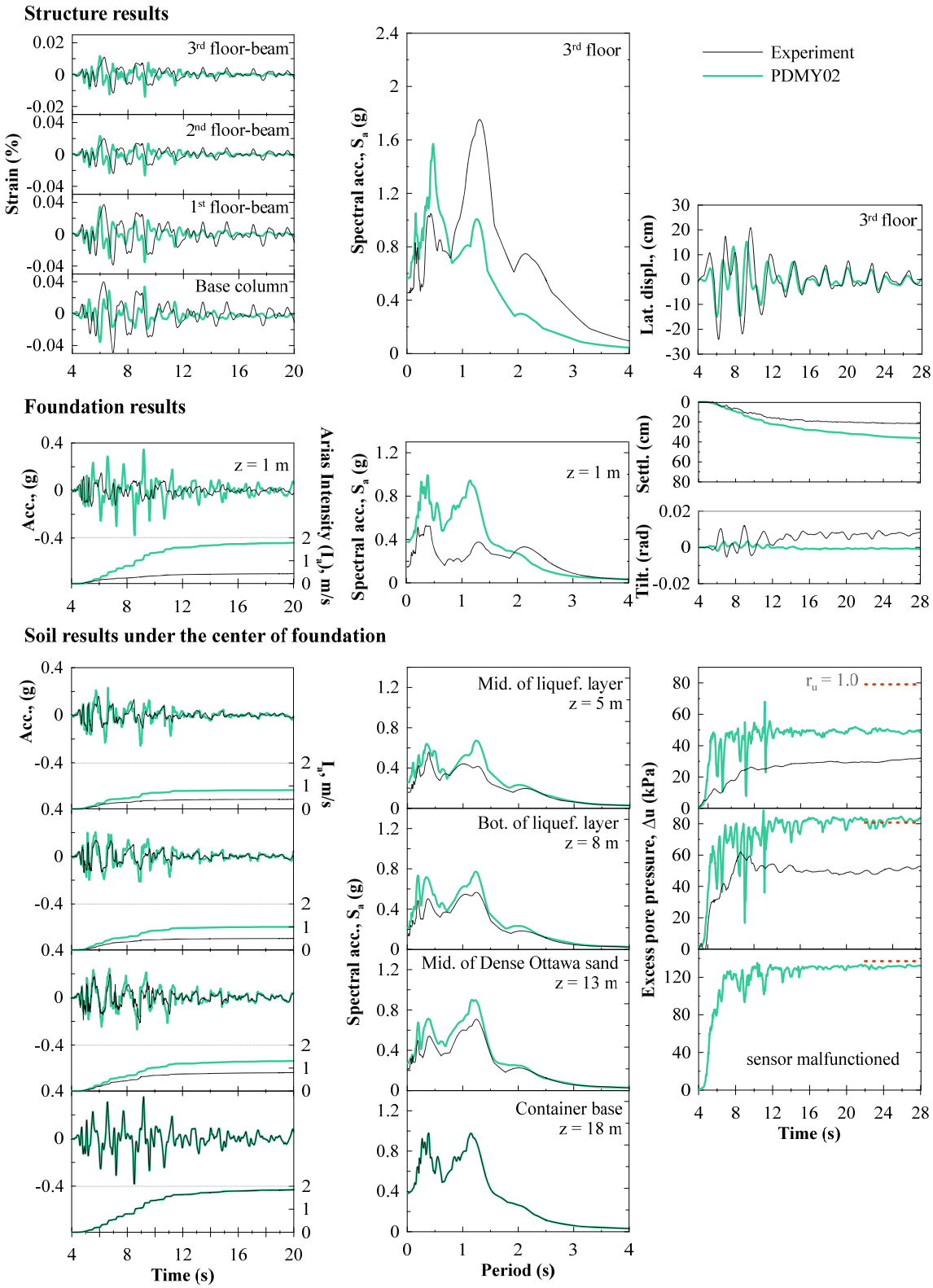

Figure E.7 Comparison of numerical and experimental results for A2$_{DS-6}$

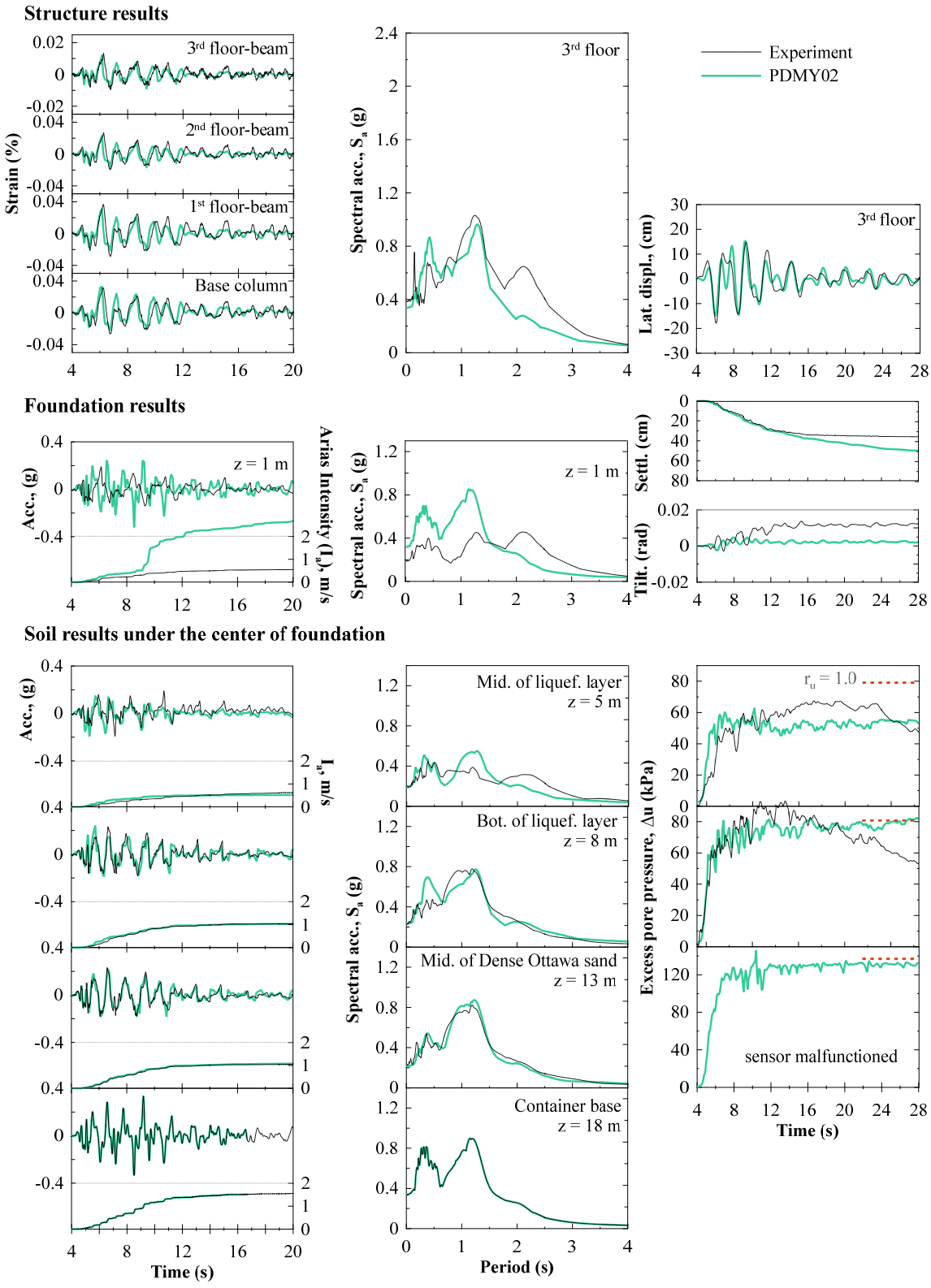

Figure E.8 Comparison of numerical and experimental results for A2$_{DR-6}$

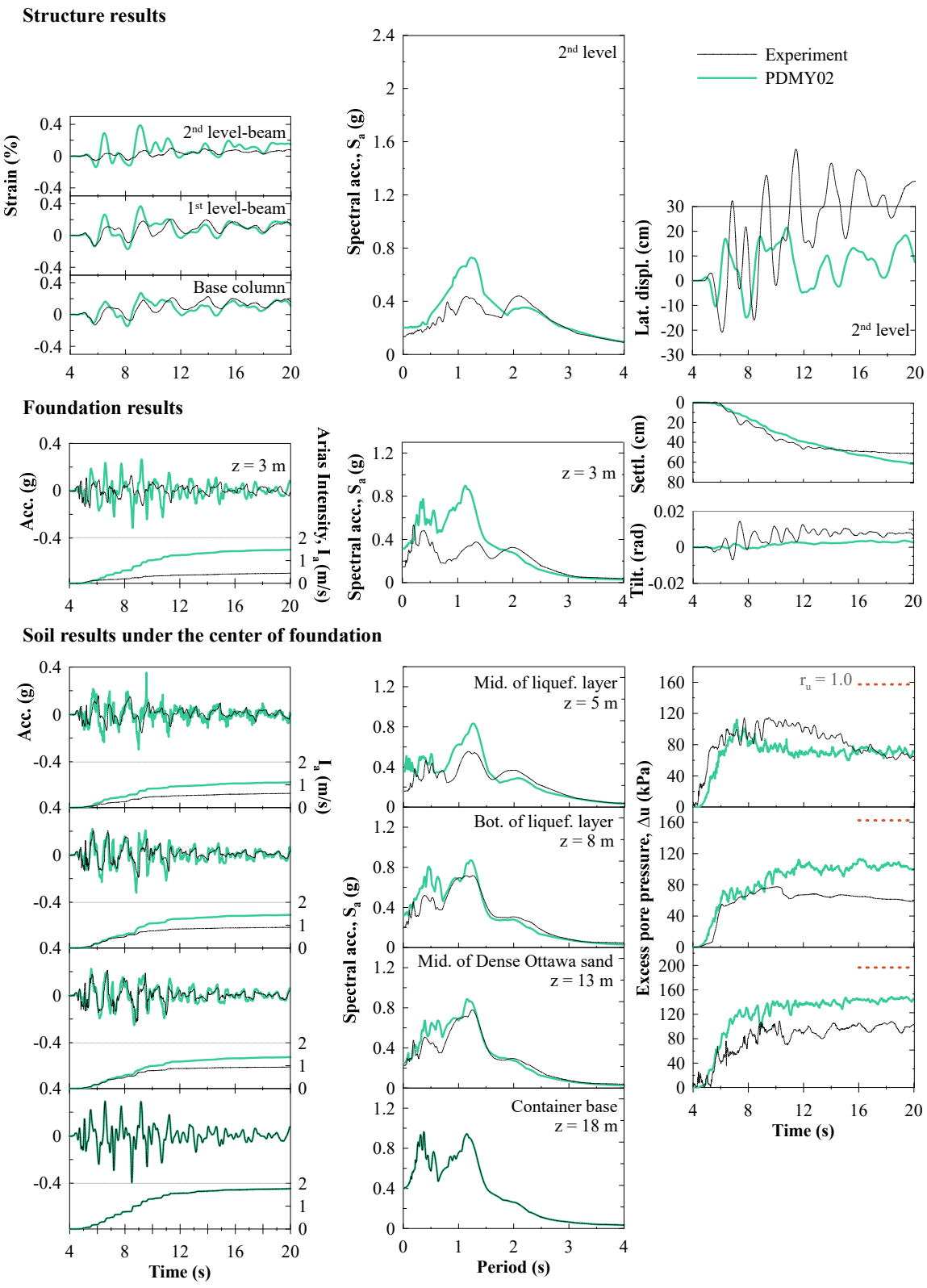

Figure E.9 Comparison of numerical and experimental results for B_{NM-6}

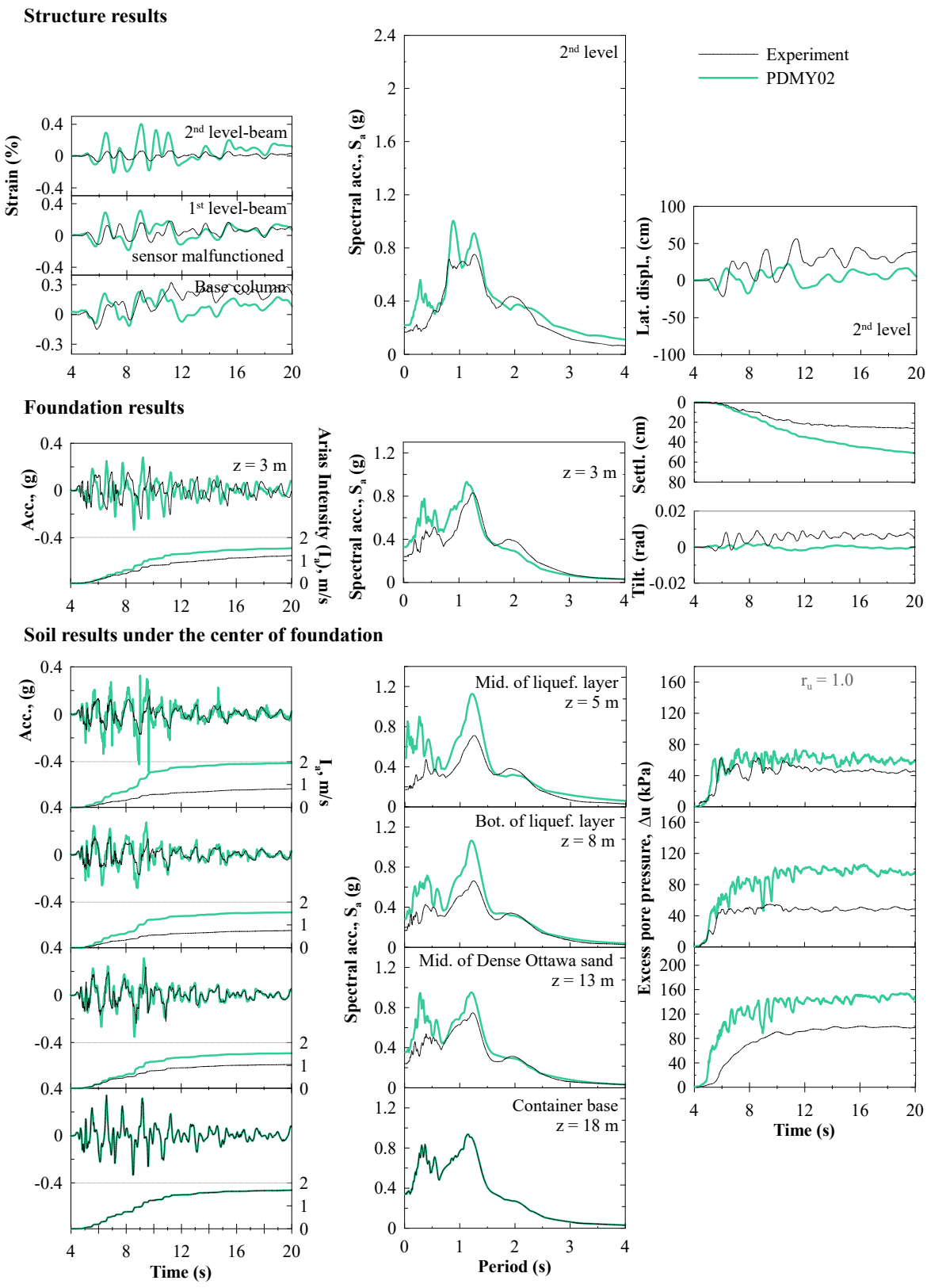

Figure E.10 Comparison of numerical and experimental results for $B_{DS\text{-}6}$

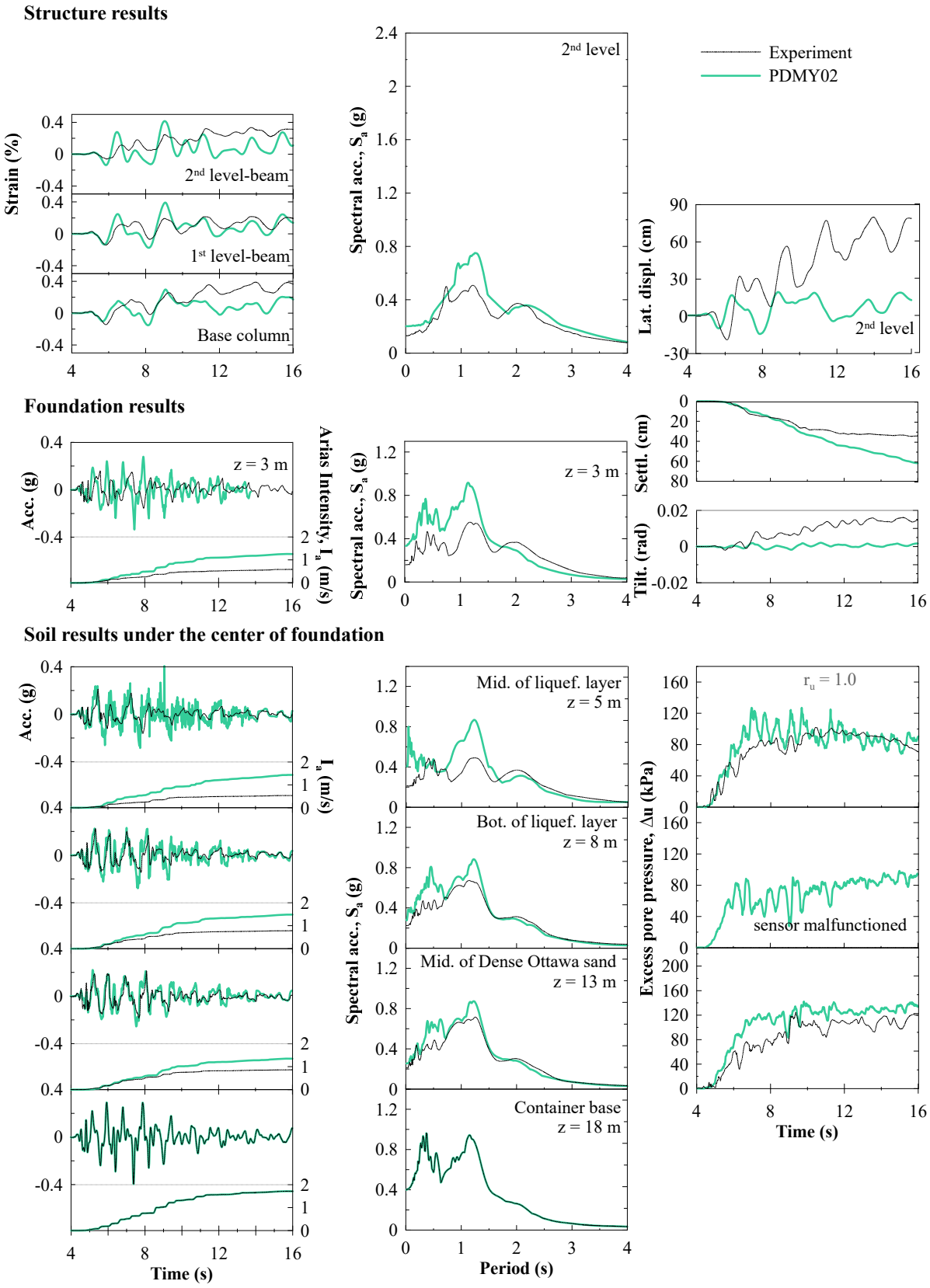

Figure E.11 Comparison of numerical and experimental results for $B_{DR\text{-}6}$